

Advances in Civil Engineering

Multi-Field Coupling Behaviors of Rock Mass and Rock Discontinuity

Lead Guest Editor: Zhi Cheng Tang

Guest Editors: Jun Peng Zou, Suguang Xiao, and Xiaobo Zhang





Multi-Field Coupling Behaviors of Rock Mass and Rock Discontinuity

Advances in Civil Engineering

Multi-Field Coupling Behaviors of Rock Mass and Rock Discontinuity

Lead Guest Editor: Zhi Cheng Tang

Guest Editors: Jun Peng Zou, Suguang Xiao, and
Xiaobo Zhang



Copyright © 2022 Hindawi Limited. All rights reserved.

This is a special issue published in "Advances in Civil Engineering." All articles are open access articles distributed under the Creative Commons Attribution License, which permits unrestricted use, distribution, and reproduction in any medium, provided the original work is properly cited.





Chief Editor

Cumaraswamy Vipulanandan, USA
















Associate Editors

Chiara Bedon , Italy
Constantin Chalioris , Greece
Ghassan Chehab , Lebanon
Ottavia Corbi, Italy
Mohamed ElGawady , USA
Husnain Haider , Saudi Arabia
Jian Ji , China
Jiang Jin , China
Shazim A. Memon , Kazakhstan
Hossein Moayedi , Vietnam
Sanjay Nimbalkar, Australia
Giuseppe Oliveto , Italy
Alessandro Palmeri , United Kingdom
Arnaud Perrot , France
Hugo Rodrigues , Portugal
Victor Yepes , Spain
Xianbo Zhao , Australia

Academic Editors

José A.F.O. Correia, Portugal
Glenda Abate, Italy
Khalid Abdel-Rahman , Germany
Ali Mardani Aghabaglou, Turkey
José Aguiar , Portugal
Afaq Ahmad , Pakistan
Muhammad Riaz Ahmad , Hong Kong
Hashim M.N. Al-Madani , Bahrain
Luigi Aldieri , Italy
Angelo Aloisio , Italy
Maria Cruz Alonso, Spain
Filipe Amarante dos Santos , Portugal
Serji N. Amirkhania, USA
Eleftherios K. Anastasiou , Greece
Panagiotis Ch. Anastasopoulos , USA
Mohamed Moafak Arbili , Iraq
Farhad Aslani , Australia
Siva Avudaiappan , Chile
Ozgur BASKAN , Turkey
Adewumi Babafemi, Nigeria
Morteza Bagherpour, Turkey
Qingsheng Bai , Germany
Nicola Baldo , Italy
Daniele Baraldi , Italy

Eva Barreira , Portugal
Emilio Bastidas-Arteaga , France
Rita Bento, Portugal
Rafael Bergillos , Spain
Han-bing Bian , China
Xia Bian , China
Huseyin Bilgin , Albania
Giovanni Biondi , Italy
Hugo C. Biscaia , Portugal
Rahul Biswas , India
Edén Bojórquez , Mexico
Giosuè Boscato , Italy
Melina Bosco , Italy
Jorge Branco , Portugal
Bruno Briseghella , China
Brian M. Broderick, Ireland
Emanuele Brunesi , Italy
Quoc-Bao Bui , Vietnam
Tan-Trung Bui , France
Nicola Buratti, Italy
Gaochuang Cai, France
Gladis Camarini , Brazil
Alberto Campisano , Italy
Qi Cao, China
Qixin Cao, China
Iacopo Carnacina , Italy
Alessio Cascardi, Italy
Paolo Castaldo , Italy
Nicola Cavalagli , Italy
Liborio Cavaleri , Italy
Anush Chandrappa , United Kingdom
Wen-Shao Chang , United Kingdom
Muhammad Tariq Amin Chaudhary, Kuwait
Po-Han Chen , Taiwan
Qian Chen , China
Wei Tong Chen , Taiwan
Qixiu Cheng, Hong Kong
Zhanbo Cheng, United Kingdom
Nicholas Chileshe, Australia
Prinya Chindaprasirt , Thailand
Corrado Chisari , United Kingdom
Se Jin Choi , Republic of Korea
Heap-Yih Chong , Australia
S.H. Chu , USA
Ting-Xiang Chu , China

Zhaofei Chu , China
Wonseok Chung , Republic of Korea
Donato Ciampa , Italy
Gian Paolo Cimellaro, Italy
Francesco Colangelo, Italy
Romulus Costache , Romania
Liviu-Adrian Cotfas , Romania
Antonio Maria D'Altri, Italy
Bruno Dal Lago , Italy
Amos Darko , Hong Kong
Arka Jyoti Das , India
Dario De Domenico , Italy
Gianmarco De Felice , Italy
Stefano De Miranda , Italy
Maria T. De Risi , Italy
Tayfun Dede, Turkey
Sadik O. Degertekin , Turkey
Camelia Delcea , Romania
Cristoforo Demartino, China
Giuseppe Di Filippo , Italy
Luigi Di Sarno, Italy
Fabio Di Trapani , Italy
Aboelkasim Diab , Egypt
Thi My Dung Do, Vietnam
Giulio Dondi , Italy
Jiangfeng Dong , China
Chao Dou , China
Mario D'Aniello , Italy
Jingtao Du , China
Ahmed Elghazouli, United Kingdom
Francesco Fabbrocino , Italy
Flora Faleschini , Italy
Dingqiang Fan, Hong Kong
Xueping Fan, China
Qian Fang , China
Salar Farahmand-Tabar , Iran
Ilenia Farina, Italy
Roberto Fedele, Italy
Guang-Liang Feng , China
Luigi Fenu , Italy
Tiago Ferreira , Portugal
Marco Filippo Ferrotto, Italy
Antonio Formisano , Italy
Guoyang Fu, Australia
Stefano Galassi , Italy

Junfeng Gao , China
Meng Gao , China
Giovanni Garcea , Italy
Enrique García-Macías, Spain
Emilio García-Taengua , United Kingdom
DongDong Ge , USA
Khaled Ghaedi, Malaysia
Khaled Ghaedi , Malaysia
Gian Felice Giaccu, Italy
Agathoklis Giaralis , United Kingdom
Ravindran Gobinath, India
Rodrigo Gonçalves, Portugal
Peilin Gong , China
Belén González-Fonteboa , Spain
Salvatore Grasso , Italy
Fan Gu, USA
Erhan Güneyisi , Turkey
Esra Mete Güneyisi, Turkey
Pingye Guo , China
Ankit Gupta , India
Federico Gusella , Italy
Kemal Hacıfendioglu, Turkey
Jianyong Han , China
Song Han , China
Asad Hanif , Macau
Hadi Hasanzadehshooiili , Canada
Mostafa Fahmi Hassanein, Egypt
Amir Ahmad Hedayat , Iran
Khandaker Hossain , Canada
Zahid Hossain , USA
Chao Hou, China
Biao Hu, China
Jiang Hu , China
Xiaodong Hu, China
Lei Huang , China
Cun Hui , China
Bon-Gang Hwang, Singapore
Jijo James , India
Abbas Fadhil Jasim , Iraq
Ahad Javanmardi , China
Krishnan Prabhakan Jaya, India
Dong-Sheng Jeng , Australia
Han-Yong Jeon, Republic of Korea
Pengjiao Jia, China
Shaohua Jiang , China

MOUSTAFA KASSEM , Malaysia
Mosbeh Kaloop , Egypt
Shankar Karuppannan , Ethiopia
John Kechagias , Greece
Mohammad Khajehzadeh , Iran
Afzal Husain Khan , Saudi Arabia
Mehran Khan , Hong Kong
Manoj Khandelwal, Australia
Jin Kook Kim , Republic of Korea
Woosuk Kim , Republic of Korea
Vaclav Koci , Czech Republic
Loke Kok Foong, Vietnam
Hailing Kong , China
Leonidas Alexandros Kouris , Greece
Kyriakos Kourousis , Ireland
Moacir Kripka , Brazil
Anupam Kumar, The Netherlands
Emma La Malfa Ribolla, Czech Republic
Ali Lakirouhani , Iran
Angus C. C. Lam, China
Thanh Quang Khai Lam , Vietnam
Luciano Lamberti, Italy
Andreas Lampropoulos , United Kingdom
Raffaele Landolfo, Italy
Massimo Latour , Italy
Bang Yeon Lee , Republic of Korea
Eul-Bum Lee , Republic of Korea
Zhen Lei , Canada
Leonardo Leonetti , Italy
Chun-Qing Li , Australia
Dongsheng Li , China
Gen Li, China
Jiale Li , China
Minghui Li, China
Qingchao Li , China
Shuang Yang Li , China
Sunwei Li , Hong Kong
Yajun Li , China
Shun Liang , China
Francesco Liguori , Italy
Jae-Han Lim , Republic of Korea
Jia-Rui Lin , China
Kun Lin , China
Shibin Lin, China

Tzu-Kang Lin , Taiwan
Yu-Cheng Lin , Taiwan
Hexu Liu, USA
Jian Lin Liu , China
Xiaoli Liu , China
Xuemei Liu , Australia
Zaobao Liu , China
Zhuang-Zhuang Liu, China
Diego Lopez-Garcia , Chile
Cristiano Loss , Canada
Lyan-Ywan Lu , Taiwan
Jin Luo , USA
Yanbin Luo , China
Jianjun Ma , China
Junwei Ma , China
Tian-Shou Ma, China
Zhongguo John Ma , USA
Maria Macchiaroli, Italy
Domenico Magisano, Italy
Reza Mahinroosta, Australia
Yann Malecot , France
Prabhat Kumar Mandal , India
John Mander, USA
Iman Mansouri, Iran
André Dias Martins, Portugal
Domagoj Matesan , Croatia
Jose Matos, Portugal
Vasant Matsagar , India
Claudio Mazzotti , Italy
Ahmed Mebarki , France
Gang Mei , China
Kasim Mermerdas, Turkey
Giovanni Minafò , Italy
Masoomah Mirrashid , Iran
Abbas Mohajerani , Australia
Fadzli Mohamed Nazri , Malaysia
Fabrizio Mollaioli , Italy
Rosario Montuori , Italy
H. Naderpour , Iran
Hassan Nasir , Pakistan
Hossein Nassiraei , Iran
Satheeskumar Navaratnam , Australia
Ignacio J. Navarro , Spain
Ashish Kumar Nayak , India
Behzad Nematollahi , Australia

Chayut Ngamkhanong , Thailand
Trung Ngo, Australia
Tengfei Nian, China
Mehdi Nikoo , Canada
Youjun Ning , China
Olugbenga Timo Oladinrin , United Kingdom
Oladimeji Benedict Olalusi, South Africa
Timothy O. Olawumi , Hong Kong
Alejandro Orfila , Spain
Maurizio Orlando , Italy
Siti Aminah Osman, Malaysia
Walid Oueslati , Tunisia
SUVASH PAUL , Bangladesh
John-Paris Pantouvakis , Greece
Fabrizio Paolacci , Italy
Giuseppina Pappalardo , Italy
Fulvio Parisi , Italy
Dimitrios G. Pavlou , Norway
Daniele Pellegrini , Italy
Gatheeshgar Perampalam , United Kingdom
Daniele Perrone , Italy
Giuseppe Piccardo , Italy
Vagelis Plevris , Qatar
Andrea Pranno , Italy
Adolfo Preciado , Mexico
Chongchong Qi , China
Yu Qian, USA
Ying Qin , China
Giuseppe Quaranta , Italy
Krishanu ROY , New Zealand
Vlastimir Radonjanin, Serbia
Carlo Rainieri , Italy
Rahul V. Ralegaonkar, India
Raizal Saifulnaz Muhammad Rashid, Malaysia
Alessandro Rasulo , Italy
Chonghong Ren , China
Qing-Xin Ren, China
Dimitris Rizos , USA
Geoffrey W. Rodgers , New Zealand
Pier Paolo Rossi, Italy
Nicola Ruggieri , Italy
JUNLONG SHANG, Singapore



Nikhil Saboo, India
Anna Saetta, Italy
Juan Sagaseta , United Kingdom
Timo Saksala, Finland
Mostafa Salari, Canada
Ginevra Salerno , Italy
Evangelos J. Sapountzakis , Greece
Vassilis Sarhosis , United Kingdom
Navaratnarajah Sathiparan , Sri Lanka
Fabrizio Scozzese , Italy
Halil Sezen , USA
Payam Shafigh , Malaysia
M. Shahria Alam, Canada
Yi Shan, China
Hussein Sharaf, Iraq
Mostafa Sharifzadeh, Australia
Sanjay Kumar Shukla, Australia
Amir Si Larbi , France
Okan Sirin , Qatar
Piotr Smarzewski , Poland
Francesca Sollecito , Italy
Rui Song , China
Tian-Yi Song, Australia
Flavio Stochino , Italy
Mayank Sukhija , USA
Piti Sukontasukkul , Thailand
Jianping Sun, Singapore
Xiao Sun , China
T. Tafsirojjan , Australia
Fujiao Tang , China
Patrick W.C. Tang , Australia
Zhi Cheng Tang , China
Weerachart Tangchirapat , Thailand
Xiabin Tao, China
Piergiorgio Tataranni , Italy
Elisabete Teixeira , Portugal
Jorge Iván Tobón , Colombia
Jing-Zhong Tong, China
Francesco Trentadue , Italy
Antonello Troncone, Italy
Majbah Uddin , USA
Tariq Umar , United Kingdom
Muahmmad Usman, United Kingdom
Muhammad Usman , Pakistan
Mucteba Uysal , Turkey

Ilaria Venanzi , Italy
Castorina S. Vieira , Portugal
Valeria Vignali , Italy
Claudia Vitone , Italy
Liwei WEN , China
Chunfeng Wan , China
Hua-Ping Wan, China
Roman Wan-Wendner , Austria
Chaohui Wang , China
Hao Wang , USA
Shiming Wang , China
Wayne Yu Wang , United Kingdom
Wen-Da Wang, China
Xing Wang , China
Xiuling Wang , China
Zhenjun Wang , China
Xin-Jiang Wei , China
Tao Wen , China
Weiping Wen , China
Lei Weng , China
Chao Wu , United Kingdom
Jiangyu Wu, China
Wangjie Wu , China
Wenbing Wu , China
Zhixing Xiao, China
Gang Xu, China
Jian Xu , China
Panpan , China
Rongchao Xu , China
HE YONGLIANG, China
Michael Yam, Hong Kong
Hailu Yang , China
Xu-Xu Yang , China
Hui Yao , China
Xinyu Ye , China
Zhoujing Ye, China
Gürol Yildirim , Turkey
Dawei Yin , China
Doo-Yeol Yoo , Republic of Korea
Zhanping You , USA
Afshar A. Yousefi , Iran
Xinbao Yu , USA
Dongdong Yuan , China
Geun Y. Yun , Republic of Korea


Hyun-Do Yun , Republic of Korea
Cemal YİĞİT , Turkey
Paolo Zampieri, Italy
Giulio Zani , Italy
Mariano Angelo Zanini , Italy
Zhixiong Zeng , Hong Kong
Mustafa Zeybek, Turkey
Henglong Zhang , China
Jiupeng Zhang, China
Tingting Zhang , China
Zengping Zhang, China
Zetian Zhang , China
Zhigang Zhang , China
Zhipeng Zhao , Japan
Jun Zhao , China
Annan Zhou , Australia
Jia-wen Zhou , China
Hai-Tao Zhu , China
Peng Zhu , China
QuanJie Zhu , China
Wenjun Zhu , China
Marco Zucca, Italy
Haoran Zuo, Australia
Junqing Zuo , China
Robert Černý , Czech Republic
Süleyman İpek , Turkey

Contents

Study on Catastrophe Information Characteristics of Water Inrush in Karst Tunnel by Drilling and Blasting Method

Jiaqi Guo , Erbo Wang, Yongbiao Lai , Zhenyu He, and Fan Chen
Research Article (23 pages), Article ID 9228569, Volume 2022 (2022)

Analysis of Mechanical Properties and Slope Stability of Red Bed Soft Rock: A Case Study in Xinjiang Irrigation Diversion Channel

Da Liu , Jianglin Gao, Fang Chen , Songtao Hu, Xiaohua Zhao , and Yan Li
Research Article (9 pages), Article ID 9453702, Volume 2022 (2022)

Study on Evolution Law and the Mechanical Mechanism of Strong Mine Tremors in a Deep Coal Mine

Chao Wang, Man Wang, Siyuan Gong, Junpeng Zou, and Kunbo Wu 
Research Article (10 pages), Article ID 1066833, Volume 2022 (2022)

Predicting Tunnel Groundwater Inflow by Geological Investigation Using Horizontal Directional Drilling Technology

Xialin Liu 
Review Article (12 pages), Article ID 6578331, Volume 2022 (2022)


A Study of a Flow Model in Dual Permeability Reservoir Based on Similar Structure Theory

Tianhong Zhou , Jie Shen , Man Wang, and Yun Wu
Research Article (12 pages), Article ID 1303558, Volume 2022 (2022)

Experimental Study on Gas Permeability Semiempirical Model of Granite after Heat Treatment

Jinquan Wu 
Research Article (7 pages), Article ID 2812413, Volume 2022 (2022)

Differential Analysis and Prediction Optimization of Ground Surface Settlement Induced by Quasi-Rectangular Shield and Pipe Jacking Tunnelling

Xue Liu, Peinan Li , Jun Liu, Zeyu Dai, Peixin Chen, Xiaoyong Kou, and Jie Fan
Research Article (14 pages), Article ID 3884494, Volume 2022 (2022)

Research Article

Study on Catastrophe Information Characteristics of Water Inrush in Karst Tunnel by Drilling and Blasting Method

Jiaqi Guo ¹, Erbo Wang,¹ Yongbiao Lai ², Zhenyu He,³ and Fan Chen¹

¹School of Civil Engineering, Henan Polytechnic University, Jiaozuo 454003, China

²China Construction Railway Investment Construction Group Ltd, Beijing 102601, China

³Henan Geological Engineering Survey Institute Co., Ltd., Zhengzhou 450001, Henan, China

Correspondence should be addressed to Yongbiao Lai; 48084108@qq.com

Received 7 August 2022; Accepted 13 September 2022; Published 23 November 2022

Academic Editor: Xiaobo Zhang

Copyright © 2022 Jiaqi Guo et al. This is an open access article distributed under the Creative Commons Attribution License, which permits unrestricted use, distribution, and reproduction in any medium, provided the original work is properly cited.

When building tunnels in karst areas, the hidden high-pressure water-bearing karst caves are prone to cause geological disasters such as water inrush and mud gushing. In order to study the disaster process of water and mud resistant rock mass with the quasi-masonry structure and the accompanying catastrophe information of water inrush in karst tunnels by the drilling and blasting method, a new method based on the DEM and fictitious joint technology is adopted to simulate the evolution process of water inrush and study the evolutionary characteristics of catastrophe information like seepage pressure and displacement under the conditions of different joint inclination angles, tunnel depths, and thickness of the water and mud resistant rock mass. The research results show that (1) the seepage pressure and displacement in the water and mud resistant rock mass decrease and increase respectively along the water and mud resistant rock mass from top to bottom in the process of water inrush. (2) The displacement and seepage pressure in the water and mud-resistant rock mass increases with the increase of the joint inclination angle. The greater the tunnel depth and thickness of the water and mud-resistant rock mass, the faster the propagation speed of the fissure zone. (3) With the increase of the water and mud-resistant rock mass thickness, the failure mode of the tunnel outburst layer structure gradually changes from the overall collapse to the partial collapse of the vault to form a relatively stable slump arch. The research results can provide some guidance for tunnel construction in the karst tunnel.

1. Introduction

Karst geomorphology accounts for about 15% of the global area and is one of the most frequent adverse geological in the construction of underground transportation, water conservancy tunnels, and mine roadways and it is also a thorny problem faced by the world's engineers [1, 2]. As an important part of the traffic road network, tunnel projects often encounter various karst geological disasters during the construction of karst areas due to complex engineering geology and hydrogeology, development of karst disaster-causing structures, and active groundwater. The water inrush is one of the most common and extremely destructive geological disasters [3, 4]. Hundreds of water inrush accidents have occurred in China during the past few years, which have caused serious economic loss, engineer

casualties, and environmental disruption [5–11] (see Figure 1). During the construction of the Maluqing tunnel of the Yichang-Wanzhou railway, 19 serious water and mud inrush disasters occurred one after another, and the instantaneous water inrush reached the highest level of railway construction in the world. Only two extraordinarily serious disasters occurred on January 21, 2006, and April 11, 2008, resulting in 15 deaths [12]. During the construction of the Yesanguan Tunnel, there was a sudden influx of water and mud, and the water inflow was about $5 \times 10^4 \text{ m}^3/\text{h}$. The disaster-caused 52 constructors to be trapped, many pieces of equipment washed, and 10 people dead [12]. When the construction mileage of the Telmo Tunnel for the Chengdu-Kunming railway capacity expansion and reconstruction project reached DK274 + 580, several water inrush disasters occurred on the tunnel face, which caused project shutdown

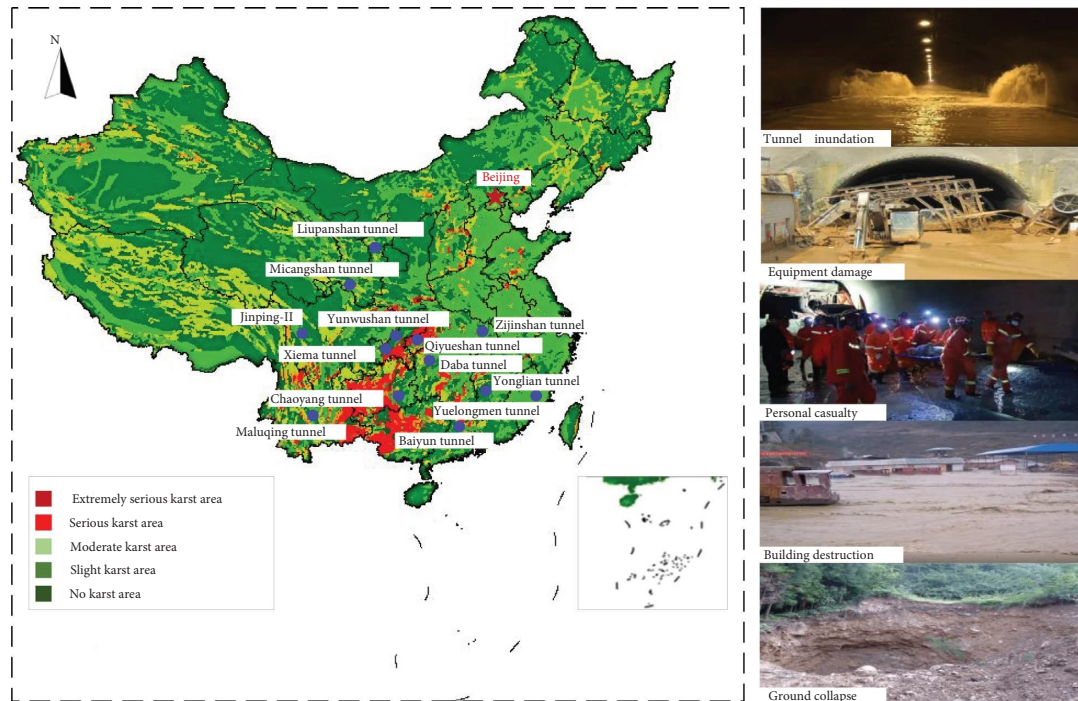


FIGURE 1: The typical water inrush accidents of karst tunnels and their effects in China.

and delay [13]. The main reason for the above disasters is that the research on the water inrush mechanism in karst tunnels drops behind the development of production practice. Therefore, it is of great significance to carry out relevant research about the evolution process and catastrophe evolution information characteristics of water inrush for prevention and control of water inrush in karst tunnel.

Water inrush in karst tunnels is a destabilizing process of outburst-proof rock mass under the coupled influence of multiple factors and is conditions and triggered by excavation disturbance. At present, many scholars have done a lot of research on the mechanism and the information characteristics of water inrush through theoretical analysis, model tests, and numerical simulation. In the field of theoretical analysis, Li et al. [14] deduced the critical water pressure of cracks that occurred through compression shear expansion failure under the action of explosion stress waves. Xu et al. [15] used slice synthetic and elastic mechanics theory to analyze the mechanical properties of filled karst caves located at the top, bottom, and sides of the tunnel and deduced the minimum safe thickness formula of water and mud resistant rock mass. Fu et al. [16] deduced the formula for calculating the minimum safe thickness of the karst cave below the excavation tunnel. Guo et al. [17] used a theoretical analysis method to study the stability of the outburst prevention rock mass between the tunnel and the latent cavity. The above instability criterion based on theoretical analysis can only be used to judge the rock stability in the final stage of the water inrush of karst tunnels. The water inrush in a tunnel involves crack initiation, expansion, and penetration, which is a highly nonlinear problem in mathematics. The model test can accurately simulate the

rupture and instability processes of the outburst-preventing rock mass and truly reproduce the evolution process of water inrush. In the field of the model test, Li et al. [18] conducted a model test to discuss the influence of in-situ stress, water pressure, and the thickness of water and mud-resistant rock mass on the water inrush in karst tunnels. Kirsch [19] and Idinger et al. [20] studied the stability of tunnel faces through physical model tests. Huang et al. [21] carried out a model test to study the influence of excavation disturbance and aquifer thickness on the seepage failure of the intact water and mud-resistant rock mass. Due to the limitation of measuring elements number and their function, it is impossible to obtain enough macro information about the water inrush and it is also unable to grasp the meso information such as crack initiation, crack propagation, and the complex interaction process between water and rock. While the numerical simulation method could solve the above problems, and it has the function of visualizing the rupture process of outburst-proof rock.

At present, many scholars have used the numerical simulation method to study water inrush. Liu et al. [22] used the finite difference numerical calculation program to analyze the evolution law of the plastic zone, displacement field, and seepage field of the rock mass when the tunnel excavation approached the upper and lower lateral karst pipes. Zhao et al. [23] used the finite element numerical calculation method to study the influence of cavity sizes and the distances between the cavity at the top and the tunnel on the stability of surrounding rock. Qin et al. [24] used FLAC3D to analyze the distribution of releasable elastic strain energy and failure zone under different hidden cave widths. Lei [25] used a three-dimensional finite difference

program to simulate and analyze the influence of a water-filled hidden cave at the top on the stability of surrounding rock and established a mathematical model for predicting the minimum safe thickness between the cave and the tunnel through multiple regression analysis. Most of the above numerical simulations regard the outburst-proof rock as a porous continuous medium and do not consider the impact of tunnel blasting excavation. It also cannot simulate the formation, expansion, and penetration process of the seepage channel and the collapse process of surrounding rock. The discrete element method has obvious advantages in simulating the fracture process of rock mass, and it has been widely used in the field of civil engineering.

In view of this, this paper uses a new method based on the DEM considering the structural characteristics of water and mud resistant rock mass and explosive load in drilling and blasting method. This method is employed to simulate the process of water inrush in karst tunnel and reveals the influence law of joint dip angle, tunnel depth, and the thickness of water and mud resistant rock mass on the catastrophe characteristics of water inrush in karst tunnel. Moreover, the evolution characteristics of catastrophe information, including water pressure and displacement, were analyzed. The research results had great significance for early warning and prevention of water inrush in karst tunnel.

2. The Fluid-Structure Interaction Theory and Calculation Model Based on DEM

2.1. Numerical Solution Method

2.1.1. Motion Equation of Deformed Block. In the discrete element, the rock mass is divided into multiple deformable blocks by joints, and the deformable block is discretized into multiple constant-strain triangular elements by the grid, and the movement and deformation of the entire rock mass are reflected by the movement of the cell points [26].

(1) The equation of motion at cell point i :

$$\mu_i = \frac{\sum f_i + f_p + f_b}{m} + g_i, \quad (1)$$

$$f_i = f_i^c + \sum_{l=1}^M \left[\sigma_{ij} \sum_{k=1}^N \left(n_j^k \Delta s^k \right) \right]_l,$$

$$f_b = 2(\rho C_p) v_n, \quad (2)$$

$$C_p = \sqrt{\frac{K + 4G/3}{\rho}},$$

where μ_i is the displacement of the cell point; m is the concentrated mass assigned to the cell point; g_i is the acceleration of gravity; M is the number of elements connected to node I ; N is the number of element nodes; n_j^k is the unit normal vector of the k -th edge in the element; Δl^k is the length of the k -th edge in the element; d is the thickness of the element; Δs^k is the element area; σ_{ij} is the element stress; f_i^c is the contact force between the blocks. f_p is the water pressure; f_b is the blasting load; ρ is the medium density; v_n is the longitudinal wave velocity; C_p is the normal velocity of

the input particle; K is bulk modulus; and G is the shear modulus.

2.1.2. Laws of Fluid Motion. Assuming that the joints and fissures are smooth walls, the fluid flow in the joints and fissures follows Darcy's law [27]:

$$q_i = -k(p - \rho_f x_f g_i), \quad (3)$$

where k is the rock mobility coefficient; ρ_f is the fluid density; g_i is the components of the gravity vector.

2.1.3. Simulation Principle of Fracture Seepage

(1) Influence of Stress Field on Seepage Field. Discrete element numerical analysis can analyze the flow of fluid in the fissures of the impermeable block system. It is assumed that in the process of fluid flowing in the fissures, the rock mass is an impermeable material, and the fluid affects the displacement of the rock mass and changes the normal displacement of the block, thereby affecting the joint width affects the permeability of the jointed rock mass, namely [27]:

$$a = a_0 + \mu_n. \quad (4)$$

(2) Influence of Seepage Field on Stress Field. The change of the pressure of the fluid in the joint on the joint wall causes the change in the stress state of the rock mass, and finally affects the deformation of the fractured rock mass. The osmotic pressure increase caused by the confluence of the fluid at a point is [27]:

$$\Delta q = \frac{k_w}{V} (Q\Delta t - \Delta V), \quad (5)$$

where k_w is the bulk modulus of the fluid; Q is the total flow of the fluid entering the node; ΔV is the volume change. After deformation, the fluid penetration pressure and penetration force (see Figure 2) are as follows:

$$p = p_0 + k_w Q \frac{\Delta t}{V} - k_w \frac{\Delta V}{V_m}, \quad (6)$$

$$F_i = p n_i L, \quad (7)$$

where F_i is the seepage force of the joint and fissure; L is the length of the joint and fissure; and V_m is the mean volume. Substitute formula (7) into the f_i in formula (2), the displacement of the grid point under the influence of seepage pressure can be calculated, and the effect of the seepage pressure on the stress can be calculated.

2.2. Computation Model of Discrete Element Numerical

2.2.1. Water and Mud Resistant Rock Mass with the Quasi-Masonry Structure. The karst geological conditions are extremely complex. However, most of the existing numerical simulations assume that the karst strata are continuous homogeneous materials, and the influence of blasting,

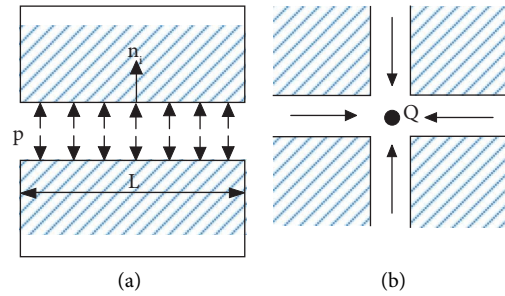


FIGURE 2: Effect of seepage pressure on stress field. (a) The effect of fluid on the block. (b) Increase in block seepage pressure.

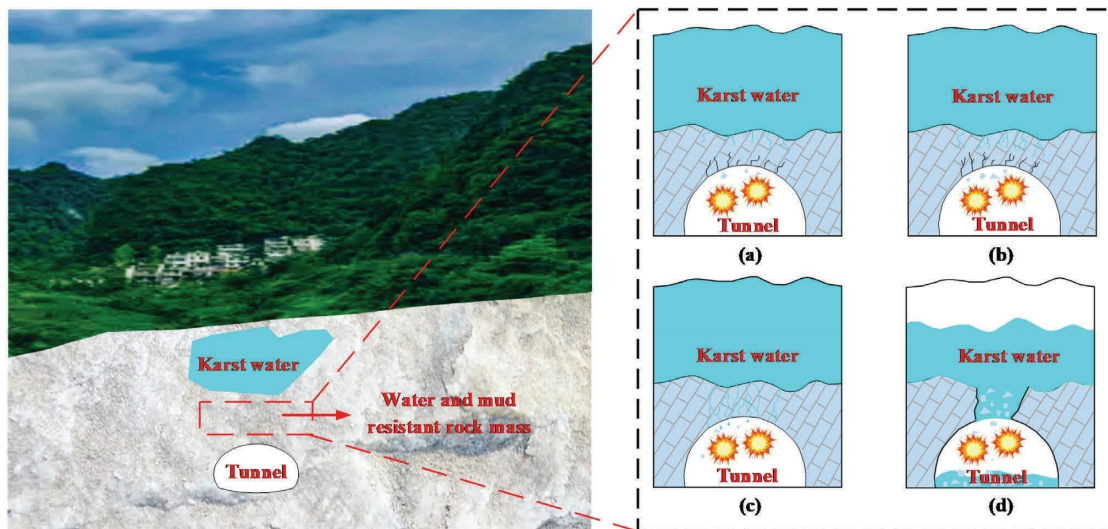


FIGURE 3: Sketch of the quasi-masonry structure of water and mud-resistant rock mass and water inrush process. (a) Crack initiation is induced by blasting excavation and hydraulic pressure. (b) Crack dilation in the surrounding rock. (c) Crack network and leakage. (d) Water inrush.

excavation disturbance, structural characteristics of rock mass, and discontinuous surfaces such as bedding, joints, and fissures are ignored [3, 4, 28, 29]. In fact, the rock in karst strata has an obvious bedding structure such as foliated rock, and there is a set of joints orthogonal to the bedding, as shown in Figure 3. The left side of Figure 3 shows the structural characteristics of limestone in the karst area and the spatial relationship between karst water cavities and tunnels. The right side of Figure 3 is a schematic diagram of the water inrush disaster process of the karst tunnel under the disturbance of blasting excavation. As shown in Figure 3, the process of water inrush disaster is the result of the initiation, expansion, and penetration of the initial discontinuity under the combined action of blasting excavation and karst water pressure. Moreover, most of the existing studies simplify the karst shape into circular (two-dimensional) or spherical (three-dimensional) holes, which are far from the actual karst shape. So, in order to better simulate and analyze the dynamic evolution process of information characteristics, this paper uses the discrete element software that can consider the blasting excavation effect and crack development, simplify the karst cavity into an ellipse, and perform a series of numerical simulations about karst tunnel water inrush implements.

2.2.2. Numerical Model and Boundary Conditions. The calculation size of the model is $80\text{ m} \times 80\text{ m}$, the cross-section of the tunnel is a three-centered circle, the height of the tunnel is 9.5 m , the tunnel span is 8.5 m , and the tunnel depth is 500 m . The hidden cavity above the tunnel is simplified to an ellipse with a 20 m long axis and a 12 m short axis, and the thickness of the outburst prevention layer between the tunnel and the cavity is 3 m . The thickness of the layered rock mass is 1 m , with a total of 80 layers (as shown in Figure 4).

According to the tunnel depth, the weight of the overlying rock is converted into a vertical uniform load and applied to the top boundary of the model. The left, right, and upper boundaries of the model are stress boundaries, and the values are $kq_0 + \gamma h$, $kq_0 + \gamma h$, and kq_0 , respectively. The bottom boundaries of the model are set as fixed boundaries. The karst water pressure is 1 MPa and the lateral pressure coefficient (k) is 1.2 , as shown in Figure 5. The mechanical properties of the numerical model are determined by the mechanical parameters of the blocks and the mechanical properties of the joints between the blocks. Since the block material is regarded as a large number of deformed microblocks, in order to balance the accuracy of the calculation. Therefore, the Mohr-Coulomb model (The

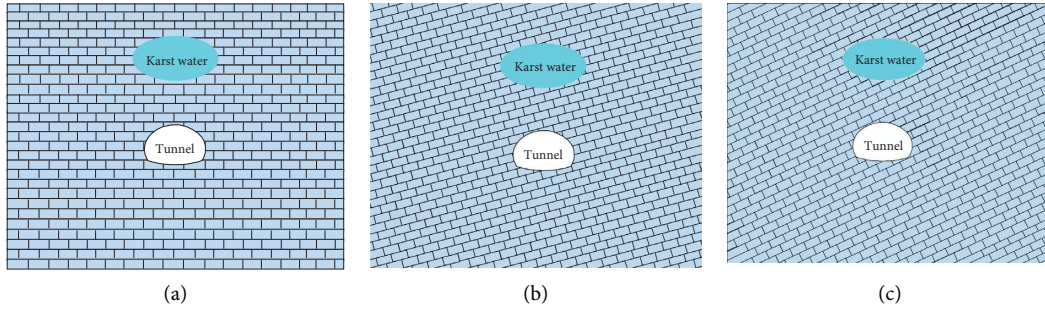
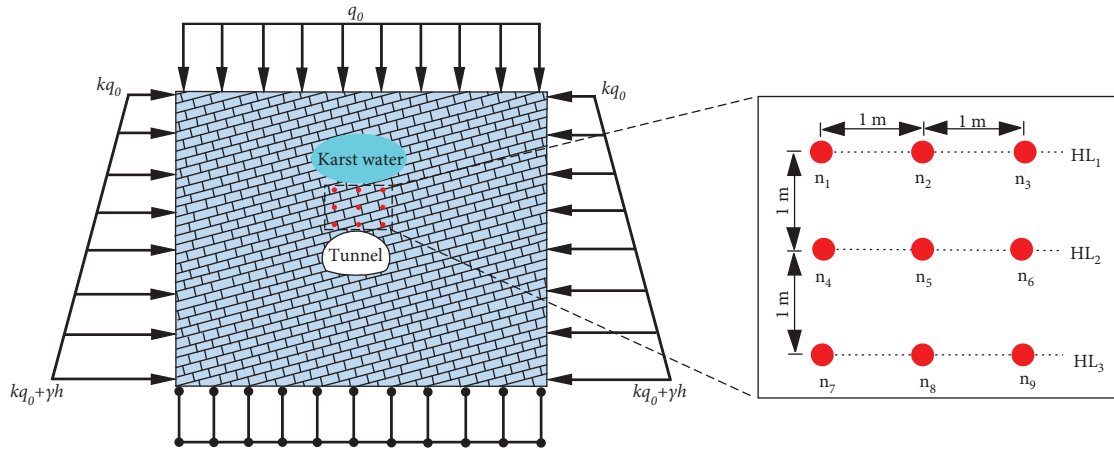
FIGURE 4: Simulation calculation model. (a) $\theta=0^\circ$. (b) $\theta=15^\circ$. (c) $\theta=30^\circ$.

FIGURE 5: Boundary conditions and measuring points arrangement.

TABLE 1: Block and joint mechanical parameters in numerical simulation [32].

Material	Unit weight	Elastic bulk modulus	Poisson's ratio	Friction angle	Cohesion (MPa)	Normal stiffness	Tangential stiffness
Block	24 kN/m ³	30 GPa	0.25	35°	0.8	—	—
Joint	—	—	—	33°	0.5	180 GPa/m	144 GPa/m

cons = 2) is used for the water and mud-resistant rock mass in the tunnel face; the Coulomb sliding model (The $j_{\text{cons}}=1$) is used for the layered joints. The mechanical parameters of the blocks and joints in the model are shown in Table 1. Nine measuring points were set up to obtain the variation law of displacement and water pressure in the water and mud-resistant rock mass under the action of blasting excavation and high karst water pressure, as shown in Figure 5. In the process of dynamic calculation, the model boundary is a nonreflective boundary. According to the research literature [30, 31], the blasting load curve is triangular, and the peak value of the equivalent blasting load is 30 MPa. The load rise time is 0.009 s, and the positive pressure action time is 0.04 s.

2.2.3. Numerical Simulation Scheme. According to the existing research [33–35], the layered joints angle, the tunnel depth, and the outburst prevention rock thickness have an important impact on the stability of the surrounding rock in karst tunnels. Therefore, this paper designs the simulation scheme shown in Table 2 to study the influence of these

influencing factors on the catastrophic mechanism of water inrush in karst tunnel.

3. Simulation Results and Discussion

3.1. Catastrophe Information of Water Inrush in Karst Tunnel under Different Joint Inclination Angles

3.1.1. Evolution Characteristics of Displacement under Different Joint Inclination Angles. Figure 6 is the evolution process of the displacement values of the water and mud resistant rock mass under the conditions that the tunnel depth is 500 m, the thickness of water and mud resistant rock mass is 3 m, and the joint inclination angles are 0°, 15°, and 30°, respectively.

Under the continuous action of blasting load, the water and mud-resistant rock masses located at different joint inclination angles have different degrees of displacement. When the inclination angle of the joint is 0°, the surrounding rock of the tunnel is in a stable state as a whole, and the vertical displacement of the water and mud-resistant rock mass is relatively small (At $t=7s$, the displacement is

TABLE 2: Numerical calculation scheme.

Number	Influencing factors		
	Joint inclination (°)	Tunnel depth (m)	The thickness of water and mud-resistant rock mass (m)
1	0	500	3
2	15	500	3
3	30	500	3
4	15	200	3
5	15	500	3 </td
6	15	800	3
7	15	500	2
8	15	500	3
9	15	500	4

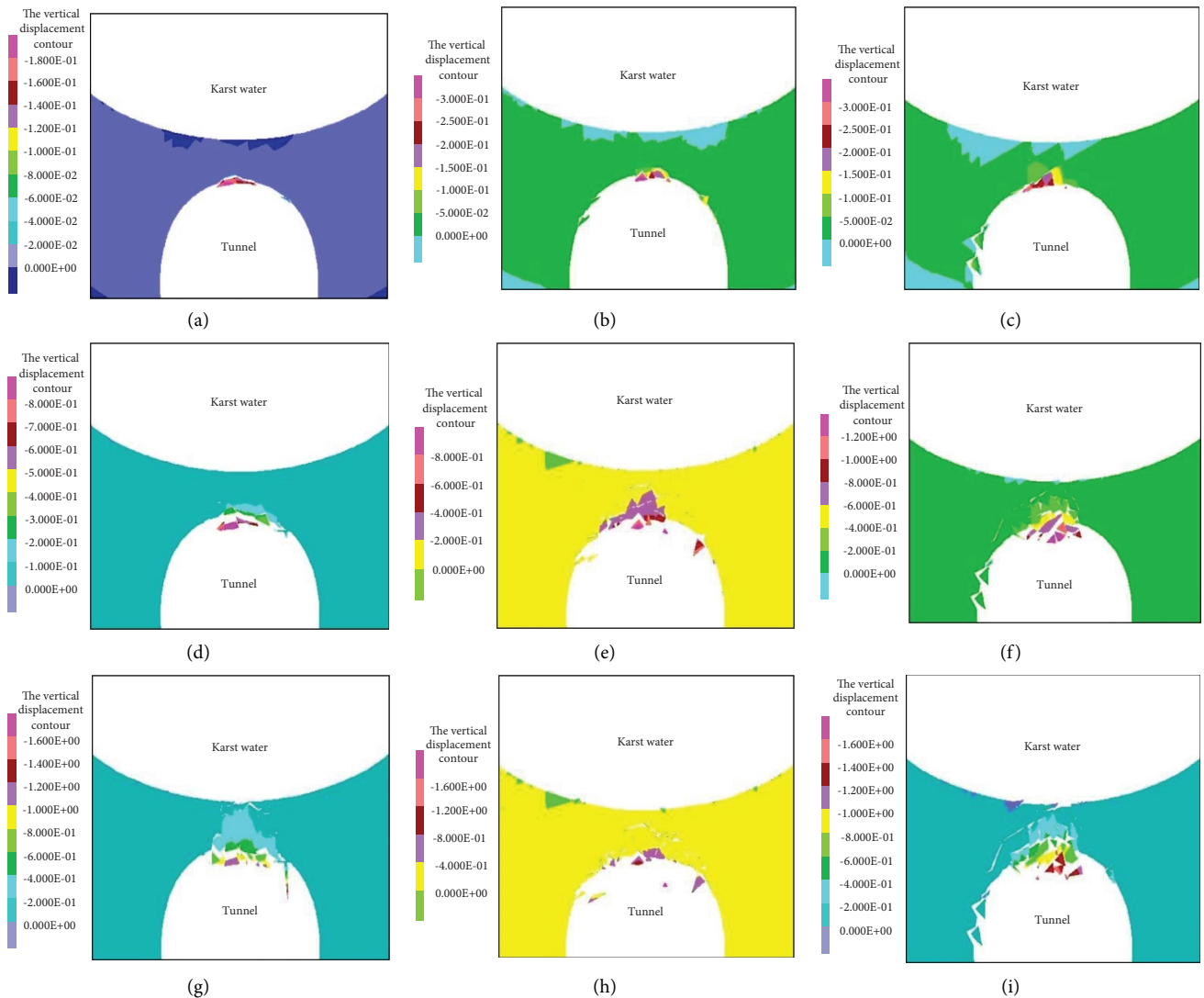


FIGURE 6: Continued.

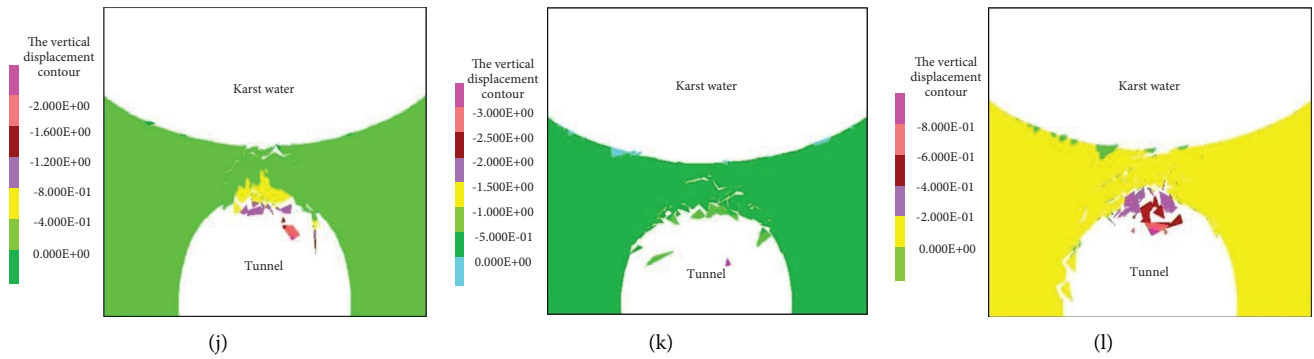


FIGURE 6: Evolution characteristics of displacement under different joint inclination angles. (a) $t = 1$ s, $\theta = 0^\circ$. (b) $t = 1$ s, $\theta = 15^\circ$. (c) $t = 1$ s, $\theta = 30^\circ$. (d) $t = 3$ s, $\theta = 0^\circ$. (e) $t = 3$ s, $\theta = 15^\circ$. (f) $t = 3$ s, $\theta = 30^\circ$. (g) $t = 5$ s, $\theta = 0^\circ$. (h) $t = 5$ s, $\theta = 15^\circ$. (i) $t = 5$ s, $\theta = 30^\circ$. (j) $t = 7$ s, $\theta = 0^\circ$. (k) $t = 7$ s, $\theta = 15^\circ$. (l) $t = 7$ s, $\theta = 30^\circ$.

-0.34 m; the negative sign indicates that the displacement is vertically downward in the y -direction). However, as the inclination angle of the joints increased to 15° and 30° , the fracture degree and vertical displacement in the water and mud-resistant rock mass increased significantly (At $t = 7$ s, the displacements are -0.56 m and -0.64 m, an increase of 64.7% and 88.2%, respectively). The reason is that the increase of the inclination angle of the joints reduces the stability of the surrounding rock. Under the combined action of blasting and excavation disturbance and joint inclination, the stress stored in the surrounding rock is further released, and the cracks in the rock stratum rapidly sprout and expand, resulting in further expansion of the damaged area. Especially when the inclination angle of the joint is 30° , there are obvious blocks falling off, and the number and connectivity of the cracks in the water and mud-resistant rock mass increase rapidly, which makes the instability of the water and mud-resistant rock mass rapidly increase. Therefore, the higher the inclination angle of the joints, the more unstable the water and mud resistant rock mass is, and the more significant the effects of blasting load are, the more serious the fracture of the water and mud resistant rock mass is, the weaker the anti-outburst ability, and the more prone to water inrush in the tunnel.

Figure 7 shows the evolution process of the vertical displacement of each measuring point in the water and mud-resistant rock mass. Comparing the vertical displacement of each measuring point at the same joint inclination angle, it can be seen that the displacement change values increase significantly with the increase of blasting action time, and the displacement change values of the measuring points that are close to the tunnel excavation surface are significantly higher than those of other measuring points. Taking the joint inclination angle $\theta = 15^\circ$ and selecting the measuring points n_7 - n_9 on HL₃ as an example, when the blasting load action time $t = 1$ s, the y -direction displacement values are -0.025 m, -0.223 m, -0.179 m (the negative sign indicates that the displacement is vertically downward in the y -direction); when the blasting load action time $t = 5$ s, the y -direction displacements values are -0.284 m, -0.489 m, -0.463 m. With the continuous action of the blast stress wave, the cracks in the water and mud-resistant rock mass

quickly initiate, expand, and penetrate each other, which makes the displacement of the measuring point on the side close to the tunnel profile increase significantly. At the same time, the displacement of n_8 on the measuring surface HL₃ is higher than that of n_7 or n_9 , and correspondingly, the vertical displacement growth of n_3 and n_5 on HL₁ and HL₂ is higher. This shows that the degree of fragmentation at the vault of the tunnel is relatively serious during the blasting excavation process.

3.1.2. Evolution Characteristics of Seepage Pressure under Different Joint Inclination Angles. Figure 8 shows the evolution characteristics of seepage pressure value of the water and mud resistant rock mass under different joint inclination angles when the tunnel depth is 500 m, the thickness of water and mud resistant rock mass is 3 m. The joint inclination angles of the three columns in Figure 8 are 0° , 15° , and 30° , respectively.

It can be seen from Figure 8 that with the continuous increase of the inclination angle of the joints, the seepage area and the expansion degree of the cracks in the water and mud-resistant rock mass increase significantly under the continuous action of the blasting load. Before the tunnel is excavated, a stable seepage field has been formed near the cavity. The blasting and unloading of the surrounding rock induce significant changes in the seepage field, especially in the water and mud-resistant rock mass between the cavern and the tunnel. When the inclination angle of the joint is 0° , under the dual action of karst water pressure and blasting excavation disturbance, relatively few cracks are generated in the upper and middle parts of the water and mud-resistant rock mass, and the cracks do not extend to the tunnel vault, and the macro water inrush channel is not formed ($t = 7$ s). With the continuous increase of the inclination angle of the joints, under the influence of the explosion stress wave, the seepage damage of the rock mass is gradually intensified, and the surrounding rock continues to have crack initiation and expansion ($\theta = 15^\circ$, $t = 7$ s). When the inclination angle of the joint increases to 30° , the stability of the water and mud-resistant rock mass is further reduced. Under the continuous action of the blasting load, its internal cracks rapidly expand

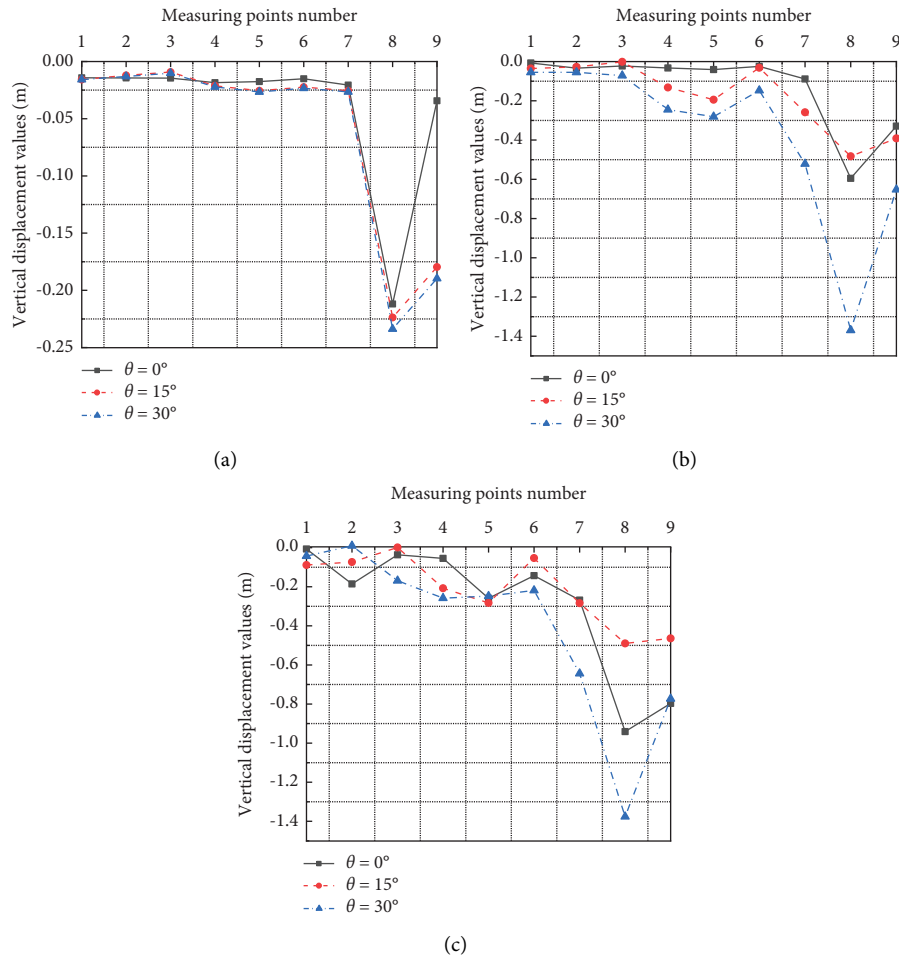


FIGURE 7: Evolution characteristics of displacement in the measuring points. (a) $t = 1$ s. (b) $t = 3$ s. (c) $t = 5$ s.

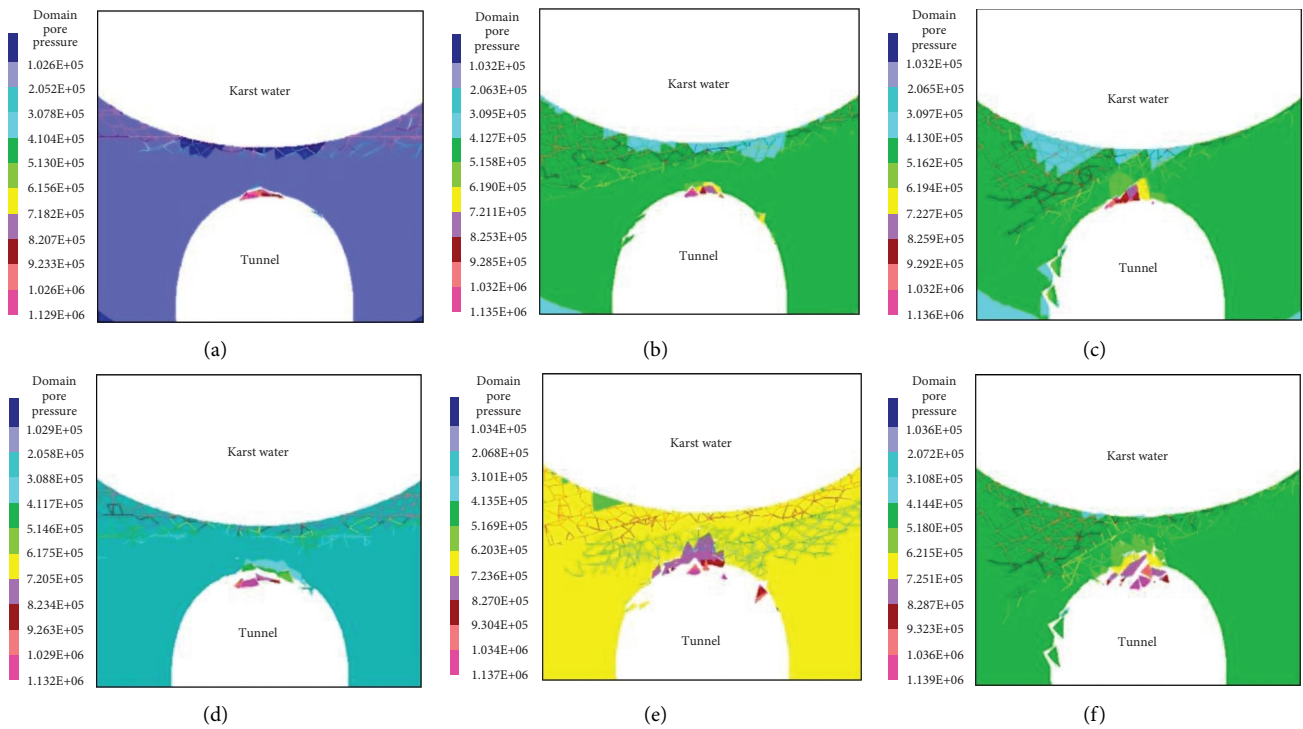


FIGURE 8: Continued.

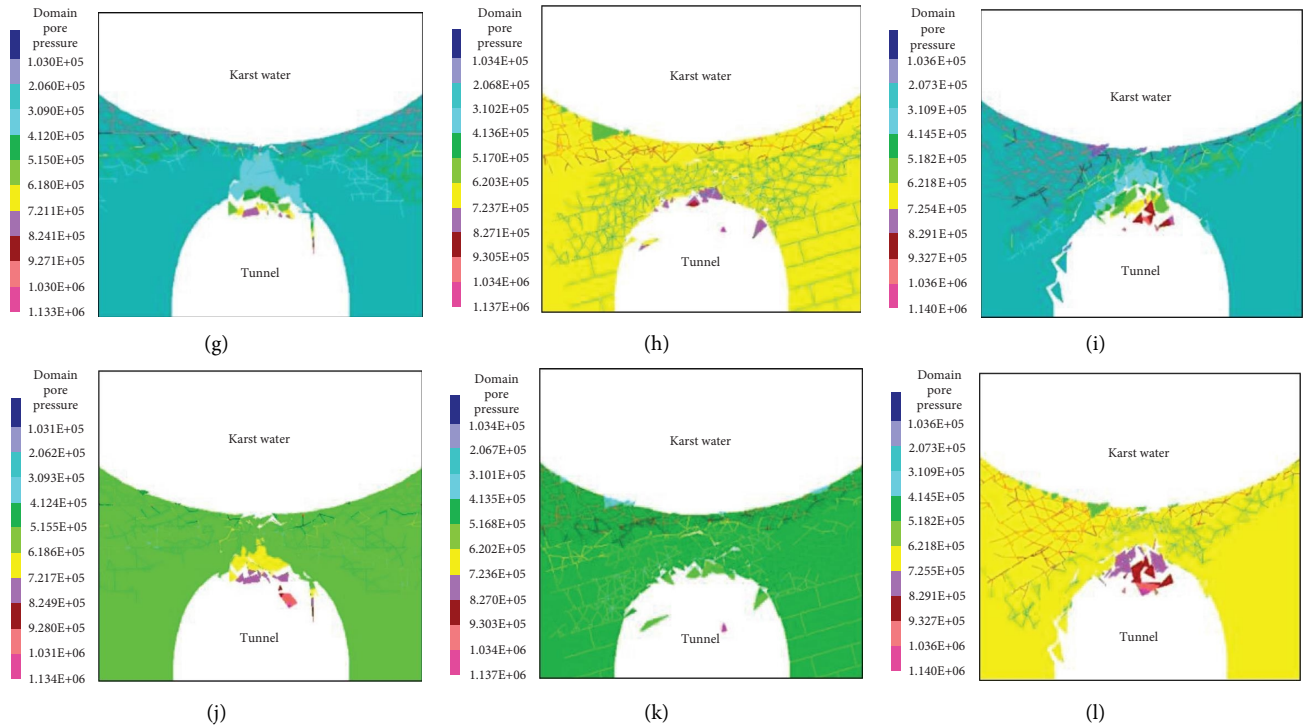


FIGURE 8: Evolution characteristics of seepage pressure under different joint inclination angles. (a) $t = 1 \text{ s}$, $\theta = 0^\circ$. (b) $t = 1 \text{ s}$, $\theta = 15^\circ$. (c) $t = 1 \text{ s}$, $\theta = 30^\circ$. (d) $t = 3 \text{ s}$, $\theta = 0^\circ$. (e) $t = 3 \text{ s}$, $\theta = 15^\circ$. (f) $t = 3 \text{ s}$, $\theta = 30^\circ$. (g) $t = 5 \text{ s}$, $\theta = 0^\circ$. (h) $t = 5 \text{ s}$, $\theta = 15^\circ$. (i) $t = 5 \text{ s}$, $\theta = 30^\circ$. (j) $t = 7 \text{ s}$, $\theta = 0^\circ$. (k) $t = 7 \text{ s}$, $\theta = 15^\circ$. (l) $t = 7 \text{ s}$, $\theta = 30^\circ$.

and penetrate to form a macroscopic water inrush channel; the rapid inflow of karst water into the tunnel further destabilizes the water and mud-resistant rock mass; and the water inrush disaster occurs in the karst tunnel ($t = 7 \text{ s}$). Therefore, the higher the inclination angle of the rock joints is, under the combined action of the continuous disturbance of blasting excavation and the karst water pressure, the primary fissures in the water and mud-resistant rock mass are easy to develop and penetrate, thus forming the water inrush channel.

Figure 9 shows the evolution process of seepage water pressure at each measuring point in the water and mud-resistant rock mass under different joint dip angles. Under the dual action of blasting and excavation disturbance and karst water pressure, the seepage pressure for each measuring point in the water and mud resistant rock mass gradually increased and showed a decreasing trend from top to bottom along the water and mud resistant rock mass. Since the measuring surface HL_1 is close to the karst cavity, the seepage pressures of the $n_1 \sim n_3$ measuring points quickly reach the karst water pressure of 1 MPa ($\theta = 0^\circ, 15^\circ$, and 30°). Under the continuous action of the blasting load, the fissures in the water and mud-resistant rock mass gradually expand and penetrate, and the karst water gradually penetrates the fissures under the action of hydraulic pressure. When the seepage pressure exceeds the critical fracture pressure of the fracture, the fracture begins to initiate and expand, and these fractures can extend to the $n_1 \sim n_6$ measuring points. Therefore, no matter whether the joint inclination angle is $0^\circ, 15^\circ$, or 30° , it can be seen from Figure 8 that the seepage

pressure values of the measuring points $n_1 \sim n_6$ are much higher than the seepage pressure values of $n_7 \sim n_9$ at the bottom of the water and mud-resistant rock mass. When the inclination of the joint is 0° , the water pressure of $n_4 \sim n_6$ is 0.12 MPa, 0.10 MPa, and 0.19 MPa, respectively (at $t = 3 \text{ s}$); When the inclination of the joint is 0° , the water pressure of $n_4 \sim n_6$ is 0.64 MPa, 0.45 MPa, 0.52 MPa (at $t = 3 \text{ s}$), respectively. It shows that due to the influence of the joint dip angle, the surrounding rock structure is unstable and prone to cracks, and the karst water easily penetrates into the aquifer, which increases the seepage pressure value and forms a wider range of seepage.

3.2. Catastrophe Information of Water Inrush in Karst Tunnel under Different Tunnel Depths

3.2.1. Evolution Characteristics of Displacement under Different Tunnel Depths. Figure 10 is the evolution process of the displacement value of the water and mud resistant rock mass under the conditions of joint inclination angle $\theta = 15^\circ$, the water and mud resistant rock mass are 3 m, the pressure of karst water is 2 MPa, and the depth of tunnel is 200 m, 500 m, and 800 m, respectively.

It can be seen from Figure 10 that the water and mud-resistant rock masses of karst tunnels in different burial depths are damaged to varying degrees and have obvious blocks falling under the disturbance of blasting excavation. When the buried depth of the tunnel is 200 m, with the increase of blasting load action time, the stability of the water

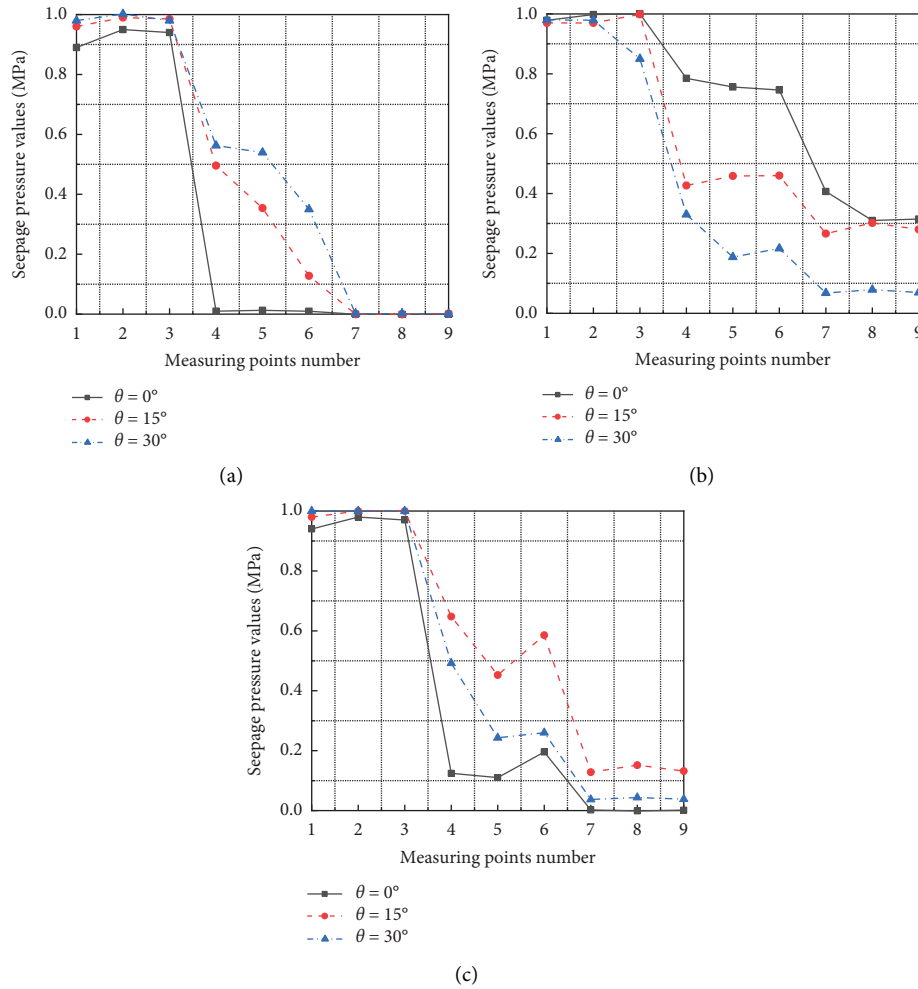


FIGURE 9: Evolution characteristics of seepage pressure in the measuring points.(a) $t = 1$ s. (b) $t = 3$ s. (c) $t = 5$ s.

and mud resistant rock mass gradually decreases, and the rock mass at the lower part of the water and mud resistant rock mass gradually collapses in a high area. When the blasting time $t = 7$ s, the entire water and mud-resistant rock mass is almost destroyed and some blocks fall to the bottom of the tunnel. When the buried depth of the tunnel is 500 m, the vertical displacement of the water and mud-resistant rock mass is relatively reduced, and the stability of the structure is enhanced. Although some blocks fell, the scale of the rock mass was reduced, and the water and mud-resistant rock mass did not completely collapse. When the depth of the tunnel was 800 m, the structural stability of the aquifer was the best. Although some of the blocks fell, the size of the blocks and the degree of fragmentation for the water and mud-resistant rock mass were relatively reduced. When the blasting time $t = 7$ s, the remaining complete thickness of the water and mud-resistant rock mass is the largest, and no obvious crack channel is formed in the rock layer. The numerical calculation results fully show that under the continuous action of blasting load, with the increase of tunnel burial depth, the stability of the water and mud-resistant rock mass and the ability to resist water inrush are gradually enhanced.

Figure 11 shows the evolution process of the vertical displacement of each measuring point located in the water and mud-resistant rock mass under the condition that the tunnel depth is 200 m, 500 m, and 800 m, respectively. It can be seen from Figure 11 that the vertical displacement change value and growth rate of each measuring point are different at different tunnel depths. When the depth of the tunnel is 200 m, the blasting action time is $t = 1$ s, 3 s, and 5 s, respectively, and the maximum displacement of each measuring point is -0.26 m, -1.08 m, -1.85 m (the negative sign indicates that the displacement is vertically downward in the y -direction), the displacement change value is significantly higher than the buried depth of 500 m and 800 m. This shows that the greater the buried depth of the tunnel, the stronger the overall stability of the water and mud-resistant rock mass, which can reduce the negative effect of blasting load on it. With the increase of blasting action time (at $t = 5$ s), the vertical displacement growth value of each measuring point on the measuring surfaces HL_1 and HL_2 decreases relatively, and the changing trend of each measuring point is relatively uniform. The vertical displacement growth value of each measuring point on HL_3 is relatively significant, indicating that the blasting excavation disturbance has a limited impact on the surrounding rock of

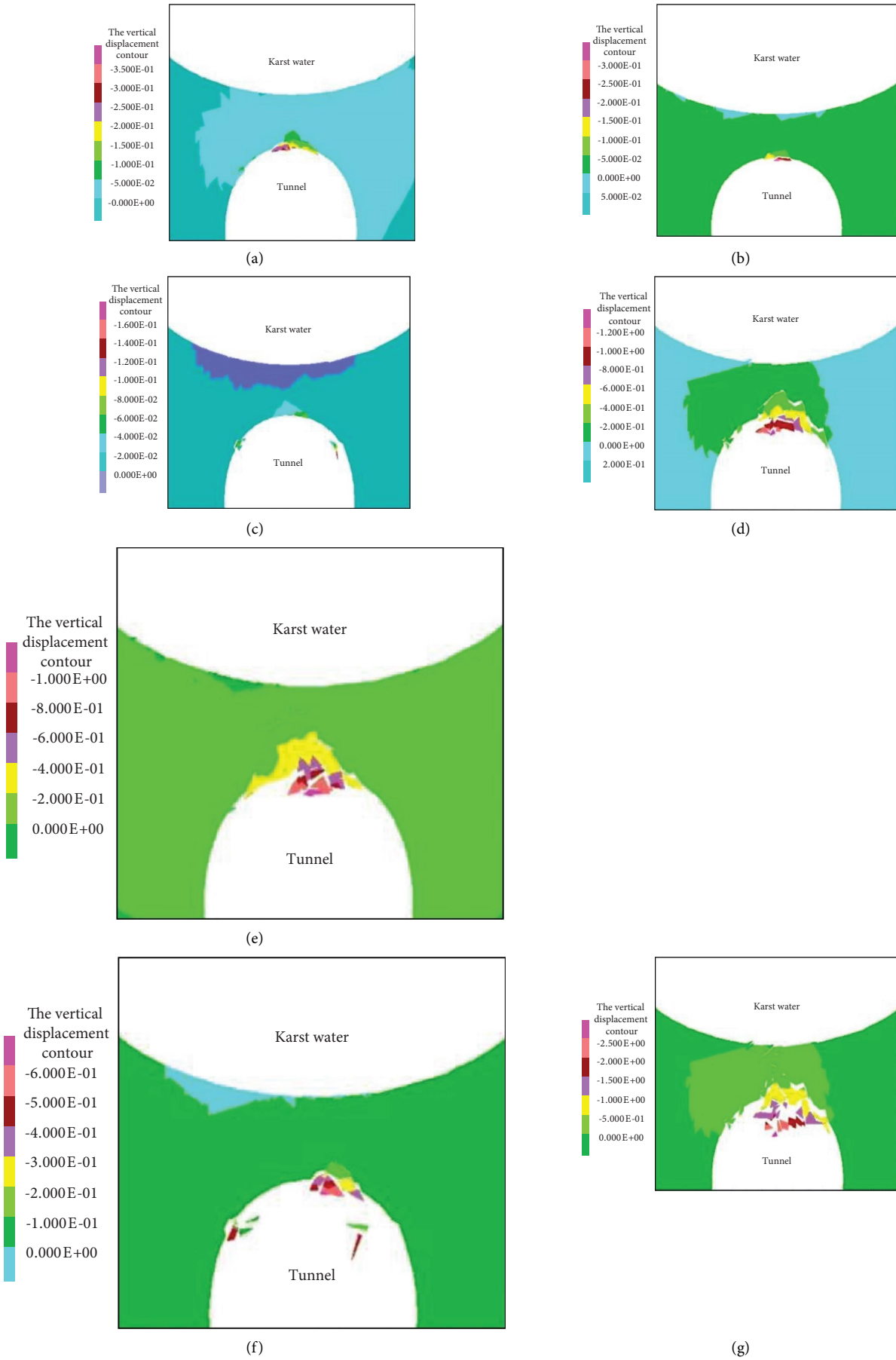


FIGURE 10: Continued.

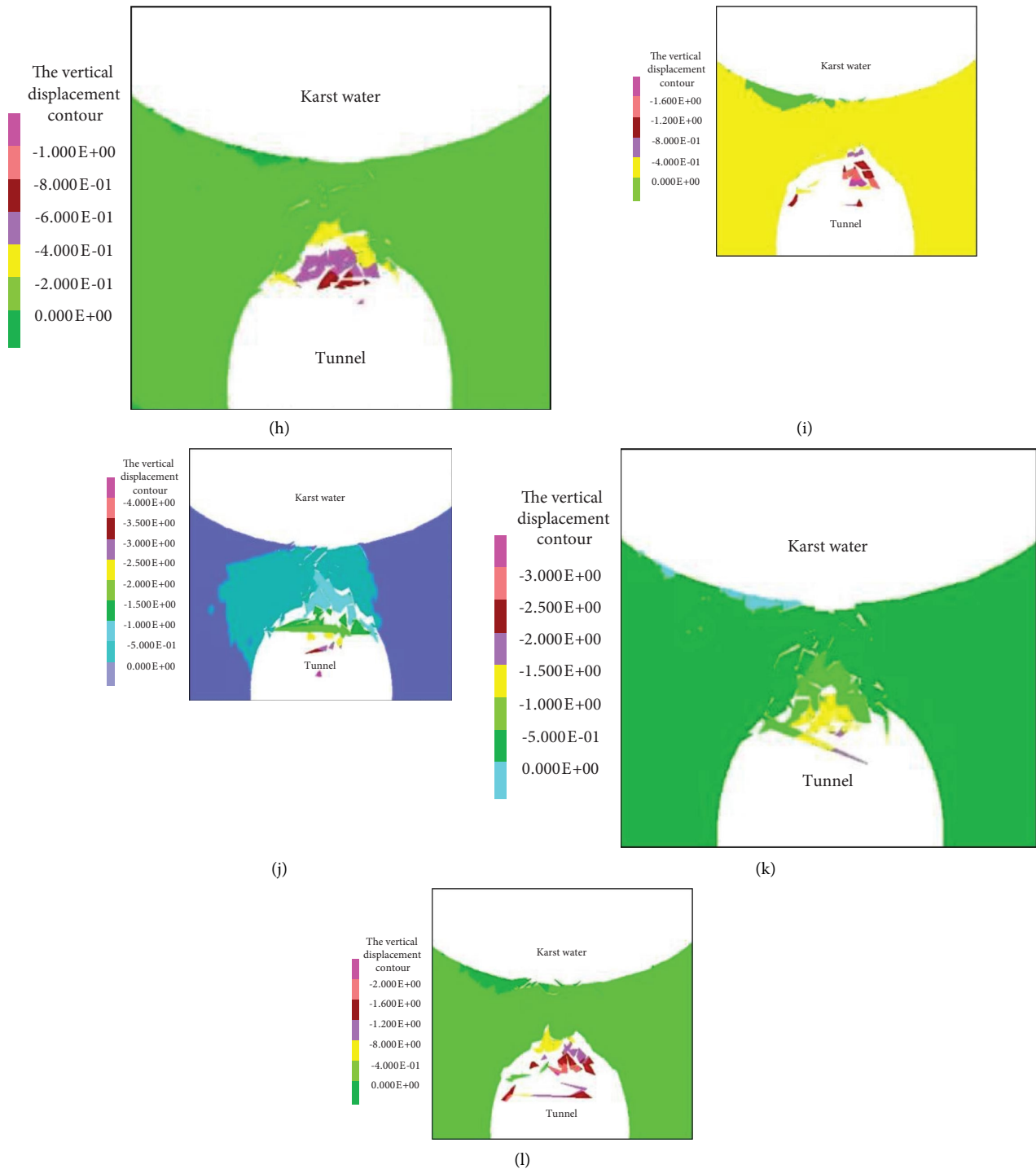


FIGURE 10: Evolution characteristics of displacement under different tunnel depths. (a) $t = 1 \text{ s}, h = 200 \text{ m}$. (b) $t = 1 \text{ s}, h = 500 \text{ m}$. (c) $t = 1 \text{ s}, h = 800 \text{ m}$. (d) $t = 3 \text{ s}, h = 200 \text{ m}$. (e) $t = 3 \text{ s}, h = 500 \text{ m}$. (f) $t = 3 \text{ s}, h = 800 \text{ m}$. (g) $t = 5 \text{ s}, h = 200 \text{ m}$. (h) $t = 5 \text{ s}, h = 500 \text{ m}$. (i) $t = 5 \text{ s}, h = 800 \text{ m}$. (j) $t = 7 \text{ s}, h = 200 \text{ m}$. (k) $t = 7 \text{ s}, h = 500 \text{ m}$. (l) $t = 7 \text{ s}, h = 800 \text{ m}$.

the tunnel and has a greater impact on the surrounding rock structure of the adjacent tunnel.

3.2.2. Evolution Characteristics of Seepage Pressure under Different Tunnel Depths. Figure 12 shows the evolution process of the seepage field of the water and mud resistant

rock mass under the conditions of the karst water pressure of 2 MPa, the thickness of water and mud resistant rock mass is 3 m, the joint inclination angle is 15° , and the tunnel depth is 200 m, 500 m, and 800 m, respectively.

Similar to the evolution process of the seepage field of the water and mud-resistant rock mass in Section 3.1.2, the karst water gradually infiltrated the vault and spandrel of the

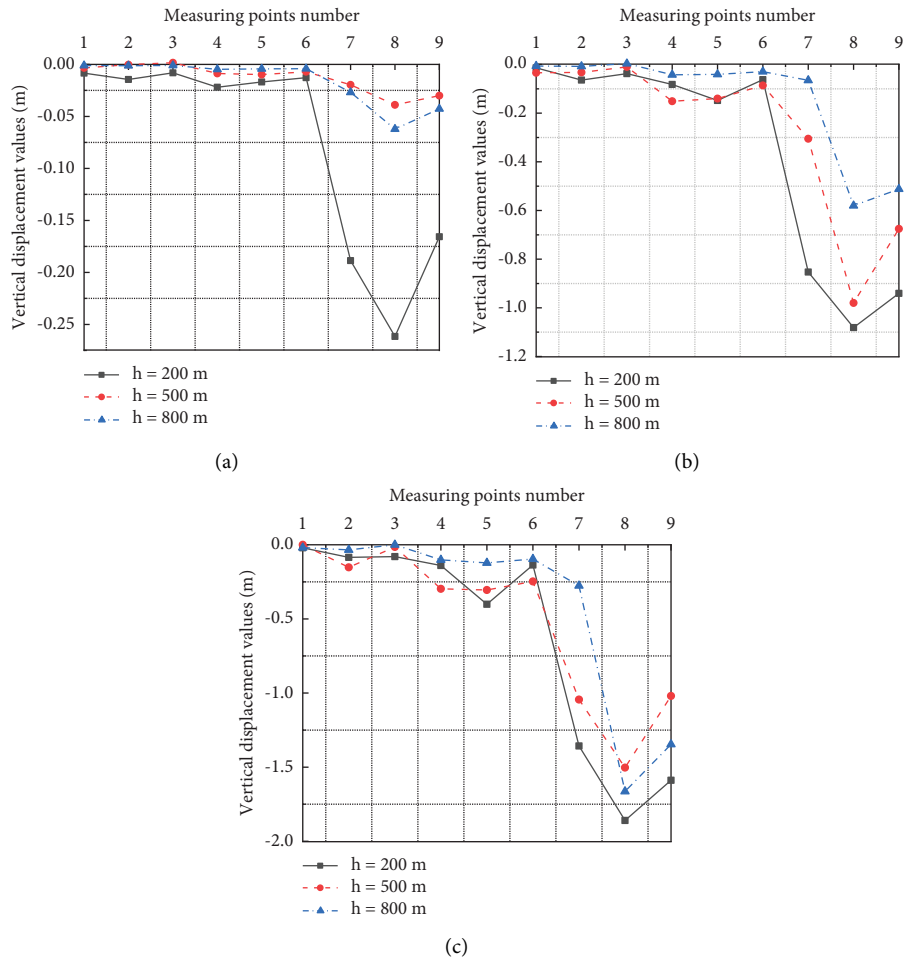


FIGURE 11: Evolution characteristics of displacement in the measuring points.(a) $t = 1$ s. (b) $t = 3$ s. (c) $t = 5$ s.

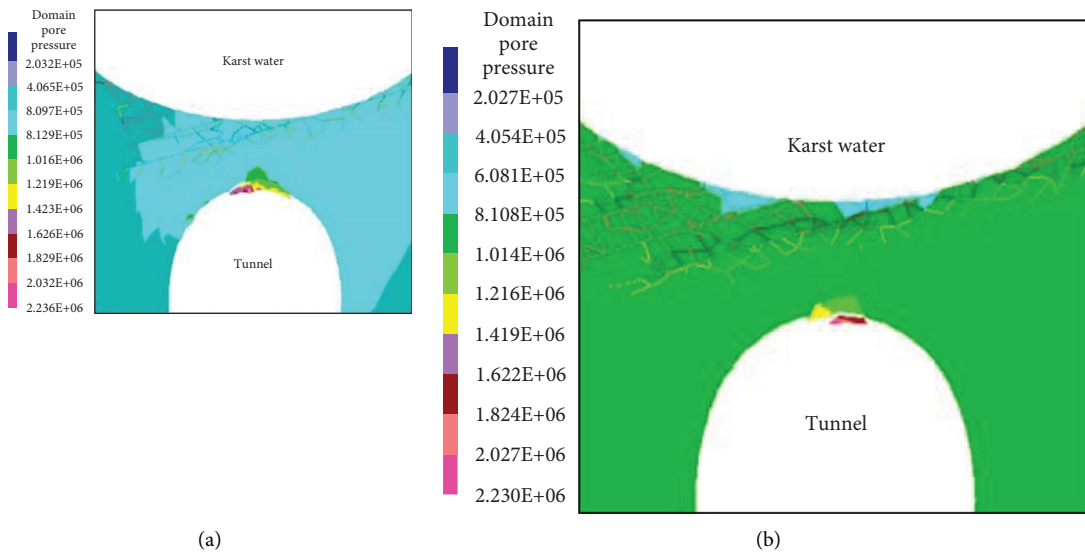


FIGURE 12: Continued.

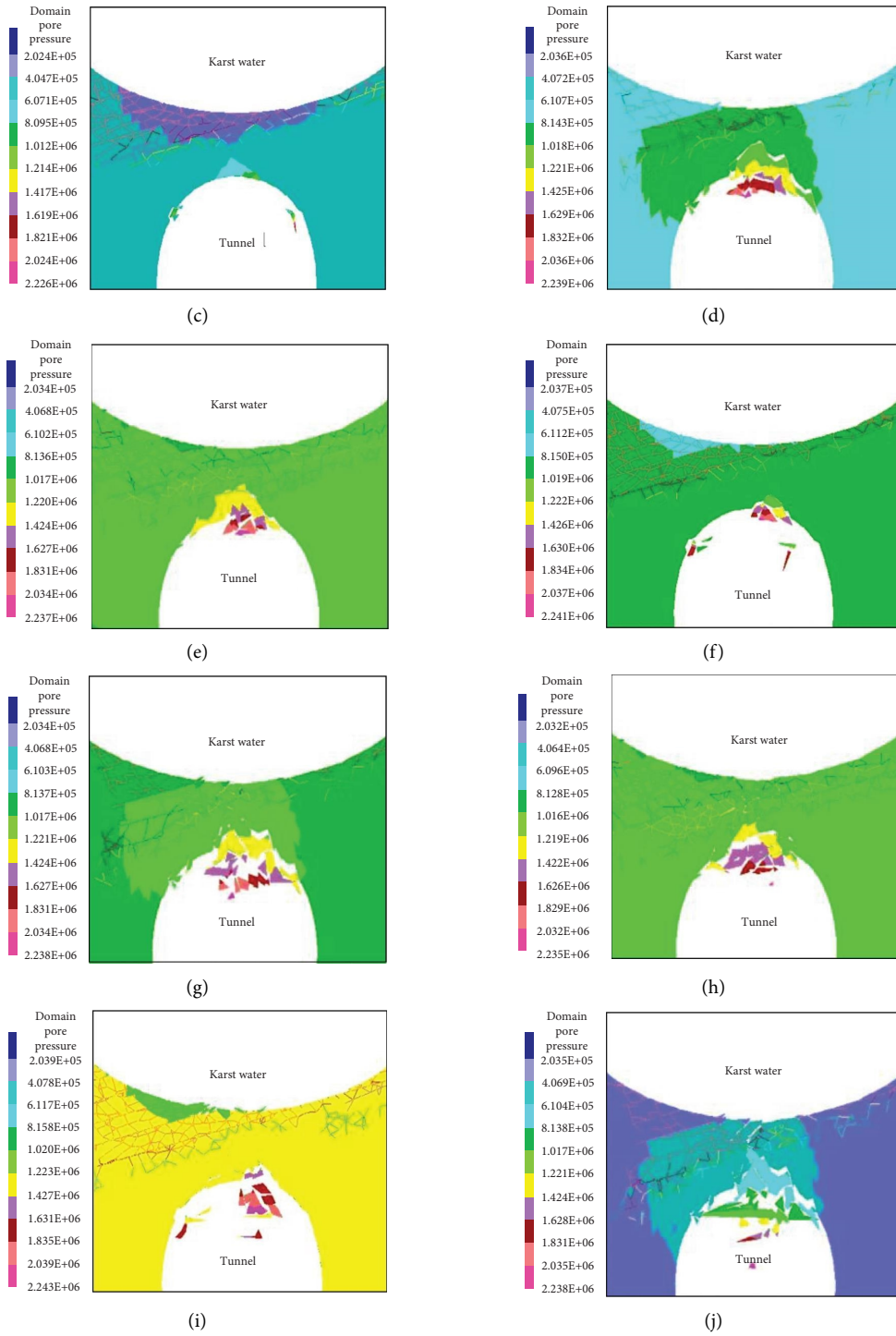


FIGURE 12: Continued.

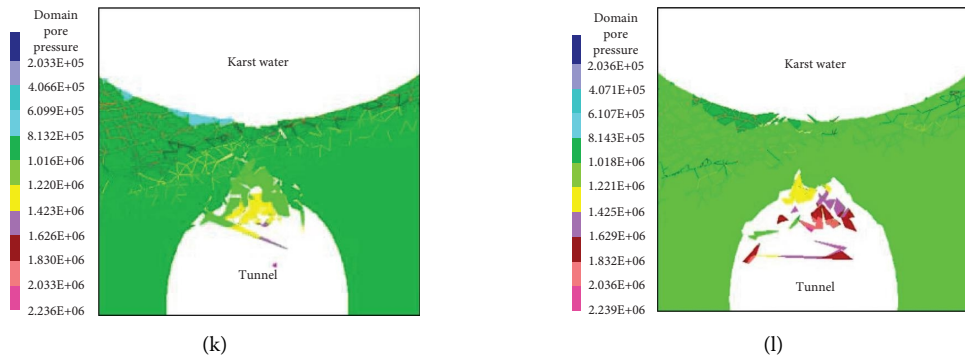


FIGURE 12: Evolution characteristics of seepage pressure under different tunnel depths. (a) $t = 1$ s, $h = 200$ m. (b) $t = 1$ s, $h = 500$ m. (c) $t = 1$ s, $h = 800$ m. (d) $t = 3$ s, $h = 200$ m. (e) $t = 3$ s, $h = 500$ m. (f) $t = 3$ s, $h = 800$ m. (g) $t = 5$ s, $h = 200$ m. (h) $t = 5$ s, $h = 500$ m. (i) $t = 5$ s, $h = 800$ m. (j) $t = 7$ s, $h = 200$ m. (k) $t = 7$ s, $h = 500$ m. (l) $t = 7$ s, $h = 800$ m.

tunnel through the fissures in the water and mud-resistant rock mass. Due to the difference in tunnel depth, the seepage velocity of karst fissure water and the propagation velocity of fissures are different. When the buried depth of the tunnel is 200 m, under the continuous action of the blasting load, the water and mud-resistant rock mass rapidly develop and penetrate to form an obvious water inrush channel (at $t = 1 \sim 7$ s). When the buried depth of the tunnel is 500 m, the development speed of cracks in the water and mud-resistant rock mass decreases somewhat (at $t = 1 \sim 7$ s). When the buried depth of the tunnel is 800 m, no obvious crack water inrush channel is formed in the water and mud-resistant rock mass (at $t = 1 \sim 7$ s). In addition, it can be seen that the distribution area of the seepage area for the tunnel's surrounding rock in the water and mud-resistant rock mass decreases significantly with the increase of the tunnel depth. When the blasting time $t = 7$ s, the degree of fracture and the scale of water inrush in the water and mud-resistant rock mass of the tunnel surrounding rock with a buried depth of 200 m reach their maximum in the above three cases. This phenomenon shows that under the combined action of hydraulic pressure and blasting excavation disturbance, the smaller the tunnel depth, the greater the disturbance of the water and mud-resistant rock mass by blasting load, and the easier it is to form higher cracks, which will speed up the formation of water inrush channels and the occurrence of water inrush disasters.

Figure 13 shows the evolution process of the seepage pressure value at each measuring point of the water and mud-resistant rock mass of karst tunnels with different burial depths under blasting excavation. It can be seen from Figure 13 that the seepage pressure values of the $n_1 \sim n_3$ measuring points on the horizontal plane HL₁ can reach the karst water pressure of 2 MPa in a very short time under the conditions of different burial depths ($h = 200$ m, 500 m, and 800 m). When the buried depth of the tunnel is 200 m, the seepage pressure values of $n_4 \sim n_9$ measuring points in the water and mud-resistant rock mass decrease with the increase of blasting time (At $t = 1$ s, the measuring points of $n_4 \sim n_6$ are 0.74 MPa, 0.58 MPa, and 0.18 MPa; At $t = 3$ s, the measuring points of $n_4 \sim n_6$ are 0.440 MPa, 0.06 MPa, and

0.05 MPa; At $t = 5$ s, the measuring points of $n_4 \sim n_6$ are 0.62 MPa, 0.37 MPa, and 0.03 MPa). The reason for this phenomenon is that the continuous disturbance of blasting excavation accelerates the formation of water inrush channels in the cracks. Therefore, the water pressure at each measuring point in the water and mud-resistant rock mass has decreased. When the buried depth of the tunnel is 500 m and 800 m respectively, the seepage pressure value at each measuring point of HL2 and HL3 increases to varying degrees. This is because the stability of the aquifer structure gradually increases with the increase in the buried depth of the tunnel, and the effect of blasting excavation disturbance is weakened. There is no obvious crack channel in the aquifer, and the energy loss of karst water in the flow process is less. Therefore, the seepage pressure values of the $n_4 \sim n_6$ measuring points have increased.

3.3. Catastrophe Information of Water Inrush in Karst Tunnel under Different Thickness

3.3.1. Evolution Characteristics of Displacement under Different Thickness. Figure 14 shows the evolution process of the displacement values of the water and mud-resistant rock mass under the conditions of the karst water pressure is 1 MPa, the inclination of the joint is 15° , the tunnel depth is 500 m, and the thicknesses of water and mud-resistant rock mass are 2 m, 3 m, and 4 m, respectively.

The process of water inrush disaster in the water and mud-resistant rock mass based on the displacement values evolution in Figure 14 is roughly similar to that in Figures 6 and 10, but due to the different thickness of the water and mud-resistant rock mass, the evolution characteristics of each displacement value are significantly different (the negative sign indicates that the displacement is vertically downward in the y -direction). With the increase in the calculation time, the broken area in the water and mud-resistant rock mass gradually expands to the upper part in different thicknesses of water and mud-resistant rock mass. When the thickness of the water and mud resistant rock mass is 2 m, the structure of the water and mud resistant

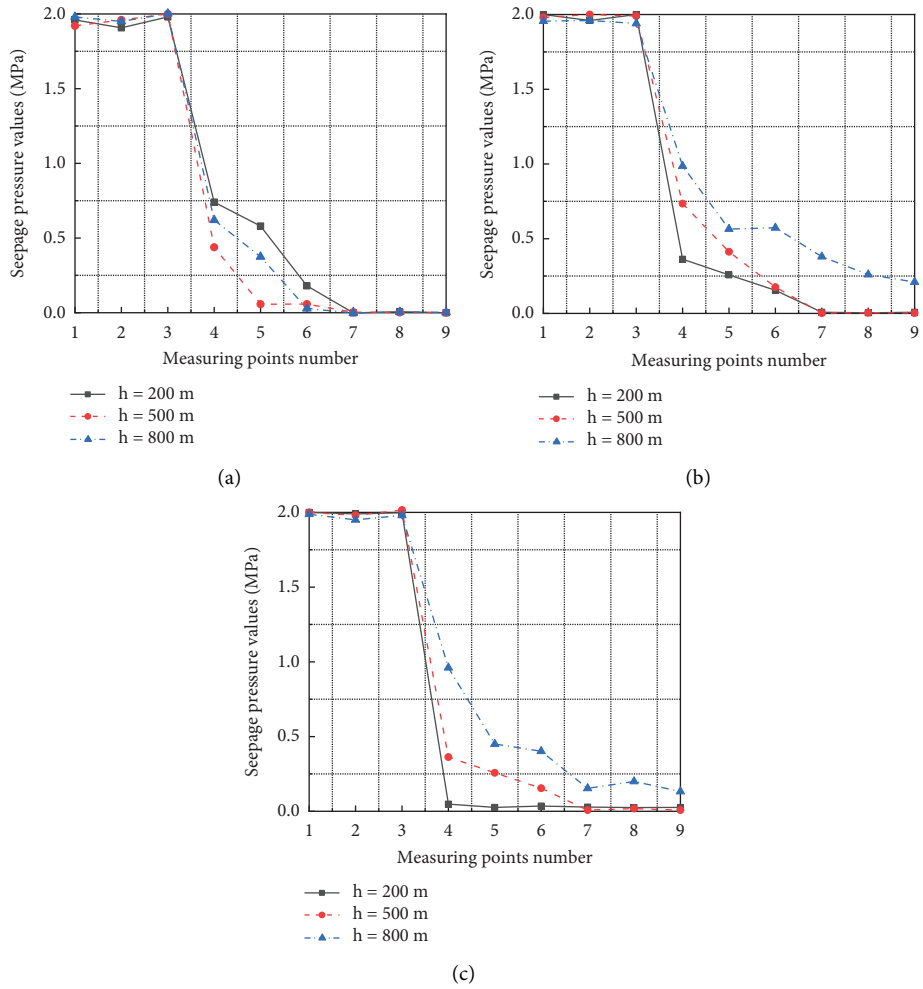


FIGURE 13: Evolution characteristics of seepage pressure in the measuring points. (a) $t = 1$ s. (b) $t = 3$ s. (c) $t = 5$ s.

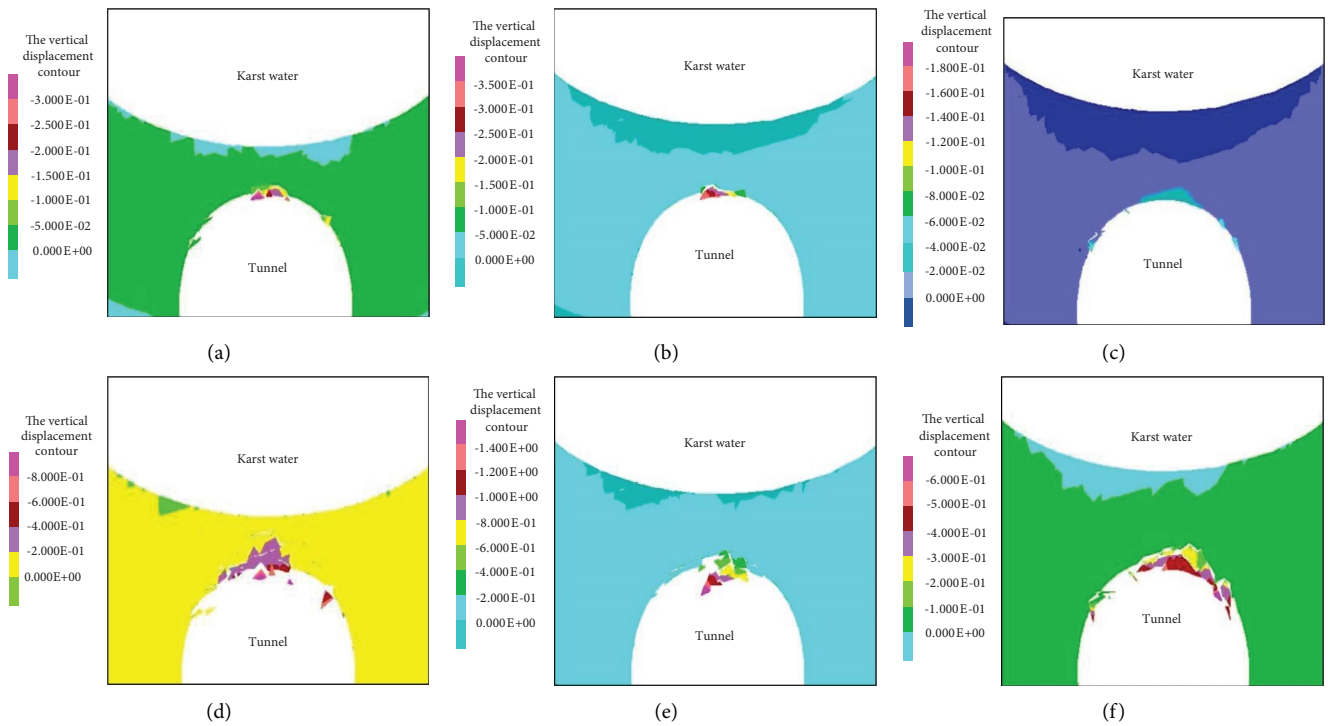


FIGURE 14: Continued.

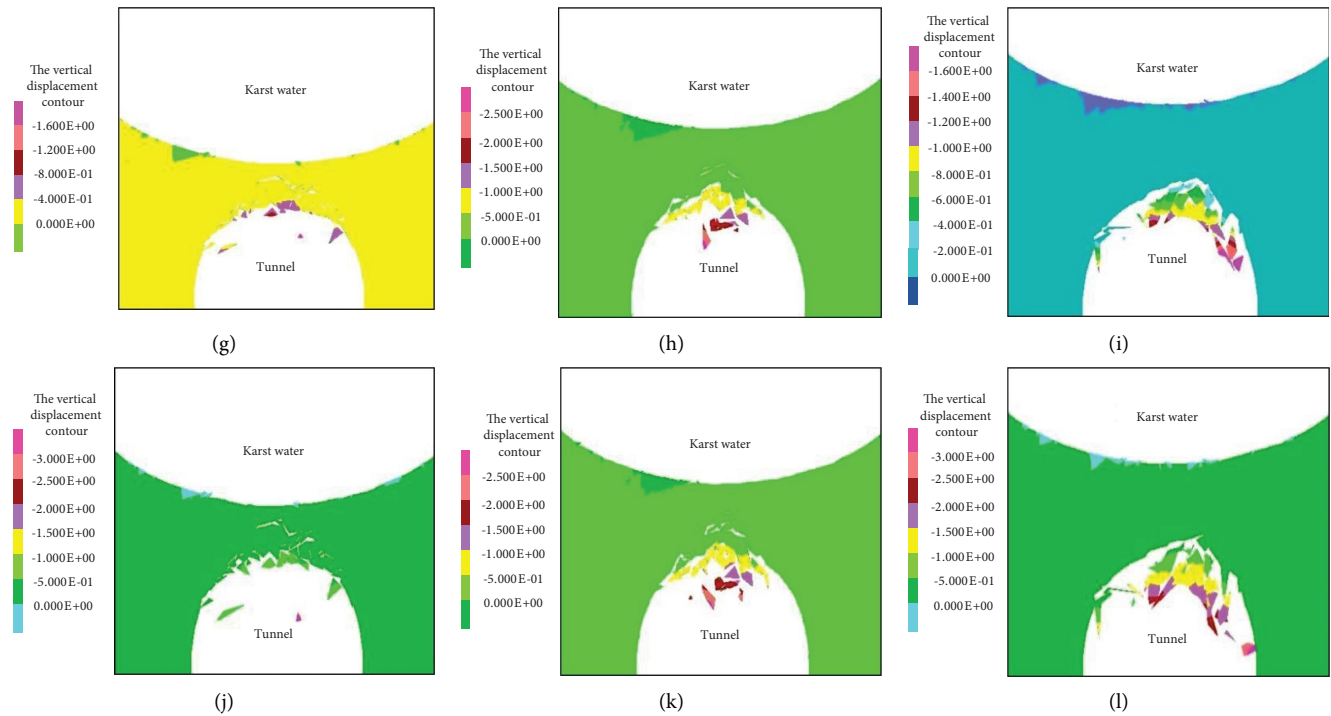


FIGURE 14: Evolution characteristics of displacement under different thicknesses. (a) $t = 1$ s, $d = 2$ m. (b) $t = 1$ s, $d = 3$ m. (c) $t = 1$ s, $d = 4$ m. (d) $t = 3$ s, $d = 2$ m. (e) $t = 3$ s, $d = 3$ m. (f) $t = 3$ s, $d = 4$ m. (g) $t = 5$ s, $d = 2$ m. (h) $t = 5$ s, $d = 3$ m. (i) $t = 5$ s, $d = 4$ m. (j) $t = 7$ s, $d = 2$ m. (k) $t = 7$ s, $d = 3$ m. (l) $t = 7$ s, $d = 4$ m.

rock mass shows an overall layer-wise failure trend under the action of excavation disturbance. With the continuous increase of the thickness of water and mud-resistant rock mass, the surrounding rock located within 1.5 m of the tunnel vault suffered severe damage along the way, resulting in the formation of obvious slump arches. It can also be seen from the calculation results in Figure 13 that when the thickness of the water and mud-resistant rock mass is 2 m, the structure of the antioutburst rock mass undergoes significant displacement, the entire structure is severely broken, and obvious crack channels have been formed inside. When the thickness of the water and mud resistant rock mass increases to 3 m and 4 m, although some blocks fall off, the remaining structure of the water and mud resistant rock mass is relatively complete, and no obvious crack channel is formed. It can be seen that with the continuous increase of the safety thickness of the water and mud resistant rock mass, the stronger the stability of the water and mud resistant rock mass, the higher the critical water pressure when water inrush occurs.

Figure 15 shows the evolution process of the vertical displacement of each measuring point in different water and mud-resistant rock mass thicknesses. It can be seen from the results in Figure 15 that in the case of any thickness of the water and mud resistant rock mass (2 m, 3 m, and 4 m), the y -direction displacement of the water and mud resistant rock mass gradually increases with the increase of the blasting load action time. And it can be seen from Figure 15 that the y -direction displacement of the antioutburst layer gradually increases from top to bottom along its thickness.

The thickness of the antiburst layer is 3 m as an example, and the measuring points n_7 , n_8 , and n_9 are selected. When the blasting action time $t = 3.0$ s, the y -direction displacements are -0.412 m, -0.557 m, and -0.464 m, respectively (The negative sign indicates that the displacement is vertically downward in the y -direction). When the blasting action time $t = 5.0$ s, the y -direction displacement is 0.896 m, 1.359 m, and 0.996 m, and the displacement increases downward by 117.4%, 143.9%, and 114.6%. When the thickness of the water and mud resistant rock mass is 4 m, although some blocks at the bottom of the water and mud resistant rock mass appear to be peeling and slipping, the vertical displacement of the water and mud resistant rock mass is relatively weakened from the perspective of the overall structure of the water and mud resistant rock mass. No matter how high the safety thickness is, each measuring point on the measuring section at the bottom of the water and mud-resistant rock mass has a high vertical displacement, and the damage degree at the dome is relatively serious.

3.3.2. Evolution Characteristics of Seepage Pressure under Different Thickness. Figure 16 shows the evolution process of the seepage field in the water and mud-resistant rock mass under the different safety thicknesses ($d = 2$ m, 3 m, and 4 m), the karst water pressure is 1 MPa, the tunnel depth is 500 m, and the inclination of the joint is 15° .

It can be seen from Figure 16 that in different thicknesses of the water and mud-resistant rock mass, the process of progressive seepage failure in the entire water and mud-

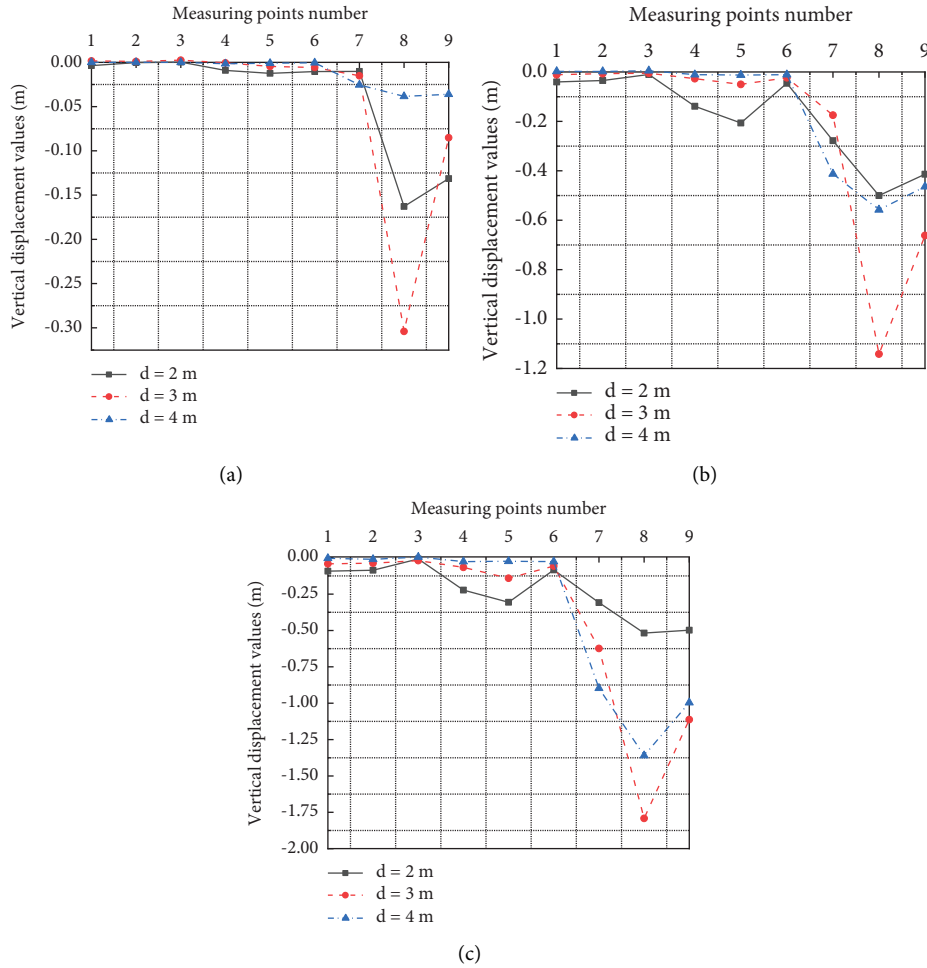


FIGURE 15: Evolution characteristics of displacement in the measuring points. (a) $t = 1$ s. (b) $t = 3$ s. (c) $t = 5$ s.

resistant rock mass is similar. That is to say, the combined effect of karst water pressure and blasting excavation disturbance causes the continuous initiation of fissures in the water and mud-resistant rock mass, and the effect of seepage erosion is gradually prominent, and the seepage path is continuously adjusted with the initiation of cracks. The expansion and penetration of the cracks in the water and mud-resistant rock mass will eventually lead to the failure of seepage instability. Through the comparative analysis of the numerical results in Figure 16, it can be seen that the different thicknesses of the water and mud-resistant rock mass have a significant effect on the seepage pressure and seepage area of karst water. When the thickness of the water and mud resistant rock mass is 2 m, the fracture and fragmentation degree of the entire water and mud resistant rock mass and the influence range of the seepage area are more extensive than those when the thickness is 3 m and 4 m. The numerical calculation results show that the smaller the thickness of the water and mud-resistant rock mass in the karst tunnel, the weaker the stability of the water and mud-resistant rock mass structure under the influence of external factors, the more serious the degree of rupture and fracture, the wider the influence of the seepage area, and the more likely the tunnel will occur.

Figure 17 shows the evolution process of the seepage pressure at different measuring points in different thicknesses of the water and mud-resistant rock mass. Regardless of the thickness of the water and mud-resistant rock mass, the fissure water in the water and mud-resistant rock mass can always penetrate to the $n_1 \sim n_3$ measuring points under the action of karst water pressure, and the seepage pressure value is stable at about 1 MPa. When the thickness of the water and mud-resistant rock mass is 2 m, the seepage pressure values of measuring points are significantly higher than those of other thicknesses. This is because when the thickness is 2 m, with the increase in calculation time, the rock mass structure in the water and mud-resistant rock mass is cracked under the action of karst water pressure, and the karst water gradually seeps and migrates along the crack channel. At $t = 5$ s, the karst water has covered the entire water and mud-resistant rock mass, and the karst water inrush channel is completely connected. Therefore, the water pressure value of each measuring point is relatively high when the thickness of the water and mud-resistant rock mass is 2 m. When the thickness is 3 m or 4 m, due to the increase in the safety thickness of the water and mud-resistant rock mass, the stability of the entire structure is significantly enhanced. During the numerical calculation process, the

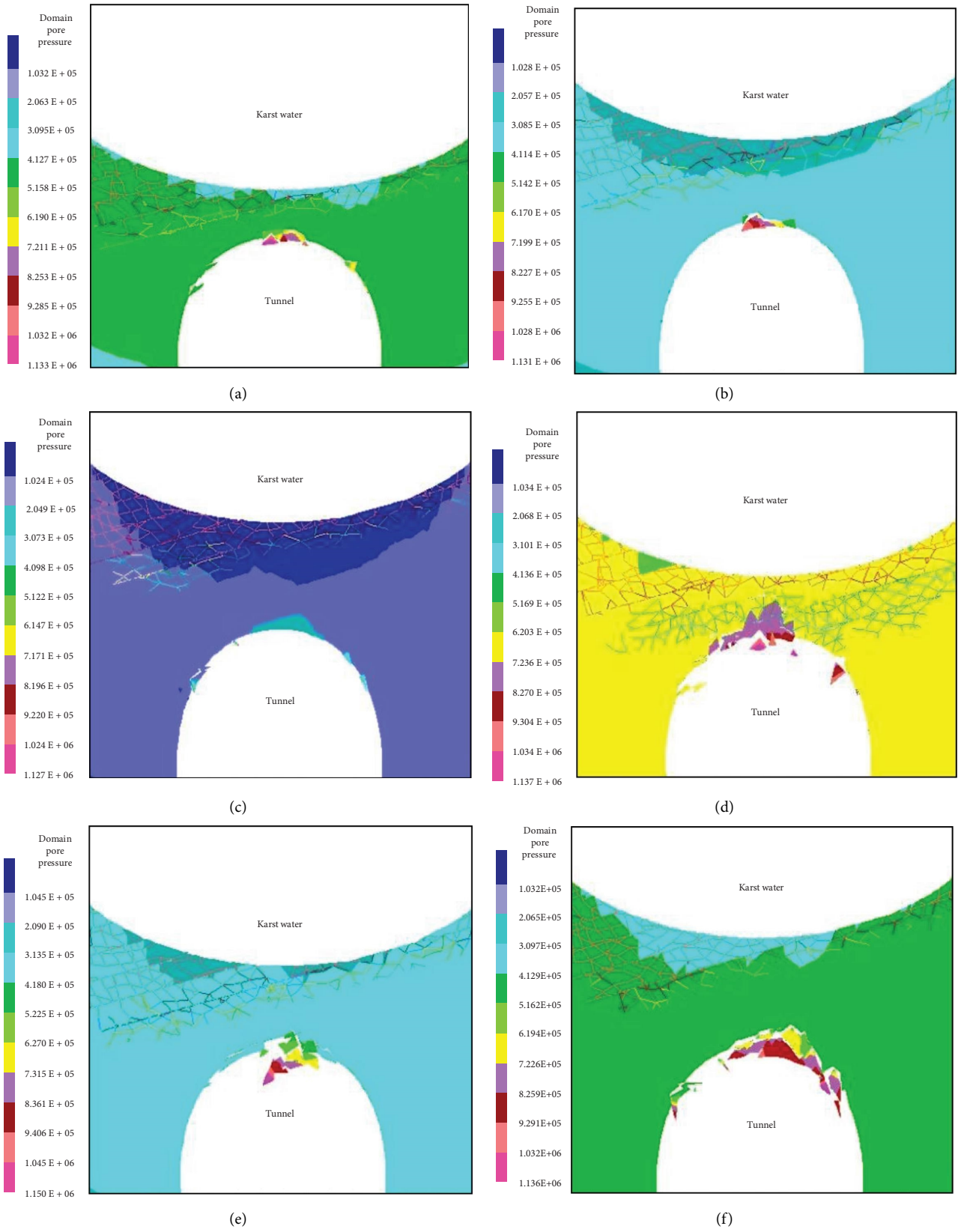


FIGURE 16: Continued.

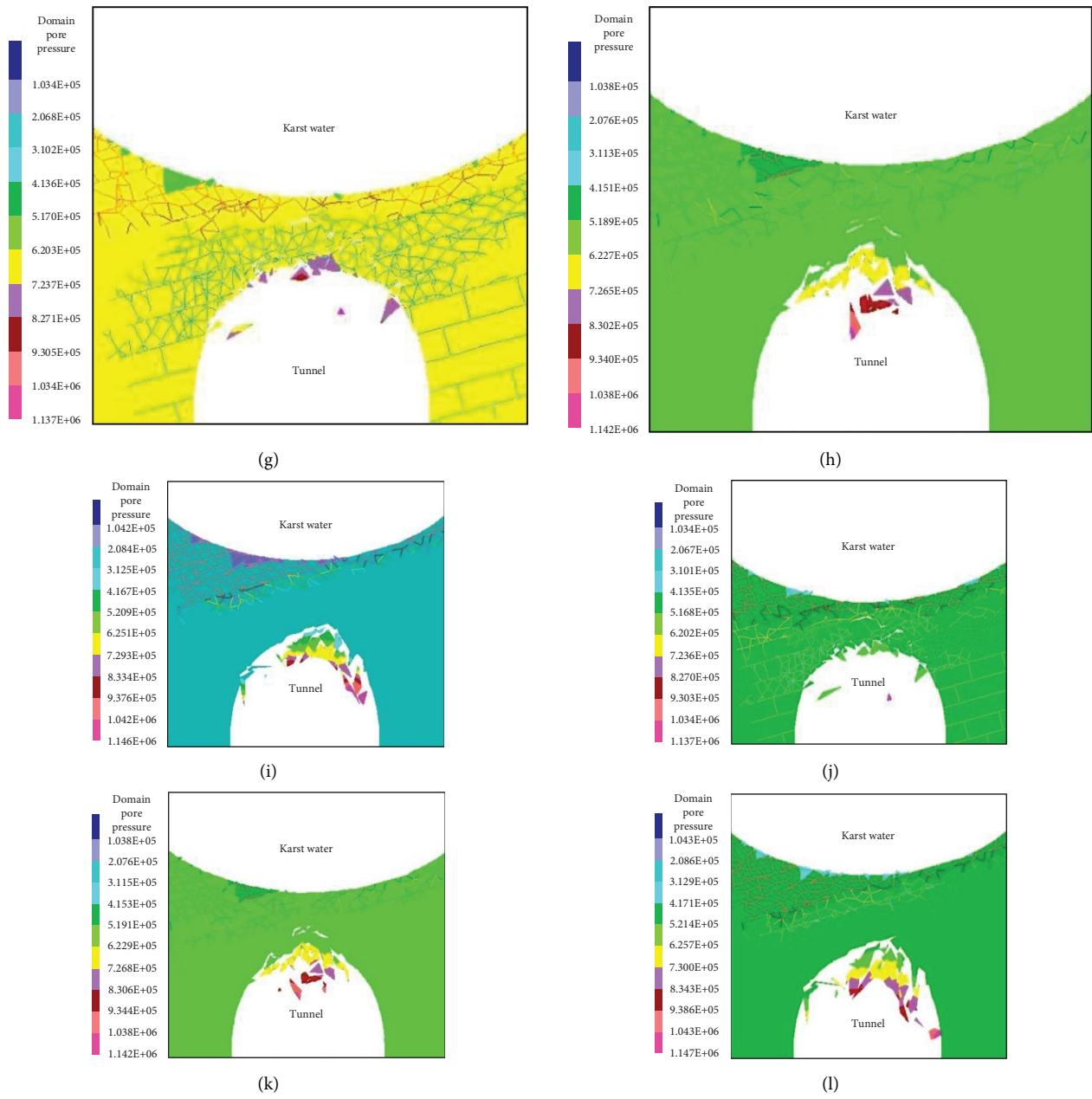


FIGURE 16: Evolution characteristics of seepage pressure under different thicknesses. (a) $t = 1 \text{ s}, d = 2 \text{ m}$. (b) $t = 1 \text{ s}, d = 3 \text{ m}$. (c) $t = 1 \text{ s}, d = 4 \text{ m}$. (d) $t = 3 \text{ s}, d = 2 \text{ m}$. (e) $t = 3 \text{ s}, d = 3 \text{ m}$. (f) $t = 3 \text{ s}, d = 4 \text{ m}$. (g) $t = 5 \text{ s}, d = 2 \text{ m}$. (h) $t = 5 \text{ s}, d = 3 \text{ m}$. (i) $t = 5 \text{ s}, d = 4 \text{ m}$. (j) $t = 7 \text{ s}, d = 2 \text{ m}$. (k) $t = 7 \text{ s}, d = 3 \text{ m}$. (l) $t = 7 \text{ s}, d = 4 \text{ m}$.

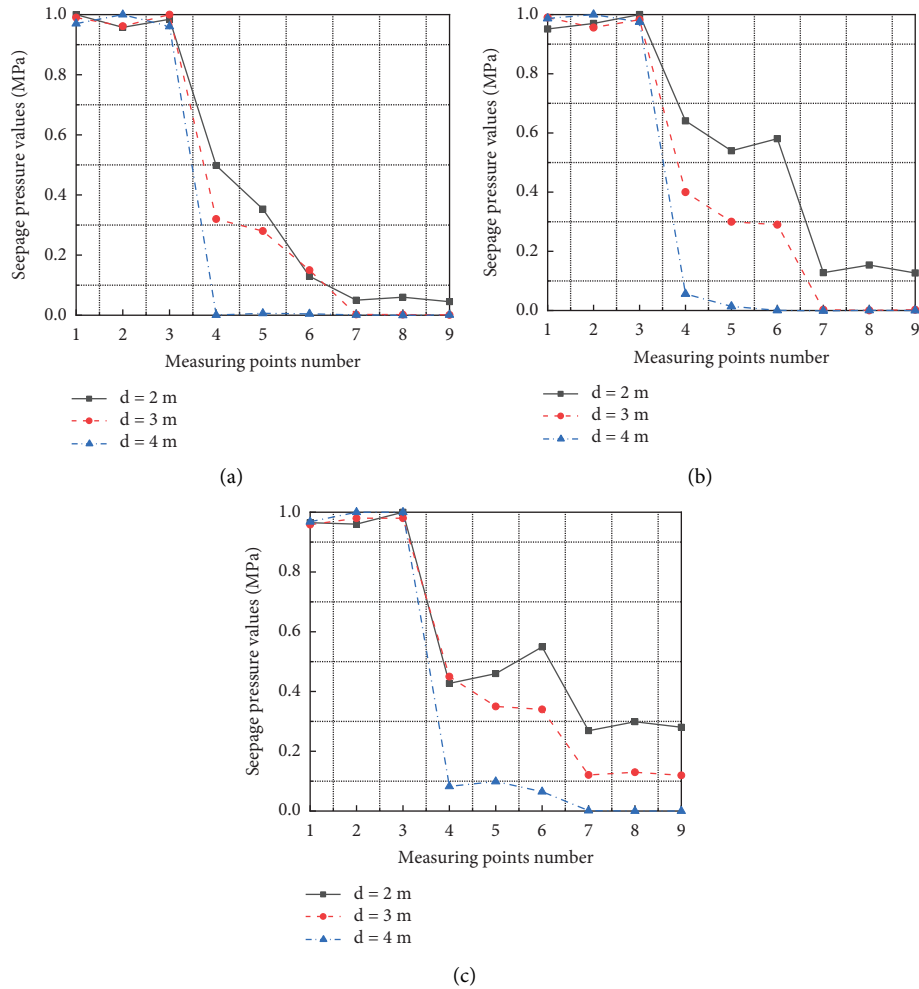


FIGURE 17: Evolution characteristics of seepage pressure in the measuring points. (a) $t = 1$ s. (b) $t = 3$ s. (c) $t = 5$ s.

water inrush channel is not completely formed, the water and mud resistant rock masses are relatively complete, and the water inrush resistance is stronger.

4. Conclusions

To investigate the evolution characteristics of catastrophe information in the water inrush under different conditions of joint dip angle, tunnel depth, and thickness of water and mud-resistant rock mass, a series of numerical simulation analyses based on DEM were conducted. Some conclusions can be drawn from the following:

- (1) As the inclination angle of the joint increases, the vertical displacement value of each measuring point increases significantly, and the fracture area, fracture degree, and seepage pressure of the aquifer also increase rapidly. The seepage pressure of measuring points in the water and mud-resistant rock mass increases with the increase in the inclination angle of the joint. The seepage pressure values of different measuring points showed a decreasing trend from HL_1 to HL_3 .

- (2) The area and magnitude of the water and mud-resistant rock mass displacement decrease with increasing tunnel depth. The seepage velocity and fracture propagation velocity of karst water vary greatly with the tunnel burial depth. As the depth of the tunnel increases, the distribution area of water cracks and hydraulic cracks decreases significantly, and water inrush is less likely to occur.
- (3) With the increase of the water and mud-resistant rock mass thickness, the failure mode of the tunnel outburst layer structure gradually changes from the overall collapse to the partial collapse of the vault to form a relatively stable slump arch. The greater the thickness of the water and mud-resistant rock mass, the higher the critical water pressure for failure and instability, and the stronger the anti-outburst ability.

Data Availability

The data used to support the findings of this study are available from the corresponding author upon request.

Conflicts of Interest

The authors declare that they have no conflicts of interest.

Acknowledgments

This research was financially supported by the National Natural Science Foundation of China (Grant no. 52178388), the National Key Basic Research and Development Plan (973 Plan) Project (Grant no. 2013CB036003), the China Post-doctoral Science Foundation Fund (Grant no. 2018M631114), and the Key Scientific and Technological Project of Henan Province, China (Grant no. 212102310292).

References

- [1] S. C. Li, J. Wu, Z. H. Xu, L. Zhou, and B. Zhang, "A possible prediction method to determine the top concealed karst cave based on displacement monitoring during tunnel construction," *Bulletin of Engineering Geology and the Environment*, vol. 78, no. 1, pp. 341–355, 2017.
- [2] W. L. Wu, X. L. Liu, J. Q. Guo, F. Y. Sun, X. Huang, and Z. G. Zhu, "Upper limit analysis of stability of the water-resistant rock mass of a karst tunnel face considering the seepage force," *Bulletin of Engineering Geology and the Environment*, vol. 80, pp. 5813–5830, 2021.
- [3] H. R. Zarei, A. Uromeihy, and M. Sharifzadeh, "Evaluation of high local groundwater inflow to a rock tunnel by characterization of geological features," *Tunnelling and Underground Space Technology*, vol. 26, no. 2, pp. 364–373, 2011.
- [4] F. Gutiérrez, M. Parise, J. De Waele, and H. Jourde, "A review on natural and human-induced geohazards and impacts in karst," *Earth-Science Reviews*, vol. 138, pp. 61–88, 2014.
- [5] Y. X. Lv, Y. J. Jiang, W. Hu, M. Cao, and Y. Mao, "A review of the effects of tunnel excavation on the hydrology, ecology, and environment in karst areas: current status, challenges, and perspectives," *Journal of Hydrology*, vol. 586, Article ID 124891, 2020.
- [6] S. C. Li, Z. Q. Zhou, L. P. Li, Z. H. Xu, Q. Q. Zhang, and S. S. Shi, "Risk assessment of water inrush in karst tunnels based on attribute synthetic evaluation system," *Tunneling and Underground Space Technology incorporating Trenchless Technology Research*, vol. 38, pp. 50–58, 2013.
- [7] P. Jeannin, A. Yves, and D. Malard, "Assessing karst-hydraulic hazards in tunneling—the Brunnenmühle spring system—Bernese Jura, Switzerland," *Environmental Earth Sciences*, vol. 74, pp. 7655–7670, 2015.
- [8] Y. G. Xue, F. M. Kong, D. H. Qiu, M. Su, Y. Zhao, and K. Zhang, "The classifications of water and mud/rock inrush hazard: a review and update," *Bulletin of Engineering Geology and the Environment*, vol. 80, no. 3, pp. 1907–1925, 2021.
- [9] X. X. Liu, S. L. Shen, Y. S. Xu, and Z. Y. Yin, "Analytical approach for time-dependent groundwater inflow into shield tunnel face in confined aquifer," *International Journal for Numerical and Analytical Methods in Geomechanics*, vol. 42, no. 4, pp. 655–673, 2018.
- [10] Y. J. Zhao, F. G. Wang, C. S. Li, Y. Q. Cao, H. L. Tian, and L. Borrelli, "Study of the corrosion characteristics of tunnel fissures in a karst area in southwest China," *Geofluids*, vol. 2018, pp. 1–19, Article ID 6234932, 2018.
- [11] Z. Huang, W. Zeng, Y. Wu, S. J. Li, and K. Zhao, "Experimental investigation of fracture propagation and inrush characteristics in tunnel construction," *Natural Hazards*, vol. 97, no. 1, pp. 193–210, 2019.
- [12] M. Q. Zhang, H. J. Huang, S. X. Zhang, J. Wu, and X. H. Li, "Treatment technology for water and mud bursting on 1.21 in Maluqing tunnel of Yichang-Wanzhou railway," *Journal of Railway Engineering Society*, vol. 11, pp. 49–56, 2008.
- [13] C. H. Bai, *Research on Intelligent Prediction Method of Hazard Risk of Water and Mud Inrush in Karst Tunnel Based on Machine Learning*, Shandong University, Jinan, China, 2021.
- [14] S. C. Li, Y. C. Yuan, L. P. Li, Z. H. Ye, Q. Q. Zhang, and T. Lei, "Water inrush mechanism and minimum safe thickness of rock wall of karst tunnel face under blast excavation," *Chinese Journal of Geotechnical Engineering*, vol. 37, pp. 313–320, 2015, (in Chinese).
- [15] Z. H. Xu, J. Wu, S. C. Li, B. Zhang, and X. Huang, "Semi analytical solution to determine minimum safety thickness of rock resisting water inrush from filling-type karst caves," *International Journal of Geomechanics*, vol. 18, no. 2, pp. 1–11, 2018.
- [16] F. Huang, L. H. Zhao, T. H. Ling, and X. L. Yang, "Rock mass collapse mechanism of concealed karst cave beneath deep tunnel," *International Journal Of Rock Mechanics And Mining Sciences*, vol. 91, pp. 133–138, 2017.
- [17] J. Q. Guo, J. X. Chen, F. Chen, S. X. Huang, and H. Y. Wang, "Using the schwarz alternating method to identify critical water-resistant thickness between tunnel and concealed cavity," *Advances in Civil Engineering*, vol. 2018, pp. 1–14, Article ID 8401482, 2018.
- [18] L. Li, X. L. Rong, M. Y. Wang, H. Lu, and Y. P. Xia, "Development and application of 3d model test system for water inrush geohazards in long and deep tunnels," *Chinese Journal of Rock Mechanics and Engineering*, vol. 35, pp. 491–497, 2016, (in Chinese).
- [19] A. Kirsch, "Experimental investigation of the face stability of shallow tunnels in sand," *Acta Geotechnica*, vol. 5, no. 1, pp. 43–62, 2010.
- [20] G. Idinger, P. Aklík, W. Wu, and R. I. Borja, "Centrifuge model test on the face stability of shallow tunnel," *Acta Geotechnica*, vol. 6, no. 2, pp. 105–117, 2011.
- [21] Z. Huang, S. J. Li, K. Zhao, Y. Wu, and Z. Wu, "Liquid-solid coupling model test to investigate seepage failure mechanism of intact confining rocks of tunnels," *Journal of Basic Science and Engineering*, vol. 27, pp. 1345–1356, 2019.
- [22] Z. W. Liu, M. C. He, and S. R. Wang, "Study on karst water burst mechanism and prevention countermeasures in Yuanliangshan tunnel," *Rock and Soil Mechanics*, vol. 27, pp. 228–232, 2006.
- [23] M. J. Zhao, X. H. Liu, J. H. Ao, and B. Wang, "Numerical analysis of influence of karst caves in top of tunnel on stability of surrounding rock masses," *Rock and Soil Mechanics*, vol. 24, pp. 445–449, 2003.
- [24] L. Qin, L. Wei, J. X. Chen, Y. B. Luo, P. Huang, and Y. Y. Wang, "Stability analysis of water and mud resistant rock mass in karst tunnel based on releasable elastic strain energy," *Mathematical Problems in Engineering*, vol. 2017, pp. 1–9, 2017.
- [25] T. Lei, M. S. thesis, *Mechanism and Safety Thickness Prediction of Water Inrush for Overlying Water-Filling Karst Cave in Tunnels and Engineering Applications*, M.S. Thesis, Shandong University, Jinan China, 2015.
- [26] U. D. E. C. Itasca, *Manual: Universal Distinct Element Code Version 5.0*, Itasca Consulting Group Inc, Minneapolis, Minnesota, 2011.

- [27] E. Eker and S. Akin, "Lattice Boltzmann simulation of fluid flow in synthetic fractures," *Transport in Porous Media*, vol. 65, no. 3, pp. 363–384, 2006.
- [28] Itasca Consulting Group, Inc. *UDEC (Universal Distinct Element Code) User's Manual*, Itasca Consulting Group, Inc, Minnesota, 1996.
- [29] T. X. Liu, *Mechanism Analysis and Model Test of Karst Roof and Pile Foundation*, Ph.D. Thesis, Central South University, Changsha, China, 2003.
- [30] W. X. Zhu, *Study on Mechanism of Water Inrush in Muddy Limestone Karst Tunnel after Wetting and Drying Cycles*, Ph.D. Thesis, China University of Mining and Technology, Beijing, China, 2018.
- [31] S. G. Chen and J. Zhao, "A study of UDEC modelling for blast wave propagation in jointed rock masses," *International Journal of Rock Mechanics and Mining Sciences*, vol. 35, no. 1, pp. 93–99, 1998.
- [32] Z. Y. He, *Study on Progressive Failure and Safety Thickness of Water and Mud Inrush Resistant Rock Mass during Karst Tunnel Constructed by Drilling and Blasting Method*, M. S. Thesis, Henan Polytechnic University, Jiaozuo, China, 2017.
- [33] L. P. Li, *Study on Catastrophe Evolution Mechanism of Karst Water Inrush and its Engineering Application of High Risk Karst Tunnel*, Ph.D. Thesis, Shandong University, Jinan, China, 2009.
- [34] W. X. Zhu, H. W. Jing, L. J. Yang, B. Pan, and H. J. Su, "Strength and deformation behaviors of bedded rock mass under bolt reinforcement," *International Journal of Mining Science and Technology*, vol. 28, no. 4, pp. 593–599, 2018.
- [35] C. W. Boon, "Study of reinforcement support mechanisms for wide-span horseshoe-shaped openings in horizontally layered jointed rock using the distinct element method," *Rock Mechanics and Rock Engineering*, vol. 52, no. 4, pp. 1179–1191, 2019.

Research Article

Analysis of Mechanical Properties and Slope Stability of Red Bed Soft Rock: A Case Study in Xinjiang Irrigation Diversion Channel

Da Liu ¹, Jianglin Gao,¹ Fang Chen ¹, Songtao Hu,¹ Xiaohua Zhao ² and Yan Li¹

¹Jiangxi Hydraulic Safety Engineering Technology Research Center, Jiangxi Academy of Water Science and Engineering, Nanchang 330029, China

²School of Water Conservancy Engineering, Zhengzhou University, Zhengzhou 450001, China

Correspondence should be addressed to Fang Chen; jxgzld@126.com

Received 20 July 2022; Revised 4 September 2022; Accepted 6 September 2022; Published 16 November 2022

Academic Editor: Xiaobo Zhang

Copyright © 2022 Da Liu et al. This is an open access article distributed under the Creative Commons Attribution License, which permits unrestricted use, distribution, and reproduction in any medium, provided the original work is properly cited.

The channel slope in the red-bed soft rock area is prone to instability and collapse due to the influence of the channel flow movement, rainfall, weathering, and other factors. Under long-term operation conditions, the sediment stripped from the channel side wall is liable to silt along the process of water flow transportation in the channel, which seriously leads to elevation of the channel bottom, increase of channel width, and reduction of the horseway, which affect the normal water conveyance and operation safety of channels. In view of the collapse and instability of Zhetang diversion irrigation channel project in Xinjiang hydraulic project, through on-site sampling and indoor rock mechanics test, the strength mechanical parameters of slope rock samples are obtained, and the indoor rheological test is carried out, and the triaxial rheological law is obtained. Under different levels of stress, the axial creep strain accounts for more than 50% of the total axial strain, indicating that the rheological effect of sample rock is obvious. Based on the strength parameters of rock samples, a numerical model is established. The stability of red-bed soft rock channel bank slope is studied by using the strength reduction method of finite element method. The seepage field of channel slope under conventional working conditions is analyzed, and the slope stability under different operating conditions is compared and calculated. The results show that the slope stability safety factor of Zhetang diversion irrigation channel slope is 1.60 under conventional working conditions and 1.33 under check working conditions, which are greater than the recommended value in the specification.

1. Introduction

The red-bed soft rock slope is widely distributed in south China, which is easy to be weathered, disintegrated, and softened by water [1–3]. Most of the red-bed soft rocks can disintegrate into soil under open air or dry-wet cycle, and some even disintegrate immediately after immersion in water, or even muddy with poor engineering geological properties [4, 5]. Reservoirs and water diversion engineering channels are widely distributed and often need to run through the red-bed distribution area. The red-bed soft rock is prone to cracks, swelling, slope collapse, and other problems [6, 7], affecting the normal water delivery and operation safety of the water channel. Under long-term operation conditions, the sediment denuded from the channel sidewall is prone to siltation along the way through

the flow transportation in the channel, which seriously leads to the elevation of the channel bottom, the increase of the channel width, and the reduction of the berm [8–10]. In addition, a large amount of sediment is brought into the reservoir by water flow, resulting in the deterioration of water quality in the reservoir area and affecting the storage capacity and service life of the reservoir [11, 12]. Therefore, it is urgent to study the seepage and stability of the red-bed soft rock channel bank slope, and reveal the mechanical mechanism, formation mechanism, and evolution law of the channel bank slope instability under the interaction of water and rock, and it is of great significance for the design and application of many channel slopes under construction or built [13].

Softening in water is an important factor that leads to the reduction of physical and mechanical properties of red-bed

soft rock, as a result, the rheological characteristics of soft rock under long-term load are important parameters for geotechnical engineering design [14–16]. The deformation and strength of soft rock have a strong time effect, which is reflected in many examples of rheology of soft rock caused by excavation in rock mass engineering such as dams, slopes, and caves. Shan et al. [17] analyzed the instantaneous strength and deformation characteristics of rock specimens by triaxial compression test and triaxial unloading creep test, and discussed creep deformation characteristics and damage evolution characteristics of red sandstone in concrete project, Yang et al. [18] analyzed the creep mechanical properties of red sandstone under different temperature and water content conditions. Yu et al. [19] carried out a series of uniaxial compressive strength tests and multistage creep tests on red sandstone samples to study the creep characteristics of red sandstone under different immersion conditions. In recent decades, based on various slopes, dams, and road projects, a large number of experiments have been carried out to study the rheological phenomena of soft rocks, and many rheological models have been put forward and established, including empirical formula model, unit model, and some new combined models formed by introducing damage mechanics and fracture theory [20–23]. Therefore, the creep characteristics of sandstone is of great significance for reasonably explaining the time-dependent mechanical behavior of slope engineering, and evaluating the long-term stability and safe operation of the project.

At present, the slope stability analysis methods are relatively mature, among which the most commonly used methods are limit equilibrium method and strength reduction method [24–26]. Limit equilibrium analysis method is a commonly used deterministic analysis method which is an earlier and widely used method in slope stability analysis [27, 28]. When using limit equilibrium method to analyze slope stability, the slope body is simplified, which is somewhat different from the real slope stress mode. Compared with the limit equilibrium method, the strength reduction method does not need assumptions, and can obtain the location of the sliding surface and the corresponding minimum safety factor according to the instability criterion, which makes it widely used. Arvin et al. [29] studied the three-dimensional stability of geocell reinforced slope by strength reduction method (SRM), which considered the geotechnical compartments and their fillers and surrounding soils. Zhang et al. [15] carried out numerical research on progressive failure process of jointed rock mass slope using fracture mechanics and strength reduction method (SRM), and proposed a displacement discontinuity method including friction unit for calculating stress intensity factor. Kong et al. [30] established a three-dimensional nonlinear strength model of soil considering the coupling strength of tension-shear (T-S) and compression-shear (C-S), and analyzed the stability of saturated and unsaturated slopes by strength reduction method.

Since the Zhetang diversion irrigation channel project was completed and put into operation, the red-bed slope of the channel often collapsed and cracked. For example, the slope collapse of the section with stake No. 1 + 650~2 + 300

was aggravated, and some of the slopes below the first-class Packway collapsed seriously. Therefore, in view of the collapse and instability of Zhetang diversion irrigation channel, and based on the indoor rock mechanics test and rock rheological test, the triaxial rheological law of channel rock samples are obtained. According to the obtained strength parameters of rock samples, a numerical calculation model is established, and the seepage and stability of red-bed soft rock channel slope are studied by using the strength reduction method, and the seepage field and stability safety factor of channel slope under conventional and check working conditions are analyzed.

2. Seepage and Stability Analysis Method

2.1. Seepage Analysis Method. The relationship between flow flux and soil and water potential gradient is often used to describe the movement law in unsaturated soil:

$$q = v = -k(\theta) \frac{\partial \psi}{\partial x}, \quad (1)$$

where q is the flow flux in unsaturated soil, v is the average flow rate, $\partial \psi / \partial x$ is hydraulic gradient.

The slope is assumed to be isotropic porous media, the seepage conforms to Darcy's law, and the motion equation of water in unsaturated soil:

$$\frac{\partial}{\partial x} \left(k_x \frac{\partial H}{\partial x} \right) + \frac{\partial}{\partial y} \left(k_y \frac{\partial H}{\partial y} \right) + Q = \frac{\partial \Theta}{\partial t}, \quad (2)$$

where H is the total head, k_x , k_y are the horizontal and vertical permeability coefficients, respectively, Q is the flow of water on the boundary, Θ is the volume moisture content.

The permeability law coefficient is defined as

$$\bar{k} = \frac{k_s}{(1 + \beta \sqrt{v_w v_w})} k, \quad (3)$$

where \bar{k} is the average permeability coefficient, k is the permeability coefficient of saturated soil, k_s is the seepage coefficient, β is a coefficient reflecting the influence of velocity on permeability coefficient, and v_w is the seepage velocity.

2.2. Strength Reduction Method. The strength reduction method defines the strength reduction factor as the ratio of the maximum shear strength that the slope can actually provide to the actual shear stress generated by the external load. Then, by continuously increasing the value of the reduction factor, repeatedly calculate and analyze until the value of the reduction factor increases to a certain value, the slope reaches the critical state, and calculate the cohesion and internal friction angle of rock and soil mass when the slope reaches the state of imminent failure [22]. In order to prevent the slope from losing stability at the beginning of the calculation and ensure the elastic state of the soil at the beginning stage, the initial value of F_i is usually taken as a number less than 1, and then gradually enlarged. This method has great advantages over traditional calculation

methods such as the slice method. It does not need to assume the shape and position of the sliding surface before calculation, and it can also observe the slope failure at different times.

The shear strength parameters after reduction can be expressed as

$$\begin{aligned} c_m &= \frac{c}{F_t}, \\ \varphi_m &= \arctan\left(\frac{\tan \varphi}{F_t}\right), \end{aligned} \quad (4)$$

where c_m and φ_m are the cohesion and internal friction angle that soil can provide, c and φ are the cohesion and internal friction angle required to maintain balance or actually exerted by the soil, F_t is the strength reduction factor.

3. Experimental Study on Mechanical Properties of Rock and Soil

3.1. Project Overview. Zhetang diversion irrigation channel of Xinjiang hydraulic project is located under the jurisdiction of Jizhou district and Jishui County of Ji'an city, which belongs to Wenshi River Basin, a tributary of Ganjiang River, and situated to typical red-bed soft rock in geological conditions. The Wenshi river originates from Dachong township, Ji'an County, and flows into the Ganjiang River at Jiangkou village under the well head through Yinwanqiao reservoir in Gujiang township. The total length of the Wenshi river is 48.1 km and the drainage area is about 360 km². After the construction of the protection zone, it is necessary to guide and drain the upstream water, with a rainwater collection area of 340.6 km², and a drainage and rainwater collection area of 19.4 km². In June 2021, the slope of Gushan section of the channel appeared local collapse, and then danger removal and reinforcement were carried out, as shown in Figure 1.

3.2. Triaxial Compression and Rheological Mechanical Properties. Rock samples taken on-site are conducted triaxial compression test by TAW-2000 microcomputer-controlled rock servo triaxial pressure testing machine, as shown in Figure 2. The sample is added indenters on both ends, sealed with sealing sleeves, installed with strain sensors, and put into the pressure chamber. The confining pressure is applied to the sample to reach the preset value, and the axial pressure is applied to the sample under the condition of keeping the confining pressure unchanged until the sample is destroyed. The confining pressure is set to three states, 1 MPa, 3 MPa, and 5 MPa are applied, respectively. According to the Mohr–Coulomb failure criterion, the shear strength parameters of the wet sample are calculated. The physical and mechanical parameters of the rock sample are summarized in Table 1.

Triaxial compression rheological tests were carried out on the rock samples. Based on the test results, the rheological properties of the rock were analyzed. Sr-6 triaxial creep instrument is used for rheological test, and the confining

pressure of the test equipment uses air pressure as the pressure source. Through the pressure regulating valve, the stability of confining pressure during the test can be guaranteed. The test equipment can be controlled and automatically collect data through the software system, mainly including confining pressure, pore pressure, displacement, and deformation. The accuracy of deformation measurement is 0.01 mm. Gravity loading is adopted in axial stress loading, which can keep the axial pressure constant, and is the most commonly used loading method.

Considering the actual environmental conditions of the project, the drainage shear can more truly simulate the drainage conditions. The drainage shear is used in the test, and the test process is as follows:

- (1) Sample preparation: The soil sampler is used for sample preparation, and the size is $\varphi 61.8 \times 123.6$ mm cylindrical rock sample.
- (2) Consolidation: 500 kPa confining pressure is used for drainage consolidation, and the consolidation time is 2-3 days. It is determined according to the dissipation of pore water pressure. In order to speed up the dissipation of pore water pressure and achieve more uniform consolidation, filter strips are uniformly pasted around the specimen along the axis. After consolidation, the consolidation deformation of the specimen is calculated based on displacement.
- (3) Load: The test is carried out by using the step loading method. The loading time of each step depends on the deformation rate. Generally, if the total deformation is less than 0.01 mm within 3 days, it is considered that the creep is stable. When entering the lower-level loading, the applied stress levels are 0.4 MPa, 0.8 MPa, 1.2 MPa, and 1.6 MPa, respectively.
- (4) Data collection: Record data every 30 seconds within 30 minutes after loading, and then record data every 1 minute.

Four levels of load were applied in the rheological test, and the duration of each level of load was more than 3000 minutes, with a total duration of 16330 minutes. Figure 3 shows the rheological curve of soft rock samples under graded loading. The value on the rheological curve represents the applied axial stress at all levels. Because the test adopts the graded loading method, it is necessary to use the Boltzmann superposition principle to process the test data, and transform the rheological curve in Figure 3 into the rheological curve of rock under different stress levels, as shown in Figure 3.

According to the test results, the instantaneous strain, creep strain, and total strain of rock axial under various stress levels are summarized in Table 2.

It can be seen from Figure 3 and Table 2 that the rheological curve reflects the first stage and the second stage of rheology, that is, the attenuation rheological stage and the stable rheological stage, but the third stage of rheology, that is, the accelerated rheological stage, was not observed in the test. The axial instantaneous strain, creep strain, and total



FIGURE 1: Slope in Zhetang diversion irrigation channel. (a) Danger removal of Gushan section (in 2014 and 2019); (b) typical channel section on the left bank.



FIGURE 2: Rock mechanics test. (a) Sample sampling; (b) TAW-2000 microcomputer-controlled rock servo triaxial pressure testing machine.

TABLE 1: Rock mechanics parameters.

Sample	Water content W %	Natural state		Shear strength		Permeability coefficient K cm/s
		Wet density ρ g/cm ³	Dry density ρ_d g/cm ³	Cohesion c kPa	Friction angle φ °	
ZT-1	24.5	1.95	1.57	27	18	7.0×10^{-6}

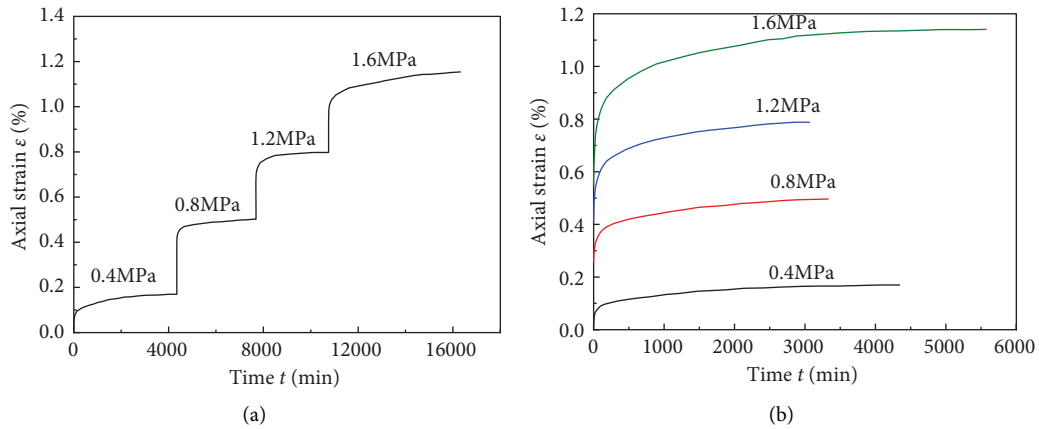


FIGURE 3: Triaxial rheological mechanical property test. (a) Graded loading rheological curve; (b) axial loading rheological curve.

strain of the specimen increase with the increase of the stress level. Under all levels of stress, the proportion of axial creep strain to the total axial strain is more than 50%, indicating

that the rheological effect of the specimen rock is obvious. Due to the weak argillaceous cementation between soft rock particles, large flow variables after rock saturation, and

TABLE 2: Axial instantaneous strain, creep strain, and total strain of rock under various stress levels.

$(\sigma_1 - \sigma_3)$ (MPa)	Axial strain			
	Instantaneous strain (%)	Creep strain (%)	Total strain (%)	Creep strain/total strain (%)
0.4	0.0483	0.1358	0.1841	0.7378
0.8	0.2536	0.2569	0.5106	0.5032
1.2	0.3924	0.3999	0.7924	0.5047
1.6	0.5469	0.6080	1.1549	0.5264

TABLE 3: Physical and mechanical parameters of rock and soil mass.

Material	Density (kg/m^3)	Modulus of elasticity (GPa)	Poisson's ratio	Internal friction angle ($^\circ$)	Cohesion (kPa)
Red-bed soft rock	1920	0.70	0.30	18.0	27.0
Weak interlayer	1840	0.50	0.33	9.5	10.0
Weakly weathered bedrock	2300	1.50	0.265	35.0	100.0

significant aging deformation, the rheological mechanical properties of rock have a great impact on the long-term stability and safe operation of the diversion project.

4. Slope Seepage and Stability Analysis

4.1. Calculation Model and Parameters. Taking Zhetang channel in Xinjiang reservoir area as the analysis object, the finite element analysis model of the channel is established, which is based on the design drawings and field survey, as shown in Figure 1. The channel model is divided into three levels of slope step on the right bank red layer soft rock slope, with the elevation of channel bottom 44.0 m and the width of slope step 3 m, in which the ratio of the first stage slope to the second stage is 1:2.0. The third and the fourth stage slope ratio is 1:1.5. The slope ratio of the first and second stage of the left bank is 1:2.0 and 1:1.5, respectively. The values of physical and mechanical parameters of rock and soil mass used in the calculation are shown in Table 3.

The calculation is divided into two working conditions, namely, conventional and check working condition. Because the rock mass strength of the weak interlayer has significant strain softening characteristics, a large number of projects show that the occurrence of landslide is often related to the penetrating weak interlayer. Therefore, in order to observe and verify the stability of the channel slope containing the weak interlayer, the dangerous working conditions containing the deep penetrating weak interlayer are set to verify the stability and safety of the channel slope, as shown in Figure 4. The physical and mechanical parameters of common soft interbeds in red beds are shown in Table 4.

Mohr-Coulomb criterion of elastic-plastic model is adopted in the constitutive model of material calculation simulating rock and soil mass, and its yield function is

$$F = \frac{1}{3} I_1 \sin \varphi + \left(\cos \theta_\sigma - \frac{1}{\sqrt{3}} \sin \theta_\sigma \sin \varphi \right) \sqrt{J_2} - \cos \varphi = 0, \quad (5)$$

where $I_1 = \sigma_x + \sigma_y + \sigma_z$ is the first stress invariant, θ_σ is the lode angle, $-30^\circ \leq \theta_\sigma \leq 30^\circ$, and $J_2 = 1/6[(\sigma_x - \sigma_y)^2 + (\sigma_y - \sigma_z)^2 + (\sigma_z - \sigma_x)^2] + \tau_{xy}^2$ is the second invariant of stress bias.

4.2. Seepage Analysis. The steady-state seepage analysis of the channel slope is carried out to analyze the seepage field of the channel slope. On the basis of the steady-state seepage, the rainfall infiltration analysis is added. Assuming that the rainfall infiltration intensity is $i = 0.02$ m/h, the slope infiltration intensity is corrected according to the slope, and the following formula is used for calculation:

$$i_\theta = i \times \cos \theta, \quad (6)$$

where i_θ is the infiltration intensity of slope surface and θ is the angle between slope and horizontal plane.

According to the pore water pressure nephogram in Figure 5, with the increase of depth, the pore pressure increases, and the maximum pore pressure is about 200 kPa. The upper part of the slope is unsaturated soil. With the gradual decrease of saturation, the greater the matrix suction, and the maximum matrix suction is about -200 kPa. The influence of rainfall on pore water pressure shown in Figure 6 is mainly reflected in the shallow surface, the pore water pressure on the top of the slope decreases, and the pore water pressure on the bottom of the slope almost remains unchanged.

4.3. Slope Stability Analysis. The slope stability calculation process is divided into two steps. The first step is the steady-state seepage, and the second step is to determine the safety factor of the slope in the critical instability state by reducing the strength factor of the channel slope under the initial equilibrium conditions calculated in the first step.

4.3.1. Conventional Working Conditions. The equivalent plastic strain nephogram and cumulative plastic strain nephogram when reduced to the critical state are shown in Figure 7. By observing that in the process of soil strength reduction, the plastic deformation develops until penetration, and the soil on the sliding surface appears plastic flow, resulting in the instability of the slope along the sliding surface, and the most dangerous arc surface of the channel slope under the critical value of strength reduction can be visually observed.

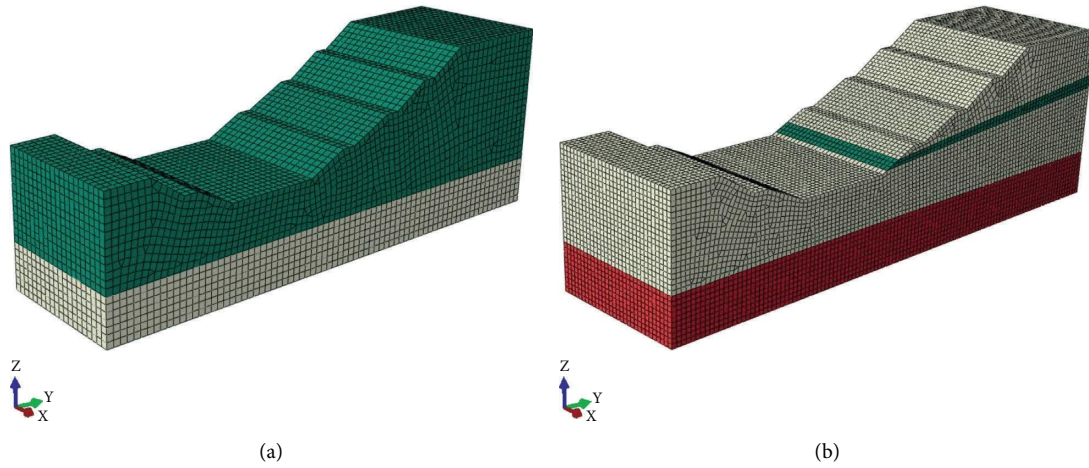


FIGURE 4: Numerical calculation model of Zhetang slope. (a) Conventional working condition; (b) check working condition.

TABLE 4: Mechanical properties of common structural planes of red-bed soft rock.

Rock	Structural plane type	Cohesion (kPa)	Friction angle (°)
Mudstone	—	0.06–0.08	20–30
Siltstone	—	0.03–0.25	20–50
Sandstone	—	0.07–1.0	15–60
—	Pure mud type	2–5	10–14
—	Mud debris type	20–50	14–19
—	Debris mud type	50–100	19–22
—	Rock fragment type	100–250	22–29
—	Closed structural plane	50–150	22–35

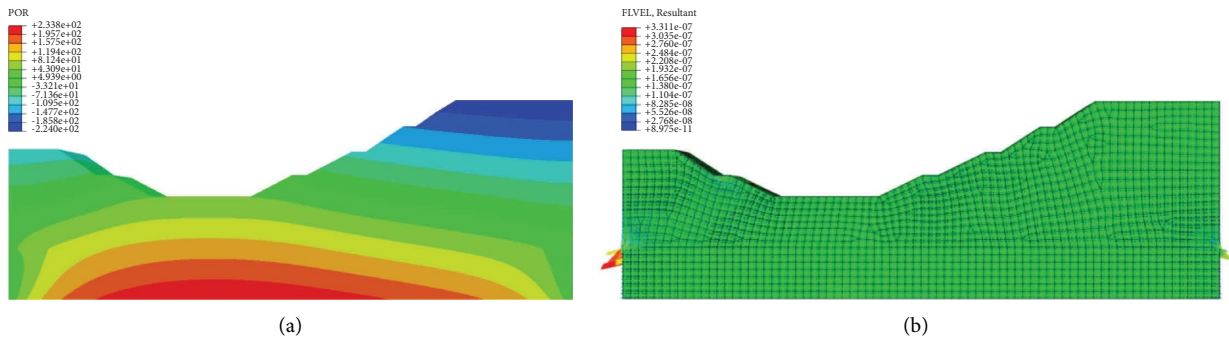


FIGURE 5: Seepage analysis of steady channel slope. (a) Pore water pressure nephogram; (b) flow field distribution.

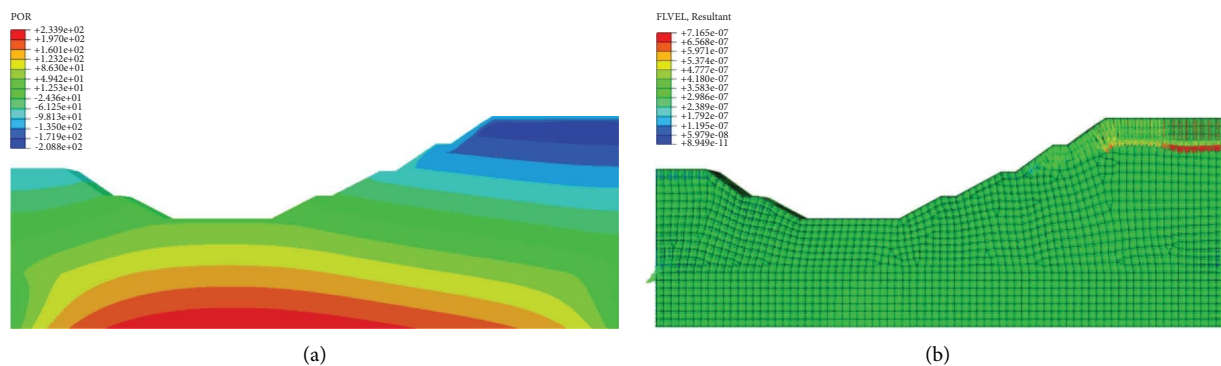


FIGURE 6: Seepage analysis under the influence of rainfall. (a) Pore water pressure nephogram; (b) flow field distribution.

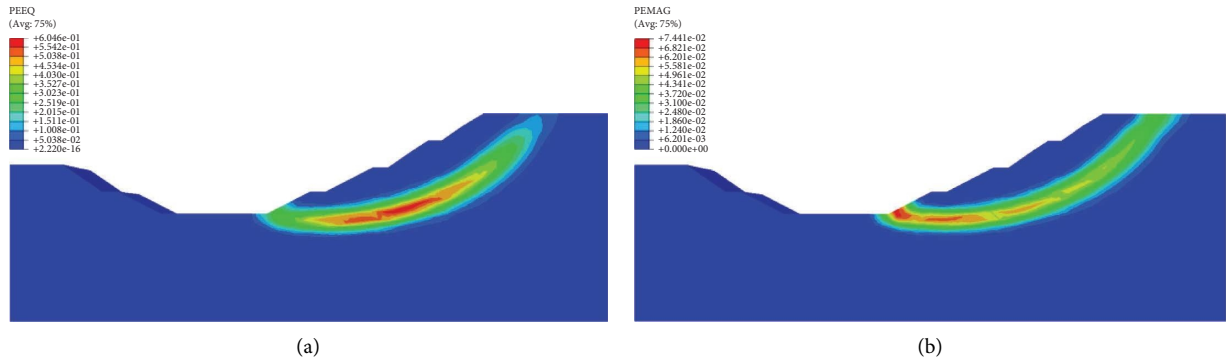


FIGURE 7: The most dangerous sliding surface under conventional working conditions. (a) Equivalent plastic strain nephogram; (b) cumulative plastic strain nephogram.

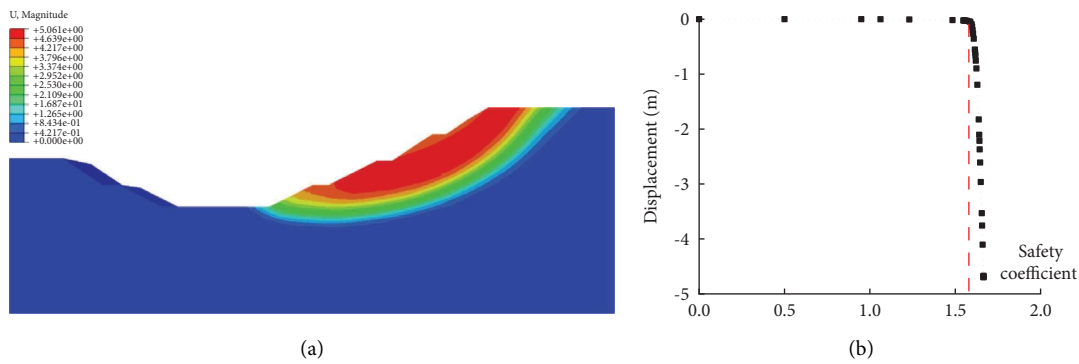


FIGURE 8: Displacement and safety factor under conventional working conditions. (a) Displacement nephogram; (b) stability safety factor.

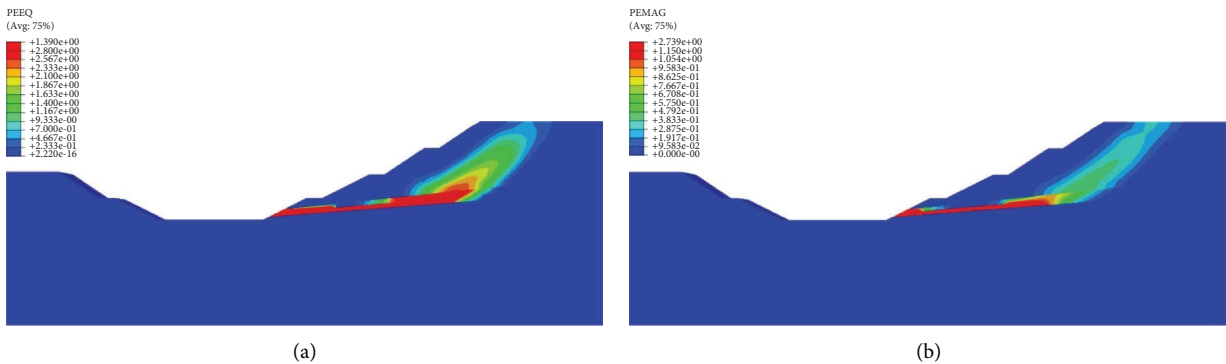


FIGURE 9: The most dangerous sliding surface under check condition. (a) Equivalent plastic strain nephogram; (b) cumulative plastic strain nephogram.

The relationship between the stability safety factor F_t and displacement at the starting point of the slope top slip arc is shown in Figure 8. With the increase of F_t , the plastic region in the slope rock mass gradually increases. A large number of practices have proved that the slope instability can be identified by observing the inflection point of displacement change mutation at the top of the slope. The analysis process of this method is similar to the slope failure process, and it also has clear physical significance. As can be seen from Figure 8(b), when the on-site variable changes to 1.59–1.62, displacement rapidly increases from 0.05 m to 0.76 m, which shows that the safety factor of slope stability in this critical state is about 1.60.

4.3.2. Check Condition. The equivalent plastic strain nephogram and cumulative plastic strain nephogram reduced to the critical state are shown in Figure 9, which can visually observe the most dangerous arc surface of the channel slope under the condition of the critical value of strength reduction. Due to the existence of deep through weak interlayer, the landslide surface is more inclined to slide along the tendency of the soft interlayer along the slope. Figure 10 shows the relationship between the stability safety factor F_t and displacement at the starting point of the slope top slip arc under check condition, in which the slope rock mass tends to slide along the weak interlayer. When the

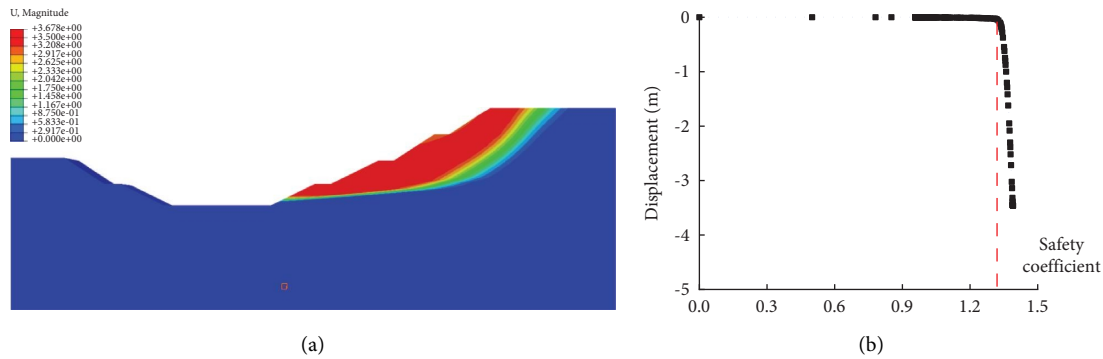


FIGURE 10: Displacement and safety factor under check condition. (a) Displacement nephogram; (b) stability safety factor.

on-site variable changes to 1.29–1.35, displacement rises rapidly from 0.02 m to 0.38 m, and the slope stability safety factor under this critical state is about 1.33.

The stability safety factor of the conventional working condition is greater than that of the check working condition. The occurrence of deep penetrating weak interlayer will induce the slope slip surface to the weak interlayer surface, and aggravate the risk of instability and failure of the channel slope.

5. Conclusion

Aiming at the channel slope project in Zhetang protection area of Xinjiang reservoir protection project, this study adopts the method of combining indoor geotechnical mechanical test and numerical calculation and carries out the stability analysis of the channel slope based on the finite element strength reduction method. The following conclusions can be drawn:

- (1) Through the test of rock and soil mechanical properties, the strength mechanical properties parameters of the slope rock samples are obtained, and the triaxial rheological law are obtained. The axial instantaneous strain, creep strain, and total strain of the samples increase with the increase of the stress level. At all levels of stress, the proportion of axial creep strain to the total axial strain is more than 50%, indicating that the rheological effect of the sample rock is obvious.
- (2) With the increase of depth, pore water pressure increases and matrix suction decreases. The influence of rainfall on pore water pressure is mainly reflected in the shallow surface, the pore water pressure on the top of the slope decreases, and the pore water pressure on the bottom of the slope almost remains unchanged.
- (3) The existence of weak interlayer and structural plane will make the slope sliding surface concentrate to the weak surface, reduce the stability safety factor, and aggravate the risk of instability and failure of the channel slope.
- (4) Based on results obtained by geotechnical test and numerical analysis, the safety factor of slope stability

under conventional and check working conditions of Zhetang channel slope is 1.60 and 1.33, respectively. The safety factor of both conventional and check working conditions is greater than the recommended value of the specification, and the channel slope is generally safe and stable. The local collapse of channel slope is mostly caused by the decline of loose rock and soil mass on the slope, which may be induced by the weathering, disintegration, and creep of red-bed soft rock.

Data Availability

The data that support the findings of this study are available from the corresponding author upon reasonable request.

Conflicts of Interest

The authors declare that they have no conflicts of interest.

Acknowledgments

This work is supported by Jiangxi Provincial Natural Science Foundation (20212BAB214044 and 20204BCJ23002), and supported by the National Natural Science Foundation of China (51779190, 51779193, and 52009126), and Jiangxi Provincial Department of Water Resources Foundation (202224ZDKT08). The authors wish to express their thanks to all supporters.

References

- [1] Z. T. Zhang, W. H. Gao, C. F. Zeng, X. Y. Tang, and J. Wu, "Evolution of the disintegration breakage of red-bed soft rock using a logistic regression model," *Transportation Geotechnics*, vol. 24, Article ID 100382, 2020.
- [2] K. Huang, B. Kang, F. Zha, Y. Li, Q. Zhang, and C. Chu, "Disintegration characteristics and mechanism of red-bed argillaceous siltstone under drying–wetting cycle," *Environmental Earth Sciences*, vol. 81, no. 12, p. 336, 2022.
- [3] C. Xia, C. Zhou, F. Zhu, Z. Liu, and G. Cui, "The critical indicator of red-bed soft rocks in deterioration process induced by water basing on renormalization group theory," *Applied Sciences*, vol. 11, no. 17, p. 7968, 2021.
- [4] T. Wen, H. Tang, Y. Wang, J. Ma, and Z. Fan, "Mechanical characteristics and energy evolution laws for red bed rock of

- badong formation under different stress paths,” *Advances in Civil Engineering*, vol. 2019, Article ID 8529329, 16 pages, 2019.
- [5] Z. Miao, P. Tang, and Y. Zhang, “Recognition of red-bed landslides over eastern sichuan through remote sensing and field investigations,” *Geofluids*, vol. 2022, Article ID 9385352, 9 pages, 2022.
- [6] Z. Zhang, X. Fu, Q. Sheng, D. Yin, Y. Zhou, and J. Huang, “Effect of rainfall pattern and crack on the stability of a red bed slope: a case study in yunnan province,” *Advances in Civil Engineering*, vol. 2021, Article ID 6658211, 2021.
- [7] Z. Liu, X. He, J. Fan, and C. Zhou, “Study on the softening mechanism and control of red-bed soft rock under seawater conditions,” *Journal of Marine Science and Engineering*, vol. 7, no. 7, p. 235, 2019.
- [8] H. Liu, D. Ma, C. Wang, X. Liu, D. Wu, and K. U. J. Khan, “Study on the frost heave mechanism of the water conveyance canal and optimized design of slope protection,” *Bulletin of Engineering Geology and the Environment*, vol. 80, no. 11, pp. 8397–8417, 2021.
- [9] C. Zhang, Zy Cai, Yh Huang, and H. Chen, “Laboratory and centrifuge model tests on influence of swelling rock with drying-wetting cycles on stability of canal slope,” *Advances in Civil Engineering*, vol. 2018, Article ID 4785960, 10 pages, 2018.
- [10] I. Abd-Elaty, H. Eldeeb, Z. Vranayova, and M. Zelenakova, “Stability of irrigation canal slopes considering the sea level rise and dynamic changes: case study el-salam canal, Egypt,” *Water*, vol. 11, no. 5, p. 1046, 2019.
- [11] P. Jamsawang, P. Boathong, W. Mairaing, and P. Jongpradist, “Undrained creep failure of a drainage canal slope stabilized with deep cement mixing columns,” *Landslides*, vol. 13, no. 5, pp. 939–955, 2016.
- [12] H. x. Chu, S. Mei, Xh Gao, Zh Fang, and J. Feng, “Analysis of formation and slope stability in caoheidian channel in bohai bay,” *China Geology*, vol. 2, no. 2, pp. 189–197, 2019.
- [13] S. Liu, Y. Lu, L. Weng, and F. Bai, “Field study of treatment for expansive soil/rock channel slope with soilbags,” *Geotextiles and Geomembranes*, vol. 43, no. 4, pp. 283–292, 2015.
- [14] S. Guo, S. Wen, H. Guo, and H. Fu, “The creep test study and macro-detail analysis of argillaceous red sandstone in different water-containing states,” *Advances in Civil Engineering*, vol. 2022, Article ID 9698675, 8 pages, 2022.
- [15] K. Zhang, P. Cao, J. Meng, K. Li, and W. Fan, “Modeling the progressive failure of jointed rock slope using fracture mechanics and the strength reduction method,” *Rock Mechanics and Rock Engineering*, vol. 48, no. 2, pp. 771–785, 2015.
- [16] G. Liu, X. Huang, and J. Pang, “The uniaxial creep characteristics of red sandstone under dry-wet cycles,” *Advances in Civil Engineering*, vol. 2020, Article ID 8841773, 13 pages, 2020.
- [17] R. I. Shan, Y. Bai, Y. Ju, Ty Han, Hy Dou, and Zl Li, “Study on the triaxial unloading creep mechanical properties and damage constitutive model of red sandstone containing a single ice-filled flaw,” *Rock Mechanics and Rock Engineering*, vol. 54, no. 2, pp. 833–855, 2021.
- [18] X. Yang, A. Jiang, and X. Guo, “Effects of water content and temperature on creep properties of frozen red sandstone: an experimental study,” *Bulletin of Engineering Geology and the Environment*, vol. 81, no. 1, p. 51, 2021.
- [19] C. Yu, S. Tang, C. Tang et al., “The effect of water on the creep behavior of red sandstone,” *Engineering Geology*, vol. 253, pp. 64–74, 2019.
- [20] Y. Song, Y. Che, L. Zhang, J. Ren, S. Chen, and M. Hu, “Triaxial creep behavior of red sandstone in freeze-thaw environments,” *Geofluids*, vol. 2020, Article ID 6641377, 20 pages, 2020.
- [21] D. Wang, G. Chen, D. Jian, J. Zhu, and Z. Lin, “Shear creep behavior of red sandstone after freeze-thaw cycles considering different temperature ranges,” *Bulletin of Engineering Geology and the Environment*, vol. 80, no. 3, pp. 2349–2366, 2021.
- [22] Y. Song, L. Zhang, H. Yang, J. Ren, and Y. Che, “Experimental study on the creep behavior of red sandstone under low temperatures,” *Advances in Civil Engineering*, vol. 2019, Article ID 2328065, 9 pages, 2019.
- [23] S. Q. Yang and B. Hu, “Creep and long-term permeability of a red sandstone subjected to cyclic loading after thermal treatments,” *Rock Mechanics and Rock Engineering*, vol. 51, no. 10, pp. 2981–3004, 2018.
- [24] B. S. Firincioglu and M. Ercanoglu, “Insights and perspectives into the limit equilibrium method from 2D and 3D analyses,” *Engineering Geology*, vol. 281, Article ID 105968, 2021.
- [25] A. Kaur and R. K. Sharma, “Slope stability analysis techniques: a review,” *International Journal of Engineering Applied Sciences and Technology*, vol. 1, no. 4, pp. 52–57, 2016.
- [26] S. M. Seyed-Kolbadi, J. Sadoghi-Yazdi, and M. A. Hariri-Ardebili, “An improved strength reduction-based slope stability analysis,” *Geosciences*, vol. 9, no. 1, p. 55, 2019.
- [27] S. Liu, Z. Su, M. Li, and L. Shao, “Slope stability analysis using elastic finite element stress fields,” *Engineering Geology*, vol. 273, Article ID 105673, 2020.
- [28] D. Dong-ping, L. Liang, W. Jian-feng, and Z. Lian-heng, “Limit equilibrium method for rock slope stability analysis by using the Generalized Hoek–Brown criterion,” *International Journal of Rock Mechanics and Mining Sciences*, vol. 89, pp. 176–184, 2016.
- [29] M. R. Arvin, A. Zakeri, and M. Bahmani Shoorijeh, “Using finite element strength reduction method for stability analysis of geocell-reinforced slopes,” *Geotechnical & Geological Engineering*, vol. 37, no. 3, pp. 1453–1467, 2019.
- [30] X. Kong, G. Cai, Y. Cheng, and C. Zhao, “Numerical implementation of three-dimensional nonlinear strength model of soil and its application in slope stability analysis,” *Sustainability*, vol. 14, no. 9, p. 5127, 2022.

Research Article

Study on Evolution Law and the Mechanical Mechanism of Strong Mine Tremors in a Deep Coal Mine

Chao Wang,¹ Man Wang,² Siyuan Gong,³ Junpeng Zou,⁴ and Kunbo Wu ⁴

¹Shandong Energy Group Co. Ltd., Jinan, Shandong 250014, China

²School of Information Engineering, Wuhan Business University, Wuhan 430056, China

³School of Mines, China University of Mining and Technology, Xuzhou, Jiangsu 221116, China

⁴Faculty of Engineering, China University of Geosciences, Wuhan, Hubei 430074, China

Correspondence should be addressed to Kunbo Wu; wukunbo_cug@126.com

Received 25 July 2022; Accepted 11 October 2022; Published 12 November 2022

Academic Editor: Angelo Aloisio

Copyright © 2022 Chao Wang et al. This is an open access article distributed under the Creative Commons Attribution License, which permits unrestricted use, distribution, and reproduction in any medium, provided the original work is properly cited.

Strong mine tremor occurs frequently in deep mines, which have brought great hidden dangers to the safety of mine production. This paper takes panel 63/06 in No. 6 mining area of Dongtan coal mine as the research background, through geological survey, laboratory test, theoretical analysis, numerical simulation, on-site microseismic monitoring, the seismic evolution law and its mechanical mechanism, etc., and the conclusions are as follows: (1) there are three sets of key layer groups between the surface of the panel 63/06 and the coal seam, among which there is a large amount of energy in the thick Jurassic red layer and the lower key layer, which provides an energy basis for the red-bed to break and generate strong mine tremors; (2) on the plane, most of the strong tremors occurred in front of the mining position of the working face and tended to transfer to the side of the gob, and longitudinal, high-energy mine tremors are mainly distributed in high-level red sandstone; (3) the release location of high-energy mining earthquakes does not match the location of microseismic accumulation, indicating that there is no elastic energy accumulation in the lower surrounding rock before the strong mining earthquake occurs, and it highlights the characteristics of structural occlusal instability rather than energy abrupt instability in the rupture of the red and thick sandstone; and (4) the Dongtan red-bed type strong mine tremors have a large focal rupture radius, a long rupture duration, a small corner frequency, and a weak initial *P* wave, and the characteristics of low stress drop and no catastrophic nature indicate that the thick and low-strength red-bed is prone to large-scale fractures, which should belong to the structural instability type mine shock dominated by tensile fracture.

1. Introduction

With the increase of mining depth, strong mine tremors induced by deep mining show a trend of increasing frequency and energy, which seriously restricts the normal safe production of mines and threatens the safety of underground miners and ground residents. The deep rock mass has the characteristics of high in-situ stresses, high temperature, high gas and water pressure under complex engineering geological conditions and harsh mechanical environments [1–3]. Strong tremors prevention and control management become the focus and difficulty of safe and efficient production in deep mines. A total of nearly 118

strong tremors are effectively located during the mining process in No.6 mining area of Dongtan coal mine. As of February 17, 2021, more than 20 strong tremor events have occurred at panel 63/06, which is being mined.

Thick and hard strata are developed during the formation of coal measure strata in East China [4, 5], among which thick-bedded sandstones (generally known as red-bed) are the most common ones. Tremors are triggered by the fracturing and violent movement of thick and hard strata [4, 6, 7]. Red-bed could form large hanging areas and cause higher stress concentrations above the coal seam under coal excavation. Based on key strata theory [8–10], thick and hard strata occur instantaneously and fracture and break to

release a large amount of elastic energy when the dynamic and static load of the overhanging position exceeds the critical stress. The key is to prevent the emergence of a large overhanging roof under the thick and hard rock strata structure because the occurrence of mine tremors is closely related to red-bed. So far, researchers have done lots of studies on the difficult challenge. To avoid or reduce strong mine tremors, hydraulic fracturing [11, 12], deep-hole blasting [13–15], nonpillar mining technologies are applied to break and weaken the roof [16–18] and have achieved a good effect in deep mines.

The mechanism of mine tremors and the prevention and control technology have been investigated by researchers. Based on the source location, energy, and waveform characteristics, seisms are categorized into three types: mining fracture, huge thick overburden, and high-energy vibration [19, 20]. Combined with the movement pattern of thick and hard rock strata, the roof motion tremors could be classified as fracture, return, and slip [21–23]. Research shows that the structural evolution of the overburden is closely related to the occurrence of mine seismicity [24–27]. Dou et al. [16, 28] made a study on the relationship between the evolution of overburden spatial structure and the occurrence law of mine seismicity and proposed the corresponding prevention and control measures according to different overburden structures. The risk of mine tremors occurrence is studied by Huang et al. [29], Xiao et al. [30], and Ju and Xu [31] through the fracture and energy accumulation-release characteristics of rock strata above the coal seam.

The mechanism for the occurrence of nonhazardous strong tremors induced by deep mining has not been clarified. It has been indicated that strong tremors do not cause damage to the roadway because they mostly occur in the goaf and its effective attenuation of vibration impact energy [32, 33]. From the waveforms recorded by the microseismic system, it could be shown that the strong mine tremor in Dongtan coal mine has a longer vibration duration, single main frequency component that is mainly low frequency, weak initial motion, low amplitude, and difficulty in localization compared with the impact rock burst signal. It is likely that the specificity of its red-bed sandstone fracture dynamics, rather than just the location of the seismic occurrence, determines the type of mine tremors [4, 34, 35]. In this paper, the characteristics of red-bed type strong tremors induced by deep mining are investigated, and the causes of frequent tremors are explained, and the induced mechanical mechanisms are revealed to provide theoretical guidance for the prevention and control of dynamic disasters in deep mines.

2. Engineering Background

Dongtan coal field with an area of 59.96 km² is located in the bordering area of Zoucheng, Yanzhou, and Qufu cities in Shandong Province, China. It is geologically located in the core and deep zone of the Yanzhou syncline. Currently, all mining activities are taking place at the first level (–660 m). The main mining coal seam is 3-coal-seam (3, 3 upper, and 3 lower), of which the 3upper coal seam has a buried depth of

about 670 m with an average value of 5.41 m. Dongtan coal mine is divided into seven mining areas, and the No.6 mining area is located in the south of the coal mine. The stopped panels include the 63upper03 panel, 63upper04 panel, and 63upper05 panel in the No.6 mining area. The panel 63upper06 has been mined for 550 m.

The design track length of the panel 63upper06 is 1499 m, the transport length is 1489 m, the inclined width is 261 m, the elevation is –604.5 to –670.3 m, and the average is –637.4 m. The panel 63upper06 is mined on February 11, 2020. The division of panels is shown in Figure 1. Fully mechanized mining technology is adopted. The coal seam inclination is large in the west, with a maximum inclination of 14° at the starting cut and an overall average inclination of about 4°. The coal seam has a hardness of $f=2 \sim 3$ on the Protodyakonov scale.

The geo-formation structure revealed by drill holes #170 and #O2-D7 within the range of panel 63upper06 is analysed statistically. As shown in Figure 2, three key layers can be identified between the surface and the coal seam, whose average thicknesses are 141 m, 217 m, and 30 m, and the distances from the coal seam are 331 m, 111 m, and 13 m, respectively. Key strata 2 and 3 are Jurassic sandstone layers and referred to as red-bed. Physical and mechanical tests find that key layer 1 is harder, with compressive strengths up to 88.2–127.5 MPa. However, the compressive strength of the red-bed ranges from 20 to 80 MPa, which is significantly weaker compared to the strength of the lower rock strata.

From the microseismic monitoring results during the mining process of panels in No.6 mining areas at the early stage, and it is known that the thickness of the red-bed in the area of frequent mine seismicity is 480 m ~ 520 m (see Figure 3). The distance between the red-bed and coal seam generally does not exceed 100 m. Therefore, the red-bed fractures instantaneously and releases a large amount of energy, resulting in strong tremors when the thickness of the red-bed increases and is close to the coal seam.

3. Stress Evolution and Energy Accumulation Characteristics of Overburden

3.1. Numerical Modeling. A three-dimensional numerical simulation model of deep mining in No.6 mining areas is constructed based on the principles of following the distribution of the goaf and the thickness and the physical and mechanical properties of rock strata. In Figure 4, the length, width, and height of the model are 2003 m, 1680 m, and 286 m, respectively. The stress evolution, degree of stress concentration, and energy accumulation characteristics of rock strata above the coal seam during the mining process of panel 63upper06 are calculated.

3.2. Stress Evolution and Energy Accumulation Characteristics of Panels. The panel 63upper06 has advanced 550.2 m. Panels 63upper03, 63upper04, and 63upper05 have been excavated. The existence of goafs will inevitably have a great impact on the stress distribution and energy accumulation in the panel [27, 36]. When the load on the overlying rock

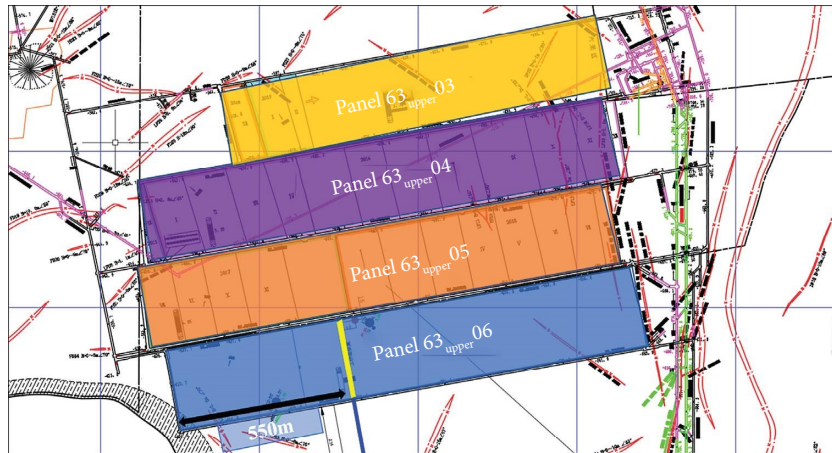


FIGURE 1: The division of panels in No.6 mining area.

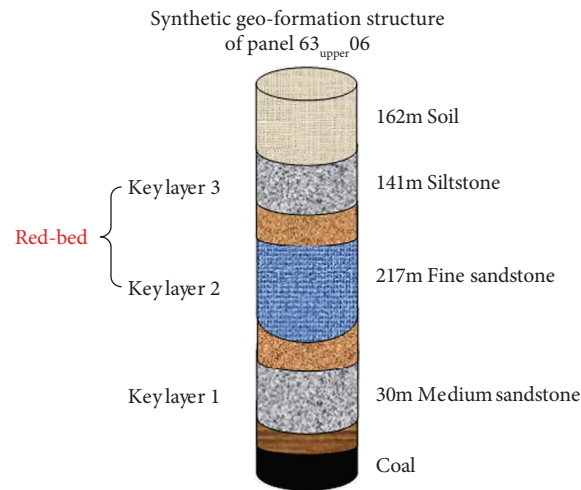


FIGURE 2: Analysis of key layers in the overburden above coal seam.

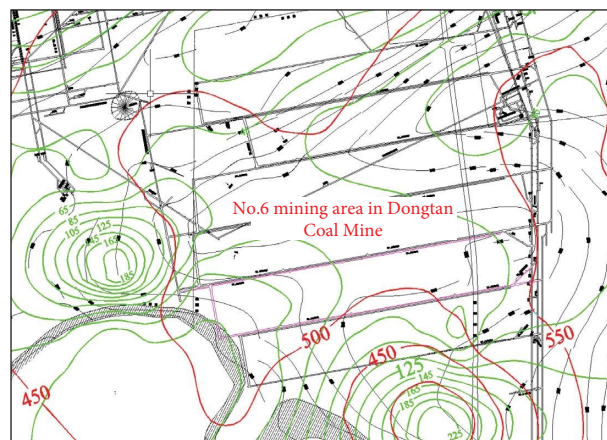


FIGURE 3: Distribution of the red-bed iso-thickness line (red), the red-bed bottom boundary, and the roof above coal seam iso-distance line (green).

strata exceeds its strength, the overburden collapses. In Figure 5, the maximum principal stress within the mining area is distributed within a limited range around the panel, and the maximum principal stress value has reached 68 MPa.

The maximum principal stress distribution in the coal seam and overlying strata during the continuation of the work face 63upper06 to 1350 m is analyzed. Figure 6 shows the evolution of the maximum principal stress along the

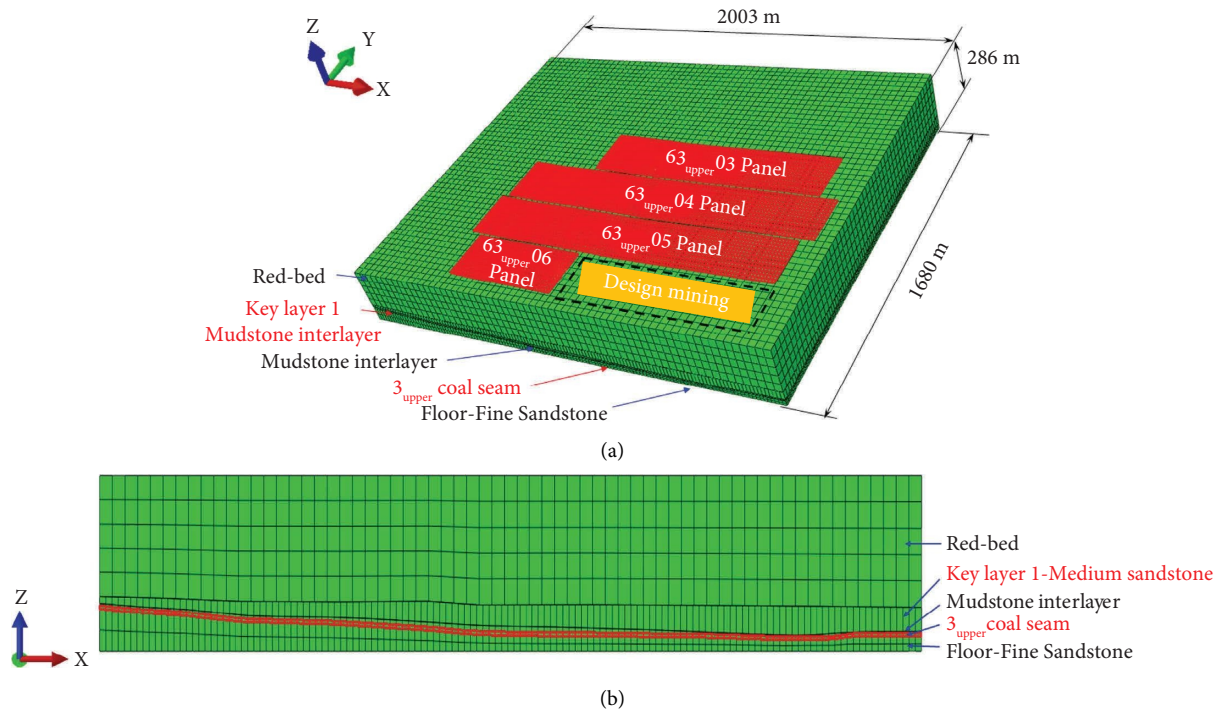


FIGURE 4: Numerical calculation model for overlying strata movement law in No.6 mining area. (a) 3D numerical simulation model. (b) Front view profile.

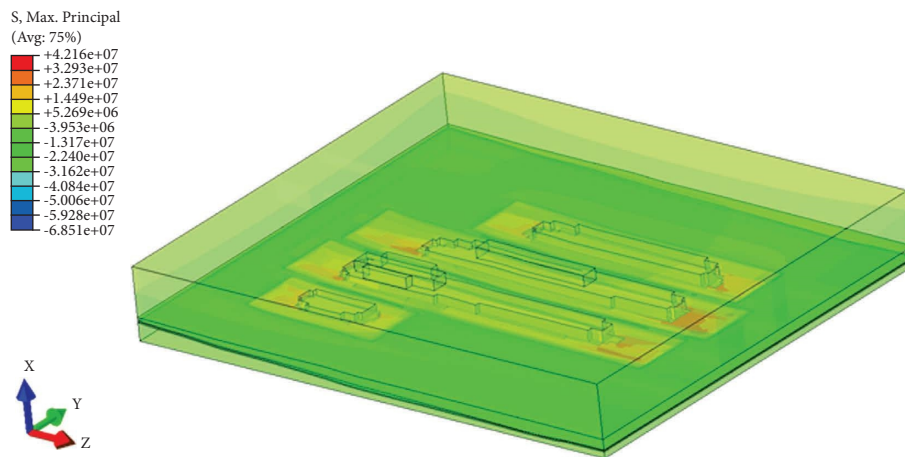


FIGURE 5: Maximum principal stress distribution in No.6 mining areas.

mining direction with the advancement of the working face. The distribution of the maximum principal stress in the spatial three-dimensional range of panel 63_{upper}06 shows that the maximum principal stress value reaches 59.8 MPa. In Figure 7, the maximum principal stress in the current state of the working face 63_{upper}06 up to about 650 m advance is at the highest value. The maximum principal stress tends to decrease during the subsequent advance. The working face advances to about 750 m to reach the lowest value, and then gradually rises.

As shown in Figure 8, a large amount of energy exists in the red-bed sandstone and key layers above the coal seam when the working face 63_{upper}06 is advanced to 650 m,

which provides an energy basis for generating strong mine tremors.

4. Study on Evolution Law of Strong Mine Tremors

4.1. Spatial Distribution Law of Strong Mine Tremors. A total of 25 strong mine tremors are effectively located on panel 63_{upper}06 during the production period (March 13, 2020 to November 30, 2020). After fine-tuning the *P*-wave initial arrival times of tremors, the distribution of strong mine tremors is obtained as shown in Figure 9. Tremors are mainly concentrated at a distance of approximately 230 to

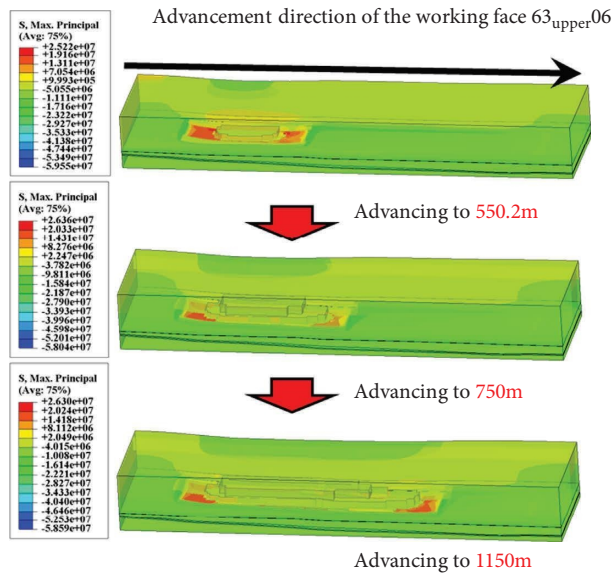


FIGURE 6: Cloud diagram of the maximum principal stress during the advance of the working face 63_upper06.



FIGURE 7: Relationship between the maximum principal stress around the working face and the advancing distance.

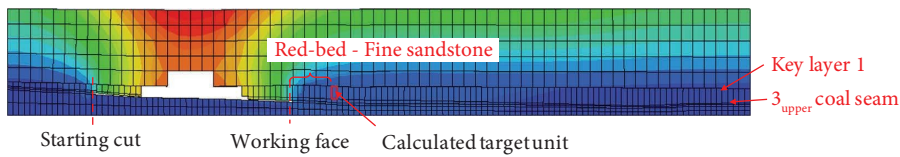


FIGURE 8: Schematic diagram of target element for calculating strain energy.

489 m from the starting cut, roughly in the area between 1st square and 2nd square.

Strong mine tremors mainly occur in the 300 m range before and after the working face (see Figure 10). With the gradual advancement of the working face, most tremors occur in front of the working face and are in a fluctuating state, except for the first strong tremor which occurs behind the starting cut of the panel. With mining, strong mine tremors occur first at positions far from the extraction location, gradually approaching the working face, and then transferring to the front of the working face. Overall, there is

a tendency for strong mine tremors to shift to the side of the goaf. It indicates that strong mine tremors at panel 63_upper06 are influenced by the overburden structure.

In Figure 11, large-energy mine tremors are mostly distributed in key layers 2 and 3 from the spatial distribution of tremors. Considering factors such as the thinness of key layer 1 and the influence of locating accuracy, there are fewer mine tremors occurring directly in key layer 1. The great majority of strong mine tremors have a low impact on mine safety production. Therefore, it could be verified that strong mine tremors occurring in key layers 2 and 3 are not

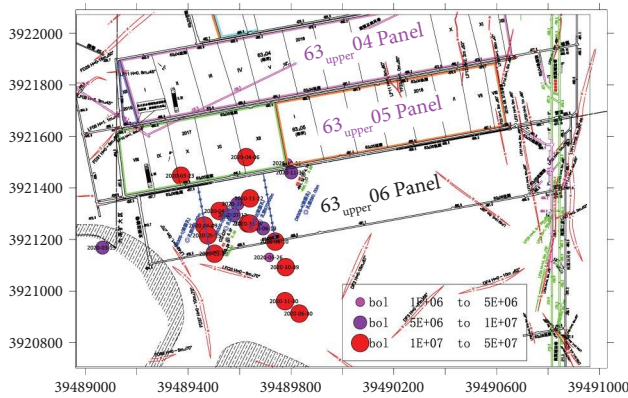


FIGURE 9: Plan of strong mine tremors distribution.

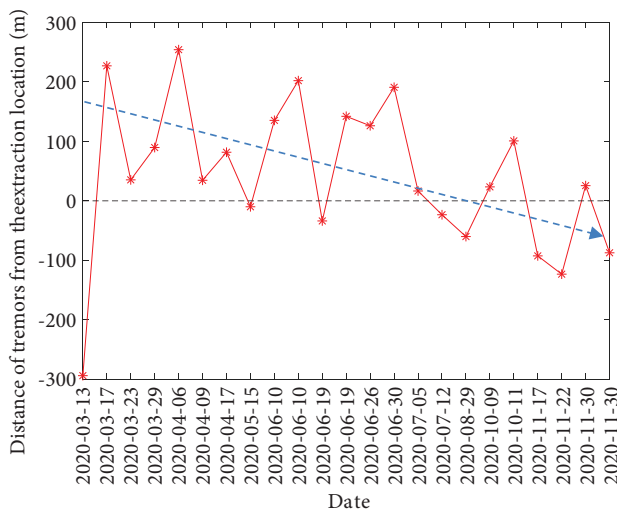


FIGURE 10: The curve of strong mine tremors relationship with extraction location.

significant in terms of inducing disasters, but they will cause strong shocks on the ground. Meanwhile, large-energy mine seismic signals are also monitored at lower rock strata. Take the strong mine seismic signal that occurred on November 30, 2020, at 09:41:29 as an example. The error calculation shows that its Z-direction elevation error is 46.8 m. After correction, it should be located in key layer 1 in spatial position.

Strong mine tremors at panel 63upper06 have a tendency to develop from far-field strata to lower rock strata. After the fracture of key layers, several strong mine tremors will accompany the lower strata [4, 28, 37]. The fracture of far-field strata will be acting as a load directly on the near-field strata, which is extremely negative for the normal break of the lower layers, especially for key layer 1 [38–40]. The energy released by the breakage of near-field rock strata immediately is applied to the coal seam and has greater disaster-causing effects than far-field strata because it is closer to the coal seam and has higher strength. Therefore, it can be inferred from the above analysis that it is more important to treat the lower rock strata than the higher ones.

4.2. Characteristics of Strong Mine Tremors Energy Release. Figure 12 shows the statistical curves of mine seismic energy and also frequency and extraction location at panel 63upper06 from February 15, 2020, to November 29, 2020. The large-energy mine tremors are mostly in the form of single peaks, indicating that the strong tremors at panel 63upper06 have an individual character in Figure 12(a). There are no significant energy and frequency changes in the source area and the surrounding area before and after the occurrence of strong tremors, reflecting more structural occlusion instability than instantaneous energy unsteadiness.

Strong tremors mainly occur in a range of 540 m in front and behind the working face, which could affect up to 300 m area in the direction of advancement and 240 m area in the direction of the goaf. However, the unfavorable case is that large-energy tremors occur near the extraction location of the working face during the statistical time period, which increases the risk of induced rock burst of disaster-causing mine seisms.

The distribution law of the frequency and energy of mine tremors in panel 63upper06 is shown in Figure 12(b) after eliminating large-energy tremors (>105 J). It could be seen that there is a strong consistent frequency curve and energy curve, which is similar to the trend of most mine regulations. The statistical analysis of tremors in Dongtan coal mine shows that large-energy seisms mostly occur in higher strata, and small-energy seisms mainly occur in lower strata above coal seams. The peak of the effect of the lower strata super-elevation is approximately at the position of 130 m, which is the main area of concentrated mine seismic release, and the farthest location that can be affected is 370 m.

As a result, strong mine tremors caused by the breakage of the high-level roof at panel 63upper06 and small-energy seisms occurring within the lower roof and coal are released in two different types of energy. Strong tremors are distributed both in front and behind the working face, while small-energy seisms are mainly distributed in front of the working face. Considering the correlation between the far-field rock strata and the near-field strata breakage, the comprehensive determination of panel 63upper06 mining supervision could have an influence on the range of about 350 m.

5. Study on the Mechanical Mechanism of Strong Mine Tremors

It is generally believed that the harder the rock strata the more difficult it is to fracture, but the breakage frequency of red-bed sandstone is significantly higher. On the other hand, it means that the overlying high red-bed is easier to be fractured with the mining of No.6 mining area, which will result in the high-energy mine tremors phenomenon. The reason is that the red-bed is not hard but strong integrity and large thickness exist in a close relationship. As shown in Figure 13, most of the strong tremors that occurred in No.6 mining area of Dongtan coal mine are low-frequency-type seisms. The average dominant frequency of strong mine tremors at panel 63upper06 is found to be 2–4 Hz after statistical analysis of the waveform of 25 seismic events. The

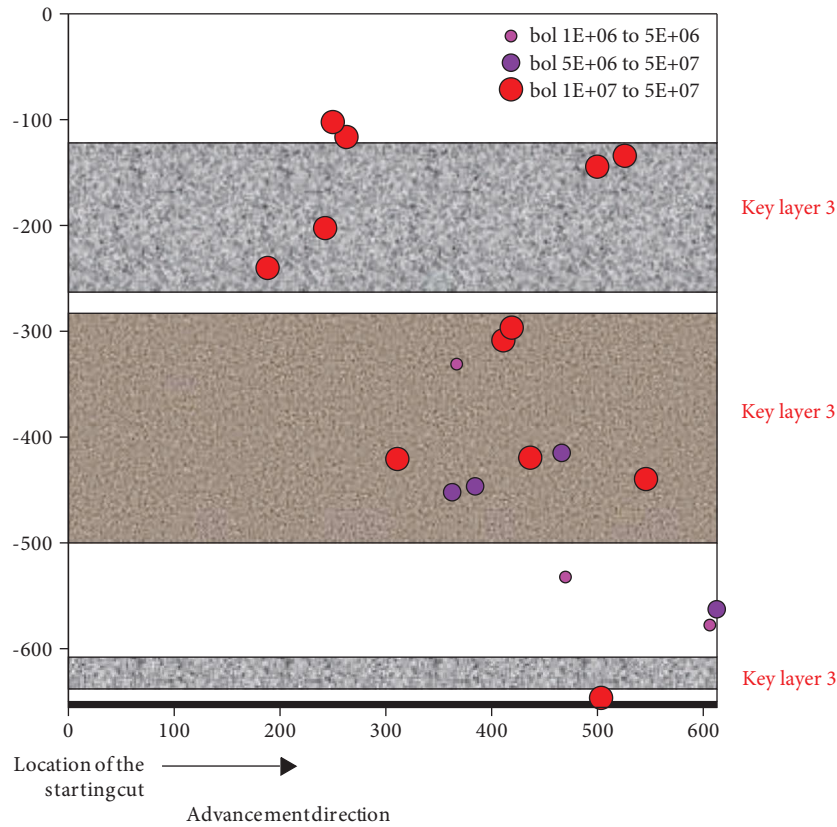


FIGURE 11: Profile of the location of strong mine tremors at panel 63upper06.

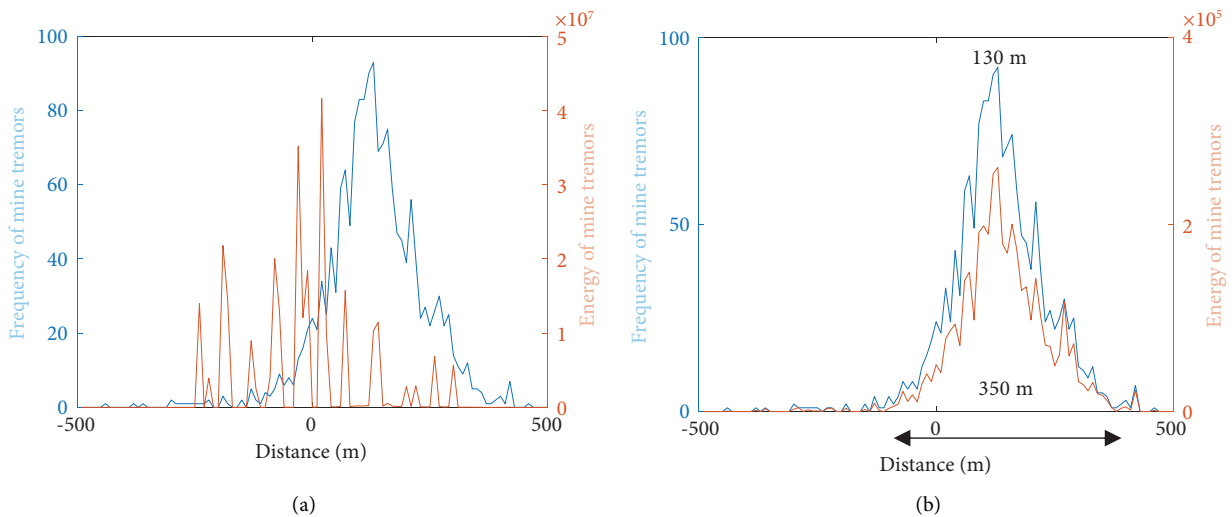


FIGURE 12: The distribution law of mine tremors near the extraction location of panel 63upper06. (a) Statistical results including all mine tremors. (b) Statistical results after eliminating mine tremors over 10^5 J.

waveform signal is commonly characterized by the long fracture duration and less over-range, reflecting the weak disaster-causing feature of strong tremors.

To further analyze and determine the mechanism of strong tremor occurrence, the seismic signal in Figure 13 is used as an example, and its source parameters are calculated

by geophysical methods (e.g., seismic moment, corner frequency, circular source radius, and stress drop) [41–44]. It could be seen that the longer the duration of seismic fracture, the larger the circular source radius, and the smaller the stress drop, which is the primary reason for the weak effect of rock burst induced by strong red-bed type mine tremors. By

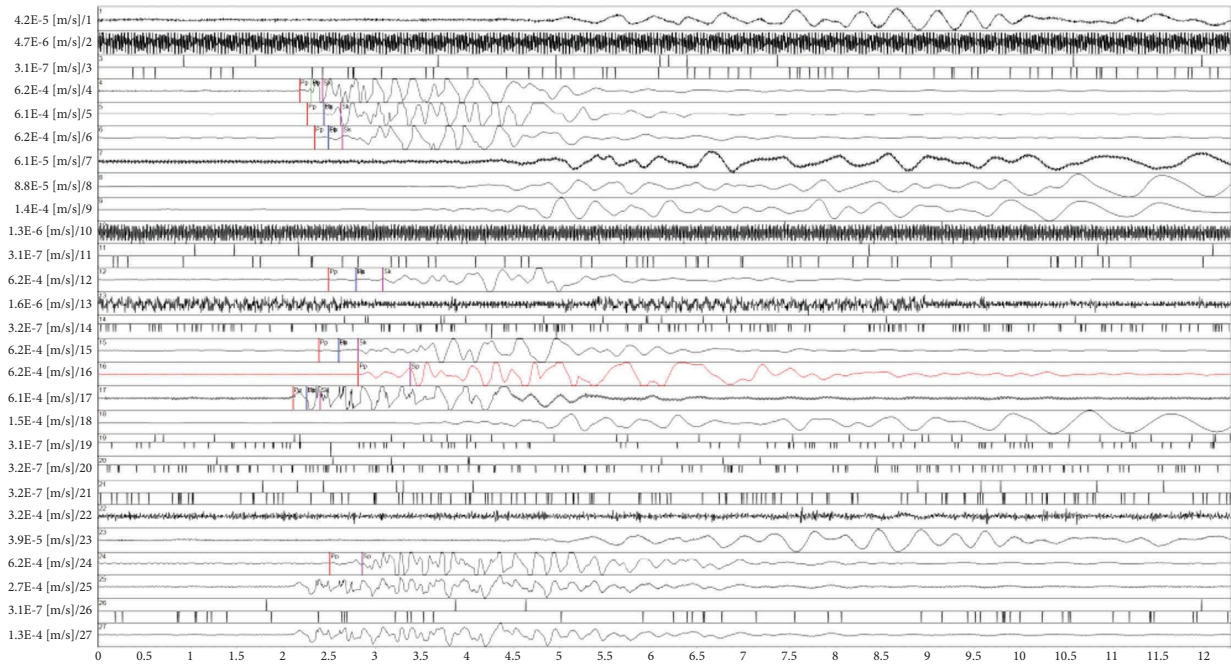


FIGURE 13: Recording of strong tremor signals on November 30, 2020, at 09:41:49.

TABLE 1: Results of seismic source parameters solution.

Date	Circular source radius (m)	Corner frequency (Hz)	Seismic moment (N·m)	Seism magnitude	Stress drop (MPa)	Fracture duration (s)
2020-11-30 09.41.49	150	2.98	9.07 E + 11	1.97	0.12	0.34

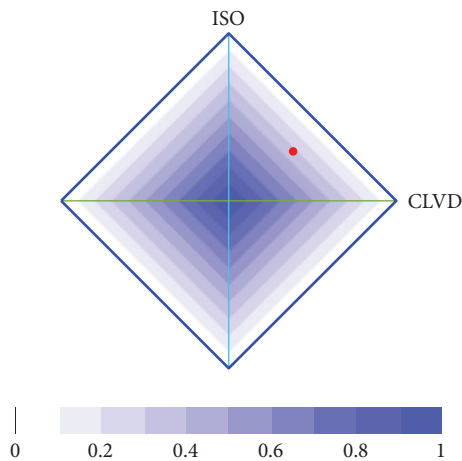


FIGURE 14: The focal mechanism solution results of the strong mine tremor on November 30, 2020, at 09:41:49.

comprehensive analysis of p-wave initial motion signals recorded by 25 seisms, it is revealed that the weak initial motion of red-bed type seismic signals is consistent with the low stress drop. The results indicate that red-bed type strong mineral seismicity may not require a high stress

environment to be generated. The preliminary inference is that it belongs to the red-bed structural instability type mine tremor. The released energy originates mainly from the gravitational potential energy of the red-bed (Table 1).

Based on the moment tensor inversion method to analyze the focal mechanism [41, 45, 46], the solution results are given in Figure 14. The results show that the red-bed mine tremor contains both shear-fracturing and tensile-fracturing components, and the comprehensive performance is a mixed fracturing mechanism dominated by tensile failure.

6. Conclusions

The mechanical mechanism of strong mine tremors is not clarified under the mining of deep coal seam. In this paper, based on numerical simulation, on-site microseismic monitoring, and moment tensor inversion, the spatial distribution characteristic and mechanical mechanism of mine tremors as well as the evolution law of overburden stress are revealed. The following conclusions can be drawn:

- (1) Three key layers could be determined between the surface and coal seam by comprehensive analysis of the stratigraphic structure in No.6 mining area of Dongtan coal mine. The numerical simulation results

indicate that a large amount of energy is accumulated in the thick and hard rock strata above the coal seam, which provides the energy basis for the rock layer fracture to generate strong mine tremors.

- (2) Most of strong mine tremors occur in front of the extraction location at the panel, and there is a tendency to transfer to the goaf. It shows that the strong seism at panel 63upper06 is dominantly affected by the local area overburden structure. Meanwhile, large-energy mine tremors are concentrated in the high-level key layer, but a little occurs in the lower key layer.
- (3) Mismatch between the position of high-energy mine seismic release and microseismic accumulation is seen by analyzing the distribution of high-energy and low-energy mine tremors as the working face extraction. It means that there is no elastic energy accumulation in the lower surrounding rock mass before the occurrence of strong mine tremors. It highlights that the red-bed breakage presents structural occlusion instability rather than instantaneous energy unsteadiness, which brings great difficulties to the early warning of large-energy seisms.
- (4) The red-bed type strong mine tremor has the characteristics of large circular source radius, long fracture duration, small corner frequency, weak p-wave initial motion, low stress drop, and no disaster-causing property in Dongtan coal mine. This suggests that the huge thick and low-strength red-bed is easily fractured on the large scale. Seism events belong to the strong mine tremor of structural instability dominated by tensile failure.

Data Availability

The datasets generated during and/or analyzed during the current study are available from the corresponding author on reasonable request.

Conflicts of Interest

The authors declare that they have no conflicts of interest.

References

- [1] P. G. Ranjith, J. Zhao, M. H. Ju, R. V. D. Silva, T. D. Rathnaweera, and A. K. Bandara, "Opportunities and challenges in deep mining: a brief review," *Engineering*, vol. 3, pp. 546–551, 2017.
- [2] H. P. Xie, M. Z. Gao, R. Zhang, G. Y. Peng, W. Y. Wang, and A. Q. Li, "Study on the mechanical properties and mechanical response of coal mining at 1000 m or deeper," *Rock Mechanics and Rock Engineering*, vol. 52, no. 5, pp. 1475–1490, 2019.
- [3] H. P. Xie, C. Li, Z. Q. He et al., "Experimental study on rock mechanical behavior retaining the in situ geological conditions at different depths," *International Journal of Rock Mechanics and Mining Sciences*, vol. 138, Article ID 104548, 2021.
- [4] Y. Y. Jiao, K. B. Wu, J. P. Zou et al., "On the strong earthquakes induced by deep coal mining under thick strata—a case study," *Geomechanics and Geophysics for Geo-Energy and Geo-Resources*, vol. 7, no. 4, p. 97, 2021.
- [5] P. F. Lyu, J. B. Lu, E. Y. Wang, and X. H. Chen, "The mechanical criterion of activation and instability of normal fault induced by the movement of key stratum and its disaster-causing mechanism of rockburst in the hanging wall mining," *Advances in civil engineering*, vol. 2021, Article ID 6618957, 11 pages, 2021.
- [6] C. Xu, Q. Fu, X. Y. Cui, K. Wang, Y. X. Zhao, and Y. B. Cai, "Apparent-depth effects of the dynamic failure of thick hard rock strata on the underlying coal mass during underground mining," *Rock Mechanics and Rock Engineering*, vol. 52, no. 5, pp. 1565–1576, 2019.
- [7] M. L. Yu, J. P. Zuo, Y. J. Sun, C. N. Mi, and Z. D. Li, "Investigation on fracture models and ground pressure distribution of thick hard rock strata including weak interlayer," *International Journal of Mining Science and Technology*, vol. 32, pp. 137–153, 2022.
- [8] L. X. Wu, M. G. Qian, and J. Z. Wang, "The influence of a thick hard rock stratum on underground mining subsidence," *International Journal of Rock Mechanics and Mining Sciences*, vol. 34, pp. 341–344, 1997.
- [9] M. G. Qian, X. X. Miao, J. L. Xu, and X. B. Mao, *Key Strata Theory in Ground Control*, China University of Mining and Technology Press, Xuzhou, China, 2000.
- [10] Y. Y. Lu, T. Gong, B. W. Xia, B. Yu, and F. Huang, "Target stratum determination of surface hydraulic fracturing for far-field hard roof control in underground extra-thick coal extraction: a case study," *Rock Mechanics and Rock Engineering*, vol. 52, no. 8, pp. 2725–2740, 2019.
- [11] B. X. Huang, Y. Z. Wang, and S. G. Cao, "Cavability control by hydraulic fracturing for top coal caving in hard thick coal seams," *International Journal of Rock Mechanics and Mining Sciences*, vol. 74, pp. 45–57, 2015.
- [12] J. Zou, Y. Y. Jiao, F. Tan, J. Lv, and Q. Zhang, "Complex hydraulic-fracture-network propagation in a naturally fractured reservoir," *Computers and Geotechnics*, vol. 135, Article ID 104165, 2021.
- [13] P. Gong, Y. H. Chen, Z. G. Ma, and S. X. Cheng, "Study on stress relief of hard roof based on presplitting and deep hole blasting," *Advances in Civil Engineering*, vol. 2020, Article ID 8842818, 12 pages, 2020.
- [14] G. F. Wang, S. Y. Gong, L. M. Dou, W. Cai, X. Y. Yuan, and C. J. Fan, "Rockburst mechanism and control in coal seam with both syncline and hard strata," *Safety Science*, vol. 115, pp. 320–328, 2019.
- [15] X. P. Lai, C. Jia, F. Cui et al., "Microseismic energy distribution and impact risk analysis of complex heterogeneous spatial evolution of extra-thick layered strata," *Scientific Reports*, vol. 12, no. 1, Article ID 10832, 2022.
- [16] L. M. Dou, C. P. Lu, Z. L. Mu, and M. S. Gao, "Prevention and forecasting of rock burst hazards in coal mines," *Mining Science and Technology*, vol. 19, pp. 585–591, 2009.
- [17] X. Y. Liu, M. C. He, J. Wang, and Z. M. Ma, "Research on non-pillar coal mining for thick and hard conglomerate roof," *Energies*, vol. 14, pp. 299–312, 2021.
- [18] G. L. Zhu, R. L. Sousa, M. C. He, P. Zhou, and J. Yang, "Stability analysis of a non-pillar-mining approach using a combination of discrete fracture network and discrete-element method modeling," *Rock Mechanics and Rock Engineering*, vol. 53, no. 1, pp. 269–289, 2020.
- [19] G. Mutke, A. Lurka, and Z. Zembaty, "Prediction of rotational ground motion for mining-induced seismicity – case study from upper silesian coal basin, Poland", engineering

- geology,” *Engineering Geology*, vol. 276, Article ID 105767, 2020.
- [20] C. P. Lu, G. J. Liu, Y. Liu, N. Zhang, J. H. Xue, and L. Zhang, “Microseismic multi-parameter characteristics of rockburst hazard induced by hard roof fall and high stress concentration,” *International Journal of Rock Mechanics and Mining Sciences*, vol. 76, pp. 18–32, 2015.
- [21] M. J. Mendecki, J. Szczygieł, G. Lizurek, and L. Teper, “Mining-triggered seismicity governed by a fold hinge zone: the upper silesian coal basin, Poland,” *Engineering geology, Engineering Geology*, vol. 274, Article ID 105728, 2020.
- [22] Z. L. He, C. P. Lu, X. F. Zhang, Y. Guo, Z. H. Meng, and L. Xia, “Numerical and field investigations of rockburst mechanisms triggered by thick-hard roof fracturing,” *Rock Mechanics and Rock Engineering*, 2022.
- [23] S. L. Wang, G. L. Zhu, K. Z. Zhang, and L. Yang, “Study on characteristics of mining earthquake in multicoal seam mining under thick and hard strata in high position”, shock and vibration,” *Shock and Vibration*, vol. 55, pp. 6863–6886, Article ID 6675089, 2021.
- [24] A. Y. Cao, L. M. Dou, W. Cai, S. Y. Gong, S. Liu, and G. C. Jing, “Case study of seismic hazard assessment in underground coal mining using passive tomography,” *International Journal of Rock Mechanics and Mining Sciences*, vol. 78, pp. 1–9, 2015.
- [25] K. Ma, S. J. Wang, F. Z. Yuan, Y. L. Peng, S. M. Jia, and F. Gong, “Study on mechanism of influence of mining speed on roof movement based on microseismic monitoring,” *Advances in Civil Engineering*, vol. 2020, Article ID 8819824, 9 pages, 2020.
- [26] C. Zhou, S. T. Zhu, D. Z. Song, F. X. Jiang, J. H. Liu, and J. J. Li, “Study on the mechanism of repeated mining tremor in multiple key layers: a typical case study,” *Geotechnical & Geological Engineering*, vol. 40, no. 10, pp. 5139–5151, 2022.
- [27] L. M. Dou and H. He, “Study of OX-F-T spatial structure evolution of overlying strata in coal mines,” *Chinese journal of rock mechanics and engineering*, vol. 31, pp. 453–460, 2012.
- [28] H. He, L. M. Dou, A. Y. Cao, and J. Fan, “Mechanisms of mining seismicity under large scale exploitation with multikey strata”, shock and vibration,” *Shock and Vibration*, vol. 2015, Article ID 313069, 9 pages, 2015.
- [29] G. J. Huang, J. Ba, Q. Z. Du, and J. M. Carcione, “Simultaneous inversion for velocity model and microseismic sources in layered anisotropic media,” *Journal of Petroleum Science and Engineering*, vol. 173, pp. 1453–1463, 2019.
- [30] Y. X. Xiao, X. T. Feng, J. A. Hudson, B. R. Chen, G. L. Feng, and J. P. Liu, “ISRM suggested method for in situ microseismic monitoring of the fracturing process in rock masses,” *Rock Mechanics and Rock Engineering*, vol. 49, no. 1, pp. 343–369, 2016.
- [31] J. F. Ju and J. L. Xu, “Structural characteristics of key strata and strata behaviour of a fully mechanized longwall face with 7.0m height chocks,” *International Journal of Rock Mechanics and Mining Sciences*, vol. 58, pp. 46–54, 2013.
- [32] L. H. Wang, A. Y. Cao, L. M. Dou et al., “Numerical simulation on failure effect of mining-induced dynamic loading and its influential factors,” *Safety Science*, vol. 113, pp. 372–381, 2019.
- [33] S. Q. He, D. Z. Song, Z. L. Li et al., “Precursor of spatio-temporal evolution law of MS and AE activities for rock burst warning in steeply inclined and extremely thick coal seams under caving mining conditions,” *Rock Mechanics and Rock Engineering*, vol. 52, no. 7, pp. 2415–2435, 2019.
- [34] A. Y. Cao, L. M. Dou, W. Cai, S. Y. Gong, S. Liu, and Y. L. Zhao, “Tomographic imaging of high seismic activities in underground island longwall face,” *Arabian Journal of Geosciences*, vol. 9, no. 3, p. 232, 2016.
- [35] K. Ma, F. Z. Yuan, H. B. Wang et al., “Fracture mechanism of roof key strata in Dongjiahe coal mine using microseismic moment tensor,” *Geomatics, Natural Hazards and Risk*, vol. 12, pp. 1467–1487, 2021.
- [36] B. Yu, Z. Y. Zhang, T. J. Kuang, and J. R. Liu, “Stress changes and deformation monitoring of longwall coal pillars located in weak ground,” *Rock Mechanics and Rock Engineering*, vol. 49, no. 8, pp. 3293–3305, 2016.
- [37] D. Mondal, P. N. S. Roy, and M. Kumar, “Monitoring the strata behavior in the Distressed Zone of a shallow Indian longwall panel with hard sandstone cover using Mine-Microseismicity and Borehole Televiewer data,” *Engineering Geology*, vol. 271, Article ID 105593, 2020.
- [38] T. J. Kuang, Z. Li, W. B. Zhu et al., “The impact of key strata movement on ground pressure behaviour in the Datong coalfield,” *International Journal of Rock Mechanics and Mining Sciences*, vol. 119, pp. 193–204, 2019.
- [39] B. F. An, X. X. Miao, J. X. Zhang, F. Ju, and N. Zhou, “Overlying strata movement of recovering standing pillars with solid backfilling by physical simulation,” *International Journal of Mining Science and Technology*, vol. 26, pp. 301–307, 2016.
- [40] Z. K. Yang, Z. H. Cheng, Z. H. Li et al., “Movement laws of overlying strata above a fully mechanized coal mining face backfilled with gangue: a case study in jilishan coal mine in henan Province, China,” *Advances in Civil Engineering*, vol. 202120 pages, 2021.
- [41] J. N. Brune, “Tectonic stress and the spectra of seismic shear waves from earthquakes”, *Journal of Geophysical Research: solid Earth*, *Journal of Geophysical Research*, vol. 75, pp. 4997–5009, 1970.
- [42] K. Aki and H. Patton, “Determination of seismic moment tensor using surface waves,” *Tectonophysics*, vol. 49, pp. 213–222, 1978.
- [43] T. C. Hanks and H. Kanamori, “A moment magnitude scale”, *Journal of geophysical research: solid earth*, *Journal of Geophysical Research*, vol. 84, pp. 2348–2350, 1979.
- [44] G. Calderoni, A. Rovelli, and R. D. Giovambattista, “Stress drop, apparent stress, and radiation efficiency of clustered earthquakes in the nucleation volume of the 6 mw 6.1 L’quila earthquake,” *Journal of geophysical research: solid earth*, vol. 124, pp. 10360–10375, 2019.
- [45] M. Kozłowska, B. Orlecka-Sikora, Ł. Rudziński, S. Cielesta, and G. Mutke, “Atypical evolution of seismicity patterns resulting from the coupled natural, human-induced and coseismic stresses in a longwall coal mining environment,” *International Journal of Rock Mechanics and Mining Sciences*, vol. 86, pp. 5–15, 2016.
- [46] J. Ma, L. J. Dong, G. Y. Zhao, and X. B. Li, “Discrimination of seismic sources in an underground mine using full waveform inversion,” *International Journal of Rock Mechanics and Mining Sciences*, vol. 106, pp. 213–222, 2018.

Review Article

Predicting Tunnel Groundwater Inflow by Geological Investigation Using Horizontal Directional Drilling Technology

Xialin Liu 

CCCC Second Highway Consultants Co., Ltd., Wuhan 430056, China

Correspondence should be addressed to Xialin Liu; liuxialin@ccccltd.cn

Received 12 August 2022; Accepted 27 September 2022; Published 13 October 2022

Academic Editor: Junpeng Zou

Copyright © 2022 Xialin Liu. This is an open access article distributed under the Creative Commons Attribution License, which permits unrestricted use, distribution, and reproduction in any medium, provided the original work is properly cited.

To improve the prediction accuracy of tunnel excavation groundwater inflow, a prediction method based on a horizontal directional drilling geological survey is proposed. It relies on the monitoring and statistical analysis of groundwater inflow into a horizontal directional drilling survey borehole. Moreover, it is based on Goodman's empirical back-calculation for the surrounding rock penetration coefficient and uses the groundwater dynamics method to predict the amount of inflow into the tunnel excavation. On the basis of an analysis of the Tianshan Shengli Tunnel, the following conclusions were obtained: the tunnel excavation groundwater inflow prediction method based on a horizontal directional drilling geological survey borehole can be used to obtain the permeability coefficient value of the surrounding rock, which can be used in the groundwater dynamics method to improve the prediction accuracy; the groundwater runoff modulus method and the atmospheric precipitation infiltration method underestimate the prediction results for tunnel groundwater inflow; and the groundwater dynamics calculation results based on the horizontal survey hole prediction method are more reliable. Goodman's empirical formula was used to predict normal groundwater inflow within the 2,271 m length from the tunnel entrance: the normal groundwater inflow into the right tunnel was approximately $6,441 \text{ m}^3/\text{d}$, and the maximum groundwater inflow was approximately $19,323 \text{ m}^3/\text{d}$. When the tunnel crosses the fault zone, the groundwater inflow increases significantly. The normal groundwater inflow per unit footage is approximately $7.30 \text{ m}^3/(\text{d}\cdot\text{m})$, and the portion of the tunnel that crosses the fault zone is a medium to strong water-rich section.

1. Introduction

With the launch and implementation of a series of national strategic plans such as the Sichuan–Tibet Railway and Western Development in China, the construction of tunnel projects in China has entered a new period of growth [1]. However, the high altitudes and the necessary burial depths for ultra-long tunnel construction in mountainous areas pose various difficulties, such as problems associated with sudden water surges, e.g., property losses and casualties. These difficulties in tunnel design and construction safety are mainly due to a lack of accurate information regarding the groundwater in the rock surrounding tunnels. Therefore, it is important to carry out research on the prediction of groundwater inflow in tunnels. Many domestic and foreign scholars have carried out research on the prediction of tunnel groundwater inflow using empirical calculations,

analytical solutions, numerical analyses, and other methods to calculate tunnel groundwater inflow [1–3].

In the 1850s, deep pressurized water was developed and utilized, and scholars began to study cross-flow recharge. Goodman et al. [4] proposed a method to calculate the amount of groundwater inflow from the surrounding rock based on the theory of seepage wells, and later, Tani derived an analytical solution for groundwater inflow from the surrounding rock [5]. Hwang and Lu [6] gave a semi-analytical solution for predicting the amount of groundwater inflow considering the decline in groundwater caused by tunnel construction. Farhadian and Katibeh [7] developed a new empirical model using multiple regression analysis to evaluate groundwater inflow into circular tunnels. Chen [8] studied the calculation of subsurface unsteady well flow in a stratified, heterogeneous unconfined aquifer. He [9] constructed a tunnel water influx prediction model

based on the correlation coefficient method and limit learning machines as the theoretical basis. Zhou et al. [10] constructed an optimized combination prediction model of tunnel water influx based on a variety of single prediction models. Wang et al. [11] used the “round island model” and mapping principle as the theoretical basis to derive the prediction formula of tunnel water influx under the action of a permeable interlayer. Fu et al. [12] carried out a study on the prediction of tunnel surge based on angle-preserving mapping in the fault-affected area. The existing theories and measurement methods are mainly based on vertical drilling to predict groundwater inflow. But how to optimize the formula and parameter values to apply to the horizontal borehole is still in the initial stage.

At present, predicting tunnel groundwater inflow mainly uses methods involving traditional vertical borehole geological surveys and tunnel geological prospecting. However, the traditional vertical borehole survey method is difficult to implement in high-altitude areas with treacherous terrain and inconvenient traffic. Moreover, it is characterized by low survey efficiency, high comprehensive costs, and a long construction cycle, and, owing to the survey borehole layout, it is easy to “miss” details. The method of tunnel geological prospecting can only obtain geological information within 30–100 m of the front of the tunnel construction section, which is not ideal considering the tunnel’s construction speed. To this end, Ma et al. [13] proposed a geological survey technology, a long-distance horizontal directional drilling tunnel, for high-altitude mountainous conditions, which can turn the “a hole in the ground” of traditional vertical borehole geological survey methods into a blind spot-free survey along the tunnel axis. This is very helpful in terms of fully and accurately revealing the groundwater inflow and geological conditions of fault zones along the proposed tunnel. On this basis, this paper proposes a tunnel excavation surge prediction method based on the horizontal directional drilling geological survey technology, which is good for use with the groundwater dynamics method in terms of providing the surrounding rock permeability coefficient values and improving the accuracy of the tunnel excavation surge prediction.

2. Common Methods for Predicting Tunnel Water Surges

2.1. Groundwater Runoff Modulus Method. First, we assume that the modulus of underground runoff is equal to the modulus of surface runoff. Then, according to the infiltration of atmospheric precipitation required to recharge the flow of falling springs or the flow of rivers that are recharged by groundwater, the surface runoff modulus of the tunnel is determined, which is the subsurface runoff modulus of the tunnel basin. Thereafter, the catchment area of the tunnel is determined, and one can approximately predict the normal amount of water in the tunnel.

$$Q = MA, \quad (1)$$

Here, Q is the amount of groundwater surge (m^3/d); M is the basin underground runoff modulus ($\text{m}^3/\text{d}\cdot\text{km}^2$); and A is the catchment area of the proposed tunnel (km^2).

2.2. Atmospheric Precipitation Infiltration Method. According to the average annual precipitation in the vicinity of the tunnel, the catchment area, the topography, the vegetation, the geology, and the hydrogeological conditions are utilized to select a suitable empirical precipitation infiltration coefficient value. This can be used to approximately predict the normal amount of water discharged from the tunnel. The formula for calculating the amount of water in the tunnel is as follows:

$$Q_1 = 2.74\alpha WA, \quad (2)$$

where Q_1 is the atmospheric rainfall recharge (m^3/d); α is the precipitation infiltration coefficient; W is the multiyear average precipitation (mm); and A is the catchment area (km^2).

2.3. Groundwater Dynamics Method. The groundwater dynamics method is a conventional hydrogeological calculation method based on the principle of groundwater dynamics. It utilizes the mathematical analysis of groundwater movement under a given boundary value and the initial value conditions to establish the analytical formula and to predict the amount of tunnel groundwater inflow. After the method generalizes the hydrogeological model, it is fast and practical. Scholars have studied many related tunnel surge predictions from empirical formulae, the most common being the Oshima Yoshi formula, the Sato Bangming formula, the Lokhe Toshiro formula, the Kosgakov formula, the Gilinsky formula, the Forschheimer formula, and the Chinese empirical formula [14–16]. A part of the analytical method of the calculation formula is shown in Table 1.

At present, the groundwater dynamics method is one of the most effective for predicting tunnel groundwater inflow, and the principle is simple and easy to apply. However, the application of this method requires a series of calculation parameters, and these parameters are obtained from on-site experiments, which are difficult for ultra-long tunnel projects with high altitudes and large burial depths, so we can only refer to the empirical values.

3. Prediction Method of Groundwater Inflow in a Tunnel Based on a Horizontal Survey Borehole

3.1. Horizontal Directional Drilling Geological Survey Technology. Horizontal directional drilling (HDD) is a trenchless, pipe-laying technology that uses anchored drilling equipment to drill into the ground at a small angle of incidence relative to the ground surface, which forms a pilot hole. It then resizes the pilot hole to the required size and loads the pipe (line) into the hole by back-dragging and the traction of the drilling rig [3, 17]. This technology is widely used in municipal, oil, and gas projects and other pipeline construction industries, and it has the advantages of fast construction speed, low cost, and minimal environmental disturbance as compared with other trenchless pipe-laying technologies [18, 19].

TABLE 1: List of formulae for the prediction and calculation of the groundwater inflow analytical method.

Method	Formula	Scope of application	Definition of the symbols
Kosgakov formula	$Q_s = (2\alpha KH_0 L / \ln R - \ln r) \alpha = (\pi/2) + H_0/R$	Tunnels through phreatic aquifers	Q_s —predicted stable-state water influx through the tunnel through the aquifer (m^3/d); K —permeability coefficient of the rock (m/d); H_0 —distance from the original static-state water level to the center of the equivalent circle of the cave-body cross section (m); S —depth of groundwater level drop (m); L —tunnel through the length of the aquifer (m); R —tunnel surge radius of influence (m); r —equivalent circle radius of tunnel cross section (m); (single tunnel application to take the value of 3.5 m, double tunnel application to take the value of 7 m).
Goodman's empirical formula	$Q_0 = L2\pi kH / \ln (4H/d)$	Trans-ridge and adjacent mountain tunnels through submerged water bodies	Q_0 —predicted maximum surge into a tunnel through the aquifer (m^3); L —tunnel through the length of the aquifer (m); K —permeability coefficient of the rock (m/d); H —vertical distance from the original static-state water level to the equivalent circle center in the tunnel cross section (m); d —diameter of the equivalent circle of the tunnel body cross section (m), $d = 2r$.
Oshima Yoshi formula	$Q_{max} = (2\pi mK (H - r)L / \ln [4(H - r)/d])$	Submerged aquifers	Q_{max} —predicted maximum possible water surge through the tunnel within the aquifer (m^3/d); K —permeability coefficient of the rock (m/d); H —vertical distance from the original static-state water level in the aquifer to the tunnel floor (m); L —length of the tunnel through the aquifer (m); d —equivalent circle diameter of the tunnel cross section (m), $d = 2r$; m —conversion factor, generally taken as 0.86.
Empirical formula for railway survey procedures	$q_0 = 0.0255 + 1.9224KHq_s = KH(0.676 - 0.06K)$	Submerged aquifers	q_0 —maximum surge predicted for the tunnel through the aquifer (m^3/d); q_s —normal surge predicted for the tunnel through the aquifer (m^3/d); K —permeability coefficient of the rock (m/d); H —vertical distance from the original static-state water level to the bottom of the tunnel distance (m).

As shown in Figure 1, trenchless horizontal directional drilling technology permits efficient guidance, directional control, and long-distance drilling capabilities; thus, drilling can be realized along a predesigned trajectory. The diameter of the hole is determined according to the size of the test tool, and the length of the hole is determined by combining the preliminary survey results and the survey requirements. A series of interrupted coring, hydraulic fracturing, integrated logging, and in-hole TV tests can be carried out in the hole to accurately investigate and measure the lithological parameters and the distribution of the ground stress field in the surrounding rock [20]. This improves upon the detection range of traditional tunnel geological prediction technology, significantly increases the accuracy of the detection line, provides more effective and accurate geological data for

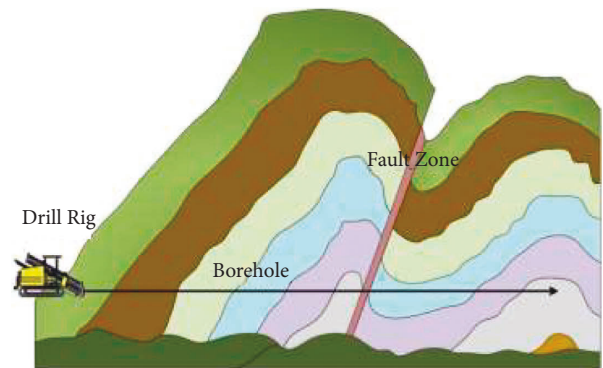


FIGURE 1: Schematic diagram showing horizontal directional drilling and tunneling for a geological survey.

tunnel construction, and effectively reduces the risk involved in tunnel construction.

3.2. Prediction Method of Groundwater Inflow Based on a Horizontal Survey Borehole. The borehole trajectory of the horizontal directional drilling survey is generally consistent with the centerline of the palm surface of the tunnel design trajectory. This is because the tunnel design trajectory generally has a herringbone slope, so the horizontal directional drilling survey in the tunnel entrance forms the survey hole with a certain slope. In this manner, the borehole passes through the water body exactly to provide a drainage path, and the water flow from the survey hole is natural, as shown in Figure 2.

On the basis of the horizontal directional drilling geological survey borehole, the method of predicting tunnel excavation groundwater inflow relies on the monitoring and statistical analysis of the groundwater inflow into the horizontal directional drilling survey borehole. The groundwater dynamics method is used to predict the tunnel excavation groundwater inflow. This mainly involves the following:

- (1) The variation in water surges in the horizontal directional drilling survey boreholes and changes in drilling footage are monitored and recorded.
- (2) The weather conditions at the tunnel site area are monitored and recorded.
- (3) According to the aforementioned parameters, the changes in groundwater inflow in the horizontal directional drilling survey borehole are recorded.
- (4) According to the changes in segmental groundwater inflow into the survey hole, Goodman's empirical formula is used to back-calculate the permeability coefficient of each segment, and then the groundwater dynamics method is used to predict the tunnel excavation groundwater inflow.
- (5) According to the weather conditions in the tunnel site area, the changes in the tunnel excavation groundwater inflow are recorded and analyzed.

4. Case Study

4.1. Project Overview. Tianshan Shengli Tunnel is the longest highway tunnel currently under construction. It is a separated, two-way, four-lane, extra-long tunnel with a width of 11.0 m and a height of 5.0 m. The length of the left tunnel is 22,105.00 m, and the maximum depth of the tunnel is approximately 1115.03 m; the length of the right tunnel is 22,006.7 m, and the maximum depth of the tunnel is approximately 1122.024 m. The middle guide tunnel (the service tunnel) is located between the left and right tunnels, with a length of 22,054.5 m and a width and height of 7 m × 5 m.

The Tianshan Victory Tunnel crosses the Tianshan Mountain Range, which is located in a high-altitude, Alpine region with a harsh and variable climate and complex geological conditions. According to the preliminary tunnel

survey data, the Boroconu–Azikuduk Fracture (Bo–A Fracture, F6), which exists approximately 1900 m from the tunnel entrance, has long-term, active characteristics, and the fracture fragmentation zone affects bedrock for a distance of approximately 300 m along the tunnel, which is a controlling geological factor in the tunnel construction process.

As shown in Figure 3, the horizontal directional drilling technique was used for the tunnel survey, i.e., from the tunnel entrance along the tunnel axis to the location of the fault zone for the geological survey. It was combined with intermittent coring, hydraulic fracturing, comprehensive logging, in-hole TV, and other tests to analyze the lithological distribution of rocks surrounding the borehole and the occurrence of joint fissures. Furthermore, these tests were used to monitor and quantify the groundwater inflow into the horizontal directional drilling survey boreholes, which was later used to predict the tunnel excavation groundwater inflow.

4.2. Drill Hole Gushing Water. The final depth of the horizontal directional drilling survey borehole for Tianshan Victory Tunnel was 2271 m, and the relationship curve of groundwater inflow in the borehole and the footage is shown in Figure 4.

From January 17 to January 21, 2020, with the continuous drilling of the borehole, the amount of groundwater inflow in the borehole exhibited an increasing trend, and the increment of groundwater inflow in the borehole was approximately 11 m³/h during the whole process, i.e., 293 m of cumulative progress. Within the weathering zone at the tunnel inlet, the rock layer was observed to be more fractured, and the joints and fissures were relatively more developed. On 21 January, the drilling stopped, and on 22 January, the groundwater inflow in the borehole decreased to 9 m³/h. On this day, the drilling was redirected. When the cumulative drilling reached 530 m on 26 January, the groundwater inflow in the borehole suddenly increased to 18 m³/h at approximately 418 m. The drilling pressure was reduced to a minimum of 5 MPa at 410 m, and the drilling speed increased to 20 m/h. At this point, the surrounding rock was densely fractured, which is conducive to the collection of surface water and groundwater, thus the groundwater inflow increased significantly.

On 26 January, the drilling stopped, and the groundwater inflow gradually decreased. On 1 February, the drilling continued, and by 4 February, the drilling had reached 634 m. Here, the groundwater inflow first increased, then slowly decreased and stabilized at approximately 8 m³/h. Similarly, when the drilling reached 1003 m, the groundwater inflow first increased, then slowly decreased and stabilized. After a cumulative drilling footage of 1003 m, the groundwater inflow continued to increase significantly, reaching a peak of approximately 35 m³/h at about 2028 m. This was caused by a survey borehole moving through the core section of the Boa fault zone. Then, the survey borehole moved into a dense granite, and the groundwater inflow dropped to a minimum of approximately 14 m³/h. At the

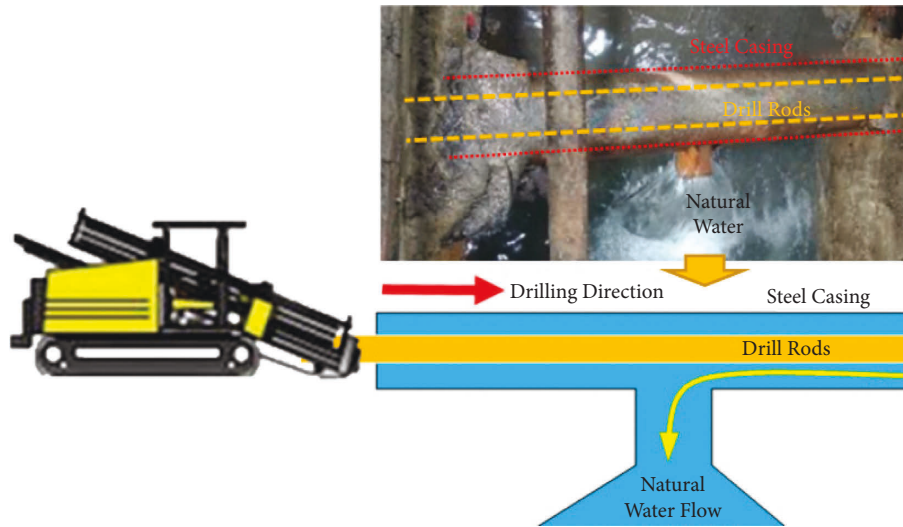


FIGURE 2: Natural water flowing from the survey hole (vertical view).



FIGURE 3: Geological survey site of the horizontal directional drilling tunnel.

end of the borehole, the survey borehole groundwater inflow suddenly increased and then decreased, perhaps due to the weather.

4.3. Parameter Values. The tunnel site is located in the tectonic denudation of a high mountain landscape area, characterized by glaciers and glacial landform development, large topographic relief, and strong rock weathering and deposition, mainly from the ice and water accumulation in debris soil.

The stratigraphy of the tunnel site area is mainly Quaternary alluvial pebbles (Q_4^{al+pl}), avalanche slope accumulation rubble (Q_4^{c+dl}), ice and water accumulation rubble (Q_4^{fgl}), Devonian upper Tianger Group gray-green tuffaceous sandstone (D_3t^b), middle Yuan Dynasty (Pt_2), Jixian System Kawabak Group II (Jxk^2) gray-brown metamorphic sandstone, sandy slate, dacite; middle Yuan Dynasty (Pt_2) Great Wall System Xingxingxia Group (CHx) gray-green quartz schist, gneiss and Hualixian intrusive light flesh-red granite porphyry ($\gamma_C^{2d}H$) gray-white granite, granite amphibolite ($\eta\gamma_D^1H$), Garridonian intrusive gray-white granite

amphibolite ($\gamma\delta_s^1Q$, $\gamma\delta_s^2Q$), and Jinning Movement intrusive gray gneissic amphibolite ($tn_{Qb}H$).

The climate of the area in which the tunnel site is located is a typical temperate continental arid climate, with a high mountain cold zone and glaciers. The surface water system is mainly composed of the Urumqi River and the Ulatai River. Groundwater is recharged mainly from atmospheric precipitation and alpine ice and snow melt.

The topographic and geomorphological conditions of the tunnel site area, the lithological characteristics of the strata, and the distribution and hydraulic head of groundwater in the aquifer were considered to determine the choice of groundwater runoff modulus method: the atmospheric precipitation infiltration method, the Kosgakov formula, the empirical railroad formula for the tunnel normal groundwater inflow prediction, the choice of Goodman's empirical formula, the Oshima Yoshi formula, and the empirical railroad formula for the tunnel maximum groundwater inflow prediction.

4.3.1. Groundwater Runoff Modulus M . According to the reports "Groundwater Resources in Xinjiang" and "Hydrogeological Survey Report of Tianshan Shengli Tunnel," the groundwater runoff modulus in the mountainous area of the Ulatai basin is $134.24 \text{ m}^3/\text{d}\cdot\text{km}^2$, the groundwater runoff modulus in the mountainous area of the Urumqi River is $216 \text{ m}^3/\text{d}\cdot\text{km}^2$, and the groundwater runoff modulus in the mountainous area of the Alagou River basin is $99.4 \text{ m}^3/\text{d}\cdot\text{km}^2$.

4.3.2. Atmospheric Precipitation Infiltration Coefficient a . According to the preliminary survey data, the rock layer at the Boa fault is extremely fractured, the fracture right-hand misalignment is large, there is a long-term activity, and there is abundant mud and sand fill. Using tunnel engineering experience, the empirical value for the Boa fault zone precipitation infiltration coefficient was determined at 0.40.

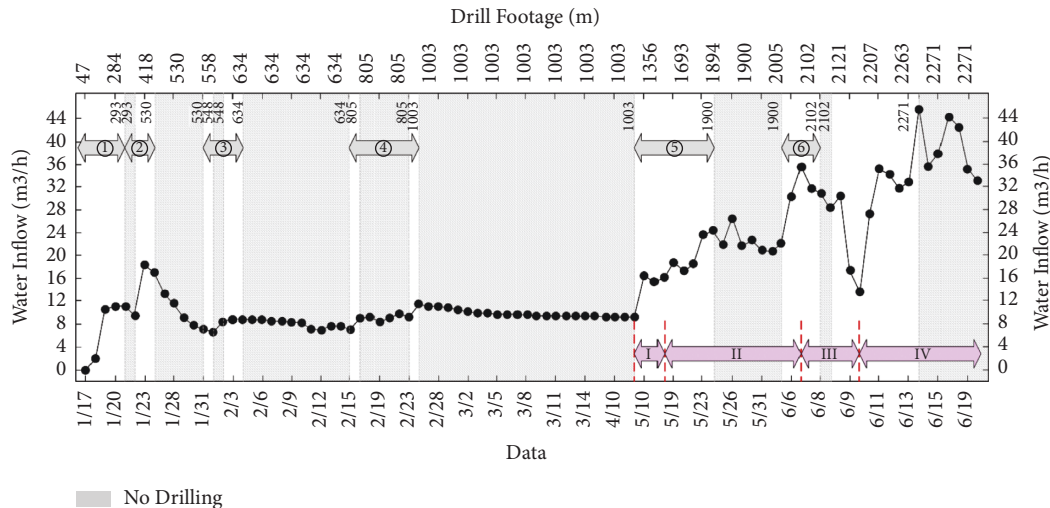


FIGURE 4: The relationship curve of groundwater inflow in the borehole and the footage.

Moreover, for the tunnel plan projection in the geomorphological unit, i.e., climate zoning, $a = 0.15 \sim 0.40$.

4.3.3. Water Hydraulic Head H . The vertical drilling information and the distribution of rivers in the tunnel site area were combined to determine the groundwater level, and H was used to establish the average difference in hydraulic head between the borehole level and the groundwater level.

4.3.4. Permeability Coefficient K . From the previous hydrogeological tests and horizontal directional drilling survey borehole, the site data were used to establish the value of the permeability coefficient K . When no site survey data are available, the *Hydrogeology Manual (Second Edition)* [20] and similar projects on the permeability coefficient K can be used to establish the empirical value. As shown in Figure 4, considering the above analysis of the groundwater inflow into the horizontal directional drilling borehole, the drilling footage was divided into seven sections using Goodman's empirical back-calculation of the permeability coefficient value for each section. The calculation results are shown in Table 2.

Because the seventh section of the survey hole groundwater inflow was affected to a large extent by weather factors, the permeability coefficient K value was established with reference to the vertical hole prehydrogeological test results. The permeability coefficient values of different lithological sections are shown in Table 3. In the fracture fragmentation zone and its influence zone, the permeability coefficient of the stratum increases significantly. Owing to a lack of relevant data on the permeability performance of the fault zone in the evaluation area, empirical values were adopted for the permeability coefficients in this area. In addition, the permeability coefficient values for the fault zone and its influence zone decrease with an increase in burial depth. The permeability coefficient values for the Boa fault and other fractures at different burial depths are shown

in Table 4. These are based on the results of existing hydrogeological tests and the characteristics of the permeability performance of the fault zones.

According to the vertical distribution characteristics of the permeability properties of the fault zone, the fault zone is regarded as composed of laminated strata with different permeabilities in the vertical direction. Thus, the equivalent permeability coefficient K of the fault zone when the groundwater flows perpendicular to the direction of the level under the tunnel burial depth condition was calculated using the following equation:

$$K = \frac{\sum_{i=1}^n M_i}{\sum_{i=1}^n M_i / K_i}, \quad (3)$$

where M_i and K_i are the thickness (m) and permeability coefficient value (m/d), respectively, of the i th stratum.

4.3.5. The Depth of the Groundwater Level Drop S . Previously, when calculating the tunnel surge, for the import section and export section of the weathered zone and through the gully zone, the difference in the hydraulic head S was often taken as the distance from the groundwater level to the tunnel floor. For the deep-buried belt, the formula proposed by Wan [21] was used to calculate the reduction in S with depth:

$$S = (1 - e^{-0.72K})H, \quad (4)$$

where K is the permeability coefficient (m/d) and H is the water head height (m).

4.3.6. Radius of the Area of Influence R . For the weathered zone and the valley-crossing zone, the radius of influence R was delineated according to the topography. For the bedrock section, it was determined according to the formula recommended by the Regulations for Hydrogeological Investigation of Railway Engineering (TB 10049-2014) [14]:

TABLE 2: Permeability coefficient of each section of the horizontal directional drilling exploration borehole, based on Goodman's empirical back-calculation.

Serial of drilling segments	Range of depth (m)	Construction	Increment of groundwater inflow Q (m ³ /h)	Height of hydraulic head H (m)	Diameter of the drilled hole d (m)	Length of water-bearing Body L (m)	Permeability coefficient K (m/d)
①	0–293	Weathered zone	11	17.5	0.25	263	0.0514
②	293–530	Through the gully zone	9	50	0.25	125	0.0368
③	530–634	Deep buried zone	2	150	0.25	112	0.0035
④	634–1003	Deep buried zone	4.29	300	0.25	369	0.00125
⑤	1003–1900	Deep buried zone	17.19	400	0.25	897	0.0016
⑥	1900–2102	Deep buried zone	13.41	400	0.25	128	0.0088

TABLE 3: Table of hydrogeological test results.

Serial	Number of drilled holes	Stakes of the mileage	Lithology of the strata	Permeability coefficient (m/d)
1	SZK01	ZK75 + 866 right 15.6 m	Tuffaceous sandstone	8.406×10^{-4}
2	SZK02	YK79 + 361 right 272.7 m	Medium-weathered granite, quartz schist	2.714×10^{-3}
3	SZK03	YK81 + 356 right 195 m	Quartz schist	2.819×10^{-3}
4	SZK04	ZK84 + 140 left 40 m	Granite	9.89×10^{-4}
5	SZK05	ZK87 + 248.7 left 40 m	Granite	9.26×10^{-4}
6	SZK06	YK93 + 300 right 120 m	Quartz schist	5.471×10^{-3}
7	SZK07	ZK93 + 493.5 left 100.5 m	Quartz schist	4.321×10^{-3}

TABLE 4: Permeability coefficient values of the tunnel passing through the fault zone and the surrounding rock in the affected zone.

Tunnel depth (m)	<80 m	80~150 m	150~250 m	250~350 m	>350 m
Permeability coefficient of Bo–A fault zone (m/d)	0.5 (experience value)	0.2	0.05	0.01	0.005
Permeability coefficients of other fault zones (m/d)	0.1 (experience value)	0.05	0.01	0.005	0.002

$$\begin{aligned} R &= 215.5 + 510.5K, \\ B &= 2R, \end{aligned} \quad (5)$$

where R denotes the groundwater inflow on the side of the tunnel affecting the width (m); K denotes the permeability coefficient of aquifers (m/d); and B denotes the inflow of water on both sides of the tunnel affecting the width (m).

For the fault zone, the Kusakin formula was used to calculate the parameters related to the radius of influence R , including the aquifer thickness H and the permeability coefficient K :

$$R = 2H\sqrt{HK}. \quad (6)$$

4.4. Analysis of Results

4.4.1. Groundwater Runoff Modulus Method. The distance from the tunnel's entrance totaled 2271 m. On the basis of the groundwater runoff modulus method for the right tunnel, the predicted groundwater inflows are shown in Table 5. The total groundwater inflow of the right tunnel based on the groundwater runoff modulus method was 618.7 m³/d. The average groundwater inflow into the tunnel per unit footage was 0.3575 m³/(d·m), the minimum value was 0.0933 m³/(d·m), the maximum value was 1.7643 m³/(d·m), and the maximum amount of groundwater inflow per unit footage is located in the Bo–A fault zone (F6).

(d·m), and the maximum amount of groundwater inflow per unit footage is located in the Bo–A fault zone (F6).

4.4.2. Atmospheric Precipitation Infiltration Method. The distance from the tunnel's entrance totaled 2271 m. On the basis of the atmospheric precipitation infiltration method for the right tunnel, the predicted water surge values are shown in Table 6. The total groundwater inflow into the right tunnel based on the atmospheric precipitation infiltration method was 1480.35 m³/d. The average groundwater inflow into the tunnel per unit footage was 0.9094 m³/(d·m), the minimum value was 0.098 m³/(d·m), the maximum value was 5.147 m³/(d·m), and the maximum amount of groundwater inflow per unit footage is located in the Bo–A fault zone (F6).

4.4.3. Groundwater Dynamics Method. The distance from the tunnel's entrance totaled 2271 m. On the basis of the groundwater dynamics method for the right tunnel, the predicted water surge values are shown in Table 7. Taking the right tunnel as an example, the normal groundwater inflow obtained by Goodman's empirical formula, the Kosgakov formula, the empirical railway formula, and the Oshima Yoshi's formula were 6441, 7593, 3313, and 4937 m³/d, respectively.

TABLE 5: Prediction of groundwater inflow into the right tunnel based on the groundwater runoff modulus method.

Serial	Segmented mileage		Length (m)	Groundwater runoff modulus $m^3/(d \cdot km^2)$	Radius of influence R	Catchment area A (km^2)	Groundwater inflow Q_s (m^3/d)	Groundwater inflow perunit footage q_s $m^3/(d \cdot m)$
1	YK75 + 815	YK75 + 948	133.0	216.0	215.9	0.057	12.4	0.093
2	YK75 + 948	YK76 + 015	67.0	216.0	241.7	0.032	7.0	0.104
3	YK76 + 015	YK76 + 063	48.0	216.0	241.7	0.023	5.0	0.104
4	YK76 + 063	YK76 + 168	105.0	216.0	217.3	0.046	9.9	0.094
5	YK76 + 168	YK76 + 265	97.0	216.0	1471.31	0.285	61.7	0.636
6	YK76 + 265	YK76 + 580	315.0	216.0	266.20	0.168	36.2	0.115
7	YK76 + 580	YK76 + 660	80.0	216.0	1297.57	0.208	44.8	0.561
8	YK76 + 660	YK77 + 273	613.0	216.0	216.1	0.265	57.2	0.093
9	YK77 + 273	YK77 + 408	135.0	216.0	2558.09	0.691	149.2	1.105
10	YK77 + 408	YK77 + 565	157.0	216.0	216.9	0.068	14.7	0.094
11	YK77 + 565	YK77 + 591	26.0	216.0	218.3	0.011	2.5	0.094
12	YK77 + 591	YK77 + 743	152.0	216.0	218.3	0.066	14.3	0.094
13	YK77 + 743	YK77 + 839	96.0	216.0	3838.17	0.737	159.2	1.658
14	YK77 + 839	YK77 + 904	65.0	216.0	216.9	0.028	6.1	0.094
15	YK77 + 904	YK77 + 994	90.0	216.0	216.9	0.039	8.4	0.094
16	YK77 + 994	YK78 + 019	25.0	216.0	2199.56	0.110	23.8	0.950
17	YK78 + 019	YK78 + 086	67.0	216.0	216.9	0.065	6.3	0.094

TABLE 6: Prediction of groundwater inflow into the right tunnel based on the atmospheric precipitation infiltration method.

Serial	Segmented mileage		Length (m)	Infiltration coefficient α	Annual average rainfall (mm)	Radius of influence R (m)	Catchment area A (km^2)	Groundwater inflow Q_s (m^3/d)	Groundwater inflow perunit footage q_s $m^3/(d \cdot m)$
1	YK75 + 815	YK75 + 948	133.0	0.25	550.0	241.7	0.064	24.23	0.182
2	YK75 + 948	YK76 + 015	67.0	0.25	550.0	241.7	0.032	12.20	0.182
3	YK76 + 015	YK76 + 063	48.0	0.25	550.0	241.7	0.023	8.74	0.182
4	YK76 + 063	YK76 + 168	105.0	0.25	550.0	217.3	0.046	17.19	0.164
5	YK76 + 168	YK76 + 265	97.0	0.4	550.0	1471.31	0.285	172.06	1.774
6	YK76 + 265	YK76 + 580	315.0	0.2	550.0	216.1	0.136	41.04	0.130
7	YK76 + 580	YK76 + 660	80.0	0.4	550.0	1297.57	0.208	125.15	1.564
8	YK76 + 660	YK77 + 273	613.0	0.2	550.0	216.1	0.265	79.87	0.130
9	YK77 + 273	YK77 + 408	135.0	0.4	550.0	2558.09	0.691	416.34	3.084
10	YK77 + 408	YK77 + 565	157.0	0.2	550.0	216.9	0.068	20.53	0.131
11	YK77 + 565	YK77 + 591	26.0	0.2	550.0	218.3	0.011	3.42	0.132
12	YK77 + 591	YK77 + 743	152.0	0.2	550.0	218.3	0.066	20.00	0.132
13	YK77 + 743	YK77 + 839	96.0	0.4	550.0	3838.17	0.737	444.22	4.627
14	YK77 + 839	YK77 + 904	65.0	0.2	550.0	216.9	0.028	8.50	0.131
15	YK77 + 904	YK77 + 994	90.0	0.2	550.0	216.9	0.039	11.77	0.131
16	YK77 + 994	YK78 + 019	25.0	0.4	550.0	2199.56	0.110	66.29	2.652
17	YK78 + 019	YK78 + 086	67.0	0.2	550.0	216.9	0.065	8.8	0.131

By comparing the calculation results of the groundwater runoff modulus method, the atmospheric precipitation infiltration method, and the groundwater dynamics method, it can be seen that the inflow values obtained by the groundwater runoff modulus method and the atmospheric precipitation infiltration method were underestimated. This is because the groundwater runoff modulus method and the atmospheric precipitation infiltration method are essentially water equilibrium methods, and it is difficult to obtain accurate data for various parameters. Moreover, the two methods do not consider the impact of steady-state groundwater reserves on tunnel groundwater

inflow, nor can they adequately characterize the impact of fault zones. Therefore, the calculation results of groundwater dynamics based on the horizontal survey hole prediction method were more reliable. In the groundwater dynamics method, the results between the various calculation formulae were also quite different, with the comprehensive comparison indicating that the normal groundwater inflow obtained by Goodman's empirical formula is superior, as the maximum groundwater inflow was three times the normal inflow.

The changes in groundwater inflow during the horizontal directional drilling of the survey borehole into the Boa

TABLE 7: Prediction of normal groundwater inflow into the right tunnel based on the groundwater dynamics method.

Seria	Segmented mileage	Length (m)	Permeability coefficient K (m/d)	Goodman's empirical ($q_s, m^3/d\cdot m$)	Kosgakov ($q_s, m^3/d\cdot m$)	Railway empirical ($q_s, m^3/d\cdot m$)	Oshima Yoshi ($q_s, m^3/d\cdot m$)	Goodman's empirical ($Q_s, m^3/d$)	Kosgakov ($Q_s, m^3/d$)	Railway empirical ($Q_s, m^3/d$)	Oshima Yoshi ($Q_s, m^3/d$)
1	YK75 + 815 YK75 + 948	133.0	0.0514	3.73	1.32	0.93	2.28	495.5	175.4	124.2	303.4
2	YK75 + 948 YK76 + 015	67.0	0.0514	6.45	3.41	2.21	4.55	432.3	228.4	148.3	304.5
3	YK76 + 015 YK76 + 063	48.0	0.0514	7.61	4.48	2.80	5.49	365.1	215.1	134.5	263.5
4	YK76 + 063 YK76 + 168	105.0	0.0035	0.61	0.42	0.24	0.45	64.2	44.5	25.3	47.2
5	YK76 + 168 YK76 + 265	97.0	0.0368	12.46	5.86	6.07	9.63	1208.8	568.2	589.3	934.3
6	YK76 + 265 YK76 + 580	315.0	0.00125	0.42	0.47	0.20	0.32	132.1	149.5	64.4	102.0
7	YK76 + 580 YK76 + 660	80.0	0.0088	4.06	2.26	2.16	3.18	325.1	181.1	172.6	254.7
8	YK76 + 660 YK77 + 273	613.0	0.00125	0.58	0.87	0.31	0.45	355.4	531.6	189.0	278.5
9	YK77 + 273 YK77 + 408	135.0	0.00645	4.67	2.52	2.76	3.71	630.2	339.7	372.4	500.8
10	YK77 + 408 YK77 + 565	157.0	0.002714	2.03	4.78	1.21	1.61	318.0	750.1	189.2	252.9
11	YK77 + 565 YK77 + 591	26.0	0.005471	4.97	14.30	3.08	3.97	129.2	371.9	80.2	103.2
12	YK77 + 591 YK77 + 743	152.0	0.005471	4.67	12.60	2.86	3.73	710.0	1914.7	434.9	566.5
13	YK77 + 743 YK77 + 839	96.0	0.0088	7.30	3.69	4.45	5.82	701.3	353.8	426.8	559.1
14	YK77 + 839 YK77 + 904	65.0	0.002819	2.41	6.56	1.48	1.92	156.8	426.3	96.1	125.1
15	YK77 + 904 YK77 + 994	90.0	0.002819	2.28	5.82	1.38	1.81	204.8	523.9	124.0	163.2
16	YK77 + 994 YK78 + 019	25.0	0.00365	2.84	1.66	1.71	2.26	71.1	41.4	42.7	56.6
17	YK78 + 019 YK78 + 169	150.0	0.002714	2.11	5.18	1.27	1.68	141.4	777.6	98.8	121.7

TABLE 8: Suggested values of normal groundwater inflow for the right tunnel.

Serial	Segmented mileage		Length L (m)	Characteristics of rock mass in the tunnel segment		Normal groundwater inflow		Water-richness zoning
	Beginning	Terminal		Stratum	Tectonics	Q_s m ³ /(d·m)	Q_s (m ³ /d)	
1	YK75 + 815	YK75 + 948	133.0	Tuffaceous siltstone	Weatherstripping	3.73	495.54	Medium water-rich section
2	YK75 + 948	YK76 + 015	67.0	Tuffaceous siltstone	Weatherstripping	6.45	432.31	Strong water-rich section
3	YK76 + 015	YK76 + 063	48.0	Tuffaceous siltstone	Weatherstripping	7.61	365.13	Strong water-rich section
4	YK76 + 063	YK76 + 168	105.0	Tuffaceous siltstone	—	0.61	64.19	Weakly water-rich section
5	YK76 + 168	YK76 + 265	97.0	Tuffaceous siltstone	Fw-5 fault zone/gully crossing zone	12.46	1208.82	Strong water-rich section
6	YK76 + 265	YK76 + 580	315.0	Tuffaceous siltstone	—	0.42	132.07	Weakly water-rich section
7	YK76 + 580	YK76 + 660	80.0	Tuffaceous siltstone	Fw-6 fault zone	4.06	325.11	Medium water-rich section
8	YK76 + 660	YK77 + 273	613.0	Tuffaceous siltstone	—	0.58	355.41	Weakly water-rich section
9	YK77 + 273	YK77 + 408	135.0	Tuffaceous siltstone	Fw-7 fault zone	4.67	630.25	Medium water-rich section
10	YK77 + 408	YK77 + 565	157.0	Granite diorite	—	2.03	317.95	Medium water-rich section
11	YK77 + 565	YK77 + 591	26.0	Variable sandstone plywood marble	—	4.97	129.17	Medium water-rich section
12	YK77 + 591	YK77 + 743	152.0	Granite diorite	—	4.67	710.00	Medium water-rich section
13	YK77 + 743	YK77 + 839	96.0	Granite diorite	F6 Boa fault zone	7.30	701.25	Strong water-rich section
14	YK77 + 839	YK77 + 904	65.0	Quartz schist	—	2.41	156.78	Medium water-rich section
15	YK77 + 904	YK77 + 994	90.0	Granite diorite	—	2.28	204.79	Medium water-rich section
16	YK77 + 994	YK78 + 019	25.0	Granite diorite	Fw-8 fault zone	2.84	71.05	Medium water-rich section
17	YK78 + 019	YK78 + 086	67.0	Granite diorite	—	2.11	141.37	Medium water-rich section

fault are shown in Figure 4. It can be seen from the following figure:

- (1) When drilling close to the Boa fault zone, the groundwater inflow during drilling began to increase significantly from 1003 m to 1616 m (area I); the groundwater inflow increased by $6 \text{ m}^3/\text{h}$, and for every 100 m drilled, the groundwater inflow increased by approximately $1 \text{ m}^3/\text{h}$.
- (2) After crossing the Boa fault, the groundwater inflow increased significantly from 1616 m to 2020 m (area II); the groundwater inflow increased by approximately $20 \text{ m}^3/\text{h}$, and for every 100 m drilled, the groundwater inflow increased by approximately $5 \text{ m}^3/\text{h}$.
- (3) The source of groundwater inflow in the Boa fault zone is mainly steady-state groundwater reserves, and the recharge is not smooth, which was observed when the horizontal drilling reached 2159 m (area III). In addition, the groundwater inflow in the whole section was reduced to $14 \text{ m}^3/\text{h}$.
- (4) After 2159 m (area IV), as a result of the frequent rainfall and snowfall and the temperature rise, a significant increase in the flow of water in the ditch was observed in the shallow burial section of the tunnel inlet section at 500 m. In addition, the water in the ditch replenishes groundwater, causing a significant increase in the amount of groundwater inflow from the horizontal directional drilling borehole survey.

For the distance within 2271 m from the entrance of the tunnel, the predicted value of the normal groundwater inflow into the right tunnel and the water-rich partition are shown in Table 8. The normal groundwater inflow into the right tunnel was approximately $6441 \text{ m}^3/\text{d}$, and the maximum groundwater inflow was approximately $19,323 \text{ m}^3/\text{d}$. When the tunnel crossed the fault zone, the groundwater inflow increased significantly, where the normal groundwater inflow per unit footage along the F6 Boa fault zone was approximately $7.30 \text{ m}^3/(\text{d}\cdot\text{m})$. The section in which the tunnel crosses the fault zone is a medium to strong water-rich section, so during the tunnel construction process, it is necessary to do advanced geological forecasting, advanced pregrouting, water blockage prevention, and water inrush prevention. In addition, the tunnel crosses the glacier and permafrost zones. In the spring, as the temperature rises, the melting of snow and ice will lead to an increase in tunnel groundwater inflow, which needs to be prevented.

5. Conclusions

With the application and development of horizontal directional drilling technology for ultra-long-distance tunnels in mountainous areas at high altitudes and with large burial depths, it is necessary to improve the accuracy in predicting the surge of groundwater into the tunnel excavation. Therefore, in this paper, we propose a method for predicting the groundwater inflow into tunnels based on horizontal

exploration boreholes. On the basis of a geological survey of a horizontal directional drilling borehole, we carried out research predicting groundwater inflow into a tunnel excavation. Using an analysis of the Tianshan Victory Tunnel Project as our foundation, our main conclusions are as follows:

- (1) The method for predicting the amount of groundwater inflow in tunnel excavation based on horizontal directional drilling boreholes can provide the permeability coefficient value of the surrounding rock, which can be used in the groundwater dynamics method and can improve the prediction accuracy. Additionally, it is still suggested to use redesigned packers to obtain more accurate groundwater inflow data for a controlled horizontal borehole, which is more practical for engineering design and construction.
- (2) The prediction results of the groundwater runoff modulus method and atmospheric precipitation infiltration method regarding the overall amount of groundwater inflow in tunnels are low, and the calculation results of groundwater dynamics based on the horizontal survey hole prediction method are more reliable.
- (3) Using Goodman's empirical formula to predict normal groundwater inflow along the 2271 m distance from the tunnel entrance, the normal groundwater inflow into the right tunnel was approximately $6441 \text{ m}^3/\text{d}$, and the maximum groundwater inflow was approximately $19,323 \text{ m}^3/\text{d}$.
- (4) When the tunnel crosses the fault zone, the groundwater inflow increased significantly, as the normal groundwater inflow per unit of the F6 Boa fault zone is approximately $7.30 \text{ m}^3/(\text{d}\cdot\text{m})$. The zone in which the tunnel crosses the fault is a medium-to-strong water-rich section;
- (5) During the tunnel construction process, it is necessary to do advanced geological forecasting, advanced pregrouting, water blockage prevention, and water inrush prevention near the fault zones. In addition, the tunnel crosses the glacier and permafrost zone. In the spring, as the temperature rises, melting snow and ice will lead to an increase in tunnel groundwater inflow, which needs to be prevented.

Data Availability

Data are available within the article.

Disclosure

The funders had no role in the design of the study; in the collection, analyses, or interpretation of data; in the writing of the manuscript, or in the decision to publish the results.

Conflicts of Interest

The author declares that there are no conflict of interest.

Authors' Contributions

Methodology, formal analysis, investigation, data curation, original draft preparation, review and editing were done by Xialin Liu. The author has read and agreed to the published version of the manuscript.

Acknowledgments

This research was supported by the Xinjiang Uygur Autonomous Region Science and Technology Major Project (No. 2020A03003-1) and the National Natural Science Foundation of China (No. 42002284).

References

- [1] S. M. Tian, W. Wang, and J. F. Gong, "Development and prospect of railway tunnels in China (including statistics of railway tunnels in China by the end of 2020)," *Tunn. Constr.* vol. 41, pp. 308–325, 2021.
- [2] J. Zou, Y.-Y. Jiao, F. Tan, J. Lv, and Q. Zhang, "Complex hydraulic-fracture-network propagation in a naturally fractured reservoir," *Computers and Geotechnics*, vol. 135, Article ID 104165, 2021.
- [3] Y.-Y. Jiao, K. Wu, J. Zou et al., "On the strong earthquakes induced by deep coal mining under thick strata—a case study," *Geomechanics and Geophysics for Geo-Energy and Geo-Resources*, vol. 7, no. 4, 2021.
- [4] R. E. Goodman, D. G. Moye, A. V. Schalkwyk, and I. Javandel, "Ground groundwater inflow during tunnel driving," *Engineering Geology*, vol. 2, pp. 39–56, 1965.
- [5] M. E. Tani, "Circular tunnel in a semi-infinite aquifer. Tunnelling & underground space technology incorporating trenchless," *Technology Research*, vol. 18, pp. 49–55, 2003.
- [6] J. H. Hwang and C. C. Lu, "A semi-analytical method for analyzing the tunnel water inflow," *Tunnelling and Underground Space Technology*, vol. 22, no. 1, pp. 39–46, 2007.
- [7] H. Farhadian and H. Katibeh, "New empirical model to evaluate groundwater flow into circular tunnel using multiple regression analysis," *International Journal of Mining Science and Technology*, vol. 3, pp. 32–38, 2017.
- [8] C. X. Chen, "Calculation method of unstable underground well flow in layered heterogeneous pressureless aquifer," *Earth Sci. -J. Wuhan Inst. Geol.* vol. 1P, 1981.
- [9] H. G. He, "Prediction of groundwater inflow in karst tunnels based on correlation criterion and R-ELM model," *Tunnel Construction*, vol. 39, pp. 1262–1269, 2019.
- [10] L. Zhou, G. Q. Yang, and Q. C. Yang, "Prediction of groundwater inflow in karst tunnels based on optimal combination model and rescaled range method," *Eng. J. Wuhan Univ.* vol. 53, pp. 875–882, 2020.
- [11] L. F. Wang, N. Tang, and Y. Mo, "Prediction of groundwater inflow of water-rich mountain tunnel with permeable interlayer," *Science Technology and Engineering*, vol. 20, pp. 13865–13871, 2020.
- [12] H. L. Fu, Z. Li, and G. W. Cheng, "Prediction of tunnel groundwater inflow in fault affected area based on conformal mapping," *Journal of Huazhong University of Science and Technology*, vol. 49, pp. 86–92, 2021.
- [13] B. S. Ma, Y. Cheng, J. G. Liu, Z. Donglin, Y. Xuefeng, and Z. Qiang, "Tunnel accurate geological investigation using long distance horizontal directional drilling technology," *Tunn. Constr.* vol. 41, pp. 972–978, 2021.
- [14] *TB 10049-2014; Regulations for Hydrogeological Investigation of Railway Engineering*, China Railway Publishing House Co., Ltd., China.
- [15] R. Goodman, D. Moye, A. Schalkwyk, and I. Javandel, *Groundwater Inflow during Tunnel Driving*, College of Engineering, University of California, Berkeley, California, 1964.
- [16] G. Q. Wang, "Research on evaluation and control of karst water Resources in a certain tunnel of dalian subway," *IOP Conference Series: Earth and Environmental Science*, vol. 153, no. 6, IOP Publishing, 2018.
- [17] B. S. Ma, *Trenchless Engineering*, People's Communications Press, Beijing, China, 2008.
- [18] C. Zeng and B. S. Ma, *Horizontal Directional Drilling Theory and Technology*, China University of Geosciences Press, Wuhan, China, 2015.
- [19] B. S. Ma, X. F. Yan, and C. Zeng, *A Horizontal Directional Drilling Engineering Geological Survey Method*. CN201910768217.X.
- [20] *China Geological Survey. Handbook of Hydrogeology*, Geological Publishing House, Beijing, China, 2012.
- [21] Y. Wan, "Experimental Study on Water Bursting Model of Tunnel in Medium-Low Permeability Medium," Master's thesis, Chengdu University of Technology, Chengdu, China, 2017.

Research Article

A Study of a Flow Model in Dual Permeability Reservoir Based on Similar Structure Theory

Tianhong Zhou ¹, Jie Shen ¹, Man Wang,¹ and Yun Wu²

¹School of Information Engineering, Wuhan Business University, Wuhan 430056, China

²School of Information Technology Application Innovation, Wuhan Polytechnic, Wuhan 436000, China

Correspondence should be addressed to Jie Shen; 20150623@wbu.edu.cn

Received 22 July 2022; Accepted 16 August 2022; Published 5 October 2022

Academic Editor: Junpeng Zou

Copyright © 2022 Tianhong Zhou et al. This is an open access article distributed under the Creative Commons Attribution License, which permits unrestricted use, distribution, and reproduction in any medium, provided the original work is properly cited.

The aim of the study is to further understand the rule of conversion of bottom hole pressure of a vertical well in a dual-permeability reservoir, which is about the dual permeability under different outer boundary (infinite, close, and constant value) conditions. However, there are few articles dealing with the model of a vertical well in a dual permeability reservoir under these three different outer boundary conditions. Hence, the paper proposes a model of a vertical well in a dual permeability reservoir under three outer boundary conditions. The model is solved with a Laplace space equation. We find the solution to the model that has a similar structure under three different outer boundary conditions by combining it with the similar structure theory. Therefore, we put forward a similar constructing method (SCM) that solves our model. The concrete steps of the SCM are given in this paper. At the same time, we draw the curves of the bottom hole pressure and pressure derivative using the modified Stehfest inversion formula and MATLAB software. In addition, we investigate the evolution of the pressure by changing the parameters (mobility ratio K , storability ratio ω , and crossflow coefficient λ). The solution to such a reservoir model obtained in this paper could be used as a basis for analyzing other typical reservoirs with vertical wells.

1. Introduction

The dual media is one of the largest storage formations in the world, and it is mainly composed of fracture and matrix media. Fluid flow in dual media can be treated in two kinds of models. One is the dual-porosity media model (Figure 1(a)), and the other one is the dual permeability media model (Figure 1(b)). In dual-porosity media, the fluid is stored in the matrix and flows into a wellbore through fractures, with a cross-flow from the fractures to the matrix, while in the dual permeability media model, the fluid flows into the wellbore not only from the fracture media but also from the matrix media, with a cross-flow between these two systems. Hence, the dual permeability is much more complicated than the dual-porosity media model. If we let the permeability of the dual permeability media model be equal to zero, then the dual permeability media model becomes the dual-

porosity media model. Thus, the dual-porosity media model can be considered as a special case for the dual permeability media model.

The study on dual permeability is mainly based on dual porosity and dual permeability. As regards the dual porosity model for horizontal wells, in 1988, Rosa and Carvalho [1] calculated the dynamic downhole pressure of horizontal wells in dual-porosity media by using the Stehfest Laplace transformation of the horizontal wells, which are widely used in the development of oil and gas reservoirs [2–8] with the progress in drilling and completion technologies. In 1994, a solution to the transient fluid flow of horizontal wells in a fractured dual porosity reservoir in Laplace space was obtained by Liu and Wang [9]. In 2012, Guo et al. studied the dual permeability flow behavior for modeling horizontal well production in fractured vuggy carbonate reservoirs [10].

In regards to the dual permeability model, in 1985, the solution to the vertical model under the outer

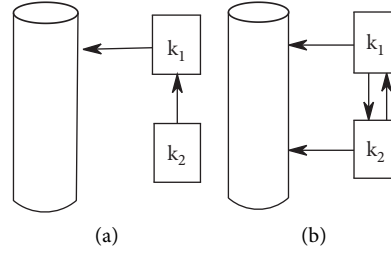


FIGURE 1: The sketch of the dual media. (a) Dual-porosity media; (b) dual permeability.

boundary infinite was first obtained through the Laplace transformation by Bourder [11]. In 1995, Liu and Wang [9] obtained the solution of the transient flow of slightly compressible fluid in the 2-D space, which provided a theoretical basis for related well test analyses. In 2006, the transient pressure in the dual permeability media of a shear-sensitive reservoir was studied by Tian and Tong [12]. In 2006, Hi and Tong [13] analyzed the effect of wellbore storage on bottom hole pressure in deformable dual permeability media by setting a mathematical model. In 2008, Liu [14] analyzed all kinds of reservoirs through the model curves under infinite boundary conditions in his literature. In 2010, Kong [15] obtained the solution of the vertical well in the dual permeability reservoir of signal and double layers by using Laplace and Weber's transformation and drew out the well test curve.

However, all the above studies are mainly based on the infinite outer boundary conditions, ignoring the close and constant outer boundary conditions. In 2004, the solution of a similar structure to the differential equation as a boundary value problem was put forward [16]. The influence of joints on the permeability and mechanical properties of rocks has been studied in some literature [17–19]. There were a lot of studies [20–26] about the vertical dual permeability reservoir under three different outer boundary conditions (infinite, close, and constant value). However, the studies in the references just stay at the math level, which cannot meet the demand of the well test analysis. Therefore, on the basis of the previous study, we set a model of a vertical well in the dual permeability reservoir under three outer boundary conditions (infinite, close, constant value) and solved the model in Laplace space. We found that the solution to the model has a similar structure under three different outer boundary conditions by combining with the similar structure theory. Hence, we put forward the SCM, and the concrete steps of the SCM are given in this paper. At the same time, we drew the curves of the bottom hole pressure and pressure derivative by using the modified Stehfest inversion formula and MATLAB software. We observed and analyzed the change law of the curves by changing the mobility ratio K , storativity ratio ω , and cross-flow coefficient λ . The solution to such a reservoir model obtained in this paper includes and improves the previous results and may then be used as a basis for analyzing other typical reservoirs with vertical wells.

2. Dimensionless Mathematics Model

The well is regarded as a point source in the paper, and supposing the outer boundary is a circular boundary. Therefore, according to [15], we can obtain the dimensionless mathematics model of the dual permeability reservoir as follows:

The seepage differential equation is as follows:

$$K \frac{1}{r_D} \frac{\partial}{\partial r_D} \left(r_D \frac{\partial P_{1D}}{\partial r_D} \right) + \lambda (P_{2D} - P_{1D}) = \omega \frac{\partial P_{1D}}{\partial t_D},$$

$$1 < r_D < R_D, t_D > 0, \quad (1)$$

$$(1 - K) \left(r_D \frac{\partial P_{2D}}{\partial r} \right) - \lambda (P_{2D} - P_{1D}) = (1 - \omega) \frac{\partial P_{2D}}{\partial t_D},$$

$$1 < r_D < R_D, t_D > 0,$$

where P is the reservoir pressure, MPa ; t is the time, h ; r represents any point in the reservoir at the radial distance of the well, m ; R is the outer boundary radius, m ; k is the permeability, μm^2 ; ω is storability ratio, dimensionless; λ is the cross-flow coefficient, dimensionless.

Initial condition is as follows:

$$P_{1D}(r_D, 0) = P_{2D}(r_D, 0) = 0. \quad (2)$$

Inner boundary condition is as follows:

$$\begin{cases} P_{wD}(t_D) = \left[P_{1D} - S_1 r_D \frac{\partial P_{1D}}{\partial r_D} \right]_{r_D=1} = \left[P_{2D} - S_2 r_D \frac{\partial P_{2D}}{\partial r_D} \right]_{r_D=1}, \\ \left[K r_D \frac{\partial P_{1D}}{\partial r_D} + (1 - K) \frac{\partial P_{2D}}{\partial r_D} \right]_{r_D=1} = - \left(1 - C_D \frac{\partial P_{2D}}{\partial t_D} \right), \end{cases} \quad (3)$$

where p_w is the bottom hole pressure, MPa ; S is the skin effect, dimensionless; C is the well storage, m^3/MPa .

Outer boundary condition is as follows:

$$P_{1D}(\infty, t_D) = P_{2D}(\infty, t_D) = 0,$$

$$\text{or } P_{1D}(R_D, t_D) = P_{2D}(R_D, t_D) = 0, \quad (4)$$

$$\text{or } \left. \frac{\partial P_{1D}}{\partial r_D} \right|_{r_D=R_D} = \left. \frac{\partial P_{2D}}{\partial r_D} \right|_{r_D=R_D} = 0,$$

where

$$\begin{aligned}
 P_{jD} &= \frac{1}{1.842 \times 10^{-3} Bq} \left(\frac{k_1 h_1}{\mu_1} + \frac{k_2 h_2}{\mu_2} \right) \\
 &\cdot [p_0 - p_j(r, t)] \quad (j = 1, 2), \\
 t_D &= \frac{3.6(k_1 h_1 / \mu_1 + k_2 h_2 / \mu_2) t}{(\phi_1 C_{t_1} h_1 + \phi_2 C_{t_2} h_2) r_w^2}, \\
 r_D &= \frac{r}{r_w}, \\
 C_D &= \frac{0.1592C}{(\phi_1 C_{t_1} h_1 + \phi_2 C_{t_2} h_2) r_w^2}, \\
 \lambda &= \alpha r_w^2 \frac{k_2 h_2 / \mu_2}{(k_1 h_1 / \mu_1 + k_2 h_2 / \mu_2)}, \\
 \omega &= \frac{\phi_1 C_{t_1} h_1}{\phi_1 C_{t_1} h_1 + \phi_2 C_{t_2} h_2}, \\
 K &= \frac{k_1 h_1 / \mu_1}{k_1 h_1 / \mu_1 + k_2 h_2 / \mu_2},
 \end{aligned} \tag{5}$$

h is the storage thickness, m ; μ is the viscosity, $mPa \cdot s$; r_w is the wellbore radius, m ; B is the oil volume coefficient, dimensionless; ϕ is the porosity, dimensionless; α is the shape factor, dimensionless.

3. Solutions in the Laplace Space

If we take the Laplace transformation of t_D of Eqs.(4)–(12), we obtain the following equation:

$$\begin{aligned}
 \bar{P}_{jD}(r_D, z) &= \int_0^\infty e^{-zt_D} P_{jD}(r_D, t_D) dt_D, \quad (j = 1, 2), \\
 \bar{P}_{wD}(z) &= \int_0^\infty e^{-zt_D} P_{wD}(t_D) dt_D,
 \end{aligned} \tag{6}$$

where z is the Laplace variable and $\bar{P}_{1D}, \bar{P}_{2D}, \bar{P}_{wD}$ are elements of Laplace space. Then, the form of the model in Laplace space can be obtained as follows:

$$\left\{ \begin{aligned}
 &K \frac{1}{r_D} \frac{d}{dr_D} \left(r_D \frac{d\bar{P}_{1D}}{dr_D} \right) + \lambda (\bar{P}_{2D} - \bar{P}_{1D}) = \omega z \bar{P}_{1D}, \\
 &(1 - K) \frac{1}{r_D} \frac{d}{dr_D} \left(r_D \frac{d\bar{P}_{2D}}{dr_D} \right) - \lambda (\bar{P}_{2D} - \bar{P}_{1D}) = (1 - \omega) z \bar{P}_{2D}, \\
 &\left[\bar{P}_{1D} - S_1 r_D \frac{d\bar{P}_{1D}}{dr_D} \right]_{r_D=1} = \left[\bar{P}_{2D} - S_2 r_D \frac{d\bar{P}_{2D}}{dr_D} \right]_{r_D=1} = \bar{P}_{wD}(z), \\
 &\left[K r_D \frac{d\bar{P}_1}{dr_D} + (1 - K) r_D \frac{d\bar{P}_2}{dr_D} \right]_{r_D=1} = - \left[\frac{1}{z} - C_D z \bar{P}_{wD} \right], \\
 &\bar{P}_{1D}(\infty, z) = \bar{P}_{2D}(\infty, z) = 0, \\
 &\text{or } \left. \frac{d\bar{P}_{1D}}{dr_D} \right|_{r_D=R_D} = \left. \frac{d\bar{P}_{2D}}{dr_D} \right|_{r_D=R_D} = 0, \\
 &\text{or } \bar{P}_{1D}(R_D, z) = \bar{P}_{2D}(R_D, z) = 0.
 \end{aligned} \right. \tag{7}$$

Theorem 1. *If boundary value problem (7) has a unique solution, then the solution can be expressed as follows:*

$$\begin{aligned} \bar{P}_{1D}(r_D, z) = & \frac{1}{z} \frac{C_D z + K a_2 + 1 - K / (1 - a_2) \Psi(1, \sigma_2) + S_2 - a_2 S_1 - K a_1 + 1 - K / (1 - a_1) \Psi(1, \sigma_1) + S_2 - a_1 S_1 / S_2 + \Psi(1, \sigma_2) / (1 - a_2) \Psi(1, \sigma_2) + S_2 - a_2 S_1 - S_2 + \Psi(1, \sigma_1) / (1 - a_1) \Psi(1, \sigma_1) + S_2 - a_1 S_1}{a_2 \Psi(r_D, \sigma_2) / (1 - a_2) \Psi(1, \sigma_2) + S_2 - a_2 S_1 - a_1 \Psi(r_D, \sigma_1) / (1 - a_1) \Psi(1, \sigma_1) + S_2 - a_1 S_1} \\ & \frac{S_2 + \Psi(1, \sigma_2) / (1 - a_2) \Psi(1, \sigma_2) + S_2 - a_2 S_1 - S_2 + \Psi(1, \sigma_1) / (1 - a_1) \Psi(1, \sigma_1) + S_2 - a_1 S_1}{\Psi(r_D, \sigma_2) / (1 - a_2) \Psi(1, \sigma_2) + S_2 - a_2 S_1 - (\Psi(r_D, \sigma_1) / (1 - a_1) \Psi(1, \sigma_1) + S_2 - a_1 S_1)} \\ \bar{P}_{2D}(r_D, z) = & \frac{1}{z} \frac{C_D z + K a_2 + 1 - K / (1 - a_2) \Psi(1, \sigma_2) + S_2 - a_2 S_1 - K a_1 + 1 - K / (1 - a_1) \Psi(1, \sigma_1) + S_2 - a_1 S_1 / S_2 + \Psi(1, \sigma_2) / (1 - a_2) \Psi(1, \sigma_2) + S_2 - a_2 S_1 - S_2 + \Psi(1, \sigma_1) / (1 - a_1) \Psi(1, \sigma_1) + S_2 - a_1 S_1}{\Psi(r_D, \sigma_2) / (1 - a_2) \Psi(1, \sigma_2) + S_2 - a_2 S_1 - (\Psi(r_D, \sigma_1) / (1 - a_1) \Psi(1, \sigma_1) + S_2 - a_1 S_1)} \\ & \frac{(\Psi(r_D, \sigma_2) / (1 - a_2) \Psi(1, \sigma_2) + S_2 - a_2 S_1) - (\Psi(r_D, \sigma_1) / (1 - a_1) \Psi(1, \sigma_1) + S_2 - a_1 S_1)}{(S_2 + \Psi(1, \sigma_2) / (1 - a_2) \Psi(1, \sigma_2) + S_2 - a_2 S_1) - (S_2 + \Psi(1, \sigma_1) / (1 - a_1) \Psi(1, \sigma_1) + S_2 - a_1 S_1)} \end{aligned} \quad (8)$$

where $\Psi(r_D, \sigma_i)$ is defined as a similar kernel function.

(i) The outer boundary condition is infinite

$$\Psi(r_D, \sigma_i) = \frac{\Phi_{0,0}^i(r_D, R_D)}{\Phi_{1,0}^i(1, R_D)} = \frac{K_0(\sigma_i r_D)}{\sigma_i K_1(\sigma_i)}, \quad (9)$$

$$(R_D \rightarrow \infty) (i = 1, 2).$$

(ii) The outer boundary condition is closed

$$\Psi(r_D, \sigma_i) = \frac{\Phi_{0,1}^i(r_D, R_D)}{\Phi_{1,1}^i(1, R_D)} (i = 1, 2). \quad (10)$$

(iii) The outer boundary condition is a constant

$$\Psi(r_D, \sigma_i) = \frac{\Phi_{0,0}^i(r_D, R_D)}{\Phi_{1,0}^i(1, R_D)} (i = 1, 2). \quad (11)$$

Here, we get

$$\begin{aligned} a_i &= 1 + \frac{(1 - \omega)z - (1 - K)\sigma_i^2}{\lambda} (i = 1, 2), \\ \sigma_{1,2}^2 &= \frac{1}{2} \left\{ \left[\frac{\omega z + \lambda}{K} + \frac{(1 - \omega)z + \lambda}{1 - K} \right] \pm \sqrt{\left[\frac{(1 - \omega)z + \lambda}{1 - K} - \frac{\omega z + \lambda}{K} \right]^2 + \frac{4\lambda^2}{K(1 - K)}} \right\}. \end{aligned} \quad (12)$$

$\Phi_{i,k}^j(r_D, \xi)$ ($i = 1, 2; l, k = 0, 1$) are called as the functions of the guide solution, i.e.,

$$\Phi_{0,0}^i(r_D, \xi) = \varphi_{0,0}(r_D, \xi, \sigma_i),$$

$$\Phi_{1,0}^i(r_D, \xi) = \frac{\partial \Phi_{0,0}^i(r_D, \xi)}{\partial r_D} = -\sigma_i \varphi_{1,0}(r_D, \xi, \sigma_i), \quad (13)$$

$$\Phi_{0,1}^i(r_D, \xi) = \frac{\partial \Phi_{0,0}^i(r_D, \xi)}{\partial \xi} = \sigma_i \varphi_{0,1}(r_D, \xi, \sigma_i),$$

$$\Phi_{1,1}^i(r_D, \xi) = \frac{\partial^2 \Phi_{0,0}^i(r_D, \xi)}{\partial r_D \partial \xi} = -\sigma_i^2 \varphi_{1,1}(r_D, \xi, \sigma_i),$$

where $\varphi_{m,n}(x, y, \tau) = K_m(x\tau)I_n(y\tau) + (-1)^{m-n+1}I_m(x\tau)K_n(y\tau)$ and $K_\nu(\bullet), I_\nu(\bullet)$ are modified Bessel functions of the order ν . τ is a parameter.

Proof 1. Firstly, we prove the closed outer boundary condition.

The general solution to the government equation in the boundary value problem can be expressed as follows (the detailed derivation is given in Appendix A):

$$\begin{aligned} \bar{P}_{1D}(r_D, z) &= a_1 D_1 \frac{\varphi_{0,1}(r_D, R_D, \sigma_1)}{I_1(R_D \sigma_1)} \\ &+ a_2 D_2 \frac{\varphi_{0,1}(r_D, R_D, \sigma_2)}{I_1(R_D \sigma_2)}, \\ \bar{P}_{2D}(r_D, z) &= D_1 \frac{\varphi_{0,1}(r_D, R_D, \sigma_1)}{I_1(R_D \sigma_1)} + D_2 \frac{\varphi_{0,1}(r_D, R_D, \sigma_2)}{I_1(R_D \sigma_2)}, \end{aligned} \quad (14)$$

where D_1, D_2 are arbitrary constants. Substitute $\bar{P}_{1D}(r_D, z)$ and $\bar{P}_{2D}(r_D, z)$ into Eq.(7) separately, the linear system about D_1, D_2 can be obtained as follows:

$$\begin{aligned} & \left[(1 - a_1) \frac{\varphi_{0,1}(1, R_D, \sigma_1)}{I_1(\sigma_1 R_D)} - (a_1 S_1 - S_2) \sigma_1 \frac{\varphi_{1,1}(1, R_D, \sigma_1)}{I_1(\sigma_1 R_D)} \right] D_1 \\ & + \left[(1 - a_2) \frac{\varphi_{0,1}(1, R_D, \sigma_2)}{I_1(\sigma_2 R_D)} - (a_2 S_1 - S_2) \sigma_2 \frac{\varphi_{1,1}(1, R_D, \sigma_2)}{I_1(\sigma_2 R_D)} \right] D_2 = 0, \\ & \left[C_D z \frac{\varphi_{0,1}(1, R_D, \sigma_1)}{I_1(\sigma_1 R_D)} + (K a_2 + 1 - K + C_D z S_2) \sigma_1 \frac{\varphi_{1,1}(1, R_D, \sigma_1)}{I_1(\sigma_1 R_D)} \right] D_1 \\ & + \left[C_D z \frac{\varphi_{0,1}(1, R_D, \sigma_2)}{I_1(\sigma_2 R_D)} + (K a_2 + 1 - K + C_D z S_2) \sigma_2 \frac{\varphi_{1,1}(1, R_D, \sigma_2)}{I_1(\sigma_2 R_D)} \right] D_2 = \frac{1}{z}. \end{aligned} \tag{15}$$

Because the boundary value problem has a unique solution, the determinant Δ of the coefficients of the linear system (namely, Eqs. (15)) about D_1, D_2 is not equal to zero. Now, according to the Cramer rule, the value of D_1, D_2 is obtained as follows:

$$\begin{aligned} D_1 &= -\frac{1}{z\Delta} I_1(\sigma_1 R_D) \left[(1 - a_2) \varphi_{0,1}(1, R_D, \sigma_2) \right. \\ & \quad \left. - (a_2 S_1 - S_2) \sigma_2 \varphi_{1,1}(1, R_D, \sigma_2) \right], \\ D_2 &= \frac{1}{z\Delta} I_1(\sigma_2 R_D) \left[(1 - a_1) \varphi_{0,1}(1, R_D, \sigma_1) \right. \\ & \quad \left. - (a_1 S_1 - S_2) \sigma_1 \varphi_{1,1}(1, R_D, \sigma_1) \right]. \end{aligned} \tag{16}$$

Where $\Delta =$

$$\begin{aligned} & \left[(1 - a_1) \varphi_{0,1}(1, R_D, \sigma_1) - (a_1 S_1 - S_2) \sigma_1 \varphi_{1,1}(1, R_D, \sigma_1) \right] \cdot \left[C_D z \varphi_{0,1}(1, R_D, \sigma_2) + (K a_2 + 1 - K + C_D S_2 z) \sigma_2 \varphi_{1,1}(1, R_D, \sigma_2) \right] \\ & - \left[(1 - a_2) \varphi_{0,1}(1, R_D, \sigma_2) - (a_2 S_1 - S_2) \sigma_2 \varphi_{1,1}(1, R_D, \sigma_2) \right] \cdot \left[C_D z \varphi_{0,1}(1, R_D, \sigma_1) + (K a_1 + 1 - K + C_D S_2 z) \sigma_1 \varphi_{1,1}(1, R_D, \sigma_1) \right]. \end{aligned} \tag{17}$$

Substituting Eq. (16) from Eq. (14), then we can obtain Eq. (8) by combining with Eqs. (9)–(11) and (12)–(13).

Similarly, when the outer boundary conditions are infinite and (7), the solution to boundary value problem can also be expressed as Eq.(8).

According to the boundary condition:

$$\left[\bar{P}_{2D} - S_2 r_D \frac{d\bar{P}_{2D}}{dr_D} \right]_{r_D=1} = \bar{P}_{wD}(z). \tag{18}$$

The dimensionless bottom hole pressure can be obtained

$$\begin{aligned} & \bar{P}_{wD}(z) \\ & = \frac{1}{z} \frac{1}{C_D z + (K a_2 + 1 - K / (1 - a_2) \Psi(1, \sigma_2) + S_2 - a_2 S_1) - (K a_1 + 1 - K / (1 - a_1) \Psi(1, \sigma_1) + S_2 - a_1 S_1) / (S_2 + \Psi(1, \sigma_2) / (1 - a_2) \Psi(1, \sigma_2) + S_2 - a_2 S_1) - (S_2 + \Psi(1, \sigma_1) / (1 - a_1) \Psi(1, \sigma_1) + S_2 - a_1 S_1)}. \end{aligned} \tag{19}$$

If let $S_1 = S_2 = S$, then Eq.(19) can be written as follows:

$$\bar{P}_{wD}(z) = \frac{1}{z} \frac{1}{C_D z + (a_2 - 1)(K a_1 + 1 - K) / (a_2 - a_1) [S + \Psi(1, \delta_1)] + (a_1 - 1)(K a_2 + 1 - K) / (a_2 - a_1) [S + \Psi(1, \delta_2)]}. \tag{20}$$

Now, we analyze the situation of $S_1 = S_2 = S$ as follows:

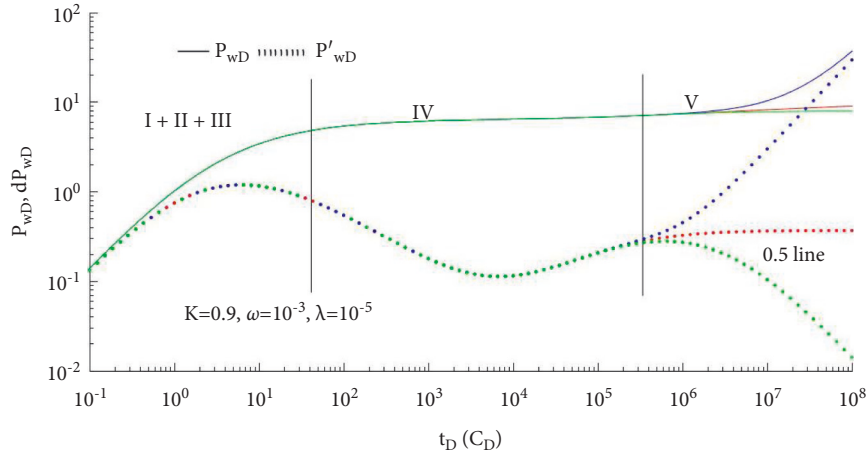


FIGURE 2: Special curves of the pressure and pressure derivative of dual permeability ($C_D e^{2S} = 1$, $K = 0.9$, $\omega = 10^{-3}$, $\lambda = 10^{-5}$).

$$\bar{P}_{wD}(z) = \frac{1}{z} \frac{1}{C_D z + 1 - K/S + \Psi(1, \sqrt{1 - \omega/1 - kz}) + K/S + \Psi(1, \sqrt{\omega/kz})}. \quad (21)$$

- (i) At the later time, when $t_D \rightarrow \infty$, $z \rightarrow 0$, then Eq. (20) can be written as follows:

$$\bar{P}_{wD} = \frac{1}{z} \frac{1}{C_D z + 1/S + \Psi(1, \sqrt{(1 - \omega/1 - k)z})}. \quad (22)$$

4. Chart Analysis

We draw the test well special curves of the dual permeability reservoir under three outer boundary conditions by using MATLAB software (Figure 2).

- (1) In Figure 2, the characteristic curves of both pressure and the pressure derivative are overlapping under three different outer boundary conditions in stages I-IV, which indicate that the changes in bottom hole pressure are the same before the pressure reaches the outer boundary.
- (2) Stages I-III are the early parts. Because of the influence of pure wellbore storage in the early times, the curves of the bottom hole pressure and pressure derivative coincide and show a line with a slope of 1. After the influence of pure wellbore storage, the curve of pressure derivative slopes downward after the peak appearance. The level of the peak value depends on the $C_D e^{2S}$.
- (3) Stage IV is the mid-party that mainly replies to the cross-flow characteristics of the transition zone, which are influenced by the mobility ratio K , storativity ratio ω , and cross-flow coefficient λ . We will conduct further analysis in part 4.2.
- (4) Stage V is the latter part that replies to the characteristics of radial flow in the dual permeability. When the outer boundary condition is closed, the pressure

derivative is a line with a slope of 1 (as shown by the blue dotted line in Figure 2). When the outer boundary condition is infinite, the pressure derivative is 0.5 line (as shown by the red dotted line in Figure 2), and when the outer boundary condition is a constant value, the pressure derivative will bend downwards (as shown by the green dotted line in Figure 2).

Now, we will analyze the impact of K, ω, λ on bottom hole pressure according to the chart (as shown in Figures 3-11). In Figures 3-5, we let $C_D e^{2S} = 1$, $\lambda = 10^{-5}$, $K = 0.9$ and let ω be equal to 10^{-1} , 10^{-2} , 10^{-3} , and 10^{-4} separately.

From Figures 3-5, we know that the changes of parameter ω have an obvious influence on the transition zone no matter how under which kind of outer boundary conditions. The stored energy ratio ω decides the width and depth of the concave pressure derivative curves in the transition section. With the decrease of a ω , the "concave" turns more deep and wide.

In Figures 6-8, we let $C_D e^{2S} = 1, \lambda = 10^{-5}, \omega = 10^{-3}$ and let K equal to 0.6, 0.9, 0.99, 0.999, respectively.

From Figures 6-8, we can obtain that the change of K has an obvious effect on the seepage zone of transition under the three different boundary conditions. For different values of K , the "concave" has different degrees of depth. The smaller the value of K , the "concave" is more shallower and approximately half of the value of the horizontal line. If $K = 5$, then we can get $k_1 h_1 = k_2 h_2$, and the characteristics of the curve are the same with the homogeneous reservoir model, the pressure derivative will not appear "concave", and the greater the value of K , the deeper the "concave".

In Figures 9-11, we let $C_D e^{2S} = 1, K = 0.9$, and $\omega = 10^{-3}$ and let λ be equal to 10^{-2} , 10^{-3} , 10^{-4} , and 10^{-5} , respectively.

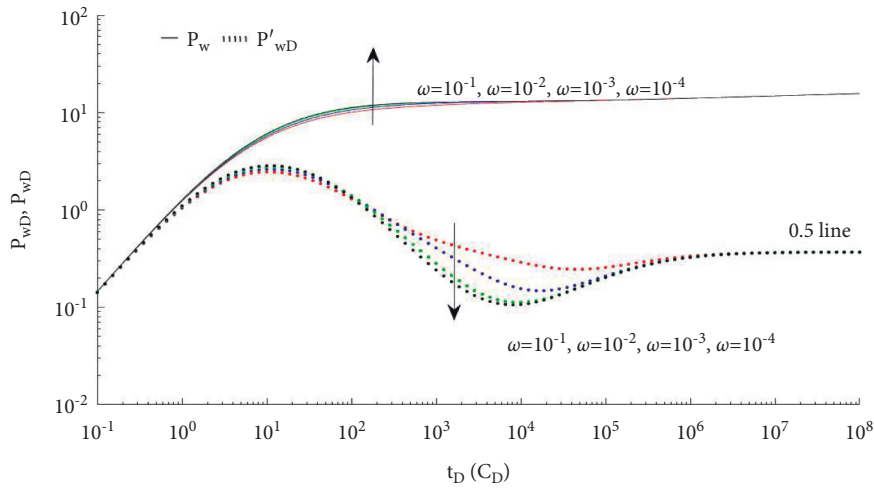


FIGURE 3: Dimensionless pressure of vertical wells under the infinite outer boundary influenced by ω ($C_D e^{2S} = 1, \lambda = 10^{-5}, K = 0.9$).

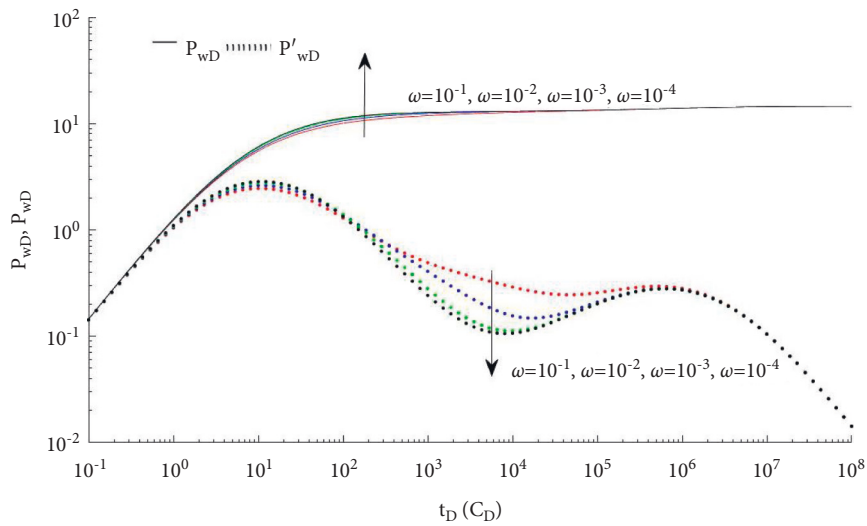


FIGURE 4: Dimensionless pressure of vertical wells under the constant outer boundary influenced by ω ($C_D e^{2S} = 1, \lambda = 10^{-5}, K = 0.9$).

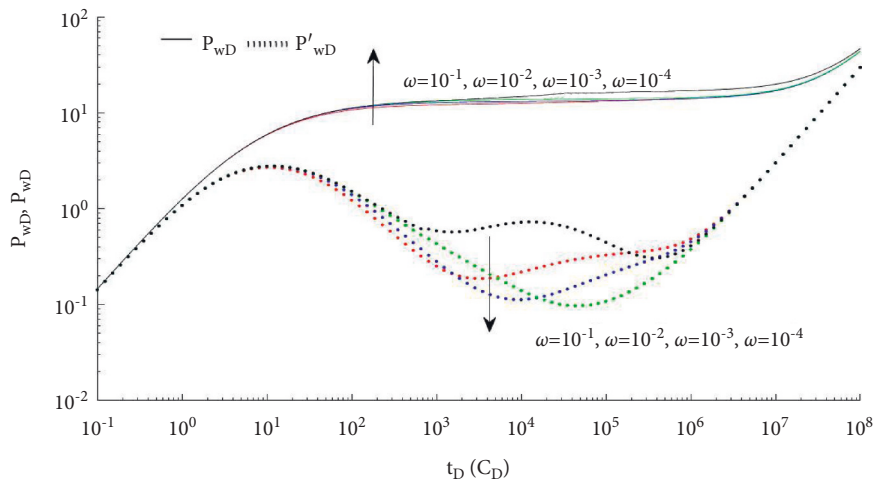


FIGURE 5: Dimensionless pressure of vertical wells under the close outer boundary influenced by ω ($C_D e^{2S} = 1, \lambda = 10^{-5}, K = 0.9$).

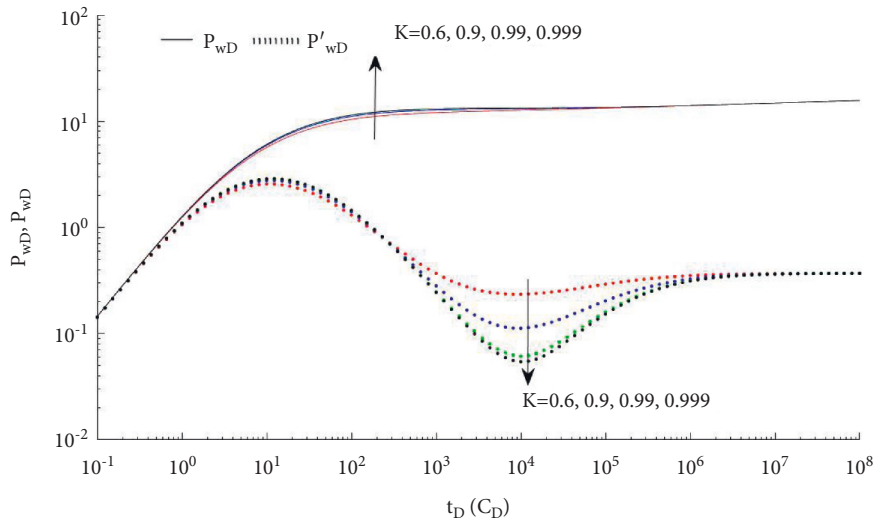


FIGURE 6: Dimensionless pressure of vertical wells under the infinite outer boundary influenced by K ($C_D e^{2S} = 1, \lambda = 10^{-5}, \omega = 10^{-3}$).

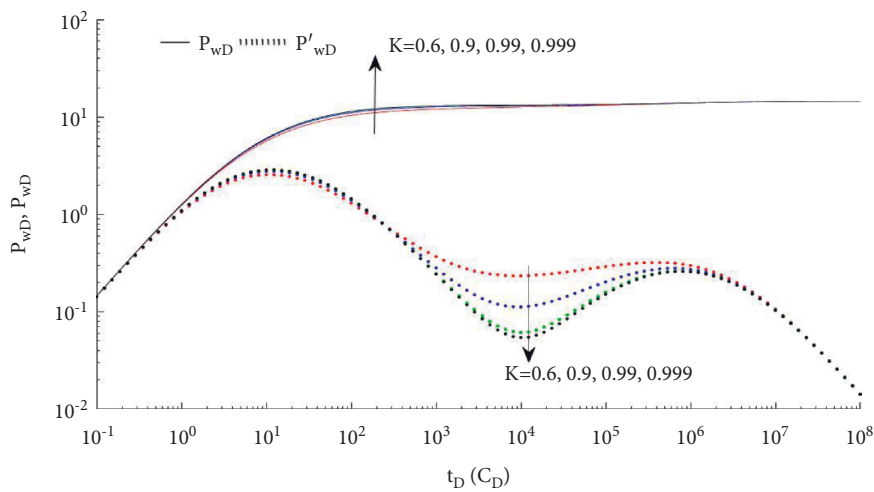


FIGURE 7: Dimensionless pressure of vertical wells under the close boundary influenced by K ($C_D e^{2S} = 1, \lambda = 10^{-5}, \omega = 10^{-3}$).

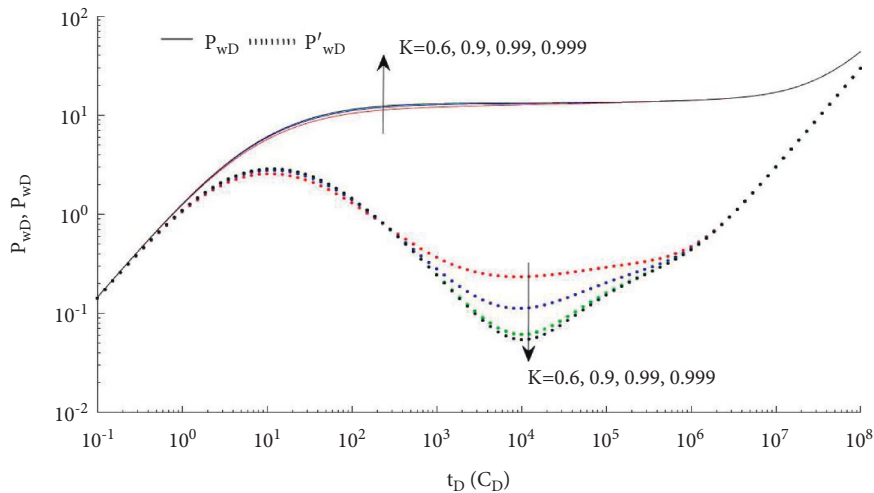


FIGURE 8: Dimensionless pressure of vertical wells under the constant boundary influenced by K ($C_D e^{2S} = 1, \lambda = 10^{-5}, \omega = 10^{-3}$).

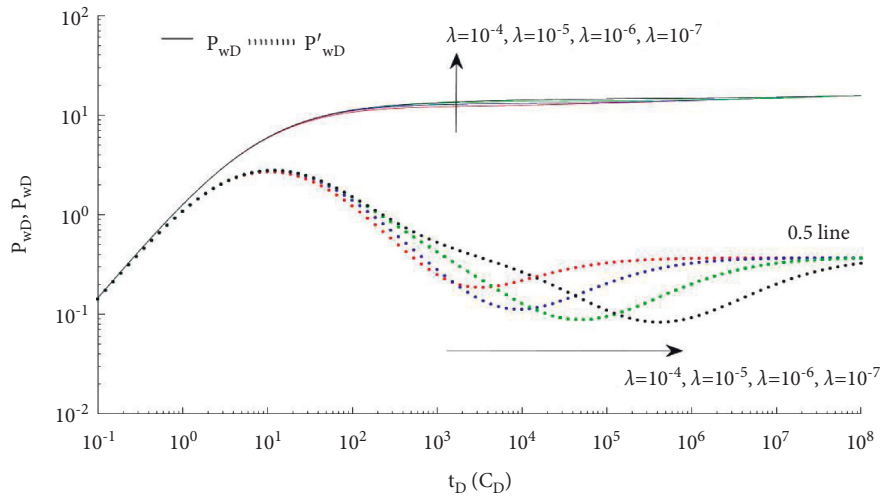


FIGURE 9: Dimensionless pressure of vertical wells under the infinite outer boundary influenced by λ ($C_D e^{2S} = 1, \omega = 10^{-3}, K = 0.9$).

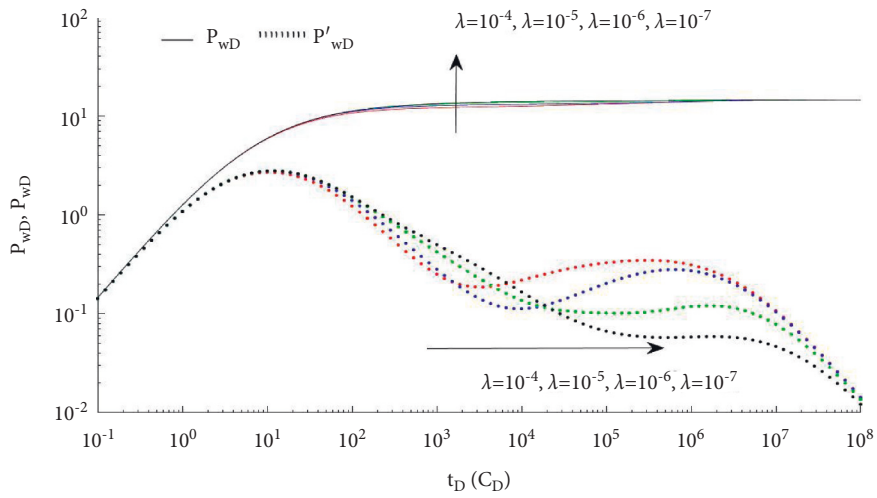


FIGURE 10: Dimensionless pressure of vertical wells under the constant value outer boundary influenced by λ ($C_D e^{2S} = 1, \omega = 10^{-3}, K = 0.9$).

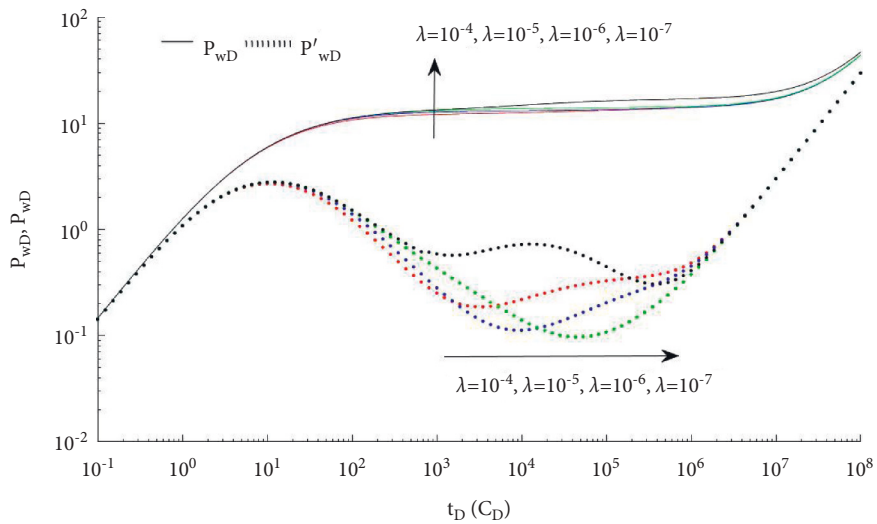


FIGURE 11: Dimensionless pressure of vertical wells under the close outer boundary influenced by λ ($C_D e^{2S} = 1, \omega = 10^{-3}, K = 0.9$).

From Figures 9–11, we can obtain that the position of the transition zone is determined by the cross-flow coefficient λ . The smaller value of λ , the later the transition zone appears, which reflects that the “concave” is on the right in Figures 9–11.

5. Conclusions

- (1) In this paper, we obtain the expression of bottom hole pressure of the dual permeability reservoir by using the SCM in Laplace space, and we provide a more complete testing chart for analyzing the change law of the pressure of dual permeability.
- (2) Using the SCM to solve the model of a vertical well in a dual permeability reservoir can avoid the cumbersome process of derivation, and the SCM only includes simple arithmetic, so it is easily understood and grasped. At the same time, the steps of SCM provide a clear algorithm flow for programs.
- (3) We obtain the simplified formula of solution (Eqs. (30) ~ (31)) for the model of the vertical well in a dual permeability reservoir, which contributes to analyzing the characteristics of the early and later parties in Figures 2–11.
- (4) We draw the curves of the bottom hole pressure and pressure derivative by using the modified Stehfest inversion formula and MATLAB software. We observe and analyze the change law of the curves by changing the mobility ratio K , storativity ratio ω , and cross-flow coefficient λ , which may provide an important theoretical value for further studying the dual permeability reservoir.

Appendix

In boundary value problem (7), the general solutions to governing system (7) can be expressed by modified Bessel functions $I_0(\sigma r_D)$, $K_0(\sigma r_D)$ as follows:

$$\begin{cases} \bar{P}_{1D}(r_D, z) = AI_0(\sigma r_D) + BK_0(\sigma r_D), \\ \bar{P}_{2D}(r_D, z) = CI_0(\sigma r_D) + DK_0(\sigma r_D), \end{cases} \quad (\text{A.1})$$

where A, B, C, D, σ are undetermined coefficients.

Substituting Eq.(A.1) into Eq (7), the system can be obtained as follows:

$$\begin{cases} AI_1(\sigma R_D) - BK_1(\sigma R_D) = 0, \\ CI_1(\sigma R_D) - DK_1(\sigma R_D) = 0, \end{cases} \quad (\text{A.2})$$

i.e.,

$$\frac{A}{B} = \frac{C}{D} = \frac{K_1(\sigma R_D)}{I_1(\sigma R_D)}. \quad (\text{A.3})$$

Substituting Eq.(A.3) into Eq.(A.1), respectively, the system can be obtained as follows:

$$\begin{cases} \bar{P}_{1D}(r_D, z) B \varphi_{0,1}(r_D, R_D, \sigma) / I_1(\sigma R_D), \\ \bar{P}_{2D}(r_D, z) D \varphi_{0,1}(r_D, R_D, \sigma) / I_1(\sigma R_D), \end{cases} \quad (\text{A.4})$$

where

$$\varphi_{m,n}(x, y, \tau) = K_m(x\tau)I_n(y\tau) + (-1)^{m-n+1}I_m(x\tau)K_n(y\tau).$$

By the property of the Bessel function [27], we know that $I_0(\sigma r_D)$, $K_0(\sigma r_D)$ satisfy the following equation:

$$Z_0''(x) = Z_0(x) + \frac{1}{x}Z_1(x). \quad (\text{A.5})$$

Substituting Eq. (A.4) into governing Eq. (7) and combining Eq.(A.5), the system can be obtained as follows:

$$\begin{cases} (K\sigma^2 - \omega z - \lambda)B + \lambda D = 0, \\ \lambda B + [(1-K)\sigma^2 - (1-\omega)z - \lambda]D = 0. \end{cases} \quad (\text{A.6})$$

According to Eq. (A.6), we obtain the equation as follows:

$$+ \frac{(\omega z + \lambda)[(1-\omega)z + \lambda] - \lambda^2}{K(1-K)} = 0. \quad (\text{A.7})$$

Solving the above equation, we obtain solutions as follows:

$$\begin{cases} \sigma_1^2 = \left\{ \frac{1}{2} \left[\frac{\omega z + \lambda}{K} + \frac{(1-\omega)z + \lambda}{1-K} \right] + \Delta \right\}, \\ \sigma_2^2 = \left\{ \frac{1}{2} \left[\frac{\omega z + \lambda}{K} + \frac{(1-\omega)z + \lambda}{1-K} \right] - \Delta \right\}, \end{cases} \quad (\text{A.8})$$

where

$$\Delta = \sqrt{\left[\frac{\omega z + \lambda}{K} - \frac{(1-\omega)z + \lambda}{1-K} \right]^2 + \frac{4\lambda^2}{K(1-K)}}. \quad (\text{A.9})$$

According to the structure principle of the solution to the homogeneous linear differential equation, we know that the linear combination of the two linear independent solutions is still the solution to the original equation. Therefore, solutions to governing system (7) can be expressed as follows:

$$\begin{aligned} & \bar{P}_{1D}(r_D, z) \\ & \bar{P}_{2D}(r_D, z) = D_1 \frac{\varphi_{0,1}(r_D, R_D, \sigma_1)}{I_1(R_D \sigma_1)} + D_2 \frac{\varphi_{0,1}(r_D, R_D, \sigma_2)}{I_1(R_D \sigma_2)}. \end{aligned} \quad (\text{A.10})$$

If Bof Eq. (A.6) recorded as aD , then we obtain

$$\begin{cases} (K\sigma^2 - \omega z - \lambda)aD + \lambda D = 0 \\ \lambda aD + [(1-K)\sigma^2 - (1-\omega)z - \lambda]D = 0. \end{cases} \quad (\text{A.11})$$

According to the above system, we can obtain

$$a = 1 + \frac{(1-\omega)z - (1-K)\sigma^2}{\lambda} \left(= -\frac{\lambda}{K\sigma^2 - \omega z - \lambda} \right). \quad (\text{A.12})$$

Hence, we obtain the following equation:

$$\begin{cases} a_1 = 1 + \frac{(1-\omega)z - (1-K)\sigma_1^2}{\lambda}, \\ a_2 = 1 + \frac{(1-\omega)z - (1-K)\sigma_2^2}{\lambda}. \end{cases} \quad (\text{A.13})$$

Data Availability

The data used to support the findings of this study are available from the corresponding author upon request.

Conflicts of Interest

The authors declare that they have no conflicts of interest regarding the publication of this article.

Acknowledgments

This work was supported by the Industry-University Research Innovation Funding of the Chinese University New Generation Information Technology Project (grant no. 2019ITA03033), 2021 Ministry of Education Collaborative Education Project (grant no. 202102588008), and the Guiding Project of the Scientific Research Plan of the Hubei Provincial Department of Education (grant no. B2021272).

References

- [1] R. S. Carvalho and A. J. Rosa, *Transient Pressure Behavior for Horizontal wells in Naturally Fractured Reservoir*, SPE 18302, Houston, Texas, USA, 1988.
- [2] K. A. Anil, A. M. Dawood, and M. Eddie, "Long-term field development opportunity assessment using horizontal wells in a thin, carbonate reservoir of the greater burgan field," *SPE Reservoir Evaluation and Engineering*, vol. 12, no. 1, pp. 14–24, 2009.
- [3] Z. D. Lei, S. Q. Cheng, X. F. Li, and H. P. Xiao, "A New method for prediction of productivity of fractured horizontal wells based on non-steady flow," *Journal of Hydrodynamics*, vol. 19, no. 4, pp. 494–500, 2007.
- [4] F. O. Jalal and T. Djebbar, "Transient pressure behavior of bingham non-Newtonian fluids for gorizontal well," *Journal of Petroleum Science and Engineering*, vol. 64, no. 1, pp. 21–32, 2008.
- [5] Y. F. He, X. G. Liu, and B. A. Xian, "Transient pressure analysis of gorizontal well for coalbed methane," *Coal Geology & Exploration*, vol. 35, no. 1, pp. 41–44, 2007.
- [6] R. H. Wang, R. C. Cheng, H. G. Wang, and Y. Bu, "Numerical simulation of transient cuttings transport with foam fluid in horizontal wellbore," *Journal of Hydrodynamics*, vol. 21, no. 4, pp. 437–444, 2009.
- [7] J. Hagoort, "A simplified analytical method for estimating the productivity of a horizontal well producing at constant rate or constant pressure," *Journal of Petroleum Science and Engineering*, vol. 64, no. 1-4, pp. 77–87, 2009.
- [8] W. J. Luo, Y. F. Zhou, and X. D. Wang, "A novel 3-D model for the water cresting in horizontal wells," *Journal of Hydrodynamics*, vol. 20, no. 6, pp. 749–755, 2008.
- [9] C. Q. Liu and X. D. Wang, "Transient anixisy-mmetrical two-dimensional flow through media with dual permeability," *Journal of Hydrodynamics*, vol. 6, no. 2, pp. 53–60, 1994.
- [10] J. C. Guo, R. S. Nie, and Y. L. Jia, "Dual permeability flow behavior for modeling horizontal well production in fractured-vuggy carbonate reservoirs," *Journal of Hydrology*, vol. 464-465, pp. 281–293, 2012.
- [11] D. Bourdet, *Pressure Behavior of Layered Reservoirs with Cross-Flow*, p. SPE13628, Bakerfield, California, USA, 1985.
- [12] J. Tian and D. K. Tong, "The flow analysis of fluids in fractal reservoir with the fractional derivative," *Journal of Hydrodynamics*, vol. 18, no. 3, pp. 287–293, 2006.
- [13] L. N. Hi and D. K. Tong, "Pressure analysis of dual permeability model in deformed medium with well bore storage effect," *Chinese Quarterly of Mechanics*, vol. 27, no. 2, pp. 206–211, 2006.
- [14] N. Q. Liu, *Interpretation of Modern Well Test Analysis*, Petroleum Industry Press, Beijing, 2008.
- [15] X. Y. Kong, *Hight Fluid Mechanics*, China Science and Technology Press, HeFei, 2010.
- [16] P. S. Zheng, S. C. Li, and Y. F. Zhang, "A class of quasilinear parameter boundary value problems for ordinary differential equations," *Journal of Northeast Normal University*, vol. 36, pp. 1–4, 2004.
- [17] J. Zou, X. Hu, Y. Y. Jiao et al., "Dynamic Mechanical Behaviors of Rock's Joints Quantified by Repeated Impact Loading Experiments with Digital Imagery," *Rock Mechanics and Rock Engineering*, 2022.
- [18] Z. C. Tang, Z. L. Wu, and J. Zou, "Appraisal of the number of asperity peaks, their radii and heights for three-dimensional rock fracture," *International Journal of Rock Mechanics and Mining Sciences*, vol. 153, Article ID 105080, 2022.
- [19] Y. Y. Jiao, K. Wu, J. Zou et al., "On the strong earthquakes induced by deep coal mining under thick strata-a case study," *Geomechanics and Geophysics for Geo-Energy and Geo-Resources*, vol. 7, no. 4, pp. 97–111, 2021.
- [20] P. L. Liu, S. C. Li, and L. Q. Zhao, "A general analysis of bottom-hole pressure distribution of dual permeability," *Oil and Gas Well Testing*, vol. 5, no. 5, pp. 9–11, 2004.
- [21] W. T. Sun, B. G. Huang, S. C. Li, and N. T. Wang, "Analysis of solving pressure of composite dual permeability reservoirs," *Journal of Southwest Petroleum College*, vol. 13, no. 5, pp. 90–95, 2006.
- [22] P. S. Zhen, S. C. Li, and W. C. Xu, "Method of well testing of dual permeability reservoirs base on similar structure of solution," *Journal of Southwest Petroleum College*, vol. 2, no. 30, pp. 108–110, 2008.
- [23] Q. Y. Li, S. C. Li, W. Li, and X. X. Xiao, "The problem of dual permeability reservoirs base on the similar structure," *Journal of Xi Hua University*, vol. 20, no. 2, pp. 64–66, 2011.

- [24] D. Wu, B. G. Huang, and S. C. Li, "The solving analysis of pressure of composite reservoirs," *Journal of Southwest Petroleum University*, vol. 29, no. 1, pp. 108–122, 2007.
- [25] X. W. Liao and P. P. Shen, *Model Well Test Analysis*, Petroleum Industry Press, Beijing, 2009.
- [26] J. Zou, W. Chen, D. Yang, H. Yu, and J. Yuan, "The impact of effective stress and gas slippage on coal permeability under cyclic loading," *Journal of Natural Gas Science and Engineering*, vol. 31, pp. 236–248, 2016.
- [27] S. S. Liu and S. D. Liu, *Special Function*, Meteorological Press, Beijing, 2002.

Research Article

Experimental Study on Gas Permeability Semiempirical Model of Granite after Heat Treatment

Jinquan Wu ^{1,2}

¹Key Laboratory of Geological Survey and Evaluation of Ministry Education, China University of Geosciences (Wuhan), Wuhan 430074, China

²Lincang Transportation Bureau of Yunnan Province, Lincang 677099, China

Correspondence should be addressed to Jinquan Wu; 951426185@qq.com

Received 7 May 2022; Accepted 18 August 2022; Published 6 September 2022

Academic Editor: Wei-yao Guo

Copyright © 2022 Jinquan Wu. This is an open access article distributed under the Creative Commons Attribution License, which permits unrestricted use, distribution, and reproduction in any medium, provided the original work is properly cited.

High temperature will cause a thermal crack of a rock, thus affecting the permeability change of rock. To explore the effects of temperature on permeability and microstructure of rock microstructure, the granite after 50–800 C thermal treatment was carried out by gas permeability test, combined with computed tomography (CT) scanning technology. The granite internal three-dimensional reconstruction was conducted after high-temperature thermal treatment, and the characteristics of the microstructure were also deeply analyzed. On this basis, the applicability of the Costa model under high temperature was discussed. Finally, the temperature-permeability model of granite after the high temperature was proposed combined with the pore fractal model. The new model was verified with experimental data.

1. Introduction

In recent years, with the rapid development of nuclear power, the output of nuclear waste has been increasing year by year. At present, the international common way of disposal is through the construction of underground nuclear waste repository thousands of meters underground and the use of geological barriers and artificial barriers to permanently block the nuclide movement. In the process of geological storage of nuclear waste, nuclides release heat energy, which leads to the increase of surrounding rock temperature. These fractures are interconnected and act as pathways for nuclides to migrate to the biosphere. Therefore, it is a key scientific problem to study the effect of high-temperature heat treatment on the evolution of microstructure and seepage characteristics of low permeability rocks [1–5].

In term of describing the fractal characteristics of the internal microstructure of rock after thermal fracture, some research used the method of the scanning electron microscope (SEM) or optical microscope to carry out 2D geometric analysis of the images of rock surface [6–9]. The result

cannot effectively reflect the 3D characteristics of the real rock's internal microstructure. For porous media, mercury intrusion porosimetry (MIP) is an effective tool to obtain the pore size distribution [10]. The basic step is to obtain the volume of mercury intrusion under different pressures by mercury injection experiments and then calculate the pore size distribution by the cumulative mercury injection volume [11–13]. In recent years, as a method that can directly reflect the three-dimensional microstructure of rock, computed tomography (CT) has been more applied [14, 15]. CT technology is characterized by no-contact, accurate, and fast. Yu et al. [16] reconstructed the digital 3D model of jointed sandstone with CT technology and applied the digital model to simulate the uniaxial compression process.

As for establishing the relationship between the permeability and the microscopic characteristics of rocks, most of the applicable permeability models are semiempirical ones due to the great discreteness and complexity of the microstructure. The K-C model, which is based on the Poiseuille equation (17), has been widely accepted by scholars. On the basis of the K-C model, many modified models have been proposed. Table 1 summarizes the main

TABLE 1: K-C model and its main modified model.

Scholars	Model	Definition of parameters
Kozeny [18], Carman [19]	$k = C_{kc}\varphi^3/(1-\varphi)^2$	$C_{kc} = c/8\tau^2s_0^2$
Rodriguez [20], Shih [21]	$k = C_{kc}\varphi^{n+1}/(1-\varphi)^n$	
Bayles [22]	$k = C_b\varphi^{2+n}/(1-\varphi)^2$	$C_b = c/8bs_0^2$
Costa [23]	$k = C_c\varphi^n/1-\varphi$	$C_c = cA_{l\mu}/b$

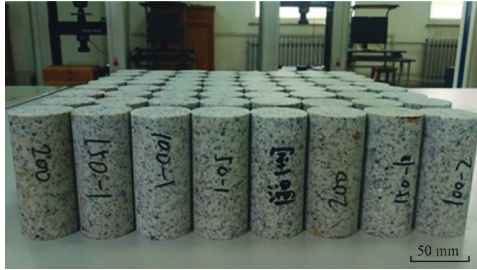


FIGURE 1: Rock specimen.

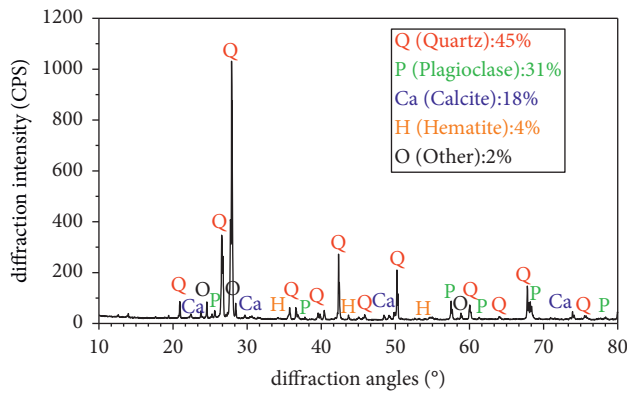


FIGURE 2: X-ray diffraction pattern of granite.

modified models and gives the definition of the empirical parameters. Although the permeability model, which reflects the relationship between macroscopic permeability and microscopic characteristics of rock, has become mature, there are few reports on the models of the variation of rock permeability with temperature after thermal treatment. Therefore, the purpose of this work is to establish the temperature-dependent permeability model of granite after high-temperature heating treatment.

(c is the geometrical equivalent factor, τ is tortuosity, s_0 is the specific surface area of particles, n is the cementation factor of Archie's equation, b is the tortuosity factor of Archie's equation, $A_{l\mu}$ is the sum of the total area of pores with diameters less than the $l\mu$).

2. Rock Specimen Preparation and Experiment

2.1. Rock Specimen Preparation. To reduce the heterogeneous of granite specimens, the granite was cored in a rock block from Hunan Province, China, at the depth of 50 ~ 70m underground. The specimen is drilled with a laboratory rig and made



FIGURE 3: Granite specimens after high-temperature heating treatment.

into cylindrical specimens with a diameter of 50 mm and a height of 100 mm for the gas permeability tests, as shown in Figure 1. Also, the upper and lower ends of the granite specimen were polished with sandpaper to ensure the degree of parallelism and verticality are less than 0.02 mm. The X-ray diffraction pattern of the granite is shown in Figure 2. The result shows that the specimens are made of quartz, plagioclase, calcite, hematite, and a small amount of other minerals.

2.2. Thermal Treatment. The heat treatment was carried out in the Rock Mechanics Laboratory of Wuhan University. The rock specimen is heated by a box-type furnace SX21012 made by Yahua Company. The heating step can be preset according to requirement, and it has a maximum heating temperature 1100 °C and a corresponding maximum error $\pm 1.0^\circ\text{C}$. The furnace chamber with a size of 250 mm \times 400 mm \times 160 mm is sufficiently large to heat 10 specimens simultaneously.

Twenty-five granite specimens were divided into five groups, and a group includes five granite specimens. The specimens were heated to 50 °C, 200 °C, 400 °C, 600 °C, and 800 °C at a rate of 10 °C/min. The temperature rises linearly to a specified value and then remains constant for 10 hours. The specimens were then naturally cooled to room temperature at a cooling rate of 10 °C/min and kept at room temperature for 24 hours before gas permeability tests were performed. Figure 3 shows granite specimens after heat treatment at different temperatures. As the temperature increases from 50 °C to 800 °C, the color of the rock specimen changes from bluish-gray to white.

2.3. Gas Permeability Test. The transient pulse decay method is widely used to measure gas permeability in low permeability materials, such as rock. The gas permeability of

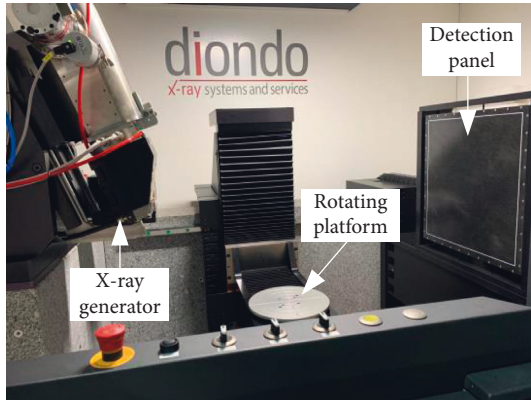


FIGURE 4: CT detection system.

granite at different temperatures was measured by a hydro-mechanical coupling system, autonomously designed by the Institute of rock and soil mechanics, and the Chinese academy of sciences. All tests are conducted at constant temperature (20°C).

First, the confining pressure of the chamber is maintained at 2.5 MPa. Nitrogen was inserted to maintain a pressure of 0.9 MPa in the upper chamber. The specimen was kept saturated in the triaxial cell of gas injection, and the gas injection was balanced at the lower chamber increasing to 0.9 MPa. Subsequently, the chamber pressure was increased to 6.95 MPa, and the effective confining pressure was maintained at 6.0 MPa. Finally, pulse attenuation tests were carried out under a hydrostatic state, and an injection 0.1 MPa brings the upper reservoir pressure to 1.0 MPa. In the process of tests, the upper and lower pressures are self-recorded by the computer every 5 seconds. Before tests, each specimen must be stored in an oven and dried at 50°C for at least three days.

Liu et al. [24] derived the expression of gas permeability in the transient-flow test. During pulse decay tests, the relation between the upper and lower differential pressure ΔP_0 at the beginning of the experiment and the upper and lower differential pressure $\Delta P(t)$ after time t of the experiment can be described as follows:

$$\frac{\Delta P(t)}{\Delta P_0} = e^{-st}, \quad (1)$$

$$s = \frac{Ak}{L\mu z} \left(\frac{1}{V_{up}} + \frac{1}{V_{dn}} \right),$$

where k is the gas permeability of the material, L , A are the length and cross-sectional area of the specimen, μ and z are the dynamic viscosity and the critical compressibility of the gas, which value is 1.80×10^{-5} Pa·s and $0.292 \text{ mm}^2 \cdot \text{C}^{-1}$, respectively, for nitrogen. V_{up} and V_{dn} are the volumes of upper and lower reservoirs, respectively. The gas permeability can be calculated by equation (1) and equation (2) using gas pressure data

3. Rock Microstructure Representation

3.1. CT Scanning. Internal microstructure of granite was obtained by a Diondo d2 high-resolution CT detection system, manufactured by German Diondogmbh, which had

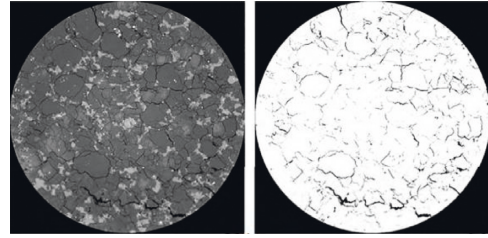


FIGURE 5: Cross-sectional gray CT image.

a spatial resolution of 20 μm . The CT detection system (Figure 4) comprises an X-ray beam, a detector panel, and a rotating platform. The X-ray beam penetrating the specimen is measured by an array of detectors. The X-ray is produced by electrons striking a Mo–W alloy target in an X-ray tube. The electron current is 80 IA, the accelerating voltage is 140 kV, and the scanning time is 4 s. The degree of X-ray attenuation depends on the density and the atomic numbers of the materials in the specimens (Savaş and Marva [25]).

Prescanning must be carried out before CT measurements. First, the granite specimen is placed on the rotating platform. Then, the granite specimen is prescanned, and the position of it is fine-tuned according to the receiving result of the detector panel. At the beginning of the measurement, the rotating platform rotates at a constant speed, and the computer collects data every fixed time. The X-ray attenuation matrix is obtained by X-ray scanning in different directions, and then, the gray-scale cross-sectional images of the granite specimen are obtained.

In order to ensure the measurement precision, the magnification is 200, and the minimum observable scale is 25 mm. Figure 5 shows a cross-sectional gray scale image result (256-order gray scale used in the study) obtained from this X-ray micro-CT scanning. It can be seen that the surface crack is clearly observed. This indicates that, in this study, X-ray micro-CT scanning has a high-resolution ability to obtain internal crack in granite material.

According to Lambert's law [9], the gray scale reflects the density of the mineral. So, the distribution of porous and various mineral components in granite can be identified by the gray scale.

3.2. 3D Micropore Structure Reconstruction Method. The internal pore or fracture in granite is a flow path, which determines its permeability. So, it is necessary to further process the obtained CT cross-sectional image to extract the pores or fractures. A method distinguishing rock matrix and rock fracture or pore was developed by Xiong et al. [26]. Figure 6 shows the fracture or pore results using this method, the fracture or pore microstructure in the granite is shown in black (Gray value = 0), and the granite matrix is shown in white (gray value = 1).

The digital image consists of a rectangular array of pixels. Each pixel is the region at the intersection of any horizontal and vertical scan lines, all of which are of equal width h . Therefore, each pixel can be considered a square element. The material structure captured in the cross-sectional CT

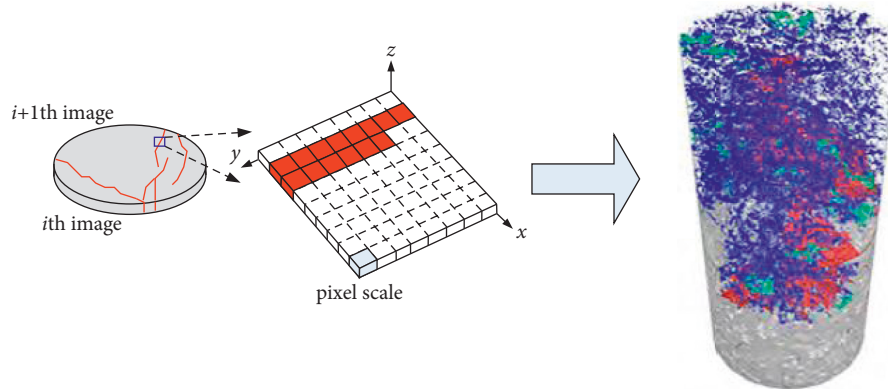


FIGURE 6: Schematic of three-dimensional reconstruction process of rock.

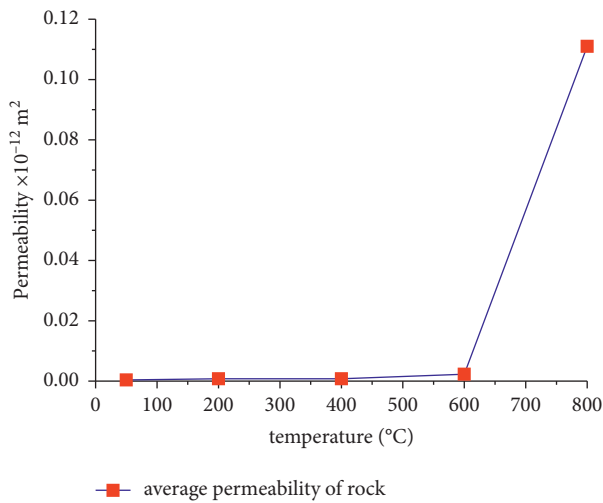


FIGURE 7: The influence of heating temperature on permeability.

image is assumed as that of a layer with a d height. Based on this, the granite microstructure represented by the image can be easily mapped to a layer of the cuboid grid of the same size, which is generated by a rectangular array of image pixels extending vertically. Figure 6 shows the generated 3D microstructure model.

4. Experiment Results

4.1. Permeability of Granite. The permeability of the granite after thermal treatment at different temperatures is shown in Figure 7. As shown in Figure 7, when the temperature is lower than 400°C , the permeability of granite changes a little. The temperature increases from 50 to 400°C , and permeability only increases from $3.8e-16$ to $7.6e-16 \text{ m}^2$. When the heating temperature is higher than 400°C , the permeability of granite increases exponentially. The permeability of granite for 800°C is 146 times higher than that of 400°C . It is indicating that temperature has a significant impact on permeability when heating temperature greater than 400°C .

4.2. 3D Micropore Structure Analysis. A three-dimensional reconstruction method was used to obtain the internal microstructure geometry structure of granites at different temperatures, as shown in Figure 8. As can be seen from Figure 8, when the temperature is lower than 400°C , the pores generated by thermal loading in granite are mostly microporous. When the temperature exceeds 400°C , the number of pores increases. When the temperature reaches to 800°C , the fracture going through the granite appears. It is predicted that the number of fractures increases as temperature increases. Figure 9 shows the volume proportion of microstructure in different volume intervals inside granite after thermal treatment at different temperatures. In terms of the proportion of microstructure in different volume intervals, when the temperature is lower than 400°C , the volume of microstructure in granite is mainly distributed in the range of $0.001-0.1 \text{ mm}^3$, the distribution curve of the volume proportion is similar, and the peak value is around 0.01 mm^3 . When the thermal treatment temperature rises to 600°C , the peak value of the volume distribution of the internal microstructure of granite moves to the right range of $0.1-1 \text{ mm}^3$, and the maximum thermal fracture pore volume is significantly increased compared with 400°C , which is located near 10 mm^3 . When the temperature reaches to 800°C , the peak value of the internal microstructure of granite appears at the right end, and the pore volume distribution in other sections is more even. The main reason for this situation is that the internal fractures develop rapidly under high temperature, and most of the isolated pores wrapped by minerals with poor thermal stability are connected with each other, thus forming large volume fractures. Finally, the pore distribution in each volume interval is relatively smooth, and the volume proportion of large volume connected fractures appears to the peak.

5. Temperature-Permeability Model and Its Verification

The Kozeny and Carman model (K-C model) and Costa model [27, 28] derived from the capillary bundle model are generally used to describe the permeability of porous and low-permeability rocks, which are expressed as

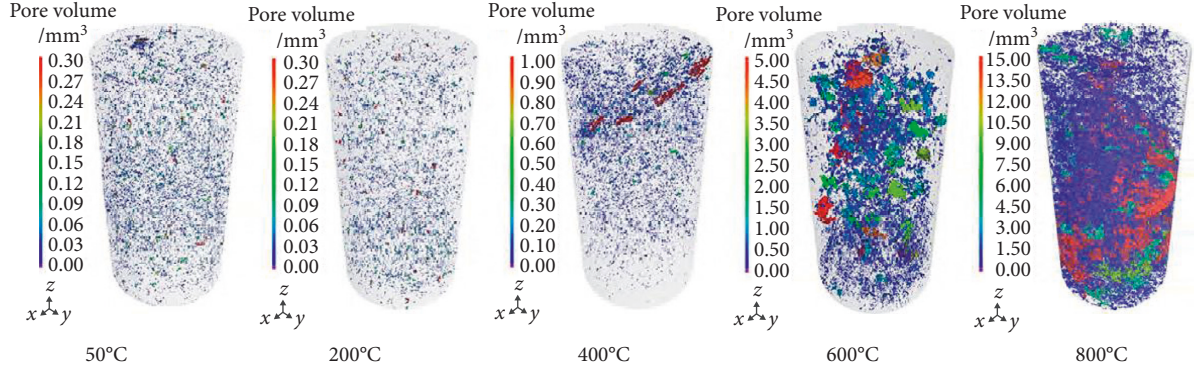


FIGURE 8: Rendering model of microfracture after thermal treatment at different temperatures.

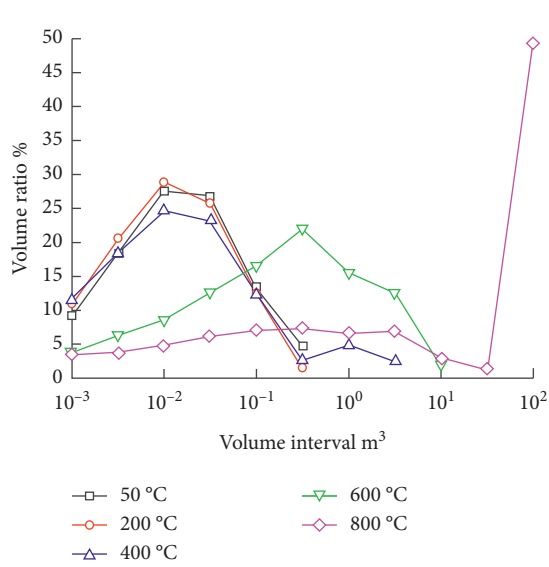


FIGURE 9: Proportion of microstructures in each volume interval of granite.

$$k = C_{K-C} \frac{\phi^3}{(1-\phi)^2}, \quad (2)$$

$$k = C_C \frac{\phi^n}{1-\phi},$$

where C_{K-C} and C_C are K-C coefficient and Costa coefficient, respectively. It is proved that the Costa model is more applicable for high pore rock [29, 30]. The pore in granite is assumed as Sierpinski shim and Menger sponge, and a fractal model of pore volume representing rock geometry can be obtained as

$$V(\geq r) = V_a \left[1 - \left(\frac{r}{L_2} \right)^{3-D} \right], \quad (3)$$

where $V(\geq r)$ is the pore volume whose pore size is greater than or equal to r . This parameter can be considered as CT scanning accuracy. V_a is the total volume of rock within the scale range L_2 , and D is the fractal dimension. Hence, the pore of rock ϕ is expressed as

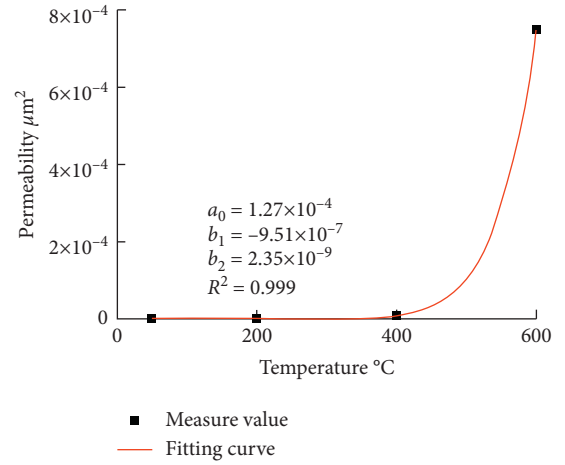


FIGURE 10: Fitting results of the temperature-permeability model.

$$\phi(\geq r) = \frac{V(\geq r)}{V_a} = 1 - \left(\frac{r}{L_2} \right)^{3-D}. \quad (4)$$

Substituting (4) into equation (4), a permeability model of granite under high temperature can be obtained as

$$k = C_C \left(\frac{L_2}{r} \right)^{3-D} \left[1 - \left(\frac{r}{L_2} \right)^{3-D} \right]^n. \quad (5)$$

Zhang et al. [31] studied the effects of thermal treatment temperature 25–1200 °C on fractal structure characteristics of granite, and their study demonstrates that the relationship between the fractal dimension D of granite and temperature T could be expressed as

$$D = a + b_1 T + b_2 T^2. \quad (6)$$

Hence, a temperature-dependent permeability model can be obtained as

$$k = C_C \left(\frac{L_2}{r} \right)^{a_0 + b_1 T + b_2 T^2} \left[1 - \left(\frac{r}{L_2} \right)^{a_0 + b_1 T + b_2 T^2} \right]^n. \quad (7)$$

The permeability data of granite after a high temperature of 50–600°C are used to fit (7). Figure 10 shows the relationship between permeability and temperature of granite.

As can be seen in Figure 10, fitting results show that the fitting degree of the new model is above 0.99, so the proposed model can be used to predict the permeability of granite after high temperature treatment. This proposed model has an important engineering significance. For example, the relationship between temperature and permeability of rock should be mastered in between geological storage of nuclear waste. Furthermore, the temperature-dependent permeability model of rock extends understanding of high-temperature rock mechanics.

6. Conclusion

The gas seepage tests and CT scanning of granite after different temperatures treatment were conducted to systematically study its evolution mechanism of the internal microstructure and permeability. A new semiempirical permeability model is proposed and verified by the experimental results, and the main conclusions are as follows:

- (1) Gas permeability test shows that the permeability of granite changes a little when the temperature of thermal treatment is lower than 400°C and increases exponentially when the temperature is greater than 400°C.
- (2) When the temperature is less than 400°C, the pores generated by thermal loading in granite are mostly microporous. When the temperature exceeds 400°C, the number of pores increases. When the temperature reaches 800°C, the fracture going through the granite appears.
- (3) Based on the Costa model, the granite temperature-dependent permeability model is deduced. The new model reflects the relationship between the temperature of thermal treatment and the permeability of granite. Finally, the new proposed permeability is verified by the gas permeability test results. The result shows that the proposed model has high accuracy to predict the gas permeability of granite after thermal treatment at different temperatures.

Data Availability

The data that support the findings of this study are available from the corresponding author upon reasonable request

Conflicts of Interest

The authors declare that they have no conflicts of interest.

Acknowledgments

This work was supported by the National Natural Science Foundation of China (Grant no. 42077243).

References

- [1] Z. C. Tang, Z. L. Wu, and J. Zou, "Appraisal of the number of asperity peaks, their radii and heights for three-dimensional rock fracture," *International Journal of Rock Mechanics and Mining Sciences*, vol. 153, Article ID 105080, 2022.
- [2] Z. Tang and M. Sun, "Mechanical properties of marble with varying slenderness ratios after high temperatures," *International Journal of Geomechanics*, vol. 22, no. 7, Article ID 04022088, 2022.
- [3] Z. C. Tang, Q. Z. Zhang, and J. Peng, "Effect of thermal treatment on the basic friction angle of rock joint," *Rock Mechanics and Rock Engineering*, vol. 53, no. 4, pp. 1973–1990, 2020.
- [4] Y. Y. Jiao, K. Wu, J. Zou et al., "On the strong earthquakes induced by deep coal mining under thick strata—a case study," *Geomechanics and Geophysics for Geo-Energy and Geo-Resources*, vol. 7, no. 4, p. 97, 2021.
- [5] S. Esmaeili, H. Sarma, T. Harding, and B. Maini, "Review of the effect of temperature on oil-water relative permeability in porous rocks of oil reservoirs," *Fuel*, vol. 237, pp. 91–116, 2019.
- [6] Z. C. Tang, M. H. Peng, and S. Xiao, "Basic friction angle of granite fracture after heating and rapid cooling treatments," *Engineering Geology*, vol. 302, Article ID 106626, 2022.
- [7] C. C. Xia, Z. C. Tang, W. M. Xiao, and Y. L. Song, "New peak shear strength criterion of rock joints based on quantified surface description," *Description Rock Mechanics and Rock Engineering*, vol. 47, no. 2, pp. 387–400, 2014.
- [8] D. Xue, H. Zhou, Y. Zhao, L. Zhang, L. Deng, and X. Wang, "Real-time SEM observation of mesoscale failures under thermal-mechanical coupling sequences in granite," *International Journal of Rock Mechanics and Mining Sciences*, vol. 112, pp. 35–46, 2018.
- [9] Q. Zhe, H. Fu, and X. Chen, "A study on altered granite meso-damage mechanisms due to water invasion-water loss cycles," *Environmental Earth Sciences*, vol. 78, no. 14, pp. 1–10, 2019.
- [10] F. Zhao, Q. Sun, and W. Zhang, "Fractal analysis of pore structure of granite after variable thermal cycles," *Environmental Earth Sciences*, vol. 78, no. 24, pp. 677–691, 2019.
- [11] E. W. Washburn, "The dynamics of capillary flow," *Physical Review*, vol. 17, no. 3, pp. 273–283, 1921.
- [12] W. Friesen and R. Mikula, "Fractal dimensions of coal particles," *Journal of Colloid and Interface Science*, vol. 120, no. 1, pp. 263–271, 1987.
- [13] H. Ranaivomanana, A. Razakamanantsoa, and O. Amiri, "Permeability prediction of soils including degree of compaction and microstructure," *International Journal of Geomechanics*, vol. 17, no. 4, Article ID 04016107, 2017.
- [14] H. Ni, J. Liu, B. Huang et al., "Quantitative analysis of pore structure and permeability characteristics of sandstone using SEM and CT images," *Journal of Natural Gas Science and Engineering*, vol. 88, Article ID 103861, 2021.
- [15] R. Lopes and N. Betrouni, "Fractal and multifractal analysis: a review," *Medical Image Analysis*, vol. 13, no. 4, pp. 634–649, 2009.
- [16] Q. Yu, S. Yang, P. G. Ranjith, W. Zhu, and T. Yang, "Numerical modeling of jointed rock under compressive loading using X-ray computerized tomography," *Rock Mechanics and Rock Engineering*, vol. 49, no. 3, pp. 877–891, 2016.
- [17] N. A. Mortensen, F. Okkels, and H. Bruus, "Reexamination of Hagen-Poiseuille flow: shape dependence of the hydraulic resistance in microchannels," *Physical Review*, vol. 71, no. 5, Article ID 057301, 2005.
- [18] J. Kozeny, "Ueber kapillare Leitung des Wassers im Boden," *Stizungsber. Akad Wiss Wien*, vol. 136, pp. 271–306, 1927.
- [19] P. Carman, "Fluid flow through granular beds," *Transactions of the Institution of Chemical Engineers*, vol. 15, pp. 150–167, 1973.

- [20] E. Rodriguez, F. Giacomelli, and A. Vazquez, "Permeability-porosity relationship in RTM for different fiberglass and natural reinforcements," *Journal of Composite Materials*, vol. 38, no. 3, pp. 259–268, 2004.
- [21] C. H. Shih and L. J. Lee, "Effect of fiber architecture on permeability in liquid composite molding," *Polymer Composites*, vol. 19, no. 5, pp. 626–639, 1998.
- [22] G. A. Bayles, G. E. Klinzing, and S. H. Chiang, "Fractal mathematics applied to flow in porous systems," *Particle & Particle Systems Characterization*, vol. 6, no. 1-4, pp. 168–175, 1989.
- [23] A. Costa, "Permeability-porosity relationship: a reexamination of the Kozeny-Carman equation based on a fractal pore-space geometry assumption," *Geophysical Research Letters*, vol. 33, no. 2, Article ID L02318, 2006.
- [24] Z. Liu, J. Shao, S. Xie, and J. Secq, "Gas permeability evolution of clayey rocks in process of compressive creep test," *Materials Letters*, vol. 139, pp. 422–425, 2015.
- [25] S. Erdem and M. A. Blankson, "Fractal-fracture analysis and characterization of impact-fractured surfaces in different types of concrete using digital image analysis and 3D nanomap laser profilometry," *Construction and Building Materials*, vol. 40, pp. 70–76, 2013.
- [26] F. Xiong, Q. Jiang, and C. Xu, "Fast equivalent Micro-scale pipe network representation of rock fractures obtained by computed tomography for fluid flow simulations," *Rock Mechanics and Rock Engineering*, vol. 54, no. 2, pp. 937–953, 2020.
- [27] F. Normant and C. Tricot, "Method for evaluating the fractal dimension of curves using convex hulls," *Physical Review*, vol. 43, no. 12, pp. 6518–6525, 1991.
- [28] D. A. Russell, J. D. Hanson, and E. Ott, "Dimension of strange attractors," *Physical Review Letters*, vol. 45, no. 14, pp. 1175–1178, 1980.
- [29] J. Hearst, P. Nelson, and F. Paillet, *Well Logging for Physical Properties*, McGraw-Hill, New York, 2000.
- [30] G. Archie, "The electrical resistivity log as an aid in determining some reservoir characteristics," *Transaction of American Institute of Mining, Metallurgical, and Petroleum Engineers*, vol. 146, no. 1, pp. 54–62, 1942.
- [31] Z. Zhang, F. Gao, Y. Gao, and X. Xu, "Fractal structure and model of pore size distribution of granite under high temperatures," *Chinese Journal of Rock Mechanics and Engineering*, vol. 35, no. 12, pp. 2426–2438, 2016.

Research Article

Differential Analysis and Prediction Optimization of Ground Surface Settlement Induced by Quasi-Rectangular Shield and Pipe Jacking Tunnelling

Xue Liu,¹ Peinan Li ,¹ Jun Liu,² Zeyu Dai,¹ Peixin Chen,³ Xiaoyong Kou,³ and Jie Fan³

¹College of Environmental Science and Engineering, Donghua University, Shanghai 201620, China

²College of Urban Railway Transportation, Shanghai University of Engineering Science, Shanghai 201620, China

³Shanghai Tunnel Engineering Co., Ltd., Shanghai 200232, China

Correspondence should be addressed to Peinan Li; lipeinan_tj@163.com

Received 16 May 2022; Accepted 2 July 2022; Published 23 August 2022

Academic Editor: Zhi Cheng Tang

Copyright © 2022 Xue Liu et al. This is an open access article distributed under the Creative Commons Attribution License, which permits unrestricted use, distribution, and reproduction in any medium, provided the original work is properly cited.

The shield method and pipe jacking method will impact the ground surface and surrounding settlement during tunnel construction. Due to their different tunnelling principles and their cross-section characteristics, the impact on the stratum is often different. To study the differences between the two construction methods on ground surface settlement, numerical simulations, Peck empirical formulas, and field measurement data were used for analysis and comparison in this work. Two correction coefficients α and λ are introduced for correction on the basis of the DOT Peck formula, and the analysis of sensitivity factors for the ground settlement for the two construction methods is carried out. The numerical simulation results show that the ground settlement induced by pipe jacking construction is smaller than that of the shield, and this simulation result is confirmed by the field measurement result. When λ is selected from 0.85 to 0.91 and α from 1 to 1.1 for the shield project, 1.2 to 1.4, and 1.4 to 1.6 for the pipe jacking project, the modified formula can better predict the ground surface settlement. According to the sensitivity factor analysis, grouting pressure and elastic modulus of grout material exert a more significant influence on pipe jacking construction. The retreat of the pipe section caused by the tunnelling pressure difference will lead to 0 mm ~ 1.93 mm fluctuation on the ground surface.

1. Introduction

With the acceleration of urbanization, the shield method and pipe jacking method are widely used in urban subway construction projects. Although the shield method and pipe jacking method may cause disturbances to the surrounding stratum, their respective construction characteristics can meet the needs of different projects [1, 2]. The ground disturbance caused by shield and pipe jacking tunnelling has been an important research topic. Many scholars have done a lot of research on the ground disturbance caused by the tunnelling of shield and pipe jacking.

For the ground settlement caused by shield or pipe jacking engineering, the theoretical analysis method [3, 4], empirical formula method [5–8], and numerical simulation method [9, 10] are usually used to study it. In terms of shield ground

settlement, Fang et al. [11] proved the influence of tunnel depth and ground loss rate on longitudinal ground settlement caused by shield construction through a series of model tests. Accordingly, a prediction formula for the final surface longitudinal settlement of shield tunnelling is established. Zhou et al. [12] revised the prediction formula for ground settlement troughs (Peck's formula) based on the field data of a double tunnel project. Also, the prediction formula for the ground settlement caused by the construction of a double tunnel was derived and validated. Hu et al. [13] studied the effect of water content in sandy soils on the distribution and range of surface and subsurface settlement induced by shields using model experiments and numerical simulations. Based on a large number of field engineering and model test data, Lu et al. [14] proposed a formula to predict the maximum ground settlement with tunnel depth and constructed a

Gaussian function to predict the transverse ground settlement. Wang et al. [15] introduced a case of predicting ground settlement caused by a double shield tunnel in Copenhagen using analytical and numerical simulation methods. Moeinossadat and Ahangari [16] used the finite difference method (FDM) to construct a numerical intelligent model for maximum ground settlement (S_{\max}) instead of numerical simulation. In the study of ground surface settlement caused by pipe jacking construction, Ma et al. [17] studied the area disturbed by pipe jacking construction. Studies have shown that surface displacement is the coupling effect of soil and forward propulsion, friction, and ground loss. There are some other factors in the tunnelling process of pipe jacking [18, 19]. For example, construction parameters, ground loss rate, and pore water pressure dissipation will affect the surface settlement. In the construction process of the pipe jacking method, the tunnel pipe section has been in a “motion” state under the thrust provided by the hydraulic cylinder in the originating well, resulting in a large disturbance of the surrounding strata. The traditional Peck formula has poor prediction accuracy for ground settlement caused by pipe jacking construction. Therefore, Yang and Li [20] proposed a modified Peck formula based on the characteristics of the repeatedly disturbed strata by the pipe jacking method and the field measurement data. But Yang et al. research results are based on small pipe jacking projects, which are not suitable for large section pipe jacking projects. Tang et al. [21] compared the settlement of practical engineering, the fitting results of the Peck formula, and the settlement predicted by random medium theory. The prediction range of pipe jacking settlement through width is clarified through research, and suggestions are put forward for the prediction method of large rectangular pipe jacking settlement. Ma et al. [22] investigated the effect of tunnel burial depth variation on the ground settlement distribution characteristics caused by pipe jacking construction via 3D numerical simulation. Researchers investigated the surface settlement induced by the shield method and pipe jacking method from various angles, but there are few research results about the differences between the shield method and pipe jacking method on surface settlement, especially in the same stratum.

Based on the project of Hangzhou Sijiqing Metro Line 9, a three-dimensional finite element model of shield method and pipe jacking method is established in this study. Combining the field measurement data and simulation results, the differences in ground surface settlement induced by shield construction and pipe jacking construction in the same stratum were studied for comparison and analysis. At the same time, the double-o-tube (DOT) Peck formulas are optimized by using the numerical simulation results and field measurement data, and sensitivity factors of surface settlement caused by two tunnelling methods are studied to guide future projects.

2. Engineering Background

2.1. Engineering and Geology. The project interval is located at the east side of the intersection of Jiefang East Road and Qiutao Road, which is arranged along Jiefang East Road in

an east-west direction. The interval crosses Qiushi viaduct and Xinkai River on Jiefang East Road. The project area is divided into two intervals: from the Sijiqing Station to the middle well is the quasi-rectangular pipe jacking interval, and from the middle well to the receive well is the quasi-rectangular shield interval, as shown in Figure 1. One $11.83\text{ m} \times 7.27\text{ m}$ earth pressure balance pipe jacking/shield dual-mode tunnelling machine is used for the construction, see Figure 2. The tunnelling machine starts from the Sijiqing Station, travels west along Jiefang East Road, crosses the Qiushi viaduct, and then arrives at the middle well. The dual-mode tunnelling machine is received from the middle well and reformed into a shield machine. From the middle well, the shield method will be used to construct the tunnel. It will be constructed along Jiefang East Road to the west, cross the Xinkai River, and then be received at the receive well.

2.2. Surface Settlement Measure Scheme. Due to the large cross section of the tunnel construction, the disturbance of the stratum generated by the construction is also large. According to the surrounding environment and geological conditions, transverse measurement sections perpendicular to the tunnel axis are installed. Transverse measurement sections are placed in the originating area, receiving area and the parts with poor geological conditions that may produce excavation surface collapse or excessive surface deformation. Ten groups of measurement sections are set for the pipe jacking interval, and twenty-one groups of measurement sections are set for the shield interval. Each group of cross sections is symmetrically arranged along the central axis of the tunnel with a total of 11 measurement points. The spacing of measurement points is 3 m, 6 m, 12 m, 24 m, and 32 m (adjusted according to the actual situation on-site) on the outside of the tunnel center axis. The measurement sections are labeled as DBC- n , where DBC is the representative measurement project code and n is the ring number, as shown in Figure 3.

3. Differential Analysis of Surface Settlement

3.1. Numerical Modeling and Parameters

3.1.1. Model Size and Boundary. The size of the numerical model has a certain influence on the rationality and efficiency of the calculation results. To guarantee that the analysis results are not affected by boundary effects, and considering both the accuracy and efficiency of the model, the size of the shield model is chosen to be 84 m in X direction, 172 m in Y direction, and 42 m in Z direction. The model size of the pipe jacking is selected as 84 m in X direction, 67 m in Y direction, and 42 m in Z direction. The model's nodes on the two boundary surfaces of the X and Y directions set fixed constraints on the X and Y directions. The nodes on the bottom of the model set fixed constraints on the X , Y , and Z directions are shown in Figures 4 and 5.

The length from Sijiqing Station to the middle well is 67.2 m, the interval's maximum longitudinal grade is -0.2% , and the burial depth of the tunnel is 10.2 m \sim 11.2 m. The strata traversed by the machine are mainly: ④4 sandy silt,



FIGURE 1: Tunnel location plan.

③5 sand with sandy silt, and ③7 sandy silt. The length of the middle well to the receive well is 163.9 m. The minimum plane radius of the interval is 700 m, the maximum longitudinal grade is -0.2% , and the burial depth of the tunnel is 10.9 m \sim 11.4 m. The stratum traversed by the machine is mainly: ③4 sandy silt, ③5 sand with sandy silt, and ③7 sandy silt, see Figure 3.

The shield machine is reformed from the pipe jacking machine in Figure 2. Both the shell thickness of the shield machine and the pipe jacking machine are 0.06 m. The shell of the machine is simulated by plate-shell elements as well as the tunnel lining. It is worth noting that the tunnel lining size of the pipe jacking and the shield are the same, but the shield tunnel has a neutral pillar see Figure 4, and the pipe section has no neutral pillar see Figure 5. In the two models, the tunnel size is $11.7\text{ m} \times 7.6\text{ m}$ and the burial depth of the tunnel is 10.7 m. To simulate the ground volume loss caused by excavation as shown in Figure 6 the equivalent layer of pipe jacking is set to 6 cm and the shield is set to 20 cm [23].

3.1.2. Calculating Parameters. This paper assumes that the stratum material in the model is continuous isotropic elastic-plastic material. In the numerical simulation process of deep foundation pit excavation and large section excavation engineering, Mohr–Coulomb constitutive will have a large uplift, which affects the rationality of the simulation results. Therefore, this paper adopts the modified Mohr–Coulomb (MMC) constitutive model provided by the finite element software. This constitutive model is improved on the basis of the Mohr–Coulomb constitutive model, and it is especially suitable for sand materials with friction characteristics.

The shield shell and lining structure adopt a linear elastic constitutive model, and the lining thickness of the quasi-rectangular pipe jacking tunnel and shield tunnel is 650 mm. The shield's segments are assembled into rings, and the pipe jacking's lining is poured with C50 concrete. As the lining strength of the shield is lower than that of pipe jacking, the corresponding reduction is made. The initial elasticity modulus of the shield grout material is 0.9 MPa. It can reach 4 MPa after 24 hours, while the modulus of elasticity of the

pipe jacking grout is 0.6 MPa since it does not harden and the grout is thinner than the shield. The specific structural parameters are given in Table 1, and the stratum material parameters are given in Table 2.

3.1.3. Simulation Process. In order to simulate the shield and pipe jacking construction process under real conditions, the stepwise method based on the lining ring width is used in the numerical simulation. The shield method assembles the segments into a ring during tunnelling, and synchronous grouting is carried out when the segment assembly is completed. The shield method and the pipe jacking method are similar during the early stages of the simulation process, the shield grout material will gradually harden over time, while the grout material of the pipe jacking will not harden. The duration of grout hardening is set to be 5 rings. When the number of excavation rings exceeds 5 rings, the short-term hardened grout material (0.9 MPa) of the N -5th ring (N means the number of rings being excavated) is replaced by the long-term hardened grout material (4 MPa).

During the jacking process, the grout material will be injected between the pipe section and the stratum, which can reduce friction and support the stratum above the pipe section. In the whole construction process, the grout material will be continuously supplemented to hold pressure. The process of numerical simulation is shown in Figure 7.

3.2. Differential Analysis of Settlement for Quasi-Rectangular Shield and Pipe Jacking

3.2.1. Analysis of Numerical Simulation Results. During the tunnelling process, the pressure applied on the excavation face is equal to the static Earth pressure of the soil ahead of the cutter head, which is 145 kPa at the uppermost of the excavated surface. Both the shield grouting pressure and the pipe jacking grouting pressure applied by the machine are set to 220 kPa, which corresponds to the Earth pressure over the tunnel.

The overall final ground surface settlements of the shield and pipe jacking model are shown in Figure 8, and the final ground surface settlements of the shield and pipe jacking model are 17 mm and 25 mm, respectively. In the shield and pipe jacking model, a ground surface transverse section above the excavation surface is selected as the measurement section. Figures 9 and 10 show the ground settlement values of shield and pipe jacking in each stage of gradual excavation. Where, “before arrival” indicates that the tunnelling machine is 7.5 m away from the excavation face, and “arrival” indicates that the machine reaches the excavation face. It can be seen from Figure 10 that the ground surface settlement curves caused by shield and pipe jacking are similar to the Peck settlement curve. The surface settlement of the two mainly occurs after the machine's tail is away from the measurement section, and the settlement caused by pipe jacking in each stage is much smaller than that caused by the shield. When crossing the measurement section, the ground settlement caused by the pipe jacking method reaches 3.6 mm, while that caused by the shield method reaches

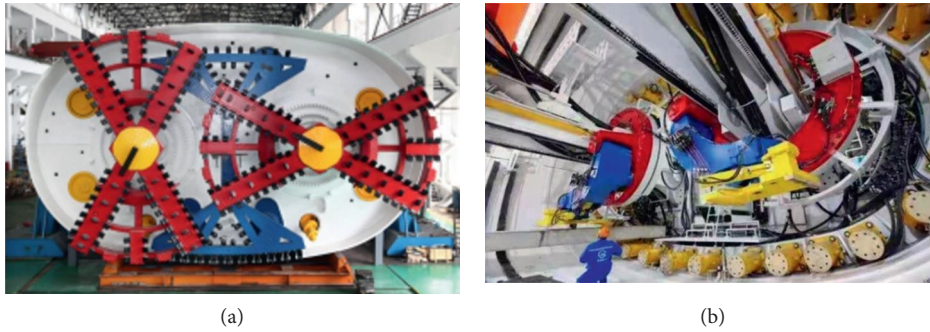


FIGURE 2: Quasi-rectangular earth pressure balance pipe jacking/shield dual-mode tunnelling machine: (a) The cutter head of dual-mode tunnelling machine. (b) Reformed shield segment assembly machine (pipe jacking machine mode without segment assembly machine).

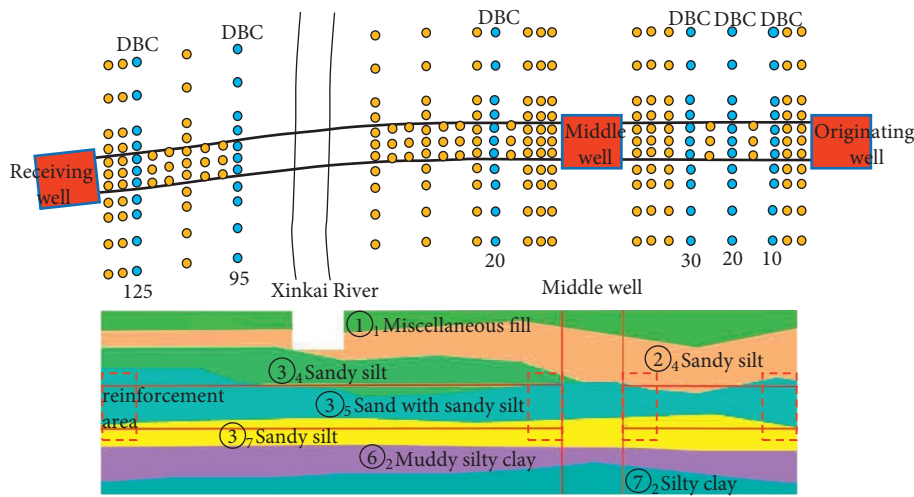


FIGURE 3: Stratum profile and field measurement section.

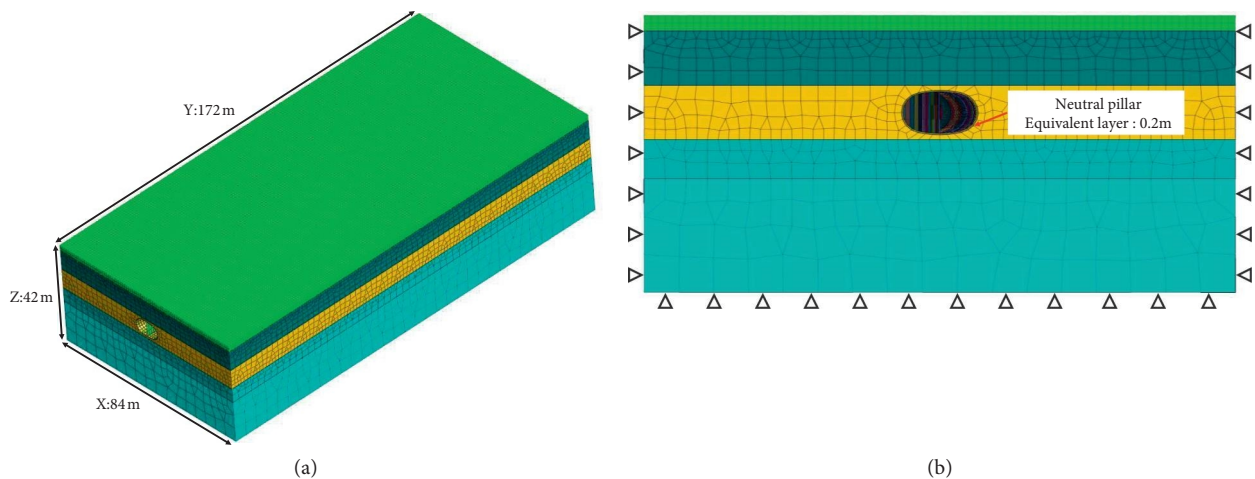


FIGURE 4: Shield model size and boundary conditions: (a) Shield model size. (b) Shield stratum and boundary condition.

7.4 mm. It can be seen that shield construction will cause greater ground settlement than pipe jacking construction. After excavation, the final settlement generated by the pipe jacking method is 17.4 mm, and the final settlement

generated by the shield method is 25.4 mm. There is little difference in the width of the settlement trough between the two, and the maximum influence range is about 3.5 times the width of the tunnel, namely, 40 m.

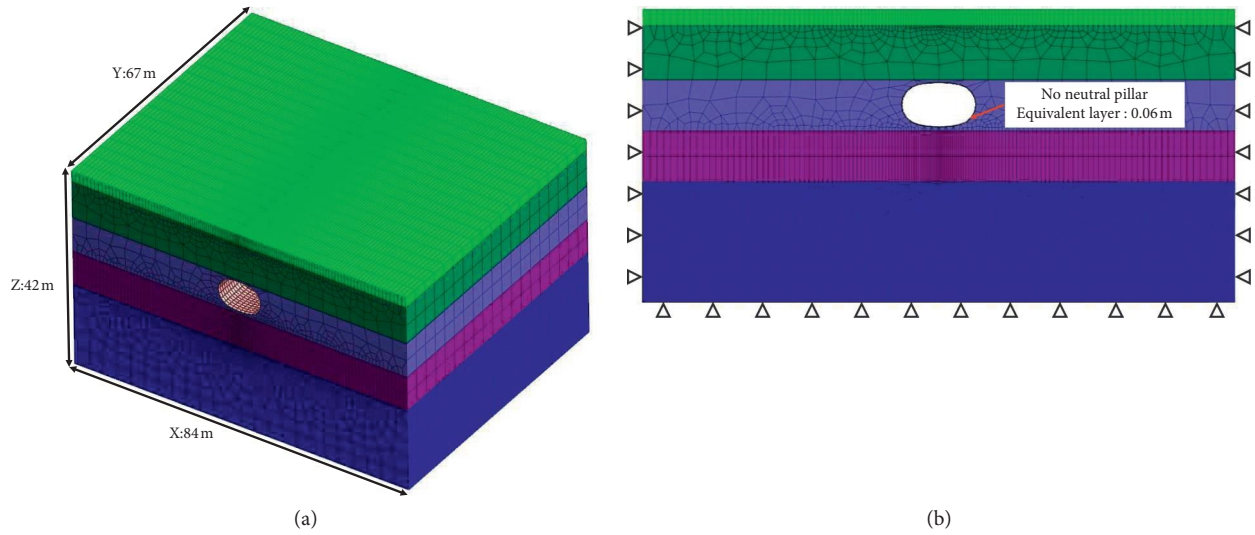


FIGURE 5: Pipe jacking model size and boundary conditions: (a) Pipe jacking model size. (b) Pipe jacking stratum and boundary condition.

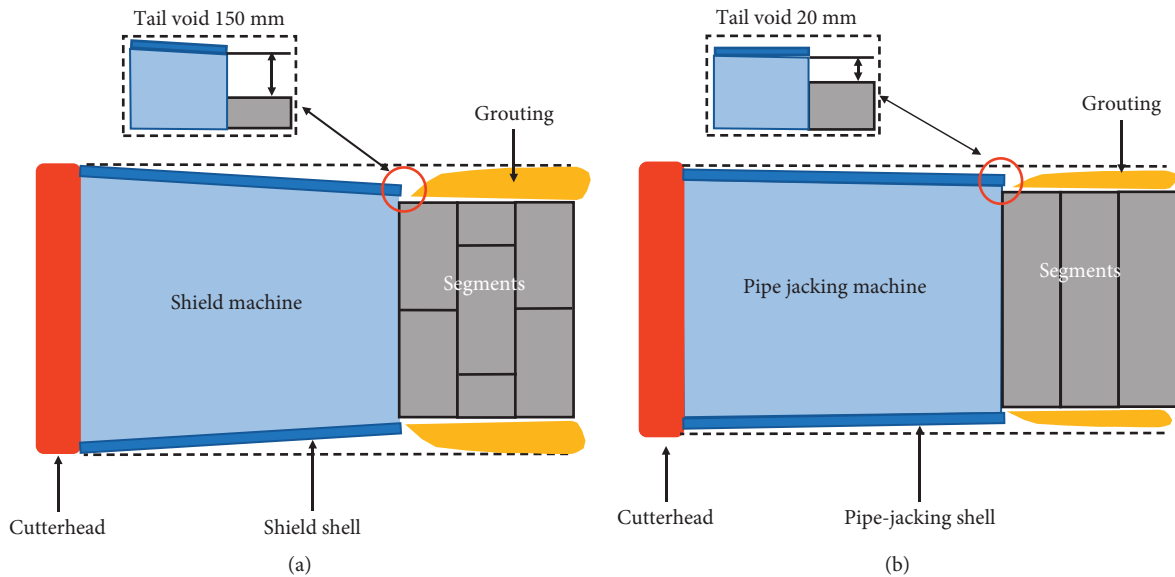


FIGURE 6: Tail void of shield and pipe jacking: (a) Shield tail void. (b) Pipe jacking tail void.

TABLE 1: Model size and structural parameters.

Name	X (m)	Y (m)	Z (m)	E (GPa)	Neutral pillar	Reduction factor	Equivalent layer (m)
Shield	172	67	42	20.7 (C50)	Yes	0.6	0.2
Pipe jacking	84	67	42	34.5 (C50)	No	1.0	0.06

3.2.2. Comparison of Numerical and Field Measurement Results. The shield machine will pass through the Xinkai River area during the tunnelling process (see Figure 3). To eliminate the influence of this area, the measurement sections of the Xinkai River and the originating area are ignored. Three measurement sections, DBC-20, DBC-95, and DBC-125, are selected for analysis. The final ground settlement of the shield is in the range of 23.1 mm–24.5 mm, and the numerical simulation value of 25.4 mm fitted the field measurement data well as shown in

Figure 11. There was no significant difference between the width of the settlement trough at the field measurement points and the numerical simulation. At the same time, as shown in Figures 11 and 12, the surface settlement of the shield measured in the field is significantly larger than that of the pipe jacking, which is in agreement with the numerical simulation results.

The final surface settlement data of three measurement sections of DBC-10, DBC-20, and DBC-30 in the pipe jacking interval are selected for analysis, and the results of

TABLE 2: Stratum physical parameters.

Stratum	K_0	γ (kN/m ³)	E_s (MPa)	ν	C (kPa)	φ (°)
①1 miscellaneous fill	0.50	17.50	3.00	0.33	8.00	15.00
②4 sandy silt	0.52	19.20	6.00	0.34	4.00	26.00
③4 sandy silt	0.45	19.20	14.00	0.32	6.00	30.00
③5 sand with sandy silt	0.37	19.70	10.00	0.28	5.00	34.00
③7 sandy silt	0.52	19.40	15.00	0.31	7.00	24.00
⑥2 muddy silty clay	0.38	19.90	4.00	0.27	12.00	10.00
⑦2 silty clay	0.45	18.20	8.50	0.34	10.00	16.00

Here ①1 represents the first layer in the first layer of the stratum and ②4 represents the fourth layer in the second layer of the stratum, etc.

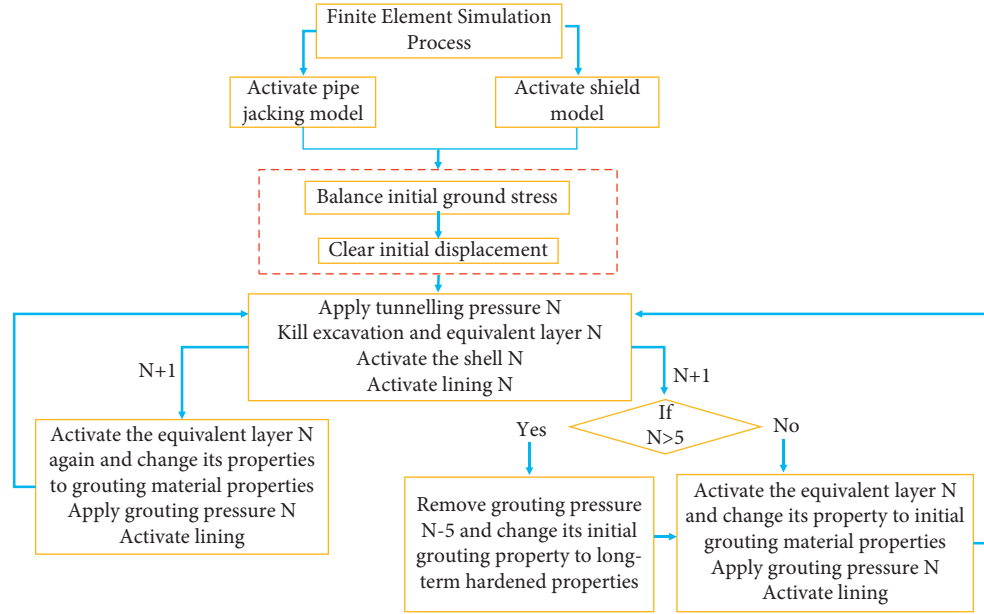


FIGURE 7: Simulation process.

numerical simulation are compared with the field measured surface settlement of pipe jacking. The results are shown in Figure 12. The final settlement measured in the field is 13.6 mm ~ 17.4 mm, which is slightly smaller than the 17.43 mm of numerical simulation. The width of the settlement trough of the numerical simulation curve is non-significant with the field measurement point, and the prediction effect of the numerical simulation is generally good.

The ground surface settlement data of the pipe jacking DBC-20 ring, shield DBC-95 ring measurement section center point (Figure 3), and the corresponding location points in the model are selected. As we can see from Figure 13, after the tunnelling machine passes the measurement point position the pipe jacking's final settlement is about 14 mm, which is smaller than the simulation result, and the settlement speed is also slower than the simulation result. The measured final settlement result of the shield is about 22 mm, which is smaller than the simulation result, and the settlement speed of the measurement results is in general agreement with the simulation results settlement speed. This is mainly due to the fact that the pipe jacking's grouting has a pressure-holding effect, so the stabilization of the final settlement

will be delayed, when there is uplift at the surface. The shield grouting has no pressure-holding effect so the settlement speed will be faster than the pipe jacking after the uplift occurs.

4. Predictive Optimization Model and Method

The total settlement profile of a quasi-rectangular tunnel is symmetrical Gaussian distribution along the tunnel axis. The classical Peck formula is no longer applicable since the difference between quasi-rectangular tunnel and circular tunnel. Zhang et al. [24] found that the settlement curve of the quasi-rectangular tunnel was between the circle Peck formula and the DOT Peck formula. By using the circle Peck formula (formula (1)) and the DOT Peck formula (formula (3)), the formulas (formulas (5) and (6)) of the surface loss rate corresponding to the maximum ground settlement are derived. The formulas (5) and (6) are used to calculate the critical ground loss rate of the circle and DOT tunnels under different buried depths, which use 30 mm as the control index of the maximum ground settlement value. The ground loss rate corresponds to the control index S_{\max}^k (the maximum ground settlement), which is called the critical ground loss rate δ . The final results are shown in

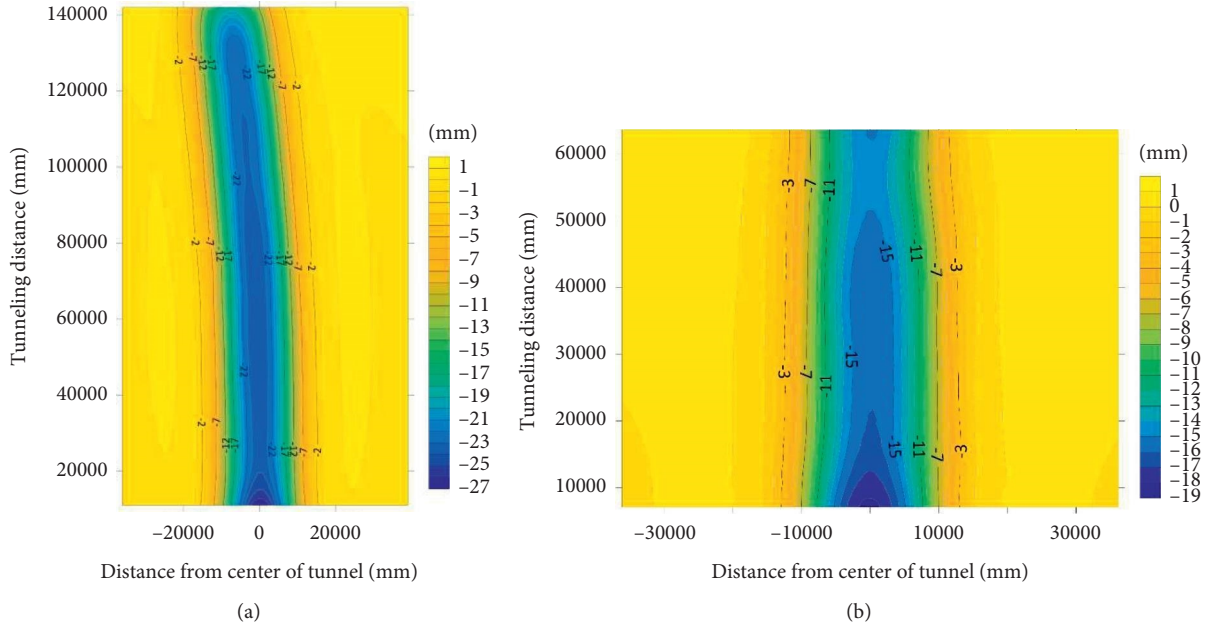


FIGURE 8: Final ground surface settlement contourline of shield and pipe jacking by numerical simulation: (a) Final settlement contourline of the shield. (b) Final settlement contourline of pipe jacking.

Table 3 and Figure 14. The critical ground loss rate δ of quasi-rectangular tunnels should be between the two, namely, $\delta_2 < \delta < \delta_1$. When the ground loss rate of quasi-rectangular tunnel is controlled below the critical value, the maximum ground settlement value can meet the control index of 30 mm.

Circular:

$$S(x) = \frac{V_s}{\sqrt{2\pi} \times i} \times \exp\left(-\frac{x^2}{2i^2}\right), \quad (1)$$

$$S_{\max} = \frac{V_s}{\sqrt{2\pi} \times i}, \quad (2)$$

DOT:

$$S(x) = \frac{V_s}{\sqrt{2\pi} \times i} \times \exp\left(-\frac{(x+2.3)^2}{2i^2}\right) + \frac{V_s}{\sqrt{2\pi} \times i} \times \exp\left(-\frac{(x-2.3)^2}{2i^2}\right), \quad (3)$$

$$S_{\max} = \frac{2V_s}{\sqrt{2\pi} \times i} \times \exp\left(-\frac{2.3^2}{2i^2}\right), \quad (4)$$

In the formulas, $S(x)$ is the ground surface settlement at the transverse distance from the center line of the DOT tunnel x , unit m. i is the width coefficient of settlement trough, unit m. V_s is DOT shield tunnel unit length ground loss, unit m^3/m .

$$\delta_1 = S_{\max}^k \times \sqrt{2\pi} \times \frac{i}{V}, \quad (5)$$

$$\delta_2 = S_{\max}^k \times \sqrt{2\pi} \times i \times \frac{\exp(2.3^2/2i^2)}{2V} \quad (6)$$

$$i = r \times \left(\frac{Z}{2r}\right)^{0.8}. \quad (7)$$

In the formulas, i is the width coefficient of settlement trough, unit m. r is the tunnel excavation radius, unit m. The noncircular tunnel can be calculated according to $r = \sqrt{W/\pi}$, W for the tunnel excavation area is shown in Figure 15. Z is the buried depth of the tunnel axis, unit m.

4.1. Peck Formula Optimization of Quasi-Rectangular Shield.

The integration of the DOT Peck formula (formula (3)) leads to formula (8), and it can be concluded that the area of the settlement trough of the DOT Peck formula is twice the V_s . Thus, the relationship between V_{sf} (Back calculation of ground losses from numerical simulation results) and V_s of DOT Peck formula can be expressed by formula (9). The predicted surface settlement curve in the numerical simulation is further back-calculated to yield a ground loss rate δ_f , which is 0.7% for the shield and 0.4% for the pipe jacking.

The back-calculated shield ground loss rate ($\delta = 0.35\%$) from the numerical simulation results is brought into the DOT Peck formula, and the calculated results are shown in Figure 16. The curve fitted by the DOT Peck formula is

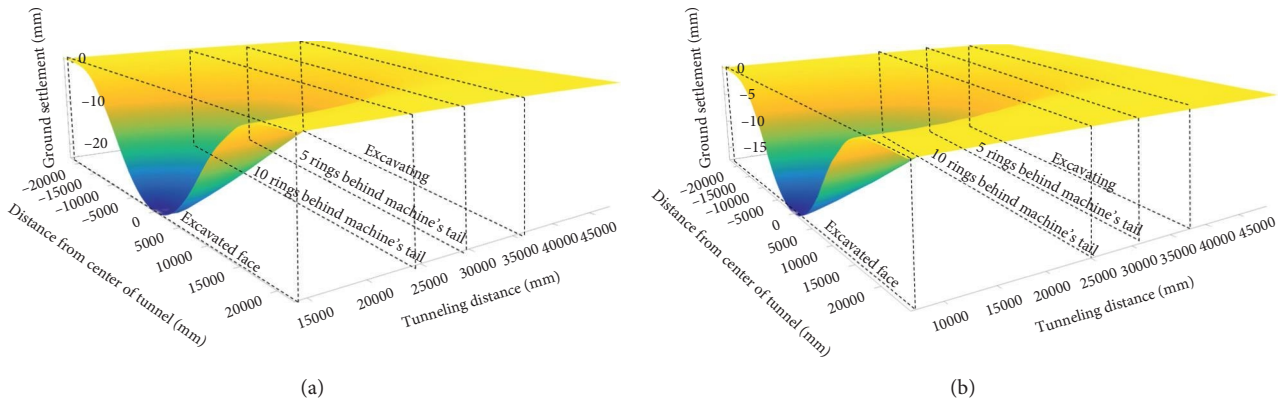


FIGURE 9: 3D surface settlement during excavation by shield and pipe jacking in numerical simulation: (a) 3D surface settlement during shield excavation. (b) 3D surface settlement during pipe jacking excavation.

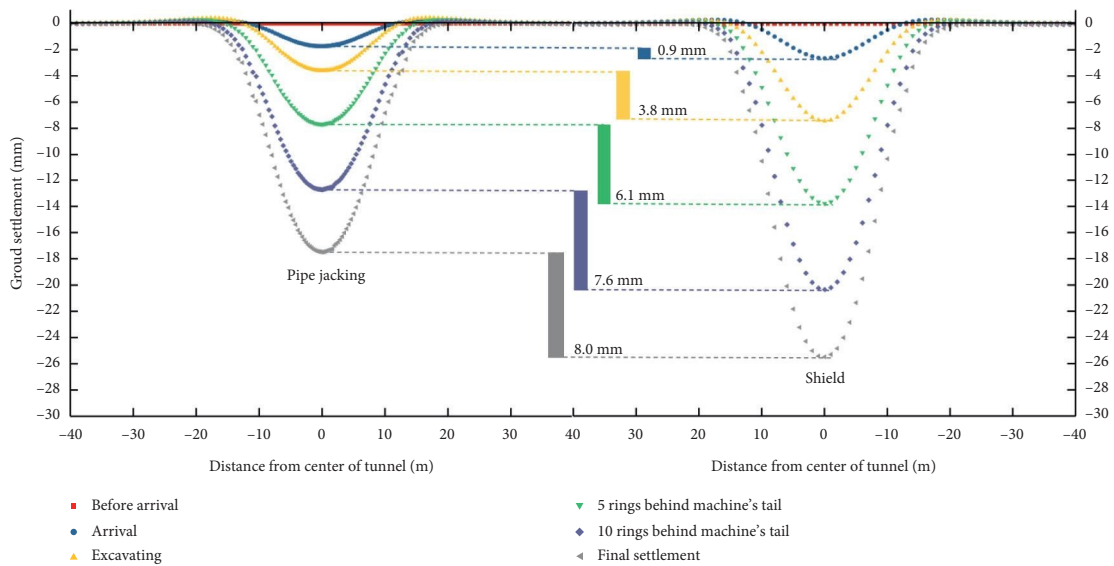


FIGURE 10: Transverse ground surface settlement of pipe jacking and shield in each stage.

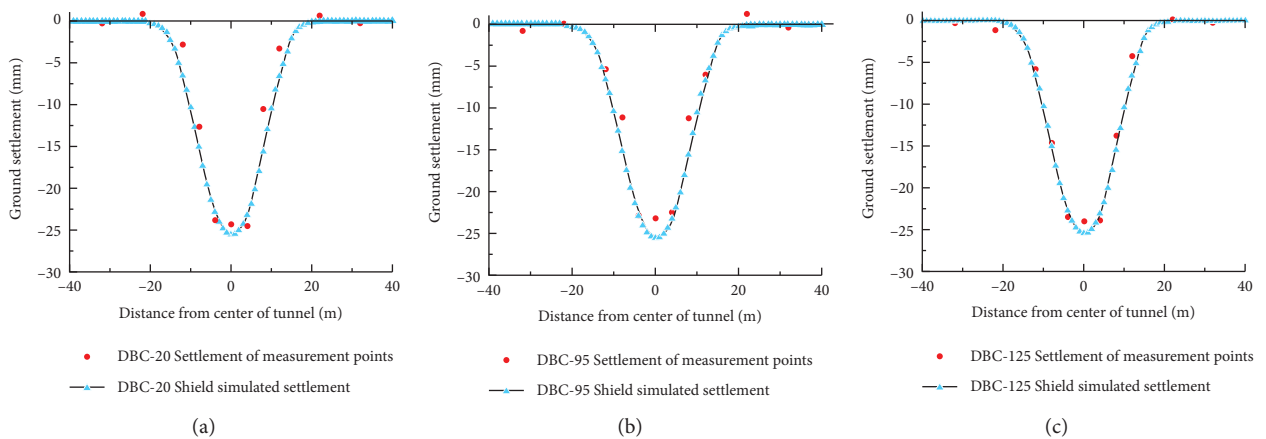


FIGURE 11: Final ground surface settlement of shield field measurement: (a) DBC-20. (b) DBC-95. (c) DBC-125.

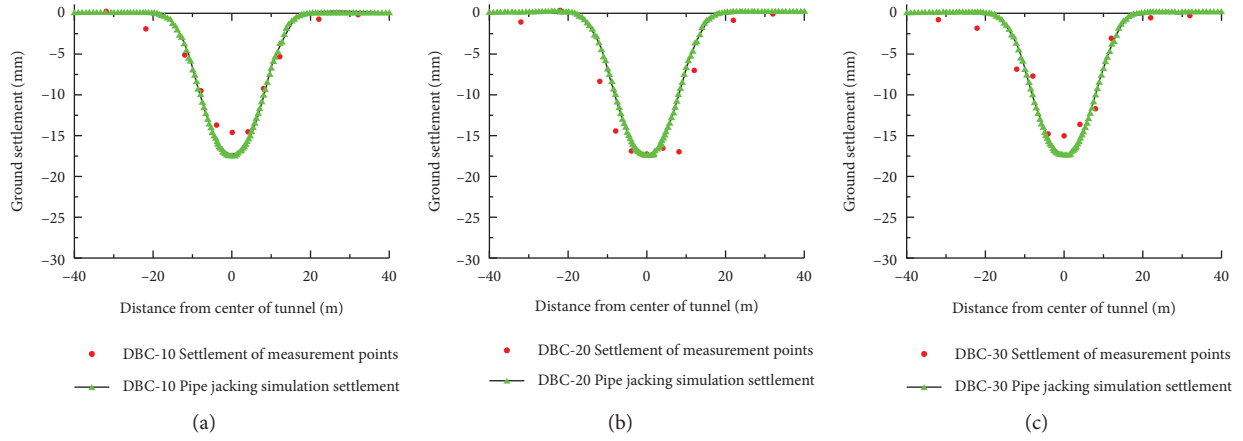


FIGURE 12: Final ground surface settlement of pipe jacking field measurement: (a) DBC-10. (b) DBC-20. (c) DBC-30.

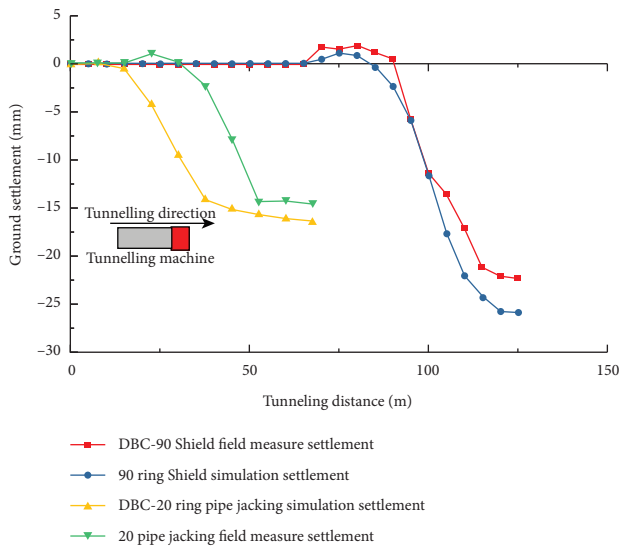


FIGURE 13: Longitudinal ground surface settlement of shield and pipe jacking.

6–8 mm larger than the measured surface maximum settlement. Therefore, the DOT Peck formula needs to be corrected to better fit the ground settlement of the shield. Because the curve shape fitted by the DOT Peck formula is related to the ground loss rate δ and the settlement trough width coefficient i . Therefore, based on the existing DOT Peck formula, two correction coefficients λ (correction coefficient of ground loss rate) and α (correction coefficient of settlement trough width) are proposed to optimize the formula (formula (10)–(13)). It can be seen from Figure 16 that when λ is 0.85~0.91 and α is 1~1.1, the correlation coefficient R of the fitting curve is 0.97~0.98. This shows that the modified formula can more accurately predict the surface settlement induced by quasi-rectangular shield tunnelling. Therefore, to achieve a better prediction effect, it is recommended to use the corresponding correction coefficient when using the range of ground loss rate δ recommended in Table 3.

$$\int_{-\infty}^{+\infty} S(x)dx = \int_{-\infty}^{+\infty} \frac{V_s}{\sqrt{2\pi} \times i} \times \exp\left(-\frac{(x+2.3)^2}{2i^2}\right) + \frac{V_s}{\sqrt{2\pi} \times i} \times \exp\left(-\frac{(x-2.3)^2}{2i^2}\right) dx = 2V_s, \quad (8)$$

$$V_{sf} = \pi r^2 \delta_f = 2V_s = 2\pi r^2 \delta. \quad (9)$$

Optimised DOT Peck formula for quasi-rectangular tunnel:

$$S(x) = \frac{V_{sx}}{\sqrt{2\pi} \times i_x} \times \exp\left(-\frac{(x+2.3)^2}{2i_x^2}\right) + \frac{V_{sx}}{\sqrt{2\pi} \times i_x} \times \exp\left(-\frac{(x-2.3)^2}{2i_x^2}\right), \quad (10)$$

$$V_{sx} = \lambda \cdot \delta \cdot \pi \cdot r^2 = \delta_x \cdot \pi \cdot r^2, \quad (11)$$

$$\delta_x = \lambda \cdot \delta, \quad (12)$$

$$i_x = \alpha \cdot i. \quad (13)$$

Here, δ_f is the ground loss rate back-calculated from the numerical simulation results, and δ is the ground loss rate in the DOT Peck formula. δ_x is the corrected ground loss rate, i_x is the corrected settlement trough width coefficient, unit m .

4.2. Peck Formula Optimization of Quasi-Rectangular Pipe Jacking. The ground loss rate ($\delta = 0.2\%$) is back-calculated based on the numerical simulation results of pipe jacking, and it can be found that the settlement trough fitted by the measured data of pipe jacking is wider than that fitted by the DOT Peck formula (Figure 17). Similarly, in order to better let the DOT Peck formula predict the ground settlement of the pipe jacking. Two correction coefficients λ and α are used to optimize the existing DOT Peck formula (formula (10)–(13)). As shown in Figure 17, when λ is in the range of 1.2~1.4 and α is in the range of 1.4~1.6, the modified

TABLE 3: The critical ground loss ratio of different tunnel depths [24].

Axis buried depth Z (m)	Width coefficient of settlement trough i (m)	Critical ground loss rate δ_1 (%)	Critical ground loss rate δ_2 (%)
6	3.29	0.344	0.194
7	3.73	0.389	0.214
8	4.15	0.433	0.233
9	4.56	0.476	0.253
10	4.96	0.518	0.273
11	5.35	0.559	0.292
12	5.73	0.599	0.311
13	6.11	0.639	0.330
14	6.49	0.678	0.349
15	6.86	0.716	0.367

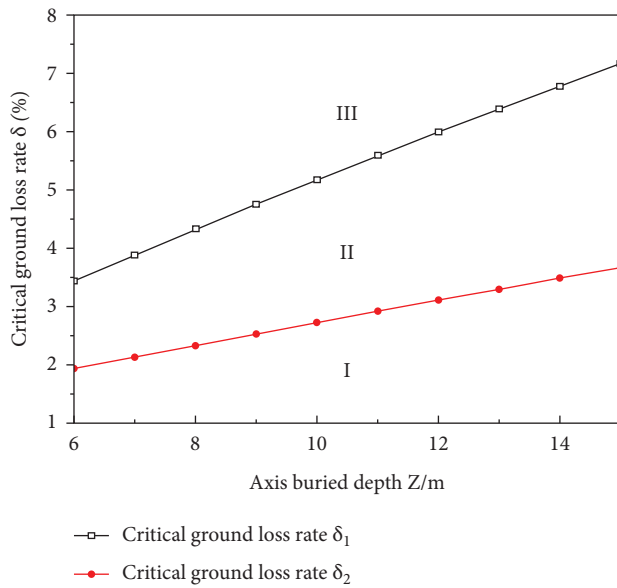


FIGURE 14: The critical ground loss ratio versus tunnel depth [24].

formula can better fit the characteristics of wide pipe jacking settlement trough. The correlation coefficient R of the improved Peck formula is in the range of 0.92~0.99. The correlation coefficient R of the uncorrected Peck formula is 0.62~0.89, as shown in Figure 17. This shows that the improved formula has a good prediction effect on surface settlement caused by quasi-rectangular pipe jacking construction.

5. Analysis of Sensitivity Factors of Ground Settlement

5.1. Analysis of Grouting Pressure. In the construction of shield and pipe jacking, the ground settlement can be controlled by adjusting the grouting pressure during the grout. Due to the difference between shield grout and pipe jacking grout, changes in grouting pressure have different effects on ground surface settlement. In this study, the sensitivity of grouting pressure to the ground settlement is studied by adjusting the variation of grouting pressure parameters.

The ground settlement of shield and pipe jacking is shown in Figure 18 under the conditions of 176 kPa (under balance

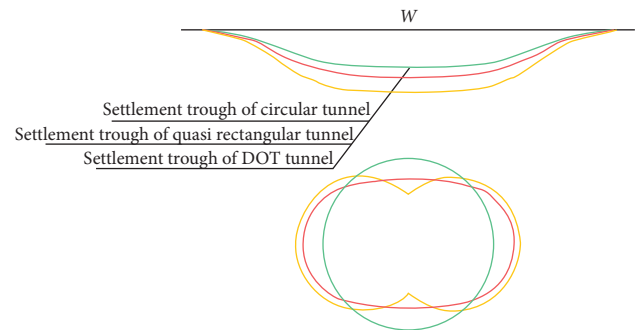


FIGURE 15: The rough sketch of surface settlement induced by circular, DOT, and quasi-rectangular tunnel shield construction. [24].

pressure 20%), 220 kPa (balance pressure), and 264 kPa (surplus balance pressure 20%). The ground settlement of the shield increased by 1.26 mm under 176 kPa and decreased by 0.68 mm under 264 kPa. The ground settlement of pipe jacking increases 8.19 mm when grouting pressure is under 176 kPa and decreases 5 mm when grouting pressure is under 264 kPa. Under the same grouting pressure change, the ground settlement of the shield is much smaller than that of pipe jacking. Since the grouting of pipe jacking has a certain pressure-holding effect, the continuous grouting pressure has a supporting effect on the stratum, which effectively reduces the surface settlement. Therefore, the control of pipe jacking grouting pressure on surface settlement is much more obvious compared with shield grouting pressure.

5.2. Analysis of Grout Materials. The change of elastic modulus of grout material will affect ground settlement [25]. In order to study the influence of grout material strength change (mainly for the elastic modulus of grout material) on shield and pipe jacking. In this study, the long-term hardening elastic modulus of shield grout material was increased by 200% (8 MPa), 250% (10 MPa), and 300% (12 MPa), respectively. The pipe jacking grout material does not harden, its elastic modulus is similar to the shield grout material's initial elastic modulus. Therefore, the pipe jacking grout material is enhanced with 0.6 MPa as the benchmark, which is increased by 150% (0.9 MPa) and 200% (1.2 MPa), respectively.

As shown in Figure 19(a), when the long-term harden elastic modulus of shield grout material increases by 200%, the

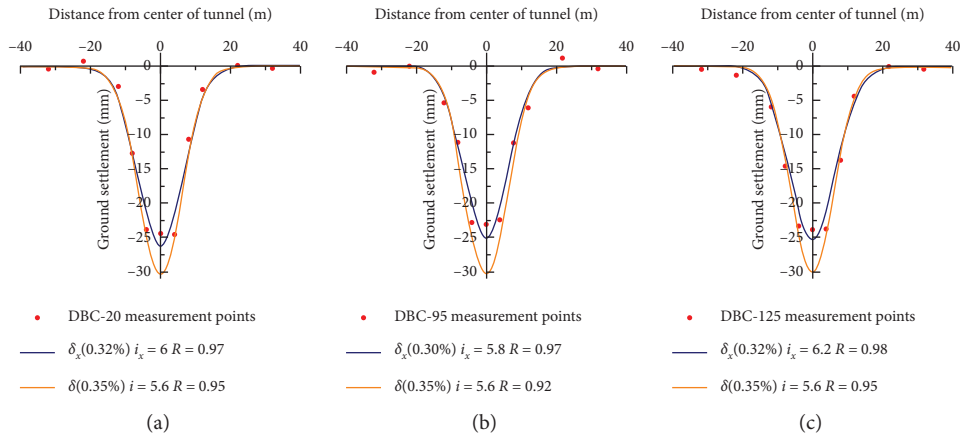


FIGURE 16: Field measurement and Peck formula optimization of shield ground surface settlement: (a) DBC-20. (b) DBC-95. (c) DBC-125.

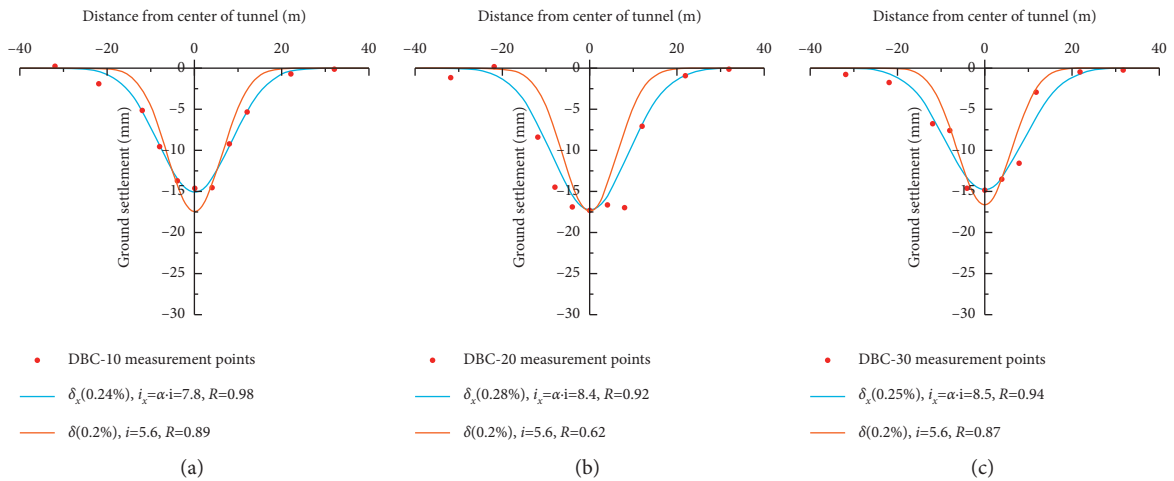


FIGURE 17: Field measurement and Peck formula optimization of pipe jacking ground surface settlement: (a) DBC-10. (b) DBC-20. (c) DBC-30.

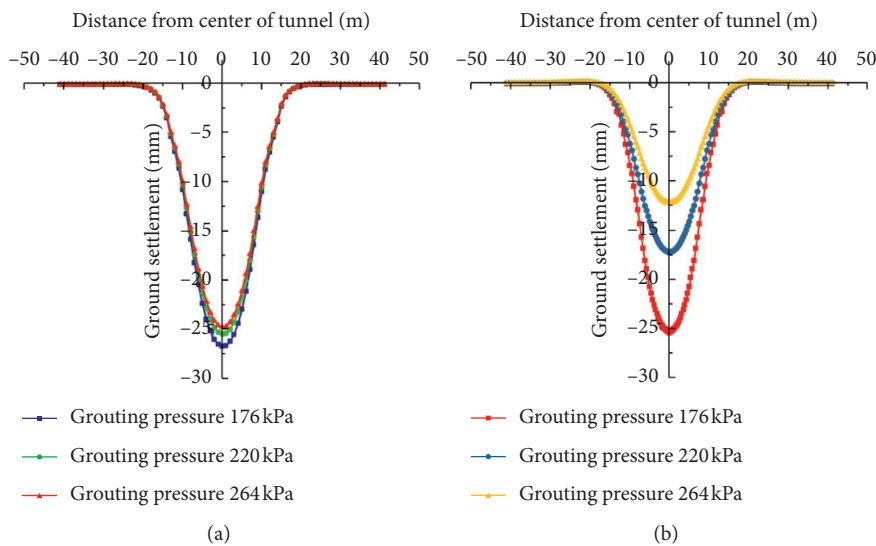


FIGURE 18: Ground surface settlement of shield and pipe jacking under different grouting pressures: (a) Ground surface settlement of shield. (b) Ground surface settlement of pipe jacking.

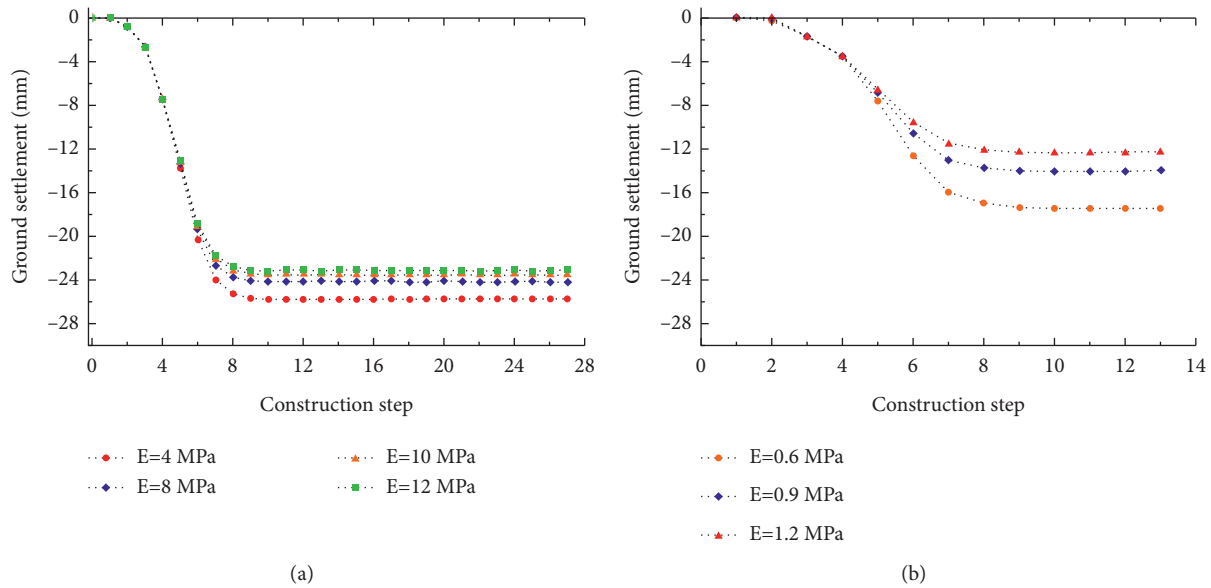


FIGURE 19: Longitudinal ground settlement of shield and pipe jacking under different elastic modulus: (a) Longitudinal settlement of shield. (b) Longitudinal settlement of pipe jacking.

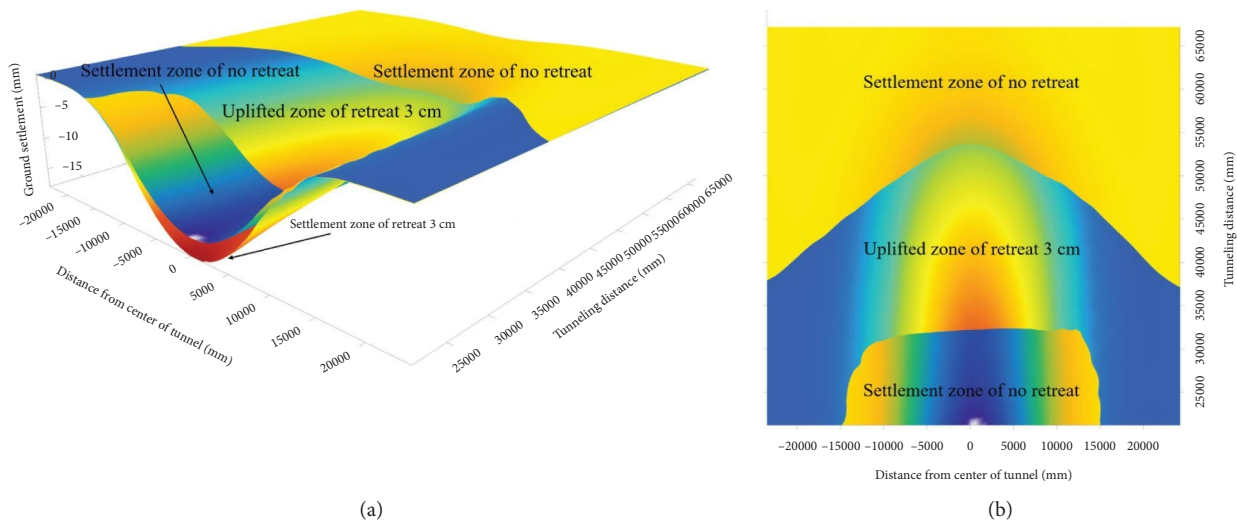


FIGURE 20: 3D map and plane map of settlement superposition when no retreat and 3 cm retreat of pipe section: (a) No retreat and retreat 3 cm settlement superimposed 3D map. (b) No retreat and retreat 3 cm settlement superposition plane map.

settlement decreases by 1.6 mm compared with that of 4 MPa. The settlement decreases by 2.2 mm when the reinforcement is 250% and 2.63 mm when the reinforcement is 300%. It can be seen from Figure 19(b) that when the elastic modulus of pipe jacking grout material increases from 0.6 MPa to 0.9 MPa, the settlement decreases by 3.4 mm, and when the elastic modulus increases to 1.2 MPa, the settlement decreases by 5 mm. By comparison, it can be found that with the enhancement of the pipe jacking grout material elastic modulus the influence on the ground settlement is more obvious than that of the shield.

5.3. Analysis of Tunnelling Pressure Difference. In the process of pipe jacking tunnel construction, due to the differential pressure between the soil pressure in front of the excavation

surface and the cutter head, the head of the machine will retreat. Compared with the grout material used in the shield method, the grout material used in pipe jacking will aggravate the overall retreat of the pipe section. In this project, it is measured that the overall retreat of the pipe jacking section is about 2 cm ~ 3 cm, and the overall retreat of the lining ring of the shield method is about 1 cm. Considering that the distance of pipe jacking interval is shorter than that of shield interval and the retreat is larger than that of shield, this study mainly focuses on the influence of pipe jacking interval retreat on ground settlement. By applying the forced displacement in the range of 1 cm ~ 3 cm in the three-dimensional model, the influence of ground settlement caused by the overall displacement of the pipe section is shown in Figure 20.

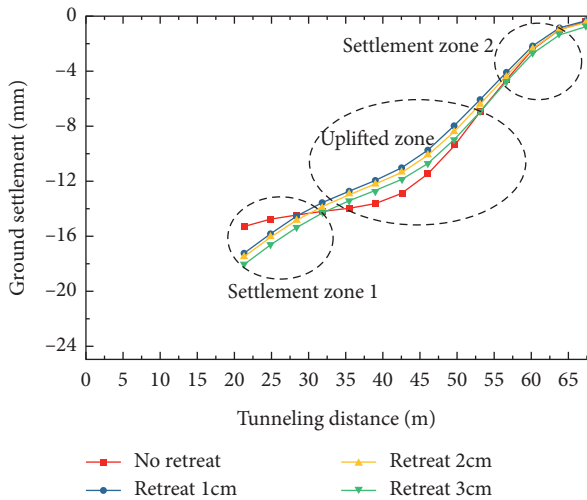


FIGURE 21: The longitudinal ground surface settlement is caused by pipe section retreat.

After the overall displacement is applied to the pipe section, it can be seen in Figure 21 that it can be divided into three impact zones: settlement zone 1 (20 m ~ 30 m), uplift zone (35 m ~ 52 m), and settlement zone 2 (55 m ~ 65 m). When the displacement of 1 cm is applied, the maximum settlement of 1.93 mm appeared on settlement zone 1. The uplift zone shows a maximum uplift of 1.9 mm. When the retreat displacement increases, the settlement in settlement zone 1 will also increase. When the retreat increases by 2 cm, the settlement of settlement zone 1 increases by 0.7 mm at most, and the uplift zone's uplift will gradually decrease, and the maximum will decrease by 0.77 mm. At the same time, with the increase of retreat, settlement zone 2 gradually appears, the maximum settlement in settlement zone 2 is 0.31 mm. The main reason for the above phenomenon is that the cutter head's retreating formed a certain gap, leading to the front soil settlement. Due to the early construction of the tunnel in the direction of the originating well, the settlement is larger than that of other areas, and the retreat of the pipe section will aggravate the settlement in the direction of the originating well, resulting in the overall rotation of the pipe section. This also reduces the settlement of the middle area.

6. Conclusions

In this study, the differences in ground settlement caused by the pipe jacking method and the shield method in the same stratum are investigated by numerical analysis. The ground surface settlement caused by the two construction methods is compared and verified with the measured settlement data. At the same time, the DOT Peck formula is modified, and the sensitive factors that have the greatest impact on ground surface settlement in the tunnelling process are given through parameter analysis.

The numerical simulation results show that the ground settlement caused by the shield is larger than that caused by pipe jacking in each stage of tunnelling process. The final ground surface settlement of pipe jacking is about 17.4 mm, and the final ground surface settlement of shield is about 25.4 mm.

Field measurement shows that the ground surface settlement range of the pipe jacking is 13.59 mm ~ 17.4 mm, and that of the shield is 23.11 mm ~ 24.5 mm, which verifies that the shield has a larger settlement than the pipe jacking. Two correction coefficients λ and α are proposed to correct the DOT Peck formula. When shield engineering λ is 0.85 ~ 0.91 and α is 1 ~ 1.1, the formula is more accurate for settlement prediction. For the pipe jacking λ in 1.2 ~ 1.4, α in 1.4 ~ 1.6. The correlation coefficient R reaches 0.92 ~ 0.99, which has a good prediction effect on quasi-rectangular pipe jacking.

By comparing the grout pressure of shield and pipe jacking under the condition of under balance pressure and surplus balance pressure, it can be concluded that the change of pipe jacking grouting pressure has a more significant influence on surface settlement. Under 176 kPa, the pipe jacking settlement increases by 8.19 mm, and the shield is 1.26 mm. The ground settlement of the pipe jacking is reduced by 5 mm and the shield is 0.68 mm under 264 kPa.

It can be found from the elastic modulus enhancement of shield and pipe jacking grout materials that pipe jacking is more conducive to reducing ground surface settlement than shield after increasing the elastic modulus of grout materials. When the long-term hardened elastic modulus of shield grout materials increases by 300%, the settlement decreases by about 2.63 mm compared with 4 MPa. When the elastic modulus of pipe jacking grout materials increases by 200%, the settlement decreases by 5 mm.

In the numerical simulation, the pipe section applied 1 cm ~ 3 cm overall retreat, and the surface settlement value increased by 1.93 mm in settlement zone 1. The surface settlement in the uplift zone will decrease by about 1.9 mm, and the surface settlement in settlement zone 2 will gradually increase with the increase of the retreat.

Data Availability

The data are available on request.

Conflicts of Interest

The authors declare that there are no conflicts of interest regarding the publication of this paper.

Acknowledgments

The following projects are appreciated for their funding to this study: "Social Development Project of Science and Technology Commission of Shanghai Municipality (21DZ1201105)," "The Fundamental Research Funds for the Central Universities (21D111320)," and "Shanghai Rising-Star Program of China (18QB1403800)."

References

- [1] Li Pei, T. Wang, and X. Zhang, "Composite Technology application study on pipe jacking and shield engineering," *Special Structures*, vol. 36, no. 1, 2019, in Chinese.
- [2] Editorial Department of China Journal of Highway and Transport, "Review on China's traffic tunnel engineering

- Research,” *China Journal of Highway and Transport*, vol. 35, no. 4, pp. 1–40, 2022, in Chinese.
- [3] J. Dalong, S. Xiang, and Y. Dajun, “Theoretical analysis of three-dimensional ground displacements induced by shield tunneling,” *Applied Mathematical Modelling*, vol. 79, pp. 85–105, 2020.
- [4] G. Wei, X. Zhang, Y. Xu, and Z. Wang, “Prediction of ground settlement due to excavation of a quasi-rectangular shield tunnel based on stochastic medium theory,” *Geotechnical & Geological Engineering*, vol. 37, no. 5, pp. 3605–3618, 2019.
- [5] J. Wang, P. Zhou, Z. Song, S. Li, and Q. Zhang, “A new calculation method for tunneling-caused stratum settlement,” *KSCE Journal of Civil Engineering*, vol. 26, pp. 1–17, 2022.
- [6] R. B. Peck, “Deep excavations and tunneling in soft ground,” in *Proceedings of the 7th International Conference on Soil Mechanics and Foundation Engineering (Mexico)*, pp. 225–290, Mexico, MX, USA, August 1969.
- [7] P. B. Attewell, “Predicting the dynamics of ground settlement and its derivatives caused by tunnelling in soil,” *Ground Engineering*, vol. 15, no. 8, pp. 13–22, 1982.
- [8] I. Ocak, “A new approach for estimating the transverse surface settlement curve for twin tunnels in shallow and soft soils,” *Environmental Earth Sciences*, vol. 72, no. 7, pp. 2357–2367, 2014.
- [9] S. L. Chen, C. Ho, and Y. C. Kuo, “Three-dimensional numerical analysis of ground surface settlement induced by the excavation of shield tunnels,” *Tunnel Management, Emerging Technologies, and Innovation*, pp. 80–87, 2011.
- [10] L. X. Gao, X. J. Yang, and L. K. Qin, “Finite element analysis of the surface settlement induced by the shield tunnel construction,” *Applied Mechanics and Materials*, Trans Tech Publications Ltd, vol. 501–504, pp. 111–114, 2014.
- [11] Y. Fang, Z. Chen, L. Tao, J. Cui, and Q. Yan, “Model tests on longitudinal surface settlement caused by shield tunnelling in sandy soil,” *Sustainable Cities and Society*, vol. 47, Article ID 101504, 2019.
- [12] Z. Zhou, H. Ding, L. Miao, and C. Gong, “Predictive model for the surface settlement caused by the excavation of twin tunnels,” *Tunnelling and Underground Space Technology*, vol. 114, Article ID 104014, 2021.
- [13] X. Hu, C. He, Z. Peng, and W. Yang, “Analysis of ground settlement induced by Earth pressure balance shield tunneling in sandy soils with different water contents,” *Sustainable Cities and Society*, vol. 45, pp. 296–306, 2019.
- [14] D. Lu, Q. Lin, Y. Tian, X. Du, and Q. Gong, “Formula for predicting ground settlement induced by tunnelling based on Gaussian function,” *Tunnelling and Underground Space Technology*, vol. 103, Article ID 103443, 2020.
- [15] X. Wang, T. von Schmettow, X. Chen, and C.-Q. Xia, “Prediction of ground settlements induced by twin shield tunnelling in rock and soil—a case study,” *Underground Space*, vol. 7, 2022.
- [16] S. R. Moeinossadat and K. Ahangari, “Estimating maximum surface settlement due to EPBM tunneling by Numerical-Intelligent approach - a case study: tehran subway line 7,” *Transportation Geotechnics*, vol. 18, pp. 92–102, 2019.
- [17] W. Ma, B. Wang, X. Wang, S. Zhou, and B. Wang, “Soil layer disturbance caused by pipe jacking: measurement and simulation of a case study,” *KSCE Journal of Civil Engineering*, vol. 25, no. 4, pp. 1467–1478, 2021.
- [18] Y. Xu, Y. Wang, and F. Chao, “Research on ground deformation caused by rectangular pipe jacking construction,” *Chinese Journal of Underground Space and Engineering*, vol. 14, no. 1, pp. 192–199, 2018, in Chinese.
- [19] D. J. Ren, Y. S. Xu, J. S. Shen, A. Zhou, and A. Arulrajah, “Prediction of ground deformation during pipe-jacking considering multiple factors,” *Applied Sciences*, vol. 8, no. 7, 2018.
- [20] X. Yang and Y. Li, “Research of surface settlement for a single arch long-span subway station using the Pipe-roof Pre-construction Method,” *Tunnelling and Underground Space Technology*, vol. 72, pp. 210–217, 2018.
- [21] J. Tang, S. Li, and Y. Zhu, “Measurement and analysis of settlement induced by rectangular pipe jacking in silt stratum,” *Advances in Materials Science and Engineering*, vol. 2021, Article ID 8347227, 17 pages, 2021.
- [22] S. Ma, M. Li, J. Jin, and K. Bai, “The influence of shallow buried double-line parallel rectangular pipe jacking construction on ground settlement deformation,” *Alexandria Engineering Journal*, vol. 60, no. 1, pp. 1911–1916, 2021.
- [23] Q. Li, *Comparison of Equivalent Circle Zone Method and Displacement Convergence Method in Analyzing Construction Effects of Shield Tunneling*, Suzhou University, Suzhou, China, 2018, in Chinese.
- [24] F. Zhang, X. Kou, and J. Huang, “Application of Peck formula and its modified versions in ground settlement prediction during quasi-rectangular tunnelling,” *Modern Tunnelling Technology*, vol. 53, no. S1, pp. 189–194, 2016, in Chinese.
- [25] X. Yang, R. Zhang, K. Fang, S. Liu, and Z. Yang, “Study on the Influence of shield synchronous grouting slurry performance and the optimization of its proportion,” *Geotechnical Engineering Technique*, vol. 35, no. 5, pp. 336–340, 2021.